Journal of Heat Transfer

Published Monthly by ASME

RESEARCH PAPERS

Experimental Techniques

Porous Media

Combustion and Reactive Flows

Natural and Mixed Convection

Radiative Heat Transfer

Micro/Nanoscale Heat Transfer

Conduction

TECHNICAL BRIEFS

(Contents continued)

The ASME Journal of Heat Transfer is abstracted and indexed in the following:

Applied Science and Technology Index, Chemical Abstracts, Chemical Engineering and Biotechnology Abstracts (Electronic equivalent of Process and Chemical Engineering), Civil Engineering Abstracts, Compendex (The electronic equivalent of Engineering Index), Corrosion Abstracts, Current Contents, E & P Health, Safety, and Environment, Ei EncompassLit, Engineered Materials Abstracts, Engineering Index, Enviroline (The electronic equivalent of Environment Abstracts), Environment Abstracts, Environmental Engineering Abstracts, Environmental Science and Pollution Management, Fluidex, Fuel and Energy Abstracts, Index to Scientific Reviews, INSPEC, International Building Services Abstracts, Mechanical & Transportation Engineering Abstracts, Mechanical Engineering Abstracts, METADEX (The electronic equivalent of Metals Abstracts and Alloys Index), Petroleum Abstracts, Process and Chemical Engineering, Referativnyi Zhurnal, Science Citation Index, SciSearch (The electronic equivalent of Science Citation Index), Theoretical Chemical Engineering

Analysis of Pulsed Thermography Methods for Defect Depth Prediction

J. G. Sun

Argonne National Laboratory,
9700 South Cass Avenue,
Argonne, IL 60439

Pulsed thermography is an effective technique for quantitative prediction of defect depth within a specimen. Several methods have been reported in the literature. In this paper, using an analysis based on a theoretical one-dimensional solution of pulsed thermography, we analyzed four representative methods. We show that all of the methods are accurate and converge to the theoretical solution under ideal conditions. Three methods can be directly used to predict defect depth. However, because defect features that appear on the surface during a pulsed thermography test are always affected by three-dimensional heat conduction within the test specimen, the performance and accuracy of these methods differs for defects of various sizes and depths. This difference is demonstrated and evaluated from a set of pulsed thermography data obtained from a specimen with several flat-bottom holes as simulated defects. [DOI: 10.1115/1.2165211]

Keywords: pulsed thermography, infrared thermal imaging, defect depth prediction, delamination

1 Introduction

Transient thermography (or thermal imaging) has been widely used to detect defects and determine defect depth. One such defect is delamination (or lateral crack) that may be present in and is of critical concern for advanced composite materials. Composite materials whose properties are sensitive to this type of defect include polymer matrix composites that are widely used for aircraft structures and ceramic matrix composites that are being developed for high-temperature engine applications. These composites consist of a fiber preform of several planar layers (plies) of fiber cloth and a continuous-phase matrix. Delaminations between the plies can significantly reduce the strength and performance of the composite components; therefore, they must be detected and evaluated [1,2].

Several thermography technologies have been developed to detect delamination defects. Two of the most frequently used modes are modulated and pulsed thermography. In modulated thermography, thermal excitation on a specimen surface is provided by a continuous wave of low-intensity thermal energy. The detection depth is related to a diffusion depth that is deeper in phase data than in amplitude data [3,4]. However, this technique is not quantitative for the determination of defect depth. In pulsed thermography, thermal energy is typically supplied by photographic flash lamps. Detection sensitivity and depth are directly related to the flash energy. Because the flash time is a well-defined instant, it can be used as a time reference for the prediction of defect depth, and essentially, all pulsed thermography methods utilize it. These pulsed thermography methods are investigated in this paper.

When pulsed thermal energy is applied, a thin layer of material on the sample surface is instantaneously heated to a high temperature. Heat conduction then takes place from the heated surface to the interior of the sample, leading to a continuous decrease of the surface temperature. The decay of the surface temperature T with time t was determined by Parker et al. [5] and is expressed as

$$T(t) = \frac{Q}{\rho C L}\left[1 + 2\sum_{n=1}^{\infty} \exp\left(-\frac{n^2\pi^2}{L^2}\alpha t \right) \right] \tag{1}$$

where Q is the heat deposited on the surface, ρ is density, C is specific heat, α is thermal diffusivity, and L is sample thickness. In deriving Eq. (1), it was assumed that the thermal flash is instantaneous, the heat is absorbed within a surface layer of negligible thickness, and there is no heat loss from the sample surfaces. Solutions for finite flash duration and finite absorption depth can also be found in the literature [6,7]. Equation (1) is the exact solution for one-dimensional (1D) heat conduction within a plate of uniform thickness under ideal flash thermography conditions as described above. Two features can be noted. First, the summation term approaches zero as time increases; thus, the surface temperature eventually reduces to $Q/\rho C L$. Because this is the temperature scale measured by an infrared camera with a fixed temperature resolution, an increase of flash energy Q will improve the detection sensitivity (higher signal output), whereas a thicker sample (large L) will reduce the detection sensitivity (at least in the deeper region). Second, the term $\alpha t/L^2$ is the only nondimensional variable in this equation. Therefore, the thermal diffusivity α and the sample thickness L cannot be independently determined from the flash thermography test. In fact, thermography is typically used to determine thermal diffusivity when thickness is measured or to determine thickness when diffusivity is known.

Figure 1 is a schematic diagram of a thermography setup for detection of a delamination (or lateral crack) within a specimen. The flash lamps provide the thermal impulse, and the infrared camera monitors the surface-temperature decay on the heated surface. When the heat flux reaches the delamination, which is filled by air with higher thermal resistance, the heat transfer rate is reduced in the region above the delamination. Therefore, the surface above this region will register a higher temperature than the surrounding areas, i.e., it is seen as a local "hot spot." The hot spot appears earlier during the transient if the delamination is shallow and later if the delamination is deep. Figure 2 illustrates the temperature variations at surface points 1 and 2 (marked in Fig. 1), where point 1 is at the region with a subsurface delamination and point 2 is at a normal (or reference) area. The temperature at point 1, T, is always higher but eventually approaches the temperature
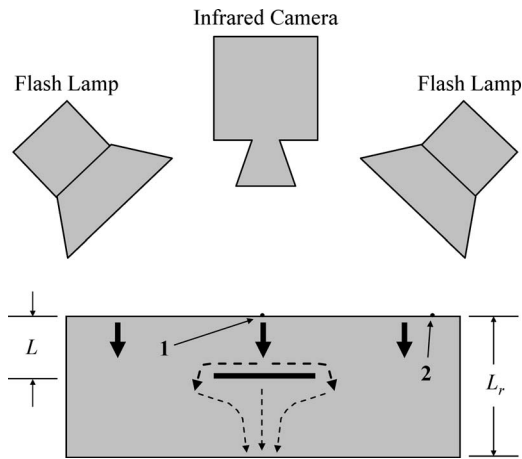
Fig. 1 Schematic diagram of pulsed thermography setup and heat conduction through and around lateral crack within test sample

Fig. 3 Temperature contrast ΔV as a function of dimensionless time ω_r for thickness ratio $y=0.2$, 0.5, and 0.8

at point 2, T_r because heat transfer around and through the delamination will eventually equalize the sample temperature.

Quantitative prediction of defect depth has been an important research topic in the past decade. Most work was based on the observation that the temperature contrast, $\Delta T = T - T_r$ in Fig. 2, can be used to determine defect depth [8–11]. Two such "empirical" methods are examined in this study: the peak temperature contrast and the peak slope of temperature contrast. Recently, Shepard et al. [12] identified a new method that is based on the peak second derivative of the temperature decay curve in the log scale. However, these three methods are experimental methods, which are presently not supported by fundamental theories. Each relies on empirical correlations by determining a characteristic time instant that can be related to the depth. A fourth method, recently developed by Sun [13], is based on least-squares fitting of a theoretical model to the temperature decay curve for a direct determination of depth. In this study, we developed the fundamental theories for the first three methods that allow for derivation of new and verification of existing empirical correlations. We show that all of these methods are derivatives of Eq. (1) and that they yield accurate results under the same ideal conditions. Theoretical analyses of these methods are presented in Sec. 2. The performance and accuracy of the methods, based on a set of thermography data, are evaluated in Sec. 3. Major findings are summarized in Sec. 4.

Fig. 2 Surface temperature decay curves T and T_r at points 1 and 2, respectively, as illustrated in Fig. 1

2 Theoretical Analysis of Thermography Methods

2.1 Peak Temperature-Contrast Method. The temperature contrast ΔT between a defect region and a reference region located in a "sound" material, as illustrated in Fig. 2, is dependent not only on the difference between the defect depth and the specimen thickness at the reference region, but also on the lateral size of the defect because of induced three-dimensional (3D) heat conduction around the defect. An analytical solution of this heat transfer process is not available. However, when the lateral size of the defect is large and the heat conduction through the air gap is negligible, the heat transfer within the central region from the surface to the defect can be considered 1D during the early period of the transient. Similarly, a region of the sound material far away from the defect can also be considered as experiencing 1D heat conduction. Therefore, these two regions can be approximated as two separate plates of different thicknesses. Temperature contrast between these two regions can be derived from the 1D heat conduction solution of Eq. (1). The effect of 3D heat conduction can be evaluated from experimental data and is discussed in Sec. 3.

When two plates of the same material but different thicknesses L and L_r are supplied with the same flash energy of Q, the temperature difference ΔT between their surfaces can be expressed as

$$\Delta T = T - T_r = \frac{Q}{\rho CL}\left[1 + 2\sum_{n=1}^{\infty} e^{-n^2\omega}\right] - \frac{Q}{\rho CL_r}\left[1 + 2\sum_{n=1}^{\infty} e^{-n^2\omega_r}\right] \quad (2)$$

where $\omega = \pi^2 \alpha t / L^2$ and $\omega_r = \pi^2 \alpha t / L_r^2$ are dimensionless times for the two plates. If we denote $y = L/L_r$ as the thickness ratio (therefore, $\omega = y^2 \omega_r$) and $V = T\rho CL_r/Q$ as the normalized temperature, Eq. (2) becomes

$$\Delta V = y^{-1} - 1 + 2\sum_{n=1}^{\infty} \left(y^{-1}e^{-n^2\omega_r/y^2} - e^{-n^2\omega_r}\right) \quad (3)$$

When time increases to infinity, the temperature difference approaches

$$\Delta V_\infty = y^{-1} - 1 \quad (4)$$

Therefore, ΔV reaches a constant at longer times, and this constant is the maximum temperature difference between the two plates. Equation (3) is plotted in Fig. 3 for $y=0.2$, 0.5, and 0.8. From the plot, we see that the temperature difference is smaller for larger y values. The asymptotic temperature difference ΔV_∞ is approximately reached for these y values when $\omega_r > 5$.

Because the temperature distribution on the specimen surface is measured directly as a function of time during a flash thermography test, temperature differences between surface points can be

Fig. 4 Slope of temperature contrast $d(\Delta V)/d\omega_r$ as a function of ω_r for $y=0.2$, 0.5, and 0.8

Fig. 5 Dimensionless peak-slope time ω_s and peak slope $d(\Delta V_s)/d\omega_r$ as functions of thickness ratio y

directly compared and analyzed with the two-plate analysis derived in Eq. (3). If T and T_r represent the surface temperatures at points 1 and 2, as illustrated in Fig. 1 (where L is the delamination depth and L_r is the specimen thickness), then ΔT represents the temperature contrast between the two points. Many studies have focused on examination of temperature contrast as a function of delamination depth. Unlike the two-plate condition, the temperature contrast will first increase with time as shown in Fig. 3, then decrease, and eventually approach zero because of the 3D conduction within the sample. It was found that the peak contrast time t_c, which corresponds to the maximum temperature contrast, is approximately proportional to the square of the defect depth (or L^2). The proportio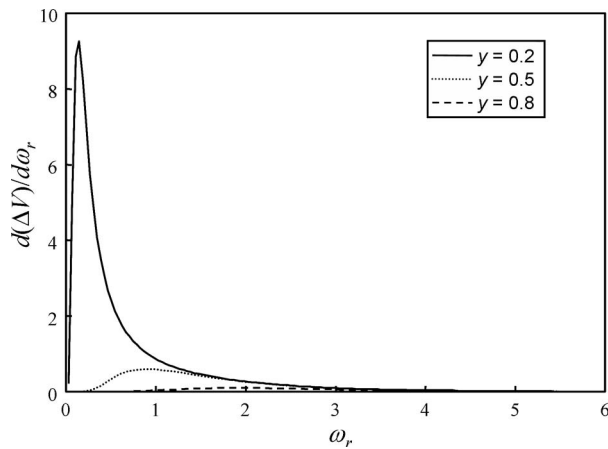nality coefficient depends on the size of the defect: the smaller the defect size, the lower the maximum contrast ΔT and the shorter the peak contrast time t_c [10]. Because ΔT should monotonically increase with time when 3D conduction is not present (see Fig. 3), the existence of a peak contrast is the result of the 3D heat conduction effect, the significance of which is related to the defect geometry and configuration.

Although temperature contrast ΔT is not a reliable parameter for quantitative determination of defect depth, it is widely used to analyze thermography data. In fact, ΔT is often considered the detection sensitivity and is the primary parameter to be investigated in all visual inspection of thermography data. ΔT has been used to determine detection sensitivity for small subsurface defects (flat-bottom holes) [14] and to evaluate thermal resistance of delamination air-gap thickness [15] and subsurface insert thickness [16]. It is noted that the observed maximum temperature contrast should be smaller than ΔV_∞ (or ΔT_∞) given in Eq. (3), and the amount of deviation is related to the significance of the 3D effect.

2.2 Peak Temperature-Contrast Slope Method. The slope or first derivative of the temperature contrast has also been examined for the prediction of defect depth [8–10]. From Eq. (3), the dimensionless temperature-contrast slope can be expressed as

$$\frac{d(\Delta V)}{d\omega_r} = \sum_{n=1}^{\infty} 2n^2 \left(e^{-n^2\omega_r} - y^{-3}e^{-n^2\omega_r/y^2}\right) \quad (5)$$

where ω_r is the dimensionless time scaled by the reference thickness. This expression is plotted in Fig. 4 for $y=0.2$, 0.5, and 0.8. It is noted that the slope reaches a maximum at an early time instant. This time instant is referred to as the peak-slope time t_s. It was found that the value of t_s is also approximately proportional to the square of the defect depth (L^2), and the proportionality coefficient does not depend on defect size [8–10]. The exact relationship between L and t_s can be determined by solving for t_s in Eq. (5) or,
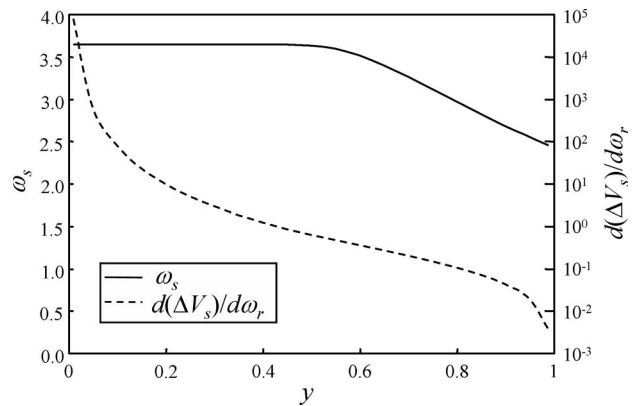
equivalently, from the condition $d^2(\Delta V)/d\omega_r^2=0$. Figure 5, where the solutions of peak slope $d(\Delta V_s)/d\omega_r$ and peak-slope time $\omega_s(=\pi^2\alpha t_s/L^2)$ are plotted as functions of y, shows that ω_s is essentially a constant at 3.6359 when $y<0.5$ (i.e., independent of y), with a maximum error of $<0.4\%$. When $y>0.5$, the numerical values plotted in Fig. 5 should be used to correlate L with t_s, once the thickness L_r (or y) is known. The peak-slope value $d(\Delta V_s)/d\omega_r$ is a strong function of the thickness ratio y, as seen in Fig. 5; thus, it could also be used to predict the defect depth. However, it is shown later that the peak-slope value is strongly affected by the 3D conduction effect whereas the peak slope time is not sensitive to the 3D effect.

Ringermacher et al. [9] found the following correlation between t_s and the defect depth L:

$$t_s = \frac{3.64L^2}{\pi^2\alpha} \quad (6)$$

In Eq. (6), the proportionality constant of 3.64 is very close to the constant of 3.6359 from the theoretical solution. However, as described above, Eq. (6) is accurate only when the defect depth is thinner than one-half the thickness at the reference point.

When applying this method, a major problem has been the prior determination of a reference point that is known on a sound material. The method developed by Ringermacher et al. [9] used the averaged temperature from the entire surface as the reference temperature, which can work well when the defect region is small and the surface is uniformly illuminated. Another concern is its accuracy in dealing with noisy data. Data processing for this method involves subtraction and differentiation of two experimental time series, and both of these operations increase noise and reduce accuracy.

From Eqs. (3) and (5), it is evident that both temperature contrast and its first derivative are zero when $y=1$. Therefore, the peak-slope method cannot determine the thickness of the reference region. When $y>1$, both temperature contrast and the first derivative will become negative and could potentially be used to predict thickness. However, because the absolute value of the temperature contrast becomes very small, it would be difficult to determine the negative peak slope. Martin and Gyekenyesi [17] attempted to determine specimen thickness with the peak-slope method. They found that the predicted sample thickness in the "good" material region varies significantly and depends on the selection of the reference region.

2.3 Logarithmic Peak Second-Derivative Method. Recently, Sheperd et al. [12] determined that the second derivative of the surface temperature in the logarithmic scale contains a peak that can be used to determine the defect depth. Unlike the situation in the temperature-contrast methods described above, the sec-
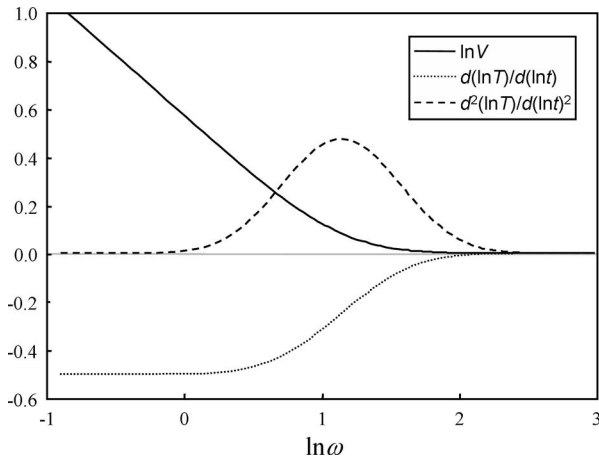
Fig. 6 Temperature and its first and second derivatives as functions of nondimensional time ω in log-log scale

ond derivative is calculated directly from the temperature decay at each surface point, without the need of a reference. This method can be directly analyzed by Eq. (1). The first derivative of the temperature is

$$\frac{d(\ln T)}{d(\ln t)} = \frac{t}{T}\frac{dT}{dt} \tag{7}$$

and the second derivative is

$$\frac{d^2(\ln T)}{d(\ln t)^2} = \frac{t}{T}\frac{dT}{dt} - \frac{t^2}{T^2}\left(\frac{dT}{dt}\right)^2 + \frac{t^2}{T}\frac{d^2T}{dt^2} \tag{8}$$

where

$$\frac{dT}{dt} = -\frac{Q}{\rho CL}\frac{2\omega}{t}\sum_{n=1}^{\infty} n^2 e^{-n^2\omega} \tag{9a}$$

and

$$\frac{d^2T}{dt^2} = \frac{Q}{\rho CL}\frac{2\omega^2}{t^2}\sum_{n=1}^{\infty} n^4 e^{-n^2\omega} \tag{9b}$$

Note that both the first and second derivatives in the logarithmic scale in Eqs. (7) and (8) are dimensionless variables. The logarithmic normalized temperature ln V and its first and second derivatives are plotted in Fig. 6, which shows that the first derivative is constant at -0.5 within a short time period and approaches zero when time increases, and the second derivative is zero at early and later time periods, and reaches a maximum in between. When Eq. (8) is solved by a numerical method, the maximum second derivative $d^2(\ln T)/d(\ln t)^2$ is 0.47366 and it occurs when the nondimensional time ω is equal to π. Therefore, the peak second-derivative time t_2 is

$$t_2 = \frac{\pi L^2}{\pi^2 \alpha} \tag{10}$$

By comparing Eq. (10) to Eq. (6), we see that the peak second-derivative time t_2 occurs slightly earlier than the peak-slope time t_s. It is commonly understood that a method based on an early characteristic time is more likely to capture the peak defect signal before it is affected by 3D conduction, which could lead to more accurate depth determination.

The capability to derive defect depth directly from the temperature data for each individual surface point represents a significant advantage for automation in thermography data processing. In the temperature-contrast methods described in Secs. 2.1 and 2.2, the requirement to provide reference data has been a major obstacle and a tedious step in quantitative analysis of thegmography data.

However, the peak second-derivative method requires second-order differentiation of the measured temperature decay curve, which normally leads to very noisy data. The method developed by Sheperd et al. [12] is based on a curve fit of measured (logarithmic) temperature by a polynomial function. Because of the complex profile of the temperature decay, a high-order polynomial is needed. Special care should be taken to ensure that the polynomial function actually fits the exact peak position of the second derivative.

2.4 Least-Squares Fitting Method. All of the methods described above are based on finding a characteristic time to correlate with defect depth. These methods are susceptible to signal noise that is typically large in thermography data. On the other hand, methods based on curve fitting are usually not sensitive to data noise and have been used in laser-flash diffusivity methods [18]. Such a curve-fitting method for depth prediction has been developed recently by Sun [13]. This method utilizes a theoretical heat transfer model to fit the temporal thermography data at each surface point.

Because Eq. (1) is the exact solution for a plate of uniform thickness under flash heating conditions, it can be used to fit the thermography data for the area of the plate that contains no subsurface defect. Close examination of the temperature decay curve of a surface point with a subsurface lateral crack (see T in Fig. 2) reveals that its initial temperature variation also follows Eq. (1). Figure 2 shows that this approximation is valid in the time period $0 < t < t_a$ (t_a to be determined later). In the time period $t_a < t < t_b$, the temperature decreases approximately linearly, due to heat conduction through and around the crack (or 3D conduction effect), as illustrated in Fig. 1. The slope s of this linear portion of the curve depends on the crack-gap thickness and the distance from the point to the crack edge. At longer times, $t > t_b$, the temperature curve T simply approaches the final steady temperature of the sample. This portion of the temperature curve is not used to calculate depth.

A theoretical model that is approximately valid for the time period $0 < t < t_b$ can be expressed as

$$T(t) \approx A\left[1 + 2\sum_{n=1}^{\infty} \exp\left(-\frac{n^2\pi^2}{L^2}\alpha t\right)\right] - st \tag{11}$$

where it is assumed that thermal diffusivity α is known. The slope s is determined by linear fitting of the experimental data in the time period $t_a < t < t_b$. It should be noted that s is usually small and is zero for a defect-free plate of uniform thickness. The time instants t_a and t_b were optimized from several calculations and were chosen as

$$t_a = \frac{L^2}{2\alpha} \quad \text{and} \quad t_b = 3t_a \tag{12}$$

The theoretical model in Eq. (11) is used to curve-fit the experimental temperature/time data to derive the amplitude A and thickness L. If a surface point is on a sound material without subsurface defect, the predicted thickness L is the sample thickness. When a surface point is on a region that contains a subsurface lateral crack, the predicted thickness L is the defect depth.

The accuracy of thickness prediction in this method is not affected by uneven surface heating during the experiment because the data analysis is performed one pixel at a time and the temperature amplitude is explicitly calculated. This method also accounts for part of the 3D heat conduction effect and therefore is expected to be more reliable and robust when the 3D effect is significant. Further optimization can be achieved if the temperature decay between $t_a < t < t_b$ is modeled by an appropriate function instead of a constant slope.

2.5 Finite-Flash-Duration Effect. Most of the flash thermography systems utilizes photographic flash lamps to provide high-energy heating on the specimen surface. Typically, the energy de-

cay time of these flash lamps is long (compared to a laser flash), ranging from several to more than ten milliseconds. The flash-duration effect for these lamps was studied by Sun and Erdman [19] and Sun and Benz [20], who found that the flash energy decay $f(t)$ typically follows an exponential curve,

$$f(t) = \frac{2Q}{\tau} e^{-(2t/\tau)} \tag{13}$$

where Q is the total flash energy and τ is a characteristic flash duration. Under the thermal impulse given in Eq. (13), Eq. (1) becomes [20]

$$T(t) = \frac{Q}{\rho CL} \left\{ 1 - \exp\left(-\frac{2t}{\tau}\right) + 2\sum_{n=1}^{\infty} \left(\frac{n^2\pi^2\tau\alpha}{2L^2} - 1\right)^{-1} \right. $$
$$\left. \times \left[\exp\left(-\frac{2t}{\tau}\right) - \exp\left(-\frac{n^2\pi^2}{L^2}\alpha t\right) \right] \right\} \tag{14}$$

Equation (14) can be used to analyze all of the methods described above. For the characteristic-time methods (Eqs. (6) and (10)), the flash-duration effect will become important when the characteristic times are comparable to flash duration. For the theoretical model in Eq. (11), the term in the square brackets should be replaced by the term in the braces in Eq. (14), i.e.,

$$T(t) \approx A\left\{ 1 - \exp\left(-\frac{2t}{\tau}\right) + 2\sum_{n=1}^{\infty} \left(\frac{n^2\pi^2\tau\alpha}{2L^2} - 1\right)^{-1} \right. $$
$$\left. \times \left[\exp\left(-\frac{2t}{\tau}\right) - \exp\left(-\frac{n^2\pi^2}{L^2}\alpha t\right) \right] \right\} - st \tag{15}$$

3 Experimental Evaluation of Thermography Methods

The three methods described in Secs. 2.2–2.4 are based on the 1D solution Eq. (1). Under ideal conditions (instantaneous flash and pure surface heating), where 1D conductions dominate within the test specimen, all methods should accurately predict the defect depth and, for the peak second-derivative and least-squares fitting methods, the specimen thickness. Only under conditions where 3D conduction is significant, such as delaminations of small lateral dimensions, these methods may differ in prediction accuracy. The theoretical model in Eq. (11) explicitly account for part of the 3D conduction effect, whereas the slope and second-derivative methods do not. The performance and accuracy of these three methods are evaluated below from the experimental data of a test sample.

3.1 Test Sample. Because it is difficult to make a calibration sample that contains well-defined delamination defects at specified depths, samples with machined flat-bottom holes are typically used to simulate delamination defects. In this study, a ceramic composite sample was used. It consisted of eight plies of SiC continuous-fiber cloth and a SiNC matrix [21]. The composite was not completely densified and contained some near-surface defects and distributed porosities. Six flat-bottom holes of various diameters and depths were machined at the back surface, as illustrated in Fig. 7. The depths, listed in Table 1, refer to the distance from the hole bottoms to the front surface, where thermography data were taken. The thickness of the sample ranged from 2.3 to 2.7 mm; its thermal diffusivity varied because of material porosities. An average thermal diffusivity was estimated to be 0.97 mm^2/s [21].

3.2 Experimental Data. The experimental temperature data were obtained by using a flash-thermography-system setup, as illustrated in Fig. 1. During the test, flash lamps were triggered at $t=0$ to deposit a nearly instantaneous thermal impulse on the sam-
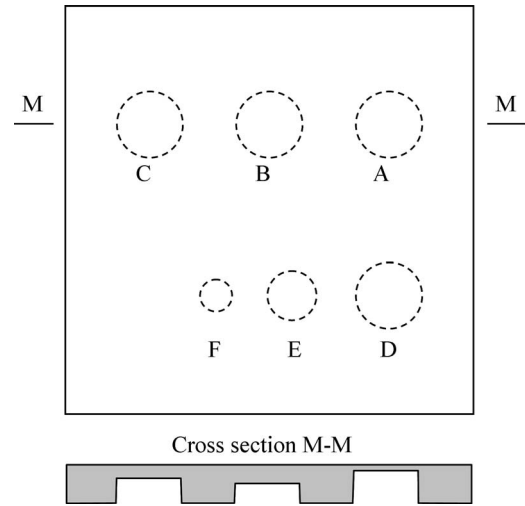
Fig. 7 Schematic illustration of ceramic sample with machined flat-bottom holes

ple's surface. The surface temperature variation was monitored by an infrared camera, which takes a series of thermal images that are stored in a PC for data processing. Each image (or frame) contains a two-dimensional (2D) array of pixels. The infrared camera used in this study was a midinfrared wavelength (3–5 μm) Phoenix camera manufactured by FLIR Systems, Inc. (Portland, OR). This camera contained a focal-plane array of 320×256-pixel infrared sensors, each converting the observed infrared radiation from a surface point to a digital value within a 14-bit dynamic range. By proper normalization of the camera, the infrared signal values in the 2D thermal images were proportional to the surface temperature. Each frame, therefore, represents a "snapshot" of the surface temperature at a particular time.

The number of total thermal images to be taken was determined by the length of the entire thermal transient period for the sample. A characteristic time for the thermal transient was the half-rise time $t_{1/2}$, which represents the time when the temperature at the back surface of the sample reaches half of the final equilibrium temperature (i.e., $Q/\rho CL$ in Eq. (1)). It is determined [5] as follows:

$$t_{1/2} = \frac{1.38L^2}{\pi^2\alpha} \tag{16}$$

In practice, the final equilibrium temperature is reached at about $5t_{1/2}$.

Pulsed thermal imaging data were taken on the front surface of the test sample shown in Fig. 7. The imaging rate was 170 Hz, with a total of 700 frames taken for a test duration of 4.1 s. For this sample, $5t_{1/2}$ is ~4.5 s. Test conditions were not optimal, to demonstrate the capabilities of the thermography methods to handle noisy experimental data. First, only one flash lamp was used (positioned at the right side); it provided nonuniform heating

Table 1 Depth predicted by various methods for flat-bottom holes A–F

Holes	Diameter (mm)	Depth (mm)	Predicted depth (mm)		
			Based on t_s	Based on t_2	Based on fit
A	7.5	0.25	0.203	0.218	0.232
B	7.5	1.12	1.16	1.18	1.147
C	7.5	0.97	1.01	1.00	0.973
D	7.5	0.87	0.916	0.911	0.893
E	5.0	0.78	0.798	0.773	0.79
F	2.5	0.85	0.823	0.804	0.857
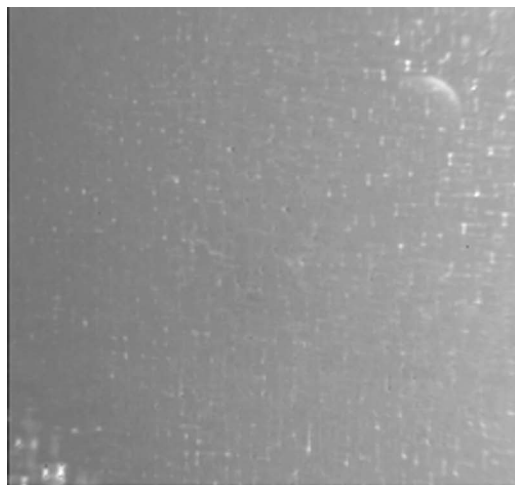
$t = 0.007$ s
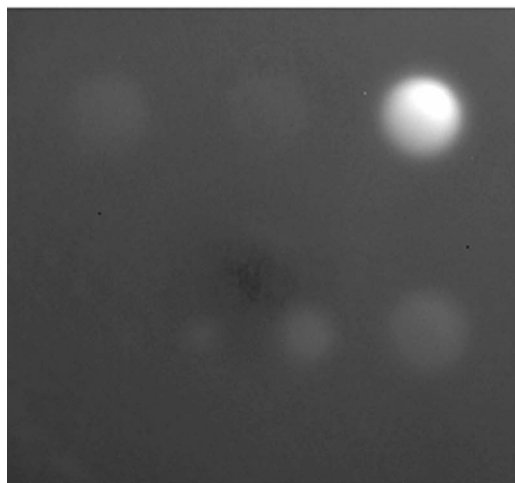
$t = 0.67$ s

Fig. 8 Thermal images on front surface of ceramic specimen taken at $t=0.007$ and 0.67 s after thermal flash

0 mm ▬▬▬▬ 3 mm

Fig. 9 Predicted depth image of ceramic sample with flat-bottom holes as illustrated in Fig. 7

bottom hole. The mean temperature curve within each area was further smoothed by time averaging. The temperature-decay and first-derivative curves for these flat-bottom-hole areas are plotted in Fig. 10 in log-log scale.

3.3 Peak-Slop Method. To establish the temperature contrast ΔT for the peak-slope method, a reference temperature is required. The selected reference area was 1.9×1.9 mm^2 and was located

on the sample surface. Second, the flash energy was kept low to prevent saturation of the data from the thinnest flat-bottom hole A. The flash duration for this lamp was 1.5 ms. In Fig. 8, two thermal images, one taken immediately after the flash and the other at 0.67 s after the flash, show that part of hole A is visible immediately after the flash because that region is thinner. We discovered that the bottoms of all the flat-bottom holes were inclined (similar to hole A); they were thinner at the top-right corner. The images in Fig. 8 also show uneven heating; the right side surface experienced relatively higher temperatures because it was closer to the flash lamp. A large defect (very thin delamination) is shown at the lower-left corner of the first frame after the flash, as are many small porosities (bright spots) distributed over the entire sample surface.

Figure 9 shows the predicted thickness image from the theoretical model of Eq. (15). The predicted depths for several points within hole A were not correct because the temperature decays for these points were too fast to be fitted (see Fig. 8). The depth variation within all of the inclined flat-bottom holes is also seen in Fig. 9.

The capability of the peak-slope, peak second-derivative, and least-squares fitting methods to predict the depths of flat-bottom holes A-F were compared to results obtained from the pulsed thermography. The analysis was carried out for a square area of 1.9 $\times 1.9$ mm^2 (10×10 pixels) located at the center of each flat-

Fig. 10 (a) Temperature and (b) first derivative of temperature as a function of time in log-log scale for flat-bottom holes A–F
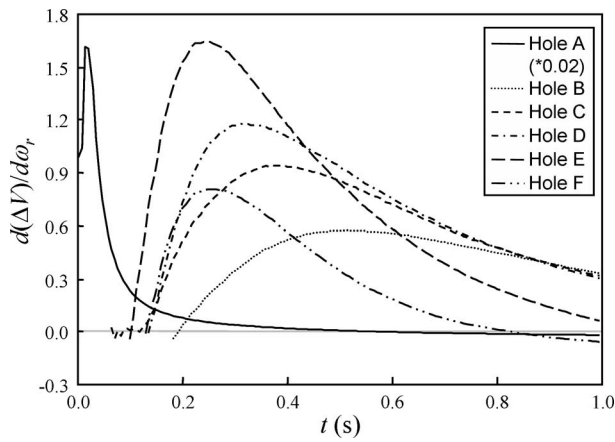
Fig. 11 Dimensionless temperature-contrast slope as a function of time for flat-bottom holes A–F

Fig. 12 Second derivative of temperature as a function of time in log-log scale for flat-bottom holes A–F

between flat-bottom holes A and D, as shown in Fig. 9. The thickness at the reference area was 2.34 mm; thus, the reference dimensionless time $\omega_r = 1.748t$ and was used for all data analysis. Because the flash energy was nonuniform over the sample surface, the maximum initial temperature rise at each flat-bottom hole was scaled to be the same as that at the reference area. With this scaling, the slopes of temperature contrasts for flat-bottom holes A-F are plotted in Fig. 11. The peak slopes and peak-slope times were determined from the curves in Fig. 11 and are listed in Table 2. The table shows that the peak-slope times are generally close to the theoretical values, whereas the peak slopes are lower than the theoretical values, excepted for hole A, which has a higher peak slope due to the flash duration effect. For hole F, the measured peak slope is much lower than theoretical. Because the diameter of hole F is only 2.5 mm, a smaller peak slope indicates a stronger 3D heat conduction effect at this region. Based on these observations, we concluded that the peak-slope value is strongly affected by experimental conditions (flash duration) and the 3D heat conduction effect; thus it cannot be reliably used to predict depth. On the other hand, depths calculated from the peak-slope times, as listed in Table 1, are more accurate.
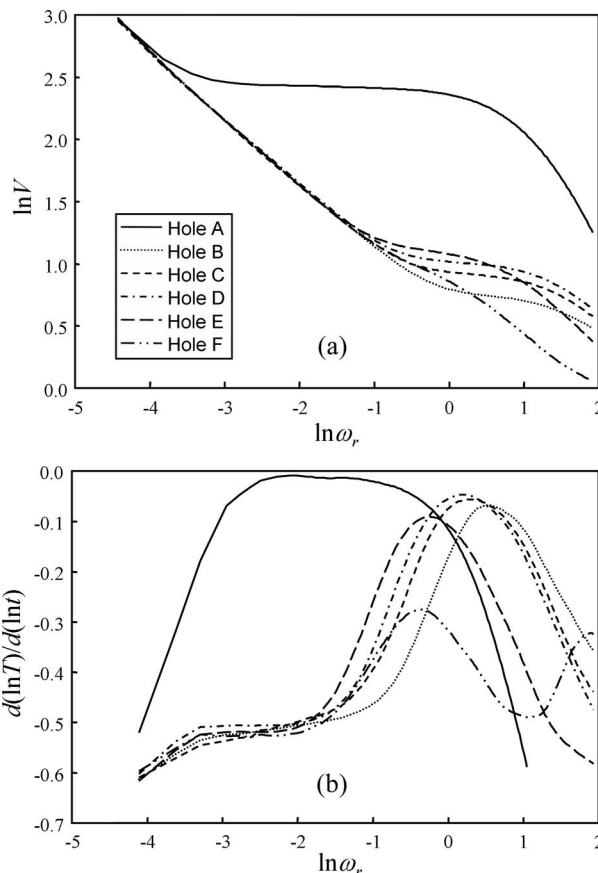
3.4 Peak Second-Derivative Method. The second derivatives of the surface temperatures for flat-bottom holes A-F are plotted in Fig. 12, which shows that all of the second derivatives display a small peak at an early time (ln $\omega_r = -3.6$). This small peak corresponds to the flash duration that is also observable in the first-derivative curves shown in Fig. 10. For hole A, the peak of the second derivative is coincident with the flash duration peak; thus, its peak value of 0.56 is higher than the theoretical value of 0.47. The peak second derivatives for all of the other holes are lower than the theoretical value because of the 3D conduction effect and the data averaging used to smooth these curves. The peak second-derivative time can be easily determined from Fig. 12 and can be used to calculate defect depth (using Eq. (10)) for

each curve. The predicted depths for all of the holes, based on the measured peak second-derivative times, are listed in Table 1.

3.5 Least-Squares Fitting Method. Figure 9 shows the predicted depth image of the specimen from the least-squares fitting method. The average depth for a 1.9×1.9 mm² area at the center of each hole can be directly read from the image in Fig. 9 and is listed in Table 1. For flat-bottom holes A, B, and F, the experimental (each for a single pixel) and fitted theoretical curves are shown in Fig. 13; data for other holes are similar to that for hole B. The experimental data reveal considerable variation at individual pixels, partially due to the nonuniformity of the sample material and partially to thermography system noise. The fitted theoretical curves generally match the entire experimental data well.

3.6 Discussion of Experimental Results. From the predicted depths listed in Table 1, it is clear that all three methods can provide accurate results that are typically within a few percent of the measured values. These methods, although all can be considered as derivatives of the 1D heat conduction theory expressed in Eq. (1), utilize different characteristics of the 1D solution. The calculation of depth in the first-and second-derivative methods is based on single characteristic times, determined from the experimental data. These characteristic times, t_s in Eq. (6) and t_2 in Eq. (10), are more than twice the half-rise time $t_{1/2}$ as defined in Eq. (16). Because the half-rise time already reflects the average material properties over the thickness (it is used to determine "aver-

Table 2 Measured and theoretical peak-slope time t_s and peak slope $d(\Delta V_s)/d\omega_r$ for the peak-slope method

Holes	Measured t_s (s)	Theoretical t_s (s)	Measured $d(\Delta V_s)/d\omega_r$	Theoretical $d(\Delta V_s)/d\omega_r$
A	0.0156	0.0237	80.7	61.3
B	0.513	0.476	0.57	0.683
C	0.384	0.357	0.949	1.051
D	0.319	0.287	1.17	1.459
E	0.242	0.231	1.64	2.034
F	0.257	0.274	0.805	1.57

Fig. 13 Measured and fitted first derivatives of temperature in log-log scale for flat-bottom holes A, B, and F

Journal of Heat Transfer

age" thermal diffusivity), these characteristic times are not affected by the minor nonuniformity of material properties along the thickness (or depth). However, longer characteristic times make these methods susceptible to the 3D conduction effect, which could prevent the corresponding first or second derivatives from reaching their theoretical maximums. This 3D conduction effect is most significant for the data of the small-diameter hole F, which has a lower slope peak in Fig. 11 and lower second-derivative peak in Fig. 12. Correspondingly, the predicted depths from these characteristic times are shallower than the measured depth, as seen in Table 1. These methods are also not well suited to incorporate the flash duration effect. The result of implementing the flash duration effect would be a look-up table, similar to that in Heckman [6], to replace the proportionality constants in Eqs. (6) and (10). Such a result would not be very practical. It is noted that the test described in this section used a flash lamp of very short duration, 1.5 ms; therefore, the flash duration effect is not expected to be significant.

The theoretical model in the least-squares fitting method accounts for part of the 3D conduction effect by adding of a constant-slope decay term. It can also easily incorporate the flash duration effect, as explicitly expressed in Eq. (15). Therefore, this method can perform better when the 3D conduction and the flash duration effects are present in the flash thermography data, as seen from the predicted depths in Table 1.

Data processing algorithms developed for these three methods differ completely and are worthy of practical consideration. For the peak-slope method, data processing involves subtraction of two time series of surface temperatures and then differentiation of the resultant series with time. Both operations can introduce considerable noise, especially in the early times. These early-time noises were more than an order of magnitude higher than the real signal in the current experiment; therefore, they w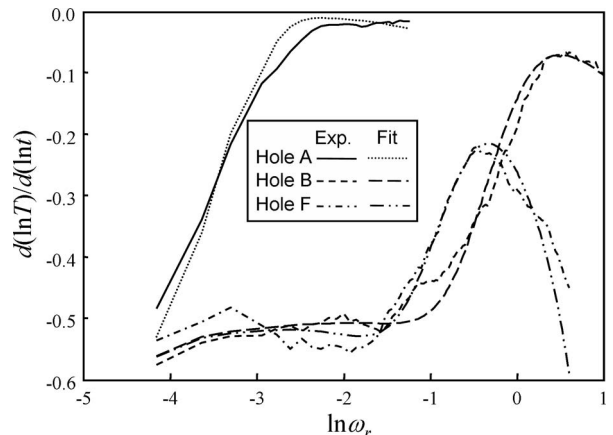ere not plotted in Fig. 11. The processing algorithm developed by Ringermacher et al. [9] utilizes a six-point-average scheme to determine the peak-slope time. For the peak second-derivative method developed by Shepard et al. [12], a high-order polynomial is used to fit each temperature-decay curve in the log-log domain. The resultant function is differentiated to determine the first and second derivatives. When considering the complex temperature decays, as illustrated in Figs. 10 and 12, caution should be taken to select the order of the fitting polynomial to ensure that it accurately fits the time of the peak second derivative. Because data noise is a major concern with respect to the accuracy of both the peak-slope and peak second-derivative methods, experimental data should have a higher signal-to-noise ratio, which can be obtained by using high-energy flash lamps.

On the other hand, the least-squares fitting algorithm directly generates a theoretical curve to fit each temperature curve by adjusting only two parameters, the magnitude A and depth L in Eq. (15). The algorithm also limits the duration of data fitting to a maximum time of t_b (Eq. (12)). Temperature data longer than t_b would either become constant (for a uniform-thickness sample) or come from 3D heat conduction and are not useful for depth calculation. Because limiting the temperature data and fitting them with a relatively simple model renders the least-squares fitting algorithm insensitive to experimental and system noise, it is more reliable in dealing with data of noisy and complex defect structures. The data processing for this method can be longer than the methods that determine characteristic times.

3.7 Discussion of Experimental Errors. Thermography data are subjected to two general types of errors: experimental system errors and experimental condition errors. When infrared detectors are used to measure surface temperature, detector linearity (between detector output and measured temperature) and noise are the major sources of system errors. Although the infrared detector can be easily normalized to respond linearly to temperature, detector noise is usually high, even for state-of-the-art infrared cameras (up to several percent). Data smoothing or filtering must be

used in processing thermography data, especially in subtraction and differentiation operations. In fact, all experimental curves presented in this paper are smoothed locally by a linear function. This type of data smoothing typically affects the magnitude but not the position of the peaks. For this reason, defect depth can be more reliably predicted by the peak times (such as t_s and t_2) than peak amplitudes.

Errors associated with deviation of actual experimental conditions from those assumed in the theoretical model include finite flash duration (when it is not accounted for in the theory), finite heat absorption depth (for translucent materials), nonuniform heating, heat loss by convection and radiation, and 3D conduction. The thermography theory assumes heat absorption within a thin layer on the surface, a condition normally satisfied for opaque materials. For translucent materials, it is a common practice to apply a black coat on the surface to prevent volume heating. Nonuniform heating usually has a negligible effect on heat transfer, but it must be explicitly or implicitly dealt with by the thermography methods. Heat losses due to convection and radiation become important at higher temperatures and are generally not concerned in room-temperature experiments [22] because of the low-temperature rises (typically within a few degrees above room temperature) involved over almost the entire duration of the experiments. This conclusion can be easily verified by testing the same sample with various thermal-pulse intensities (a much higher intensity was used in Sun [13]).

3D conduction is the most significant factor that affects the accuracy of the 1D theories. However, because it is induced from the disruption of the primary 1D conduction process by the delamination, the 3D process lags behind the 1D process, especially at the central region of large delaminations. The dimensionless parameter that is relevant to the 3D effect is the ratio of diameter to depth of the delamination, i.e., D/L. The 3D effect can be clearly identified by examining the theoretical 1D solution of $d(\ln T)/d(\ln t)$ and $d^2(\ln T)/d(\ln t)^2$ in Fig. 6 and the experimental results shown in Figs. 10(b) and 12. As seen in Fig. 6, both $d(\ln T)/d(\ln t)$ and $d^2(\ln T)/d(\ln t)^2$ should approach zero at longer times ($\ln \omega > 2.5$). For the experimental data shown in Fig. 10(b), the 3D effect can be characterized as the decrease of $d(\ln T)/d(\ln t)$ curves at longer times. For flat-bottom hole A, which has a large D/L value (=30), the 3D effect occurs much later after the 1D process is "completed." For smaller D/L, such as flat-bottom hole F ($D/L=3$), the 3D effect occurs much earlier and interferes with the 1D data. When D/L is further reduced, the 3D effect becomes dominant and, as a result, the delamination will not be detected. Experimental studies showed that delaminations with $D/L>1$ can usually be detected; delaminations with $0.5<D/L<1$ may be detected; and delaminations with $D/L<0.5$ cannot be detected [14]. For $d^2(\ln T)/d(\ln t)^2$ (see Fig. 12), the 3D effect is represented by a negative peak (may be followed by additional positive and negative peaks) after the initial positive peak from the primary 1D effect. The negative peak moves to earlier time when D/L is reduced and may eventually cancel out the positive peak from the 1D result.

Other sources of experimental errors may become important under certain conditions. Despite these errors, the depth predicted by the 1D theories presented in this paper is considered accurate. Figure 14(a) compares the predicted to actual depths, and Fig. 14(b) shows the prediction errors. The deviation of predicted depth is <0.06 mm, and the prediction error is $<5.5\%$ for all three methods when data for hole A are not included. The larger prediction error for hole A is due to the inadequate (slow) imaging speed for this shallow depth; thus, it is not indicative of the accuracy of the methods. In comparison, the ASTM standard accepts a $\pm5\%$ measurement error for using the pulsed thermography method to measure thermal diffusivity [23], where the 3D effect is
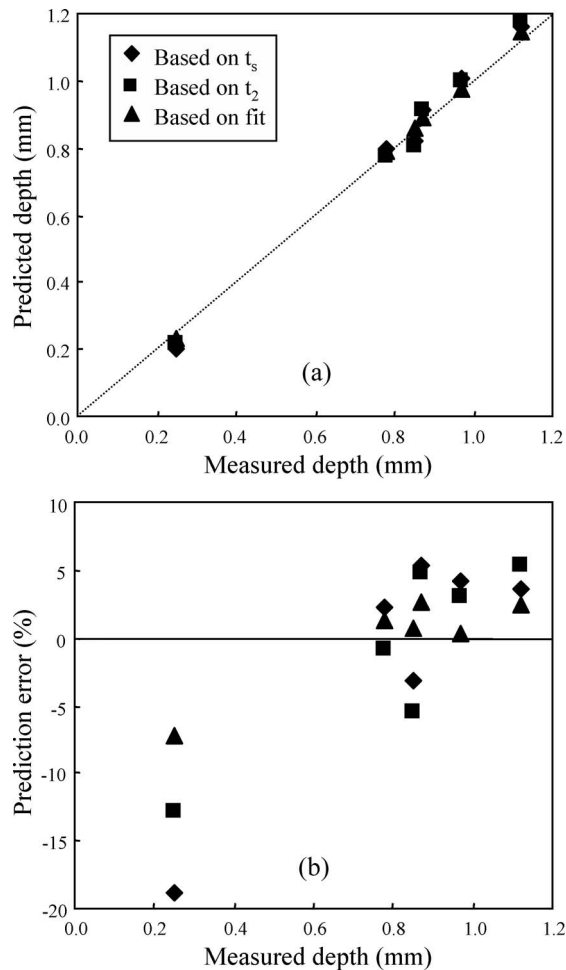
Fig. 14 (*a*) **Comparison of predicted and measured depths and** (*b*) **prediction error as function of depth for three thermography methods**

not present and detector noise is easy to handle because data reduction involves only an interpolation (no subtraction or differentiation) operation.

4 Conclusion

Determination of defect depth by pulsed thermography has been an important research topic in the last decade. Four representative methods were examined in this paper: peak temperature contrast, peak slope-of-temperature contrast, peak second derivative of temperature, and least-squares fitting of temperature. We developed the fundamental theories for the first three methods that allowed for derivation of new and verification of existing empirical correlations. Based on the theories, we determined that the peak temperature contrast method is inherently unable to determine defect depth. The other three methods can be used to determine defect depth and approach exact solution under ideal 1D heat-conduction conditions. The evaluation of the performance and accuracy of these three methods is based on a set of flash thermography data obtained with a ceramic composite flat plate that contains several machined flat-bottom holes to simulate delamination defects. Results of the theoretical and experimental analyses for these three methods are summarized below.

Theoretical results show that, in the peak-slope method, the peak-slope time is proportional to the square of the defect depth when this depth is less than half the thickness at the reference location. When defect depth is deeper, the proportionality constant depends on the reference thickness. The peak-slope value of the

temperature contrast is also a unique function of the thickness ratio between the defect and the reference. It decreases rapidly and monotonically with the ratio. Based on experimental results, the peak-slope time can be used to determine defect depth with good accuracy. The predicted depth based on the peak-slope time is slightly shallower than the real depth, when 3D heat conduction becomes dominant. On the other hand, the peak-slope value is significantly affected by the 3D heat conduction effect and the method used to smooth the experimental noise. When processing thermography data, the requirement of using a reference temperature makes this method less robust for samples with complex defect structures. In addition, this method cannot be used to determine depth that is comparable to the reference thickness.

In the peak second-derivative method, the peak second-derivative time is uniquely proportional to the defect depth (or sample thickness) squared. The peak second-derivative value in log-log scale $[d^2(\ln T)/d(\ln t)^2]$ is a constant, 0.47366. The accuracy of this method for depth prediction from experimental data is similar to that of the peak-slope method. However, because no temperature reference is required for data processing, this method is more reliable and can be easily automated.

In the least-squares fitting method, a theoretical expression is used to model the temperature decay at each surface point, which converges to the best fitting when a correct defect depth is used. It is demonstrated that finite flash duration and 3D conduction effect can be directly built into the theoretical model. Based on experimental results, this method can better predict defect depth when the 3D conduction effect is significant. It is also less sensitive to experimental and system noise because the data processing does not involve differentiation operations. Similar to the peak second-derivative method, this method can predict defect depth or sample thickness and data processing can be easily automated.

Nomenclature

A = temperature amplitude, K
C = specific heat, J/kg K
D = diameter, m
f = flash energy change with time, W/m^2
L = depth or thickness, m
Q = absorbed flash energy, J/m^2
t = time, s
$t_{1/2}$ = half-rise time, s
t_2 = peak second-derivative time, s
t_a = time scale ($=L^2/2\alpha$), s
t_b = time scale ($=3L^2/2\alpha$), s
s = temperature slope, K/s
T = temperature, K
ΔT = temperature difference, K
V = dimensionless temperature
ΔV = dimensionless temperature difference
ΔV_∞ = dimensionless temperature difference at infinity time
y = thickness ratio

Greek Symbols

α = thermal diffusivity, m^2/s
ρ = density, kg/m^3
τ = flash duration, s
ω = dimensionless time

Subscripts

c = peak contrast
r = reference

s = peak slope

References

[1] Verrilli, M. J., Ojard, G., Barnett, T. R., Sun, J. G., and Baaklini, G., 2002, "Evaluation of Post-exposure Properties of SiC/SiC Combustor Liners Tested in the RQL Sector Rig," Ceram. Eng. Sci. Proc., **23**(3), pp. 551–562.

[2] Sun, J. G., Verrilli, M. J., Stephan, R., Barnett, T. R., and Ojard, G., 2002, "Nondestructive Evaluation of Ceramic Matrix Composite Combustor Components," Rev. Prog. Quant. Nondestr. Eval., **22**, pp. 1011–1018.

[3] Busse, G., 1979, "Optoacoustic Phase Angle Measurement for Probing a Metal," Appl. Phys. Lett., **35**, pp. 759–760.

[4] Busse, G., Wu, D., and Karpea, W., 1992, "Thermal Wave Imaging With Phase Sensitive Modulated Thermography," J. Appl. Phys., **71**, pp. 3962–3965.

[5] Parker, W. J., Jenkins, R. J., Butler, C. P., and Abbott, G. L., 1961, "Flash Method of Determining Thermal Diffusivity, Heat Capacity, and Thermal Conductivity," J. Appl. Phys., **32**, pp. 1679–1684.

[6] Heckman, R. C., 1973, "Finite Pulse Time and Heat-Loss Effects in Pulsed Thermal Diffusivity Measurements," J. Appl. Phys., **44**, pp. 1455–1460.

[7] Tang, D. W., He, G. H., and Zhou, B. L., 1995, "Effects of Finite Absorption Depth and Infrared Detector Non-linearity on Thermal Diffusivity Measurement of Thin Films Using the Flash Method," Rev. Sci. Instrum., **66**, pp. 4249–4253.

[8] Deemer, C., Sun, J. G., Ellingson, W. A., and Short, S., 1999, "Front-Flash Thermal Imaging Characterization of Continuous Fiber Ceramic Composites," Ceram. Eng. Sci. Proc., **20**(3), pp. 317–324.

[9] Ringermacher, H. I., Archacki, Jr., R. J., and Veronesi, W. A., 1998, "Nondestructive Testing: Transient Depth Thermography," U.S. Patent No. 5,711,603.

[10] Han, X., Favro, L. D., Kuo, P. K., and Thomas, R. L., 1996, "Early-Time Pulse-Echo Thermal Wave Imaging," Rev. Prog. Quant. Nondestr. Eval., **15**, pp. 519–524.

[11] Maldague, X., 1993, *Nondestructive Evaluation of Materials by Infrared Thermography*, Springer, New York.

[12] Shepard, S. M., Lhota, J. R., Rubadeux, B. A., Wang, D., and Ahmed, T., 2003, "Reconstruction and Enhancement of Active Thermographic Image Sequences," Opt. Eng., **42**, pp. 1337–1342.

[13] Sun, J. G., 2003, "Method for Determining Defect Depth Using Thermal Imaging," U.S. Patent No. 6,542,849.

[14] Roth, D. J., Bodis, J. R., and Biship, C., 1997, "Thermographic Imaging for High-Temperature Composite Materials—A Defect Detection Study," Res. Nondestruct. Eval., **9**, pp. 147–169.

[15] Avdelidis, N. P., and Almond, D. P., 2004, "Through Skin Sensing Assessment of Aircraft Structures Using Pulsed Thermography," NDT & E Int., **37**, pp. 353–359.

[16] Meola, C., Calomagno, G. M., and Giorleo, L., 2004, "Geometrical Limitations to Detection of Defects in Composites by Means of Infrared Thermography," J. Nondestruct. Eval., **23**, pp. 125–132.

[17] Martin, R. E., and Gyekenyesi, A., 2002, "Pulsed Thermography of Ceramic Matrix Composites," Proc. SPIE, **4704**, pp. 82–92.

[18] Cernuschi, F., Bison, P. G., Figari, A., Marinetti, S., and Grinzato, E., 2004, "Thermal Diffusivity Measurements by Photothermal and Thermographic Technologies," Int. J. Thermophys., **25**, pp. 439–457.

[19] Sun, J. G., and Erdman, S., 2003, "Effect of Finite Flash Duration on Thermal Diffusivity Imaging of High-Diffusivity or Thin Materials," Rev. Prog. Quant. Nondestr. Eval., **23**, pp. 482–487.

[20] Sun, J. G., and Benz, J., 2004, "Flash Duration Effect in One-Sided Thermal Imaging," Rev. Prog. Quant. Nondestr. Eval., **24**, pp. 650–654.

[21] Sun, J. G., Deemer, C., Ellingson, W. A., Easler, T. E., Szweda, A., and Craig, P. A., 1999, "Thermal Imaging Measurement and Correlation of Thermal Diffusivity in Continuous Fiber Ceramic Composites," Therm. Conduct., **24**, pp. 616–622.

[22] Vavilov, V., Maldague, X., Dufort, B., Robitaille, F., and Picard, J., 1993, "Thermal Nondestructive Testing of Carbon Epoxy Composites: Detailed Analysis and Data Processing," NDT & E Int., **26**(2), pp. 85–95.

[23] ASTM Standard E1461-92, 1992, "Standard Test Method for Thermal Diffusivity of Solids by the Flash Method," American Society of Testing of Materials, Philadelphia.

Model Validation: Model Parameter and Measurement Uncertainty

Richard G. Hills

Professor
Department of Mechanical Engineering,
New Mexico State University,
Las Cruces, NM 88003
e-mail: rhills@nmsu.edu

Our increased dependence on complex models for engineering design, coupled with our decreased dependence on experimental observation, leads to the question: How does one know that a model is valid? As models become more complex (i.e., multiphysics models), the ability to test models over the full range of possible applications becomes more difficult. This difficulty is compounded by the uncertainty that is invariably present in the experimental data used to test the model; the uncertainties in the parameters that are incorporated into the model; and the uncertainties in the model structure itself. Here, the issues associated with model validation are discussed and methodology is presented to incorporate measurement and model parameter uncertainty in a metric for model validation through a weighted r^2 norm. The methodology is based on first-order sensitivity analysis coupled with the use of statistical models for uncertainty. The result of this methodology is compared to results obtained from the more computationally expensive Monte Carlo method. The methodology was demonstrated for the nonlinear Burgers' equation, the convective-dispersive equation, and for conduction heat transfer with contact resistance. Simulated experimental data was used for the first two cases, and true experimental data was used for the third. The results from the sensitivity analysis approach compared well with those for the Monte Carlo method. The results show that the metric presented can discriminate between valid and invalid models. The metric has the advantage that it can be applied to multivariate, correlated data.
[DOI: 10.1115/1.2164849]

Keywords: model validation, uncertainty

1 Introduction

As the ability to model complex physical processes increases, and our dependence on the associated experimental testing decreases, the need to develop rigorous model validation methodology becomes more critical. Because the phrase "valid model" has different meanings to different developers/users, one must maintain some flexibility as to what is considered a valid model. For example, some workers consider a model valid only if it correctly and fully represents the processes being modeled. For others, a model is valid if it is "good enough" for the application at hand.

The phrase "correctly and fully represents the process being modeled," at first, appears to be reasonable and more rigorous than "good enough." But one must remember that the ability to test models against experimental data is generally limited. Often, one can only perform experiments over a limited range of conditions due to practical constraints. The experiments may represent simplified approximations to the anticipated application of the model because one often does not know what the true field conditions will be, and these conditions can often only be approximated in the laboratory. In addition, one often uses simplified geometries for tests performed in the lab rather than the application geometries to provide more control.

Experiments contain uncertainties in the measurements, and the associated predictive models contain uncertainties in their parameters, such as thermal properties, boundary, and initial conditions. Because of these uncertainties, differences will exist between the model predictions and the experimental observations, even for perfect models. One should define measures of model validity to establish consistency between the model predictions and the experimental measurements in the presence of this uncertainty.

As more complex and multiscale physical processes are modeled, our ability to fully resolve the physics generally decreases. For example, thermal contact resistance depends on the microgeometry of the interfacial surfaces, contact pressure, and the effect of temperature on thermal induced distortion. Contact locations may be limited to small regions of the overall object or an assembly (for example, joints in an assembly). Generally, the grid resolution required to physically model the contact interfaces are much smaller than those at which we can practically model the entire assembly or component. In this case, we may not be able to correctly and fully represent the physics of thermal contact resistance, but only able to represent this resistance through some simplified approximation. Thus, the question of what constitutes "good enough" arises again.

Another area for which judgment is required is when the model is used away from the conditions at which it was tested. Generally, one speaks of model interpolation as using the model within the range of conditions for which it was tested, and model extrapolation as using the model outside this range. In either case, the model is used under conditions for which it was not tested, and judgment must be made as to the validity of the model under these conditions.

As the previous discussion indicates, the validation of models against data requires judgment. The presence of uncertainty in the validation exercise complicates the process. A search of the SciSearch Plus scientific article database (ISI [1]) reveals a significant amount of research on model validation. Investigation of this research suggests that to most authors, model validation is the comparison of model predictions to experimental observations through graphical means. The impact of experimental and/or model uncertainty on these comparisons is generally ignored. A general literature review on model validation is provided by

Oberkampf and Trucano [2] and Oberkampf et al. [3]. Additional literature on statistical methods in model validation is discussed by Hills and Trucano [4]. In recent years, there has been an increased emphasis on using statistical methodology to characterize experimental and/or parameter uncertainty in the comparisons between experimental data and model predictions. Examples of such methodology include the work by Dowding et al. [5], Easterling [6], Rutherford and Dowding [7], and the series of reports by Hills and Trucano [4,8,9], Hills and Leslie [10], and Hills et al. [11]. Overviews of validation approaches for complex engineering applications are provided by Trucano et al. [12,13].

Warren-Hicks et al. [14] explicitly discuss the role of uncertainty in model validation. They argue that prediction uncertainty must be used in the comparison of prediction to observation. Otherwise, complex models can easily fail validation tests simply due to the uncertainty in their parameters rather than due to some structural defect in the model. Warren-Hicks et al. point out that typical estimators of model accuracy are mean squared error, paired t statistics, and correlation statistic. They state that "While these statistics may or may not be valid indicators of statistical accuracy, a larger issue arises in that these statistics do not reflect the uncertainty in model use, such as the decisions made in model calibration, model structure, or choice of time step." They argue that "... a simple comparison of observations and predictions is a naïve approximation of the usefulness of the model or the expected inferences that can be drawn from the model output."

Warren-Hicks et al. discuss the use of classical statistical indicators, such as the paired t test, which use the variance in the differences between measurements and predictions as the test statistic. This estimate of uncertainty is appropriate only if the experimental data truly represents all sources of uncertainty, such as multiple builds of the experimental apparatus, manufacturing lot-to-lot differences of the materials, and uncertainties in boundary conditions over repeated independent experiments. They argue that an appropriate method to account for these effects, if not reflected in the data, is to use the Monte Carlo method to propagate these uncertainties through a model. This allows one to model important sources of uncertainty that may not be reflected in the validation experiments. Of course, one must have sufficient knowledge to adequately characterize these sources for use in a Monte Carlo analysis.

Warren-Hicks et al. [14] quantify model validity by measuring the percentage of the probability density function for the predicted measurement that lies below and above the experimental observations. When the measured value is "near the center" of the predicted distribution, the model is considered to be accurate. When the measured value is in the lower or upper portions of the predicted distribution, the model is considered to be less accurate. If the entire distribution is below or above the measured value, the model is considered to be inaccurate. No guidance as to what constitutes "near the center" of the distribution or how to measure this distance is given.

A thoughtful tutorial of model validation is provided by Roberson [15]. He separates model validation into several components as follows: Conceptual model validation is the determination "that the scope and level of detail of the proposed model is sufficient for the purpose at hand, and that any assumptions are correct." Data validation is evaluating "that the data required for model building, validation and experimentation are sufficiently accurate." White-box validation is evaluating whether "the constitutive parts of the computer model represents the corresponding real world elements with sufficient accuracy." Black-box validation is "determining that the overall model represents the real world with sufficient accuracy." Experimental validation is "determining that the experimental procedures adopted are providing results that are sufficiently accurate." Solution validation is "determining that the results obtained from the model of the proposed solution are sufficiently accurate." Solution validation takes place after the designed product is complete. It is a comparison of the final performance of the product to the predicted performance. Guidance of what constitutes or how to measure "sufficiently accurate" is not addressed.

The purpose of this paper is to provide a brief overview of issues associated with model validation in the presence of measurement and model parameter uncertainty. Multivariate statistical methods are used to develop a model validation metric. Examples using valid and invalid models are presented.

2 Uncertainty

There are multiple sources of uncertainty in model validation exercises. Sources include:

1. Measurement uncertainty (i.e., noise and bias),
2. Uncertainty in the model parameters (i.e., those that define the properties, geometry, initial and boundary conditions), and
3. Uncertainty associated with the appropriate model form.

Other forms of uncertainty include:

4. Model uncertainty associated with truncation error (i.e., lack of convergence), and
5. Model uncertainty due to coding or algorithmic error (i.e., verification).

Experimentalists often distinguish between measurement noise/bias due to diagnostic error (i.e., instrumentation noise, bias due to heat conduction through thermal couple leads) and uncertainty/variability in the system being tested. For example, some manufacturing lot-to-lot variability in thermal properties is often expected. For heterogeneous materials such as foams, one might expect that the lot-to-lot variability, as well as the spatial variability within a single sample, to be dominant sources of uncertainty. There will also be variability/uncertainty in the actual boundary conditions applied. Because these uncertainties are present, one should not expect that a model will provide predictions that pass directly through the experimentally observed data, even for a perfect model.

While we would like to use fully converged and fully verified models when performing validation tests (items 4 and 5), such expectations are not always reasonable for complex, multiphysics models. For example, if a validation experiment includes a three-dimensional multicomponent system, one may not be able to solve on a sufficiently dense computational grid so that the physics of contact resistance due to thermal distortion at interfaces is fully resolved, while modeling the entire system. However, one may be able to bound the effect.

The uncertainty addressed in item 5 is associated with model verification, the evaluation of whether the numerical implementation of the algorithm represents the mathematical equations being modeled. There are some who suggest that a computer code should be fully verified before it is used for model validation experiments. Our contention is that for very complex, multiphysics codes, this expectation is not reasonable. The probability of finding all errors in hundreds of thousands of lines of code is not 100%, and one should accept the idea that careful analysis of model validation experiments will occasionally lead to the discovery of such errors.

Generally, as system complexity increases, the number of model parameters increase as does their uncertainty. For example, in mechanical systems undergoing dynamic excitation, joint friction can play a major role near resonance. Joint friction is very difficult to model and often is simulated through simple models with calibrated constants. In thermal systems containing conduction solids, thermal contact resistance between components (or on boundaries) can possess significant uncertainties. Radiation properties such as emissivity, absorptivity, and reflectivity are difficult to specify for components undergoing aging and add considerable uncertainty to the modeling process. Rather than specifying these
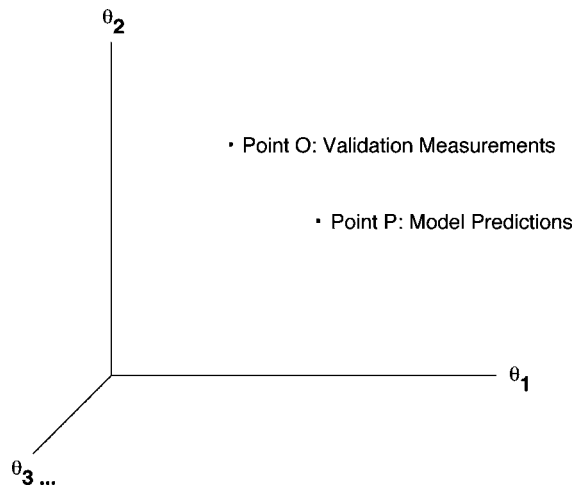
Fig. 1 Experimental observations and model predictions

Fig. 2 Uncertainty in the measurements and the model predictions

parameters deterministically, the uncertainty in these parameters can be represented through the use of probabilistic/possibilistic models. Often this requires soliciting expert opinion to specify the corresponding models for uncertainty. Given such models, one can propagate this uncertainty through the physics model to obtain estimates of uncertainty of the predictions. Such complex systems are often the systems that one wishes to model. Because of this, focus of this paper is on the evaluation of models against experimental data, given our best characterization of the model parameter and experimental uncertainty.

Here we distinguish between two types of model validation. The first is *scientific validation*—the evaluation of whether model predictions are consistent with experimental observations, within the characterized uncertainties associated with measurement error and model parameter uncertainty. This approach to model validation evaluates whether that the uncertainties associated with model form, truncation error, and uncharacterized uncertainty, are small compared to the effects of characterized experimental and parameter uncertainty.

The second type of model validation is *engineering validation*. In this case, one tests whether the model predictions are consistent with the experimental observations, within bounds that are larger than those associated with experimental and model parameter uncertainty. For example, one may be satisfied if a model overpredicts heat flux from a surface if such an overprediction is of acceptable magnitude. This overprediction may be due to model form error, model approximation error, or truncation error.

In the present work, we restrict our attention to scientific validation. Engineering validation is a very important component of model validation since one often uses approximate models to predict or bound behavior. Multivariate engineering validation is more difficult because one typically must deal with one or more one-sided estimates of significance. The focus on scientific validation in the present paper allows fundamental ideas to be introduced which can be extended to engineering validation [4].

3 Metrics

3.1 Background. To quantitatively test for model validity, some measure of the quality of the model predictions is required. Here we begin with the comparison of n model predictions to n experimental observations. This is shown graphically in Fig. 1. θ_1 represents the first measurement/prediction, θ_2 the second, and so on. Note that this figure represents a n dimensional space for the n measurements, with the n measurements and the n model predictions represented by two points. Since measurement and model parameter uncertainty always exists, one cannot expect these
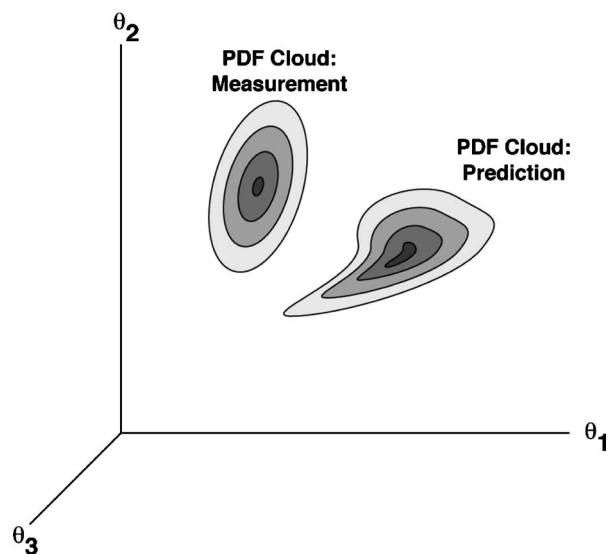
points to align. Given these two points, one asks: Are the points sufficiently far apart so that one has sufficient evidence to reject the model as valid?

To answer this question, some measure of distance is needed. An obvious choice is to use a simple Euclidian distance, i.e., the square root of the sums of squares of the differences between the model predictions and the experimental observations. A problem with this choice is that it may not represent the important effects of correlation structure induced by the model.

Figure 2 adds the effect of model parameter uncertainty and measurement uncertainty. Note that concentric ellipsoids are shown to represent measurement uncertainty and a more complex shape for the model prediction. The contour surfaces are taken to be isoprobability density function (PDF) surfaces. Independent measurements with normal probability density functions and uniform variances result in spheroidal iso-PDF surfaces. The case shown in Fig. 2 for the measurements indicates that the variances are not uniform for each measurement, as indicated by the ellipsoids for the iso-PDF surfaces. The inclined major/minor axes indicate that correlation exists between the measurements. Constant PDF surfaces for hypothetical predictions are also illustrated. A complex shape is shown to illustrate the effects of a highly nonlinear model.

At first look, one may be tempted to evaluate model validity based on the overlap of the PDF for the prediction and the PDF for the measurements. This process can be simplified by taking the differences between the model predictions and the experimental observations and considering the PDF for the differences. Iso-PDF surfaces for the differences are illustrated in Fig. 3. Note that the uncertainty in the differences is plotted around the model predictions. One can also plot these around the measurements. This figure suggests that one can use the iso-PDF surfaces to measure distance rather than simple, unweighted Euclidean distance. This has the effect of accounting for the structure of the uncertainty. In the case shown, the measurement is within the visible cloud, but near its boundaries. For example, assume that the cumulative probability within the dashed contour surface represents 95% of the total probability (i.e., 0.95). One can say that 95% of the realizations of this validation experiment would result in the observed measurement lying within or on the surface defined by the dashed surface for a valid model. Conversely, one would expect 5% of the realizations of the validation experiments to result in the measurement point outside or on this surface, for a valid model. If, in the spirit of providing the benefit of doubt to the

Fig. 3 Combined uncertainty

model, one does not reject the model unless one has less than a 5% probability of rejecting a valid model, then the observed measurement point would be required to lie outside the dashed surface for the model to be rejected.

This approach to the evaluation of distance requires that the uncertainty in the parameters can be estimated and propagated through the model. For problems with more than a few measurements, this process is very computationally expensive and requires many function evaluations to adequately resolve the iso-PDF surf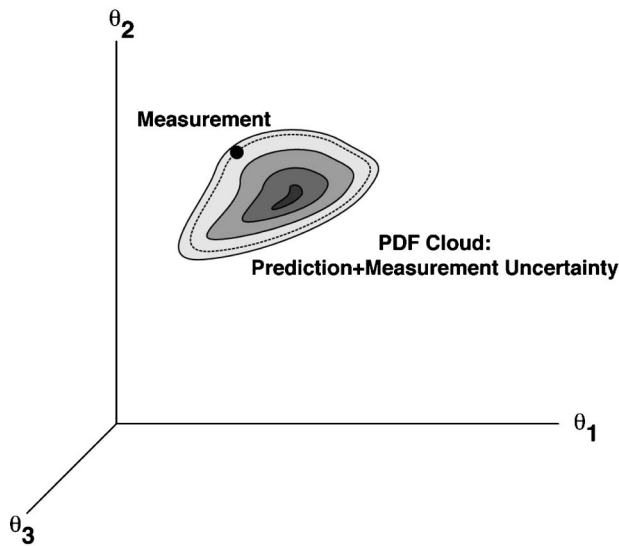aces. Here we approximate this process to first order using a sensitivity analysis. The effect of this approach is the iso-PDF surfaces of Fig. 3 are approximated by hyperellipses. A Monte Carlo analysis will be used to evaluate the quality of the first-order analysis for several specific applications.

In the above discussion, a significance level of 5% was used as an example of a significance level at which a model may be rejected as valid. This level of significance gives a large "benefit of doubt" to the model. There is no standard as to what the level of significance should be used to reject a model. Lacking other input, such as probabilistic based design specifications, we suggest the following only as guidance:

1. One has confidence in the model, to the level of modeled uncertainty of the validation exercise, if the differences between the model predictions and the experimental results are within a significance level of 33% (approximately one standard deviation for a normal distribution).
2. One has lower confidence in the model, but not sufficient evidence to reject the model as valid, if the differences are between significances levels of 33% and 5% (between approximately one and two standard deviations).
3. The model is rejected if the significance level is less than 5%.

We restate that these are suggested measures of "good enough" in the lack of additional design constraints. Models that meet criteria 1 (or 2) have been tested only to this level of uncertainty, for this particular set of conditions, and should not be considered "good enough" if the application requires less uncertainty in the predictions (for example, as defined by regulatory requirements), or if the application occurs under significantly different conditions. In the case of items 2 and 3, further investigation of the model should be performed to evaluate the cause of the discrepancy.

In the above example, a model is rejected if the point corresponding to the measurement vector lies outside the 95% prob-

ability contour (i.e., at the 5% significance level) of Fig. 3. Five percent of all predictions from a valid model lie outside the contour. There is thus a 5% probability of rejecting a valid model. Rejecting a valid model is referred to as Type 1 error [16]. The probability of committing this error can be reduced by reducing the significance at which the model is rejected to a smaller number, say 1%. Unfortunately, as the probability of rejecting a valid model decreases due to a reduction in this significance level, the probability of failing to reject an invalid model increases. Failure to reject an invalid model is referred to as a Type 2 error [16]. One would like to choose a statistical test that minimizes the probability of a Type 1 error, while minimizing the probability of a Type 2 error. In other words, one would like to choose a statistical test that minimizes the probability of rejecting a valid model while maximizing the probability of rejecting an invalid model. Generally, as more data is used, the probability of committing a Type 2 error decreases for a fixed probability of committing a Type 1 error. Multivariate metrics, such as the one defined below have this advantage, as long as one adequately estimates the correlation structure for the data.

3.2 The r^2 Metric. A metric which accounts for some of the structure of the uncertainty is the weighted least squares metric defined as follows:

$$r^2 = (\mathbf{X}_{model} - \mathbf{X}_{exp})^T [\mathbf{cov}^{-1}(\mathbf{X}_{model} - \mathbf{X}_{exp})](\mathbf{X}_{model} - \mathbf{X}_{exp}) \quad (1)$$

where $\mathbf{X}_{model}$ is the vector of model predictions and $\mathbf{X}_{exp}$ is the corresponding vector of experimental observations. The matrix $\mathbf{cov}(\mathbf{X}_{model} - \mathbf{X}_{exp})$ is the covariance of the differences between the model predictions and the experimental observations. These predictions/observations may be at different times, different spatial locations, and may even represent different quantities such as temperature and pressure. Geometrically, Eq. (1) defines a n-dimensional hyperellipse for constant values of r^2. The advantage of this metric is it measures distance based on the correlation structure of uncertainty in the model predictions and the experimental observations. Because this equation defines a hyperellipse, values for constant r^2 may only approximate the true shape of constant PDF contours as illustrated in Fig. 3.

While the metric defined by Eq. (1) is familiar to those who work in parameter estimation, the evaluation of the covariance matrix is not trivial for complex predictive models. The covariance matrix for the differences between model predictions and the experimental observations is the sum of the covariance matrices for each, if the uncertainties in the measurements are independent of the uncertainties in the model predictions.

$$\mathbf{cov}(\mathbf{X}_{model} - \mathbf{X}_{exp}) = \mathbf{cov}(\mathbf{X}_{model}) + \mathbf{cov}(\mathbf{X}_{exp}) \quad (2)$$

To approximate the uncertainty in the model predictions due to the uncertainty in the model parameters, a multivariate, first-order, sensitivity analysis presented by Hills and Trucano [8] is used here. This analysis begins by relating changes in model prediction $X(t)$ at the discrete times (can also be at discrete spatial locations, or both) $t = t_1, t_2, \ldots, t_n$, to perturbations in the model parameters from their mean.

$$\mathbf{X} = \mathbf{X_0} + \boldsymbol{\nabla}_\alpha \mathbf{X} \boldsymbol{\Delta \alpha} \quad (3)$$

where

$$\mathbf{X} = \begin{bmatrix} X_1 \\ X_2 \\ \vdots \\ X_n \end{bmatrix}, \quad \mathbf{X_0} = \begin{bmatrix} X_{m1} \\ X_{m2} \\ \vdots \\ X_{mn} \end{bmatrix}, \quad \boldsymbol{\Delta \alpha} = \begin{bmatrix} \alpha_1 - \alpha_{m1} \\ \alpha_2 - \alpha_{m2} \\ \vdots \\ \alpha_p - \alpha_{mp} \end{bmatrix} \quad (4)$$

The subscript m indicates that the quantity is evaluated at the mean value of the parameter. Equation (3) represents n measurements for a model with p parameters. The sensitivity matrix (composed of the sensitivity coefficients) is given by

$$\nabla_{\alpha}\mathbf{X} = \begin{bmatrix} \dfrac{\partial X_1}{\partial \alpha_1} & \dfrac{\partial X_1}{\partial \alpha_2} & \cdots & \dfrac{\partial X_1}{\partial \alpha_p} \\ \dfrac{\partial X_2}{\partial \alpha_1} & \dfrac{\partial X_2}{\partial \alpha_2} & \cdots & \dfrac{\partial X_2}{\partial \alpha_p} \\ \vdots & \vdots & \ddots & \vdots \\ \dfrac{\partial X_n}{\partial \alpha_1} & \dfrac{\partial X_n}{\partial \alpha_2} & \cdots & \dfrac{\partial X_n}{\partial \alpha_p} \end{bmatrix} \qquad (5)$$

The covariance matrix for the model predictions for Eq. (2) can now be estimated using the first-order sensitivity analysis (see [8])

$$\mathbf{cov}(\mathbf{X}_{\mathrm{model}}) = \nabla_{\alpha}\mathbf{X}\,\mathbf{cov}(\boldsymbol{\alpha})[\nabla_{\alpha}\mathbf{X}]^{\mathrm{T}} \qquad (6)$$

Equations (2) and (6) are used in Eq. (1) to define the metric. This metric weights distances by the inverse of the uncertainty and accounts for correlation that exists between the differences. Such correlation is normally present due to parameter uncertainty in the model. If the differences are normally distributed, then constant r^2 hyperellipses defined by Eq. (1) do indeed represent constant PDF surfaces, given the correct estimate for the covariance matrix of the differences. This metric is demonstrated in the following sections.

4 Example Applications

Three example applications are presented. In the first, a nonlinear model (Burgers' equation [17]) is used to generate simulated experimental data. The simulated data includes noise in the measurements and uncertainty in the model parameters to represent experimental uncertainty due to noise and unit-to-unit variation. The model is then tested against the data. One should expect that the validation methodology presented should show the model as valid as the data generated was from the same model.

To demonstrate the methodology for a model known to not be valid, the convective-dispersive equation (C-D) is used to model the experimental data obtained from the first case. Since the C-D equation is linear and Burgers' equation is not, this test case should result in the failure of the model, given sufficient data.

In the third test case, a simple thermal contact resistance model is tested using experimental observations taken from a thermal contact experiment. Since the experiment was carefully controlled, one may expect that the contact resistance should be well modeled.

4.1 Simulated Data for Burgers' Equation. For the first two applications, the "true" model is taken to be Burgers' equation. In contrast to the linear convective-dispersion equation for which steep gradients (or fronts) diffuse over time, the solution of Burgers' equation results in a moving front which evolves toward a steady shape.

Consider Burgers' equation with the following initial and boundary conditions:

$$\frac{\partial c}{\partial t} = D\frac{\partial^2 c}{\partial x^2} - U\frac{\partial c^2}{\partial x} = D\frac{\partial^2 c}{\partial x^2} - 2Uc\frac{\partial c}{\partial x}, \quad 0 \leqslant x \leqslant 10, \quad 0 \leqslant t \leqslant 2.5 \qquad (7)$$

$$c(x,0) = \begin{cases} 1, & 3 \leqslant x \leqslant 4 \\ 0, & \text{otherwise} \end{cases} \qquad (8)$$

$$c(0,t) = c(10,t) = 0 \qquad (9)$$

D and U are constants in time and space, but contain uncertainty. An alternative form of the right-hand side of Burgers' equation is also provided in Eq. (7) for reference. Note that the last term in Eq. (7) represents convection with a c dependent effective velocity. Assume, for illustration, that D and U are uncorrelated and normally distributed with the following means and standard deviations:
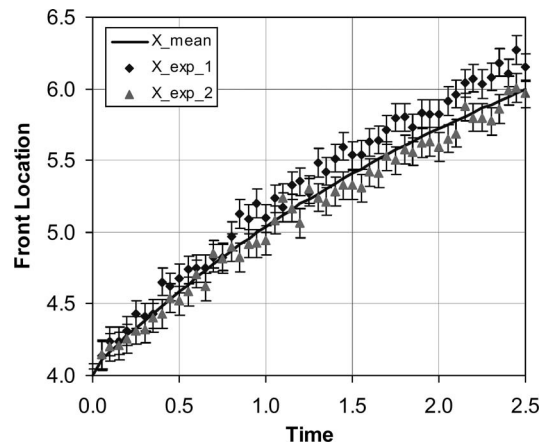
Fig. 4 Simulated experimental measurements; X_mean– prediction based on mean model parameters; X_exp_1, X_exp_2– simulated experimental data for realizations 1 and 2, respectively

$$D_{\mathrm{m}} = 0.08 \qquad (10a)$$

$$U_{\mathrm{m}} = 1.0 \qquad (10b)$$

$$\sigma_D = 0.008 \qquad (11a)$$

$$\sigma_U = 0.1 \qquad (11b)$$

This uncertainty reflects the uncertainty in the model parameters for a particular realization of a model validation experiment. The time and spatial domain were chosen so that during the simulation period, the convecting pulse does not reach either boundary. Assume that the quantity of interest is the front on the right side of the pulse. Here the front location X is defined as that location for which $c=0.25$ on the leading edge of the front.

To generate a simulated set of measurements, a normally distributed realization of D and U using the statistics defined by Eqs. (10) and (11) is generated; Burgers' equation is evaluated numerically using this parameter realization; the location of the leading edge at $c=0.25$ is evaluated as a function of time from the predictions; and noise is added to simulate measurement noise. Here the measurement noise is assumed to be normally distributed, with a mean of zero, and a standard deviation of

$$\sigma = 0.05 \qquad (12)$$

To minimize the effect of numerical diffusion, Eqs. (7)–(9) were solved numerically using an operator splitting technique. Equation (7) was split into a strictly convective equation and a dispersive equation for each time step (Hills et al. [18]). The resulting convective equation was solved using the second-order total-variation-diminishing (TVD) scheme of Roe and Sweby combined with a Superbee limiter (Roe [19,20], and Sweby [21]). Comparison of this method with other shock-capturing methods, as applied to Burgers' inviscid equation, is presented by Yang and Przekwas [22]. Equation (7) was solved using spatial and temporal discretizations of $\Delta x=0.1$ and $\Delta t=0.02$, respectively. Reducing the time step by a factor of 50 and the spatial step by a factor of 2 resulted in a shift in the predictions that were within 0.2% at $t=0.1$ and 0.04% at $t=1.0$. A more rigorous convergence analysis on the numerical algorithm was not performed since the purpose of this exercise was to generate simulated measurements that contained uncertainty. Simulated experimental data were generated on 0.05 time increments from $t=0.0$ to $t=2.5$ for a total of 51 measurements.

Figure 4 illustrates two realizations of the simulated experimental measurements along with the predictions of Burgers' equation, evaluated at the mean values of the parameters. These simulated

experimental data are used to test several models in the following sections. Uncertainty bars showing $\pm 2\sigma$ of the measurement noise are included. Note that the measurement standard deviations used here (Eq. (12)) result in noticeable variability in the simulated measurements. Significant variability in the simulated measurements exists due to the inclusion of the model parameter uncertainty to represent unit-to-unit variability.

4.2 Burgers' Equation. The metric defined by Eq. (1) can now be used to test Burgers' equation against the simulated data. For this case, the covariance matrices of the model parameters and the experimental observations are (see Eqs. (2) and (6)).

$$\mathbf{cov}\begin{pmatrix} D \\ U \end{pmatrix} = \mathbf{cov}(\boldsymbol{\alpha}) = \begin{bmatrix} 0.008^2 & 0 \\ 0 & 0.1^2 \end{bmatrix} = \begin{bmatrix} 0.000064 & 0 \\ 0 & 0.01 \end{bmatrix}$$
(13)

$$\mathbf{cov}(\mathbf{X}_{\mathrm{exp}}) = \begin{bmatrix} 0.05^2 & 0 & \cdots & 0 \\ 0 & 0.05^2 & \cdots & 0 \\ \vdots & \vdots & \ddots & \vdots \\ 0 & 0 & \cdots & 0.05^2 \end{bmatrix}$$
(14)

Time dependent measurement uncertainty can be easily addressed by using the corresponding time dependent variances in Eq. (14). Some numerical noise was found to be present in the numerical solution of Burgers' equation due to the use of the TVD limiter. Because of this, the sensitivity matrix was not approximated through finite differences. Rather, the following quadratic (Eq. (15)) was fitted to the predicted front location as a function of the parameters using the following eight points (Eq. (16)) by least squares for each measurement time. The gradient was analytically evaluated for each of the resulting n quadratics at $D=D_{\mathrm{m}}$ and $U=U_{\mathrm{m}}$. Note that these points were taken somewhat toward the tails of the probability distributions since one is interested in the behavior of the models out to these points (see discussion near the end of Sec. 3.1).

$$X(t_i,D,U) - X(t_i,D_{\mathrm{m}},U_{\mathrm{m}}) = a_{1i}D + a_{2i}U + a_{3i}D^2 + a_{4i}DU$$
$$+ a_{5i}U^2, \quad i=1,2,\ldots,n$$
(15)

$$\begin{bmatrix} D - D_{\mathrm{m}} \\ U - U_{\mathrm{m}} \end{bmatrix} = \begin{bmatrix} \sigma_D \\ 0 \end{bmatrix}, \begin{bmatrix} 0 \\ \sigma_U \end{bmatrix}, \begin{bmatrix} -\sigma_D \\ 0 \end{bmatrix}, \begin{bmatrix} 0 \\ -\sigma_U \end{bmatrix}, \begin{bmatrix} \sigma_D \\ \sigma_U \end{bmatrix},$$
$$\begin{bmatrix} -\sigma_D \\ \sigma_U \end{bmatrix}, \begin{bmatrix} \sigma_D \\ -\sigma_U \end{bmatrix}, \begin{bmatrix} -\sigma_D \\ -\sigma_U \end{bmatrix}$$
(16)

Using the above fitted approximations with both sets of data to evaluate Eq. (1) give

$$\text{X\_exp\_1:} \quad r^2 = 54.64$$
(17)

$$\text{X\_exp\_2:} \quad r^2 = 66.95$$
(18)

If the differences between model predictions and experimental observations are normally distributed, and if the covariance matrix for these differences is adequately represented by Eqs. (2) and (6), r^2 will be distributed as a $\chi^2(df)$ distribution where df is the degrees of freedom. For now, normally distributed differences will be assumed. The possible case of non-normally distributed differences will be addressed shortly. In this case, there are 51 differences, corresponding to the 51 measurements, with known variances. Since no parameters were estimated in this process, the total degrees of freedom is 51. Given the $\chi^2(51)$ distribution, the probabilities of obtaining $r^2=54.64$ and 66.95 or larger (i.e., significance) are [23]

$$\text{X\_exp\_1:} \quad P(r^2 > 54.64) = 0.338$$
(19)

$$\text{X\_exp\_2:} \quad P(r^2 > 66.95) = 0.066$$
(20)

Thus, given the models for uncertainty in the model predictions due to parameter uncertainty, and in the uncertainty in the measurements, the probability of a valid model given this large or larger value in the weighted distance squared is 33.8% for data set 1 and 6.6% for data set 2. This is more significant than the 5% specified earlier to outright reject a model. One can thus say that the data do not provide sufficient evidence to reject the model as valid. This is not surprising since this model was used to generate the simulated data. In the present work, the random realization of the model parameters for X_exp_2 was intentionally chosen such that the results would lie in the tails of the distribution, as indicated by Eq. (20), to illustrate the effect of low probability experimental outcomes. Only 6.6% of realization of the simulated validation experiments will result in a larger r^2 for a valid model.

What is the impact of the assumption of local linearity and normal differences? To evaluate this assumption, a Monte Carlo analysis of the problem was performed. The analysis was comprised of the following steps:

1. Generate a random realization of the parameters and the measurements noise using random number generators for the normal distributions defined by Eqs. (10)–(12).
2. Solve Burgers' equation for these parameters and add the measurement noise to the results. Note that this produces one realization of the 51 measurements for an experiment.
3. Repeat steps 1 and 2 sufficient times to resolve the distribution of front location as a function of time. We found that 100,000 realizations resulted is reasonably smooth quantiles as evidenced in the following results.
4. The iso-PDF curves for several slices of the 51-dimensional hyperellipse are evaluated using the MATLAB® convex hull routine convhull [23] from the realizations generated above. A convex hull for a two-dimensional slice of data is the polygon with the fewest segments whose vertices pass through the outermost points of the data set. We take this polygon as an approximation to the outermost iso-PDF curve. The points defining the polygon are then peeled away and a new polygon is evaluated. This process is repeated until we have peeled away all of the points. By counting points in each layer of the convex hull, we can estimate the cumulative probability within each hull. While this process is practical for two-dimensional slices, it is computationally very expensive for the full 51-dimensional set of points.

Because the above process is applied to two-dimensional slices of the full 51-dimensional space, each slice possesses only two degrees of freedom.

Comparison of the quantile plots, evaluated through the Monte Carlo procedure, to the corresponding ellipsoids obtained from the linear analysis are shown in Fig. 5. The equation for the linear analysis ellipsoids are (see Eq. (1))

$$r_c^2 = (\mathbf{X}_{\mathrm{model}} - \mathbf{X})^{\mathrm{T}} [\mathbf{cov}^{-1}(\mathbf{X}_{\mathrm{model}} - \mathbf{X}_{\mathrm{exp}})](\mathbf{X}_{\mathrm{model}} - \mathbf{X})$$
(21)

where r_c^2 is a constant for each ellipsoid with values defined by the $\chi^2(2)$ distribution for the two-dimensional slices (i.e., only two degrees of freedom). Specifically

$$P(r^2 > r_c^2) = 0.05, \quad r_c^2 = 5.992$$
(22)

$$P(r^2 > r_c^2) = 0.25, \quad r_c^2 = 2.773$$
(23)

$$P(r^2 > r_c^2) = 0.50, \quad r_c^2 = 1.386$$
(24)

$$P(r^2 > r_c^2) = 0.75, \quad r_c^2 = 0.575$$
(25)

The results illustrated in Fig. 5 indicate that (1) the slices of the hypervolume do result in PDF's that appear to be ellipsoidal, (2),
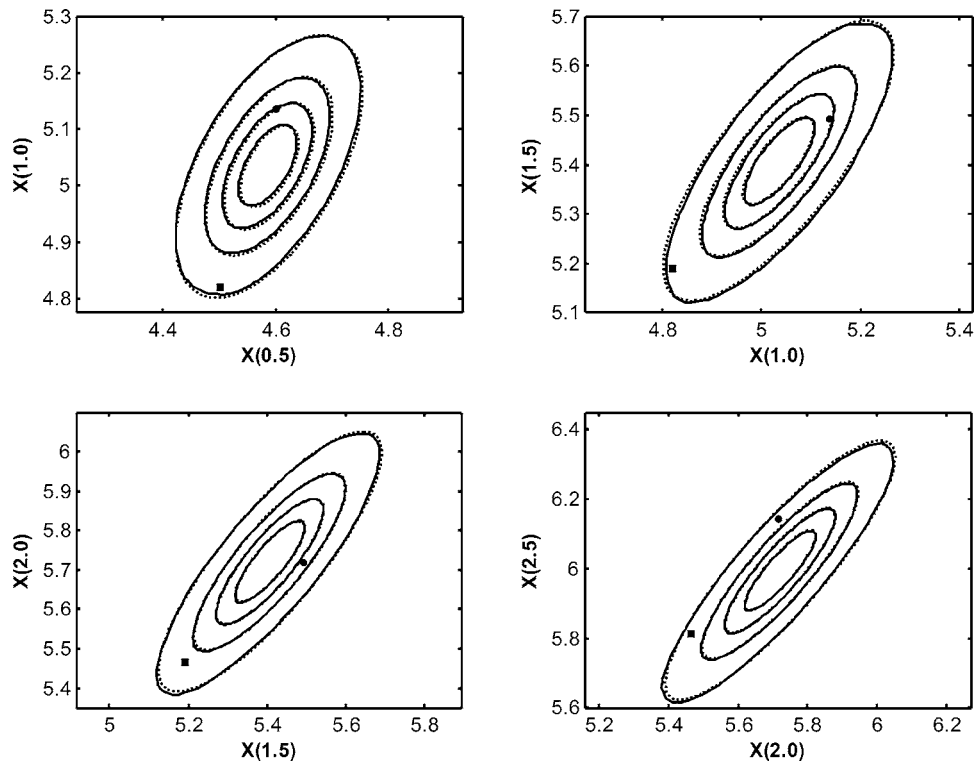
Fig. 5 PDF quantiles for front location at various times; 25%, 50%, 75%, 95% quantiles; sensitivity analysis represent by dashed lines; Monte Carlo analysis represented by solid lines; X_exp_1 and X_exp_2 measurements indicated by a circle and square respectively

the major axis of each ellipse is inclined indicating that the predicted front locations are correlated over time, (3) the correlation becomes stronger at later times indicated by the larger ratio of the inclined major to minor axes length, and (4) the approximation of the quantiles developed from the sensitivity analysis matches those of the Monte Carlo results well. The terms in the covariance matrix for the differences between prediction and observation as estimated using the Monte Carlo method and estimated using the sensitivity analysis, were found to be within 4%, 3%, 1%, and 1% for the data addressed in the upper left, upper right, lower left, and lower right subplots of Fig. 5, respectively. The impact of correlation on a measure of distance between the model prediction and the experimental observation can be seen in this figure. Because the measure quantity is positively correlated over time (the major axis has a positive slope), one expects that a model that over predicts front location at one time will tend to over predict front location at an adjacent time. Because of this, one should not interpret significant differences between prediction and observation at two adjacent points in time (or points spaced as far apart as is illustrated in Fig. 5) as providing two independent points of evidence for model validity. The definition of the metric in terms of the ellipsoids of Fig. 5 accounts for correlation by warping the measure of distance appropriately.

The Monte Carlo evaluation of the significance based on constant PDF surfaces is very expensive computationally since the shape of the convex hull which passes through the experimental observation vector must be determined for the 51-dimensional space. Rather than performing this very impractical analysis for significance, the significance of r^2 defined by Eq. (1) is evaluated using the covariance estimated directly from the Monte Carlo realizations. This is done as follows:

1. Estimate the mean vector of length 51 for the realizations of the simulated measurements for the 51 measurement times, and the corresponding 51×51 covariance matrix from the realization of the measurements described

above. This process defines the $\mathbf{cov}(\mathbf{X}_{\text{model}} - \mathbf{X}_{\text{exp}})$ term in Eq. (1) and is considerably less computationally expensive than evaluating convex hulls in the 51-dimensional space.

2. Evaluate r^2 for the difference between the mean of the simulated measurements and the experimental measurements using Eq. (1).

3. Evaluate the r^2 for the difference between each of the realizations of the simulated measurements and the mean, and count those that have a r^2 greater than that observed from step 2. The fraction of those realizations with a r^2 greater than that observed for the model (step 2) represents the significance that the r^2 of observed experimental measurements came from the population of realizations of the simulated measurements, assuming the model is valid.

For nonlinear problems which lead to non-normal distributions for the differences, the interpretation of r^2 is slightly different. As for the normal case, r^2 represents the weighted Euclidian norm where the distances are weighted by the inverse of the covariance matrix. However, in contrast to the normal case, iso-r^2 surfaces may not represent iso-PDF surfaces. The values for r^2 and the corresponding significance were found to be

$$X\_exp\_1: \quad r^2 = 55.24 \qquad (26)$$

$$X\_exp\_2: \quad r^2 = 68.07 \qquad (27)$$

$$X\_exp\_1: \quad P(r^2 > 55.24) = 0.316 \qquad (28)$$

$$X\_exp\_2: \quad P(r^2 > 68.07) = 0.056 \qquad (29)$$

While these results are close to those presented by Eqs. (17) through (20), the differences certainty reflect the nonlinear effects. The results represented by Eqs. (17) through (20) required that the

Burgers' equation be evaluated only nine times.

These comparisons indicate that for this application, little was gained by fully accounting for the nonlinearities using a Monte Carlo analysis. Our experience with some nonlinear applications (see [4]) indicates that the linear approximation works surprisingly well for many applications. Of course, there are cases for which one should not expect such good performance. These include problems which are highly nonlinear, such as lightly damped vibration near resonance, or problems for which the uncertainty in the model parameters are large relative to the value of the model parameter. Model validation experiments are often carefully designed and controlled so that the relative uncertainty in the model parameters is small.

A first-order analysis that may be suitable for carefully controlled validation experiments may not be suitable for the anticipated application of the model as more uncertainty generally exists for the anticipated applications. A rule-of-thumb approach to evaluate the suitability of the first-order approximation is to investigate whether the sensitivity matrix changes significantly over the parameter range of interest.

4.3 Convective-Dispersive Equation. In the previous case, we use a model that we knew to be valid. To illustrate the method for a model for which the physics is known to be inconsistent with the experimental data developed using Burgers' equation, consider the following convective dispersion equation:

$$\frac{\partial c}{\partial t} = D\frac{\partial^2 c}{\partial x^2} - V\frac{\partial c}{\partial x}, \quad 0 \leq x \leq 10, \quad 0 \leq t \leq 2.5 \quad (30)$$

with the boundary and initial conditions given by Eqs. (8) and (9). A simple explicit finite difference algorithm was used to solve Eq. (30), with the convective term approximated through upwinded differences. The use of this algorithm results in numerical diffusion. As in the case of the approximation for Burgers' equation, a detailed convergence study was not performed. As a result, the model and algorithm contain both nonmodeled physics (i.e., the convective term in Burgers' equation is nonlinear in c whereas here it is linear) and numerical diffusion. Since the purpose of the present work is to develop validation metrics that apply to models that invariably contain both numerical approximation and nonmodeled physics, the inclusion of numerical diffusion in our illustrative approximate model is not unrealistic. Spatial and temporal descretizations of $\Delta x = 0.1$ and $\Delta t = 0.02$ were used, respectively.

Clearly, one cannot expect the model parameters from Eq. (7) to apply to Eq. (30) as the convective term is different. So rather than arbitrarily choosing these parameters, the Burgers' data for $0 \leq t \leq 1$ from the first realization of the simulated data, X_exp_1, was used for the nonlinear calibration. The IMSL [24] function b2pol was used, which is a nonlinear optimization routine that allows for simple bounds. Specifically, D and V in Eq. (30) were selected to minimize the sum of the square of the differences between the measured front location and the predicted front location for the first 21 measurements of X_exp_1. The resulting calibrated parameters are given below and the resulting model predictions are shown in Fig. 6.

$$D = 0.1037 \quad (31a)$$

$$V = 0.816 \quad (31b)$$

We now wish to evaluate the effect of model parameter uncertainty on predicted front location to account for the uncertainty due to different experimental realizations which occur due to the variation in the parameters from experiment to experiment. Rather than use the full Monte Carlo analysis demonstrated earlier, a first-order sensitivity analysis was used. The previously defined response surface method (see Eqs. (15) and (16)) was used to evaluate the elements in the sensitivity matrix. Given the sensitivity matrix, the covariance of the model predictions was estimated from Eq. (6)
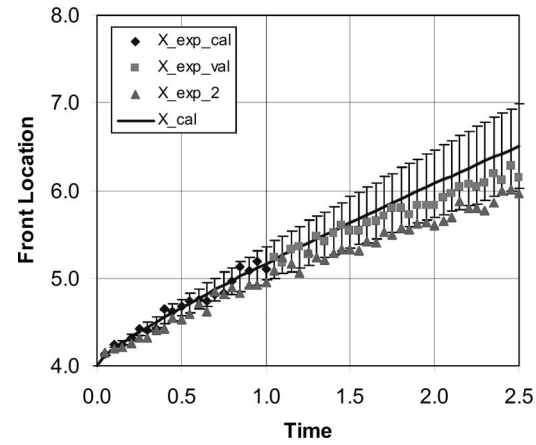

Fig. 6 Calibrated convective dispersion equation; X_exp_cal, X_exp_val – simulated experimental data used for calibration and validation respectively; X_exp_2 – experiment 2 simulated data; X_cal – calibrated model

$$\mathbf{cov}(\mathbf{X}\_\text{cal}) = \nabla_{\boldsymbol{\alpha}}\mathbf{X}\,\mathbf{cov}(\boldsymbol{\alpha})[\nabla_{\boldsymbol{\alpha}}\mathbf{X}]^{\mathrm{T}} = \nabla_{\boldsymbol{\alpha}}\mathbf{X}\begin{bmatrix} \sigma_D^2 & 0 \\ 0 & \sigma_U^2 \end{bmatrix}[\nabla_{\boldsymbol{\alpha}}\mathbf{X}]^{\mathrm{T}} \quad (32)$$

A common procedure is to estimate the covariance of the parameters from the residuals in the regression that lead to Eqs. (31). This represents the uncertainty in estimating the mean values for the parameters for the particular realization of the validation experiment. These estimates do not represent the variability in the true values of the parameters from experiment to experiment. One should model the true variability in these parameters across many experiments rather than use the uncertainty in the estimated mean values of the parameters from just the single calibration experiment. This requires either prior knowledge of these parameter distributions, or data from a sufficiently large ensemble of independent experiments such that the variability between independent experiments is well represented. Prior knowledge of the distributions of such parameters may be from carefully controlled, multiple laboratory experiments designed for the evaluation of constitutive relations, from design specifications of the experimental conditions and materials used, or in some cases, from expert opinion.

Here prior knowledge for these parameters is assumed. For illustrative purposes, the covariance of the model parameters is taken to be similar to that used for the Burgers' equation.

$$\mathbf{cov}\begin{pmatrix} D \\ V \end{pmatrix} = \begin{bmatrix} \sigma_D^2 & 0 \\ 0 & \sigma_V^2 \end{bmatrix} = \begin{bmatrix} 0.008^2 & 0 \\ 0 & 0.1^2 \end{bmatrix}$$

$$= \begin{bmatrix} 0.000064 & 0 \\ 0 & 0.01 \end{bmatrix} \quad (33)$$

The effect of the resulting parameter uncertainty is illustrated through 95% prediction intervals in Fig. 6. Note that the intervals grow as a function of time. This behavior is expected because the uncertainty in predicted front location due to the uncertainty in the velocity grows linearly with time (i.e., $X(t) \approx Vt$).

Note that at later time, the X_exp_2 data lies outside the model-parameter induced prediction intervals. Using the r^2 metric defined by Eq. (1) gives

$$r^2 = (\mathbf{X}\_\text{cal} - \mathbf{X}_{\text{exp}})^{\mathrm{T}}[\mathbf{cov}^{-1}(\mathbf{X}\_\text{cal} - \mathbf{X}_{\text{exp}})](\mathbf{X}\_\text{cal} - \mathbf{X}_{\text{exp}}) \quad (34)$$

where

Table 1 Significance of agreement: Calibrated convective-dispersion equation

	Time	r_0^2	$P(r^2 > r_0^2)$
X_exp_1			
	$0.0 < t \leqslant 2.5$	96.94	0.000
	$0.0 < t \leqslant 1.0$		
	$1.0 < t \leqslant 1.5$	6.96	0.541
	$1.5 < t \leqslant 2.0$	10.55	0.228
	$2.0 < t \leqslant 2.5$	11.35	0.183
X_exp_2			
	$0.0 < t \leqslant 2.5$	78.39	0.005
	$0.0 < t \leqslant 1.0$	22.34	0.267
	$1.0 < t \leqslant 1.5$	23.83	0.002
	$1.5 < t \leqslant 2.0$	8.74	0.365
	$2.0 < t \leqslant 2.5$	16.01	0.042

$$\mathbf{cov}(\mathbf{X\_cal} - \mathbf{X}_{exp}) = \mathbf{cov}(\mathbf{X\_cal}) + \mathbf{cov}(\mathbf{X}_{exp}) \qquad (35)$$

Since two parameters were estimated during calibration, two degrees of freedom were lost. In this case, the appropriate distribution for r^2 is the $\chi^2(n-2)$ distribution with the degrees of freedom equal to the number of measurements n minus the number of estimated parameters 2.

The corresponding significances of the calibrated model are listed in Table 1 for various time windows so that the effectiveness of the calibrated model can be assessed as one moves away from the calibration times. The significance of r_0^2 for the time window 0-1 for X_exp_1 is not shown. One should not use the same data for validation that was used for calibration without additional independent information (as is the case for the data taken over the 0–2.5 time window). Note that the significance of r_0^2 decreases with time for time greater than 1.0 for X_exp_1. This indicates that, relative to the uncertainty in the measurements and the parameters, there is evidence that the calibrated model becomes less effective as time increases. Because the significances are larger than 5%, the model cannot be rejected outright using the X_exp_1 data. However, when the full set of X_exp_1 data is used, the significance is zero (to three significant figures) and the model is rejected. The statistical test has more power when more data is used and the test is more likely to reject an invalid model (i.e., less likely to commit a Type 2 error as discussed earlier). This illustrates an important concept in model validation. Sufficient data must be available so that the model can be adequately tested. Using validation data over a parameter range very close to that for which the model was calibrated, does not provide a sufficiently independent test for model validity.

The results for X_exp_2 listed in Table 1 indicate that the trend in significance is not unimodal with time. Because the uncertainties are random, one should generally not expect an unimodal trend. Comparison of the results for X_exp_1 and X_exp_2 indicates that the significance of r_0^2 for several of the time windows for X_exp_2 is less than the 5% at which one may reject a model. This indicates that when a model is calibrated to data from one realization of the experiment, it may not represent the experimental behavior for another realization of the experiment. When the X_exp_2 data from the full time window is used, the test resolves the invalidity of the model with a significance of only 0.5%. As was the case for the X_exp_1 results, the test has more statistical power and is less likely to commit a Type 2 error when more data is used.

Inspection of Fig. 6 indicates that one should expect that the model should fail for the X_exp_2 data, since much of the data lies outside the tolerance bounds of the model. What is surprising is the model also fails for the X_exp_1 data, even though the data lies within the tolerance bounds. This is because the correlation structure of the differences between the data and the model predictions is not consistent with the correlation structure defined by

the sensitivity analysis. Or said another way, one cannot reproduce, to first order, the experimental observations using the C-D equation with a reasonably probable set of model parameters.

4.4 Contact Resistance. In the final example, the covariance based metric is applied to data derived from a validation experiment performed at Sandia National Laboratories, Albuquerque, NM. In an effort to study and test models for thermal contact resistance, an experimental program was supported through the ASCI Sub-Grid Physics Area and MAVEN. Here a brief overview of the experiment and the model is provided. Description of the experimental apparatus is provided in Blackwell, Gill, Dowding, and Easterling [25]; Emery, Blackwell, and Dowding [26]; with more details on the contact experiment provided by Voth and Gill [27].

The experimental apparatus is illustrated in Fig. 7. Two coaxial hollow right circular cylinders are pressed together with a known load to study models for contact resistance. Hollow cylinders were used to minimize variations in shear stress across the contact interface. The entire assembly was enclosed in an evacuated bell jar to minimize heat transfer to the environment and to remove trapped air from the contact interface. Each of the 304 stainless steel cylinders were instrumented with several vertical columns of 7 T-type thermocouples located on the surface of the cylinders. The axial locations of these thermocouples are listed in Table 2. The top cylinder was heated from above and the bottom cylinder cooled from below. Temperature responses were recorded at one-second intervals during the transient phase and at 60-s intervals during the near steady-state phase of the experiment.

Only a small subset of the temperature measurements provide by Dowding [28] were used here. This data was sampled from the time trace of data taken from the two thermal couples at station TC7 as listed in Table 1. The data was sampled at the ten times shown in Table 3. The readings from the two thermal couples were averaged, resulting in the average measurements (denoted as measurements) tabulated in Table 3. Also shown are estimates of the standard deviation for the average measurements as provided by Dowding [28]. These were obtained by using temperatures at similar stations, for each time. The temperatures at stations TC2 and TC13 are also included. These temperatures are used as boundary conditions for the predictive model. Cubic splines were used to interpolate between the times shown for TC2 and TC12. Additional measurements for these points were included to adequately capture the transient nature of the boundary conditions. Using the temperature measurements at these stations as boundary conditions reduces the uncertainties associated with contact resistance between the cylinders and the heating and cooling blocks. This allows one to focus on the contact resistance at the interface between the cylinders and the heat conduction within cylinders.

The model used to represent the apparatus illustrated in Fig. 7 follows:

$$\rho C_p \frac{\partial T}{\partial t} = k \frac{\partial^2 T}{\partial x^2} \qquad (36)$$

$$T(x,0) = 29.67 \qquad (37)$$

$$T(-61.7, t) = TC13(t), \quad \text{Table 3} \qquad (38)$$

$$T(61.7, t) = TC2(t), \quad \text{Table 3} \qquad (39)$$

$$q(0,t) = h(T(0^-, t) - T(0^+, t)) \qquad (40)$$

where h represents the contact conductance and is assumed to be a constant. The thermal response of the cylinders was modeled as one-dimensional transient heat conduction with contact resistance at the interface. Note that the predictive model used here for contact resistance is very simple and is not the one used by Sandia National Laboratories in their analysis of this experiment.

Three uncertain model parameters were considered: the thermal conductivity k, the volumetric heat capacity ρC_p, and the contact
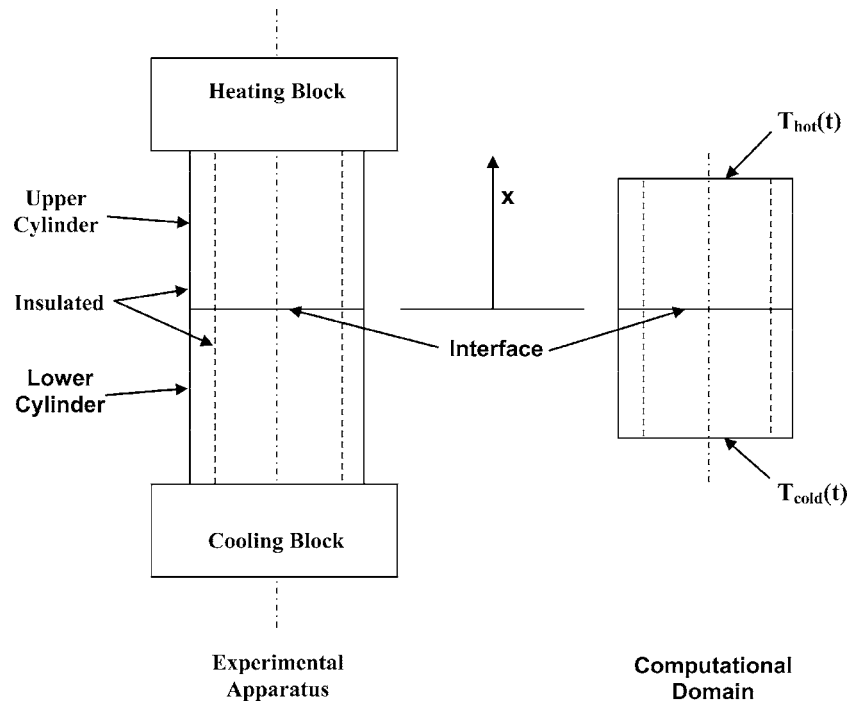
Fig. 7 Heat conduction apparatus and computational domain

conductance h. Values for these model parameters are listed in Table 4 along with estimates of their standard deviations. The standard deviations were based on discussions with the experimentalist and were provided by Dowding [28]. The standard deviations represent 5% of the thermal conductivity, 2% of the volumetric heat capacity, and 10% of the contact conductance.

The uncertainty in the temperature at the boundaries is not accounted for in the present analysis. If this uncertainty corresponds to uncorrelated noise over time, or correlated noise with a small correlation time relative to the time for which a significant pulse is felt in the interior, and if the uncertainty has zero mean (no bias), then one may expect that the effect of this uncertainty would be highly damped for the near contact surface measurements and small compared to the effects of uncertainty of the measurements and the thermal properties.

Equations (36)–(40) were modeled using a simple finite difference algorithm. This algorithm was explicit in time, using cell centered nodes with 40 equally spaced cells across the spatial region and a grid Fourier number of 0.2. Reducing the spatial grid size by half and the time step by 4 resulted in no change in

temperature at station TC7 to four significant figures.

Because the numerical algorithm used for this application does not suffer from numerically generated noise, finite differences were used to estimate the elements in the sensitivity matrix. In this case, center differences were used for each of the three model parameters with an increment of 0.0001 of the mean value for the parameter. Increasing the increment size by a factor of 10 did not

Table 2 Thermocouple axial locations

Thermocouple	Axial location (mm)
TC1	61.7
TC2	52.2
TC3	42.7
TC4	33.1
TC5	23.6
TC6	14.1
TC7	4.5
TC8	−4.6
TC9	−14.1
TC10	−23.6
TC11	−33.1
TC12	−42.7
TC13	−52.2
TC14	−61.7

Table 3 Observed temperatures and standard deviation as a function of time

Time s	T, TC7 °C	σ, TC7 °C	T, TC2 °C	T, TC13 °C
0.0	-	-	29.78	29.53
14.8	29.67	0.1536	29.78	29.53
73.8	-	-	40.81	29.53
285.7	-	-	60.72	29.76
570.7	44.95	0.3565	67.83	31.34
870.6	-	-	71.80	33.32
1140.6	53.91	0.3363	74.26	34.65
1440.5	-	-	76.33	35.68
1710.5	58.16	0.3216	77.80	36.33
2032.5	-	-	78.96	36.89
2332.4	60.44	0.3092	79.32	37.25
2932.3	61.20	0.3124	79.67	37.60
3532.2	61.46	0.3121	79.80	37.73
4132.1	61.57	0.3172	79.84	37.75
4732.0	61.61	0.3189	79.87	37.82
5331.9	61.63	0.3131	79.88	37.84

Table 4 Model parameters and measurement statistics: Normally distributed uncertainties

Parameter	Expected value $\langle \alpha \rangle$	σ
α_1 (thermal conductivity, k)	15.06 W/m C	0.753 W/m C
α_2 (volumetric heat capacity, C)	3.912×10^6 J/m^3 C	0.782×10^5 J/m^3 C
α_3 (contact conductance, h)	1337.0 W/m^2 C	133.70 W/m^2 C
d (temperature, T)		Listed in Table 3

change the following results. Double precision was used for all calculations for this example. Given this estimate for the sensitivity matrix, the corresponding r^2 (Eq. (1)) and its significance for the differences between the experimental observations and the model predictions were found to be

$$r^2 = 16.94 \qquad (41)$$

$$P(r^2 > 16.94) = 0.076 \qquad (42)$$

Because first order sensitivity analysis was used, one should interpret the 7.6% significance level with caution since such an analysis tends to be less reliable near the tails of distributions. A low value of significance can be due to one or more of the following:

1. A Type 2 error was committed and the model is in-fact, invalid. See the discussion at the end of Sec. 3.1. This may be due to the numerical implementation of the equations, the approximations used for the boundary conditions, and the form of the contact conductance model. For example, contact resistance is a function of surface roughness, temperature and its effect on contact surface distortion, and contact pressure. Voth and Gill [27] suggest that alignment issues between the two cylinders may exist in this experiment, resulting in 3 dimensional effects at the interface. They also suggest that there may be other sources of heat loss not accounted for in the present model. All of these effects were ignored here.
2. The models for the uncertainty in the model parameters are not valid. It is not unusual to underestimate uncertainty in model parameters such as contact conductance. If this is the case here, a larger uncertainty in contact conductance will result in a larger value for significance. There may also be other forms of uncertainty that were not properly accounted for in the present analysis.
3. The model is valid, but this particular realization of the experiment being fairly rare (i.e., a significance of only 7.8%).

Because the execution of the model was computationally inexpensive, the significance level was reassessed using a Monte Carlo analysis defined earlier with 10,000 realizations. This procedure yielded

$$r^2 = 16.97 \qquad (43)$$

$$P(r^2 > 16.97) = 0.076 \qquad (44)$$

The difference between this significance and that obtained from the first-order sensitivity analysis is zero for the number of significant figures shown in Eqs. (42) and (44). Clearly, the sensitivity analysis is adequate for this application with this level of uncertainty.

Finally, a modification of the contact resistance problem is provided to illustrate the effect of a non-normal distribution. The parameter that is likely to contain the most uncertainty is contact conductance. In the previous analysis, the standard deviation for the contact conductance was assumed to be 10% and the uncertainty is normally distributed. A more conservative estimate for this parameter would be to assume that the distribution is not known, but lies within a ±20% range of the mean. A common approach to use in such a case is to assume all values of the parameter are equally likely within this range, which corresponds to a uniform distribution over this range. This has the effect of assigning more cumulative probability to the tails of the distribution. Repeating the Monte Carlo process discussed earlier, with a uniform distribution for the contact conductance (with bounds that are ±20% of the mean parameter value) and the previously defined normal distributions for the remaining parameters and the measurements resulted in the following:

$$r^2 = 14.56 \qquad (45)$$

$$P(r^2 > 14.56) = 0.147 \qquad (46)$$

This model for uncertainty in the contact conductance resulted in twice the significance of the previous example. However, this larger value for significance still does not meet the level suggested earlier for good confidence in the model.

Do these results suggest that one can increase the likelihood of finding a model acceptable by increasing the uncertainty in the model parameters? The answer is generally yes. However, one should be careful not to assign unrealistic uncertainty to a parameter. Once one accepts a level of uncertainty, one should use this uncertainty in any predictions made by the model under conditions close to those of the validation experiment. In other words, the required uncertainty in the target application of the model should not be less than the uncertainty in the validation experiments as modeled by the probability distributions.

5 Discussion

In the previous sections, we introduced a validation metric based on the mean and covariance in the measurement and in the model parameters to quantify the distance between model predictions and experimental measurements in n-dimensional space, where n is the number of measurements and corresponding predictions. We demonstrated this metric for (1) a model known to be consistent with the simulated data, (2) a model known to be inconsistent, and (3) a model for which the results indicate limited consistency with the data. The advantage of this metric is it accounts for correlation in the differences between the experimental measurements and the model predictions. While we applied this metric to results from single experiments, it can easily be extended to multiple experiments (Hills and Leslie [10]).

Two approaches were used to evaluate the r^2 metric; a first-order sensitivity analysis and a Monte Carlo analysis. The Monte Carlo method is generally considered the "gold standard" as this method is applicable to highly nonlinear problems, can easily address different probability distributions, and can provide reasonable estimates of the distributions near their tails. The primary disadvantage of the Monte Carlo approach is the large number of model evaluations required to resolve the distributions, especially if one must resolve the distributions near their tails. A natural question one may ask is: *How important is the ability to fully resolve the tails of a distribution in model validation*? Unlike risk assessment, where evaluating risk at very low probabilities is often the focus of the assessment, some error in the estimate of significance of the observed value for r^2 for a model is somewhat more acceptable in model validation. Even through one may fail to reject the model outright when it should be rejected due to this error, the consequences of this failure will usually be small. This is because one should suspect the usefulness of a model that results in low significance for the r^2 value and not use the model for prediction until the source of this result is understood. A related question is: *Why not use 10% significance rather than a 5% significance as the cut-off point to reject the model*? Although one may reject a model by the 10% criteria and not by 5% criteria, both of these significances are small. One should suspect the usefulness of the model whether the model was rejected or not. In either case, the model should not be used until the source of this small significance is understood, corrected, and re-tested.

The previous example problems were chosen to be simple so that they could be more easily reproduced by the reader. For such example problems, one can easily afford to apply the Monte Carlo approach. However, even in those cases for which the Monte Carlo approach is used to evaluate r^2, we almost always apply the sensitivity analysis approach as a verification step. For those complex engineering applications for which the use of Monte Carlo methods may not be practical, approximate methods must be used, such as through the use of a first-order or higher-order sensitivity analysis, or through the use of a surrogate model for the full model.

Important issues in validation that have not been addressed here include the following:

1. The work presented here assumed that reasonably characterized models for the sources of uncertainty in the validation experiment were available. This is clearly not always the case. For example, validation experiments may possess systematic bias that is not modeled, such as occurs due to heat conduction through thermal couple leads. Often, the only knowledge available about the uncertainty in the parameters are estimates of the bounds on these values based on expert opinion. In cases such as these, one must build and/or improve the models for uncertainty from experimental observations, often using experimental observations from the systems level, or use techniques that allow for less complete information about the distribution. Bayesian analysis and Dempster-Shafer theory provide tools to address less complete information [29–31].

2. The metrics defined here are appropriate when the applications of the model are similar to the validation tests. For complex systems level models, one often performs validation tests on subcomponents rather than at the full system level. One may use a suite of validation tests to evaluate the thermal radiation component and another to evaluate the convective component. Methodology is needed to combine results from subcomponent or sub-model experiments to assess the ability of the system level model to perform adequately.

3. The validation of approximate models, especially when used for conditions different from those for which validation data is available, represents a very difficult but practical reality. In complex systems, one often uses sub-models which approximate behavior through representative surfaces (i.e., curve fits) rather than through fundamental physical arguments. Differences between experimental results and model predictions are expected in such cases. The method presented here will often find such a model invalid because the present method does now allow for a level of discrepancy that is significant relative to the uncertainty introduced due to the modeled parameter and measurement uncertainty.

The development of model validation methodology is in its early stages and the issues associated with model validation can be difficult to address. There is a great need to develop alternative rigorous methods for model validation and to develop a consensus as to the advantages/disadvantages of the various approaches.

Acknowledgment

Nomenclature

c = temperature or concentration for examples 1 and 2
C_p = specific heat (constant pressure)
D = dispersive coefficient in Burgers' equation and the convective-dispersive equation
df = degrees of freedom
h = contact conductance
k = thermal conductivity
n = number of measurements
P = probability
p = number of parameters
PDF = probability density function
r^2 = statistic
T = temperature for contact resistance example
t = time
U = velocity (Burgers' equation)
V = velocity (convective-dispersive equation)
x = spatial location
X = front location

Greek symbols

α = model parameter
χ^2 = chi-squared distribution
θ = general experimental observation or model prediction
ρ = density
σ = standard deviation

Subscripts

D = dispersivity (or diffusion)
exp = experiment
i = index
m = mean
model = model
quad = quadratic surface
U = velocity (Burgers' equation)
V = velocity (convecive-dispersive equation)

References

[1] ISI (2003), SciSearch Plus, www.isinet.com, Philadelphia.
[2] Oberkampf, W. L., and Trucano, T. G., 2002, "Verification and Validation in Computational Fluid Dynamics," Prog. Aerosp. Sci. **38** (3), pp. 209–272.
[3] Oberkampf, W. L., Trucano, T. G., and Hirsch, C., 2004, "Verification, Validation, and Predictive Capability in Computational Engineering and Physics," Appl. Mech. Rev. **57** (3), pp. 345–384.
[4] Hills, R. G., and Trucano, T. G., 1999, "Statistical Validation of Engineering and Scientific Models: Background," SAND99-1256, Sandia National Laboratories, Albuquerque.
[5] Dowding, K. J., Hills, R. G., Leslie, I., Pilch, M., Rutherford, B. M., and Hobbs, M. L., 2004, "Case Study for Model Validation: Assessing a Model for Thermal Decomposition of Polyurethane Foam," SAND2004-3632, Sandia National Laboratories, Albuquerque.
[6] Easterling, R. C., 2003, "Statistical Foundations for Model Validation: Two Papers," SAND2003-0287, Sandia National Laboratories, Albuquerque.
[7] Rutherford, B. M., and Dowding, K. J., 2003, "An Approach to Model Validation and Model-Based Prediction—Polyurethane Foam Case Study," SAND2003-2336, Sandia National Laboratories, Albuquerque.
[8] Hills, R. G., and Trucano, T. G., 2001, "Statistical Validation of Engineering and Scientific Models with Application to CTH," SAND2001-0312, Sandia National Laboratories, Albuquerque.
[9] Hills, R. G., and Trucano, T. G., 2002, "Statistical Validation of Engineering and Scientific Models: A Maximum Likelihood Based Metric," SAND2001-1783, Sandia National Laboratories, Albuquerque.
[10] Hills, R. G., and Leslie, I. H., 2003, "Statistical Validation of Engineering and Scientific Models: Validation Experiments to Application," SAND2003-0706, Sandia National Laboratories, Albuquerque.
[11] Hills, R. G., Leslie, I. H., and Dowding, K., 2004, "Statistical Validation of Engineering and Scientific Models: Application to the Abnormal Environment," SAND2004-1029, Sandia National Laboratories, Albuquerque, March.
[12] Trucano, T. G., Easterling, R. G., Dowding, K. J., Paez, T. L., Urbina, A., Romero, V. J., Rutherford, B. M., and Hills, R. G., 2001, "Description of the Sandia Validation Metrics Project," SAND2001-1339, Sandia National Laboratories, Albuquerque.
[13] Trucano, T. G., Pilch, M., and Oberkampf, W. L., 2002, "General Concepts for Experimental Validation of ASCI Applications," SAND2002-0341, Sandia National Laboratories, Albuquerque.
[14] Warren-Hicks, W., Carbone, J. P., and Havens, P. L., 2002, "Using Monte Carlo Techniques to Judge Model Prediction Accuracy: Validation of the Pesticide Root Zone Model 3.12," Envir. Toxicol. Chem. **21** (8), pp. 1570–1577.
[15] Roberson, S., 1999, "Simulation Verification, Validation and Confidence: A Tutorial," Trans. Soc. Comput. Simul. Int. **16** (2), pp. 63–69.
[16] Brownlee, K. A., 1965, *Statistical Theory and Methodology in Science and Engineering*, John Wiley & Sons, New York.
[17] Strang, G., 1986, *Introduction to Applied Mathematics*, Wellesley-Cambridge Press, Massachusetts.
[18] Hills, R. G., Fisher, K. A., Kirkland, M. R., and Wierenga, P. J., 1994, "Application of Flux-Corrected Transport to the Las Cruces Trench Site," Water Resour. Res. **30** (8), pp. 2377–2385.
[19] Roe, P. L., 1985, "Some Contributions to the Modelling of Discontinuous Flows," Lect. Appl. Math. **22**, pp. 163–193.
[20] Roe, P. L., 1986, "Characteristic-Based Schemes for the Euler Equations," Annu. Rev. Fluid Mech. **18**, pp. 337–365.

[21] Sweby, P. K., 1984, "High Resolution Schemes using Flux Limiters for Hyperbolic Conservation Laws," SIAM (Soc. Ind. Appl. Math.) J. Numer. Anal. , **21**(5), pp. 995–1011.

[22] Yang, H. Q., and Przekwas, A. J., 1992, "A Comparative Study of Advanced Shock-Capturing Schemes Applied to Burgers' Equation," J. Comput. Phys. **102**, pp. 139–159.

[23] *MatLab® Mathematics (2004), Version 7*, The MathWorks, Inc., Natick, MA.

[24] IMSL, 1997, "IMSL, Math Library, Vols. 1 and 2," Visual Numerics, Inc., Houston.

[25] Blackwell, B. F., Gill, W., Dowding, K. J., and Easterling, R. G., 2000, "Uncertainty Estimation in the Determination of Thermal conductivity of 304 Stainless Steel," *Proceedings of the International Mechanical Engineering Congress*, ASME, Orlando, FL.

[26] Emery, A. F., Blackwell, B. F., and Dowding, K. J., 2001, "The Relationship Between Information, Sampling Rates, and Parameter Estimation Models," *Proceedings of the 35th National Heat Transfer Conference*, June, Anaheim, CA.

[27] Voth, T. E., and Gill, W., 1999, "Assessment of Sub-Grid Contact Resistance Physics Effects on Thermal Simulation," Sandia National Laboratories technical memo.

[28] Dowding, K. J., 2000, personal communication, Sandia National Laboratories, Albuquerque.

[29] Leonard, T., and Hsu, J. S. J., 1999, *Bayesian Methods*, Cambridge University Press, Cambridge.

[30] Sharer, G., 1976, *A Mathematical Theory of Evidence*, Princeton University Press, Princeton, NJ.

[31] Oberkampf, W. L., and Helton, J. C., 2002, "Investigation of Evidence Theory for Engineering Applications," AIAA 2002-1569, 4th Non-Deterministic Approaches Forum, American Institute of Aeronautics and Astronautics, April 22–25, Denver, Colorado.

Qijun Yu

Department of Mechanical and Materials
Engineering,
The University of Western Ontario,
London, ON, N6A 5B8, Canada
e-mail: yu@fatfoam.com

Brian E. Thompson

Foam Application Technologies Inc.,
Mayaguez, Puerto Rico
e-mail: thompson@fatfoam.com

Anthony G. Straatman[1]

Mem. ASME
Department of Mechanical and Materials
Engineering,
The University of Western Ontario,
London, ON, N6A 5B8, Canada
e-mail: astraatman@eng.uwo.ca

A Unit Cube-Based Model for Heat Transfer and Fluid Flow in Porous Carbon Foam

A unit-cube geometry model is proposed to characterize the internal structure of porous carbon foam. The unit-cube model is based on interconnected sphere-centered cubes, where the interconnected spheres represent the fluid or void phase. The unit-cube model is used to derive all of the geometric parameters required to calculate the heat transfer and flow through the porous foam. An expression for the effective thermal conductivity is derived based on the unit-cube geometry. Validations show that the conductivity model gives excellent predictions of the effective conductivity as a function of porosity. When combined with existing expressions for the pore-level Nusselt number, the proposed model also yields reasonable predictions of the internal convective heat transfer, but estimates could be improved if a Nusselt number expression for a spherical void phase material were available. Estimates of the fluid pressure drop are shown to be well-described using the Darcy-Forchhiemer law, however, further exploration is required to understand how the permeability and Forchhiemer coefficients vary as a function of porosity and pore diameter. [DOI: 10.1115/1.2165203]

1 Introduction

There are essentially two types of porous solids: those produced by packing or sintering solid particles or cylinders together and those produced by casting or foaming a material during solidification. In both cases, the final product consists of interspersed regions of solid and fluid (or void). Depending on the final structure, the void regions may be isolated from one another (trapped phase) or continuous as in the case of an interconnected pore structure. Graphitized porous carbon foam fabricated using the ORNL patented process [1] represents a case of near-spherical interconnected pores, as shown in Fig. 1. The figure illustrates the open, interconnected structure of the foam and the near-homogeneous distribution of void size. Porous carbon foam exhibits unique thermo-physical and geometric characteristics [2] that make it suitable for heat transfer applications in microelectronics and power generation. The unique characteristics include:

1. An extremely high bulk thermal conductivity (stagnant effective thermal conductivity) between 40 and 180 W/m K [2,3]. This high effective conductivity results from the extremely high material conductivity of the graphitized carbon material ($k=800-1900$ W/m K). In contrast, similar porosity aluminum foams have effective conductivities of approximately $2-26$ W/m K, which result from material conductivities of $140-237$ W/m K (for aluminum alloys). As such, the carbon foam has a much higher capability to conduct or entrain heat into its internal structure so that infiltrated fluid can convect heat away.

2. An open, inter-connected void structure that enables fluid infiltration such that enormous increases in surface area for heat transfer are available (5000 to 50,000 m^2/m^3).

3. A low density (from 0.2 to 0.6 g/cm^3, depending upon porosity), which makes the material suitable for compact and lightweight applications. In contrast, aluminum foam has a

density of $0.3-0.8$ g/cm^3, depending upon porosity.

4. An increase in exposed surface area and a rough open structure, which leads to increased mixing at the external fluid interface.

To consider the carbon foam material for heat transfer applications, there is an immediate need for an engineering model that can be used to evaluate the thermal and hydrodynamic characteristics under different operating conditions. For a generic convective heat transfer application, the model is required to express the internal exposed surface area, the external exposed surface area, and the void window size as a function of foam porosity and pore diameter. The model can then be used to produce expressions for the surface roughness, the effective conductivity, and the permeability. The review given below provides a brief overview of previous modeling efforts in porous media and makes clear the need for a new model to characterize porous carbon foam. The review includes efforts to model the geometry, the effective conductivity, and the permeability.

The geometric condition of a porous media is typically characterized by an idealized geometry model from which the internal surface area to volume ratio, β, and all other internal and external geometry parameters can be derived. To this end, Dullien [4] considered a regularly packed bed of spheres and derived the classical expression for the surface area to volume ratio: $\beta=6(1-\varepsilon)/D_p$, where ε is the porosity of the porous media defined as $\varepsilon=V_f/V_{tot}$, D_p is the particle (sphere) diameter, and the subscript f denotes the fluid or void phase. For the same condition, Hwang et al. [5] used the empirical expression $\beta=20.346(1-\varepsilon)\varepsilon^3/D_p$ to derive an expression for the heat transfer in his experiments on packed spherical particles. The empirical expression is slightly different as it accounts for non-regular packing of the spherical bed whereas the analytical model considers perfectly regular packing. By comparing these expressions, it is evident that β is the same when $\varepsilon=0.67$; for $\varepsilon>0.67$, the empirical expression predicts slightly higher β due to the non-regular void structure. For reticulated metal foams, such as aluminum foam, simplified geometry models take the form of a unit-cell with square-barred corner elements [6]. The size of the square bars is determined
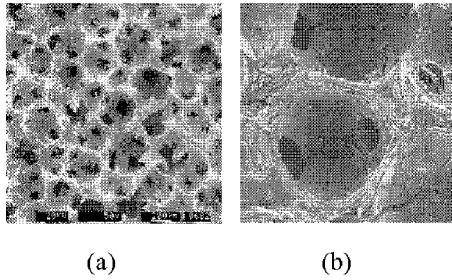

Fig. 1 (*a*) Electron micrograph of the carbon foam surface [1]; (*b*) electron micrograph of the carbon foam surface of a single pore

Fig. 2 CAD images showing the proposed unit-cube model: (*a*) a single unit-cube with spherical void; (*b*) pore block containing a number of interconnected pores

such that the porosity V_f/V_{tot} is preserved. There are no available geometry models for spherical void structures, such as that observed in porous carbon foam. Though this is essentially opposite to the packed-sphere geometry, expressions for internal and external surface areas are different and must be obtained from a new basic geometry model that represents the spherical void phase.

The effective thermal conductivity, k_e, of a porous media can be obtained experimentally by testing several different samples of a specific porous material, or analytically by solving a heat transfer problem for an idealized geometry model. Deissler et al. [7] investigated the effective thermal conductivity of two simple models: two planar layers (i.e., solid and fluid) in parallel and two layers in series. The expression for two layers in parallel is: $k_e = k_f\varepsilon + (1-\varepsilon)k_s$, whereas the expression for two layers in series is: $k_e = k_s/(\varepsilon\sigma + (1-\varepsilon))$, where σ is the ratio of solid phase to void phase conductivities. The two expressions predict effective conductivities with variations as high as 7% for $\sigma = 2$, and as high as 99% for $\sigma = 1000$ (with $\varepsilon = 0.4$). This is due to the fact that when σ is high the solid material arrangement has a great influence on the effective conductivity. As such, for high σ applications such as porous carbon foam, an accurate characterization of the internal geometry is necessary. Batchelor and O'Brien [8] derived an analytical solution for k_e of a packed bed of spheres by solving an integral equation for the temperature distribution over the sphere surface. A thermal-electrical approach was used by several authors (see, for example, Refs. [6,9]) to derive expressions for the effective conductivity of packed sphere geometries of different materials. Bhattacharya et al. [10] used both analytical and empirical relations for determining the effective thermal conductivity of metal foams. Tee et al. [11] integrated a probability density function over randomly distributed cubical cells to obtain an isotropic estimate of the effective conductivity of porous carbon foam. Klett et al. [12] proposed a conductivity model based upon the ligament conductivity and the mean flow path for a spherical void phase. Comparisons with available data for porous carbon foam showed that that the model produced good predictions, but the model parameters must be calibrated to give good characteristic results. A thermal-electrical analogy will be applied in the present study in combination with the proposed geometry model to obtain an expression for the effective thermal conductivity for a spherical void porous material.

The most widely used expression for the permeability of a porous media is the Ergun equation [13] given as: $K = \varepsilon^3 D_p^2/(150(1-\varepsilon)^2)$, however, Nakayama and Kuwahara [14] reviewed available studies on the permeability of various geometric models and proposed $K = \varepsilon^3 D_p^2/(147(1-\varepsilon)^2)$ as the most suitable generic expression for a packed bed of spheres. In the present study, the same permeability expression will be employed, but using an equivalent particle diameter that is derived from the unit-cube geometry proposed to model porous carbon foam. The model will then be calibrated against existing data for fluid pressure drop across porous carbon.
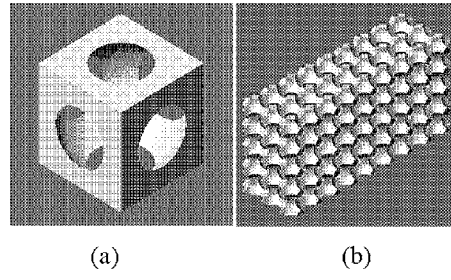
The present study proposes a unit-cube model to characterize the geometry of porous carbon foam or other open, interconnected porous media with a near-spherical void phase. The geometry model is based on a unit-cube-centered sphere, where the sphere represents the fluid or void phase. The complete geometry model is presented and all geometry parameters required for application in convective heat transfer are presented. The unit-cube model is then used to develop an expression for the effective conductivity of the porous material. The model is validated by comparing predictions of the effective conductivity, the internal convective heat transfer and the fluid pressure drop to other modeled results and to previous results obtained experimentally.

2 Geometric Model for Porous Carbon Foam

A geometric model is required for the exploration of heat transfer and flow in terms of the geometry parameters, thereby enabling optimization of the foam structure for different applications. Based on the geometry characteristics of the carbon foam [1–3], the following assumptions for the present geometric model are proposed:

1. The entire foam is assumed to have a single uniform void (pore) diameter.
2. Pores are considered to be spherical and centered inside unit-cubes.
3. Pores are regularly arranged in space, and each pore connects with six adjacent pores on the six surfaces of the unit cube.

Figure 2(*a*) shows a three-dimensional CAD image of the proposed unit-cube geometry with a spherical void phase. Figure 2(*b*) shows a pore block of unit-cubes with exposed pore surfaces that are cut at the center plane of the cube at the sides, front and top of the pore block. Figure 3 compares the internal geometry of the idealized geometry model with similar images of the porous carbon foam obtained from ORNL. The images illustrate that the idealized geometry model effectively captures the internal structure of the carbon foam. Figure 4 shows the detailed dimensions of the unit-cube model. Here, D is the pore (void phase) diameter; $H = f(D, \varepsilon)$ is the height of the unit-cube defined by the given pore diameter and the porosity; $h = (D-H)/2$ is the spherical cap height of the pore; $d = \sqrt{D^2 - H^2}$ is the interconnected pore channel diameter, which is the opening diameter of the pore interface at the unit-cube surface (also called the pore window); and $c = (H - d)/2$ is the width of the strut at the center plane of the unit cube (also called the ligament width).

The size of a unit-cube is not universally constant, rather it is determined by considering the desired porosity and pore diameter. By the definition of porosity [15], an expression relating the cube height H, the porosity ε, and the pore diameter D is derived
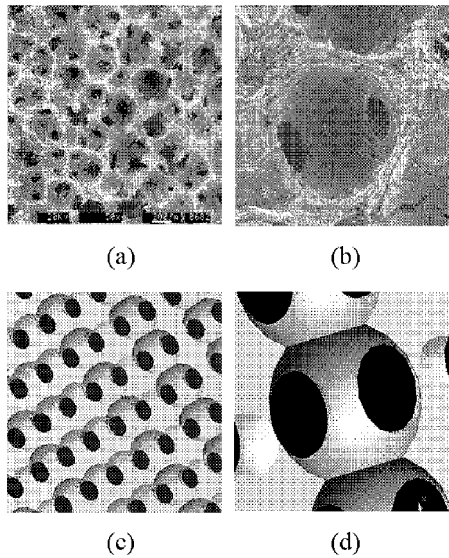
(a)   (b)

(c)   (d)

Fig. 3 A comparison of the idealized geometry (*a*) and (*b*) with the structure of porous carbon foam (*c*) and (*d*) obtained from ORNL [1]

$$H^3 - \frac{3\pi D^2}{(4\varepsilon + \pi)}H + \frac{4\pi D^3}{3(4\varepsilon + \pi)} = 0 \qquad (1)$$

The dimension of the unit-cube H is obtained by solving Eq. (1) for given values of ε and D. Once the size of the unit-cube is established, the geometry is fixed and the remaining geometric parameters can be evaluated as described below. Since the porous carbon foam has an interconnected pore structure, we are only interested in the range of pore window sizes: $0 < d < H(0.52 < \varepsilon < 0.96)$. When $d \leq 0$, the unit-spheres are isolated from one another; for $d \geq H, c \leq 0$ meaning that the ligaments connecting the solid phase are broken.

For a general application where fluid passes both across and through the porous material, information on the geometry is required for the internal structure and for the external interface between the porous material and the fluid. The internal structure is described here in terms of the area to volume ratio. The external geometry is described in terms of the exposed surface area factor and the absolute roughness of the exposed surface. While the ex-
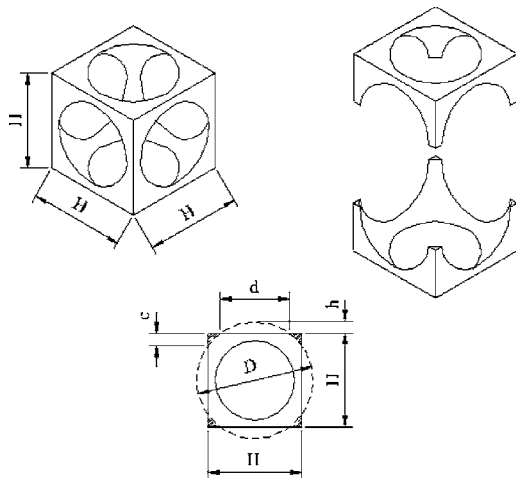

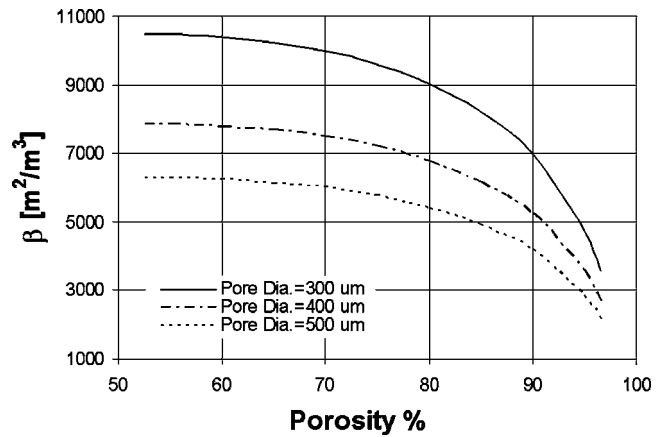**Fig. 4 Detailed dimensions of the unit cube geometry model at a cross section cut at the center plane of the unit cube**

Fig. 5 Interior surface area to volume ratio β plotted as a function of porosity for three different spherical void (pore) diameters

ternal geometry parameters are only required for cases where fluid flows across the exposed surface, they are included here for completeness and reference.

2.1 Interior Surface Area to Volume Ratio β. The ratio β quantifies the internal surface area available for convective heat transfer. For a solid unit-cube, $\beta = 0$, which represents the lower limit. For porous carbon foam made by ORNL process [1], this value can be as high as 5000–50,000 m²/m³, depending upon the porosity and void diameter. The ratio β of the proposed unit-cube geometry is expressed as: $\beta = S_{\text{int-wall}}/H^3$, where $S_{\text{int-wall}}$ is the void interior surface area in a single unit-cube obtained from:

$$S_{\text{int-wall}} = \pi D^2 - 6(\pi Dh) = \pi D(3H - 2D) \qquad (2)$$

giving the final expression

$$\beta = \frac{\pi D}{H^3}(3H - 2D) \qquad (3)$$

Figure 5 shows the variation of β for different D over the range $0.52 < \varepsilon < 0.96$, which corresponds to the limits described following Eq. (1). Here it is evident that β decreases with increasing porosity and with increasing void diameter. For high porosities, β decreases sharply due to the decrease in available solid material inside the foam. For a convective heat transfer application, the optimal value for β is evaluated by comparison of the thermal and hydrodynamic resistances. The higher the value of β, the higher the area available for internal heat exchange but this also results in higher net viscous losses resulting in a higher fluid pressure drop.

2.2 External Exposed Surface Area. To characterize surface area on the external surfaces of the foam, we introduce a surface area factor S_F, defined as the ratio of the total average open pore surface area over the flat surface area of the cube at the exposed layer, that is

$$S_F = \frac{S_{\text{exp}}}{H^2} \qquad (4)$$

The exposed surface area, S_{exp}, of the open pore structure represents the interface between the pure fluid domain and the porous domain represented by the idealized geometry model. Since the exposed interface depends upon the location of the cut, the exposed surface area is obtained by considering an average location. The exposed surface includes two parts: (1) the flat cross-section surface area cut at a location either between 0 and c or c and $H/2$; and (2) the opened pore spherical wall surface area (see Fig. 6). The flat cross-section surface area is computed from two portions: from 0 to c and from c to $H/2$. The detailed dimensions used to compute the flat cross-section surface area are shown in Fig. 7.
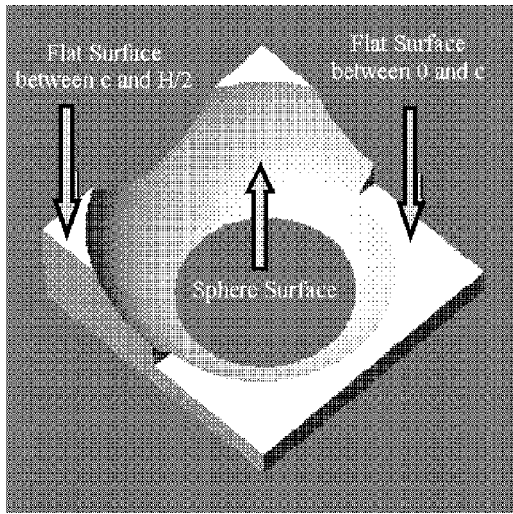
Fig. 6 Illustration of the exposed pore surface area showing the spherical wall surface and the flat surface cross section cut at a location either between 0 and c or between c and $H/2$

The flat surface area S_{1y} from 0 to c is obtained as

$$S_{1y} = H^2 - \pi r^2 \qquad (5)$$

where $r^2 = R^2 - H'^2$, and $H' = H/2 - y$. The average flat cross-section surface area from 0 to c is then calculated to be

$$S_{\text{avg1}} = \frac{1}{c} \int_0^c S_{1y} dy \qquad (6)$$

The flat surface area S_{2y} from c to $H/2$ is obtained from
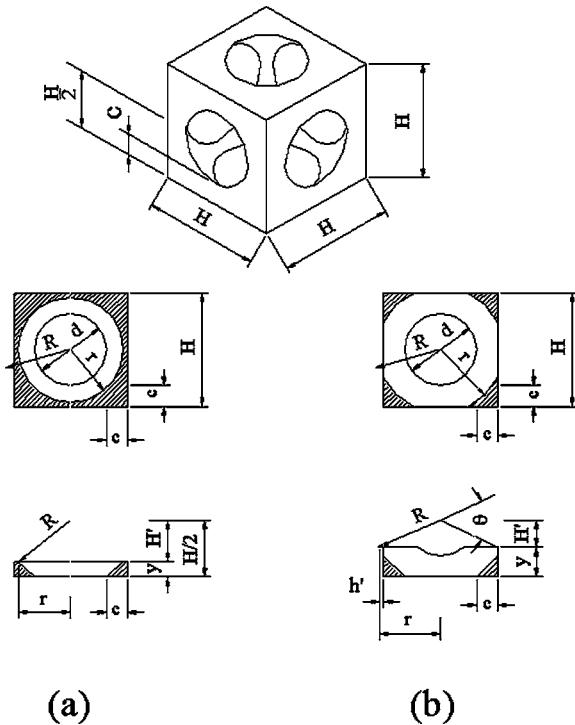

Fig. 7 (a) Flat cross-section surface cut at a location between 0 and c; (b) flat cross-section surface cut at a location between c and $H/2$
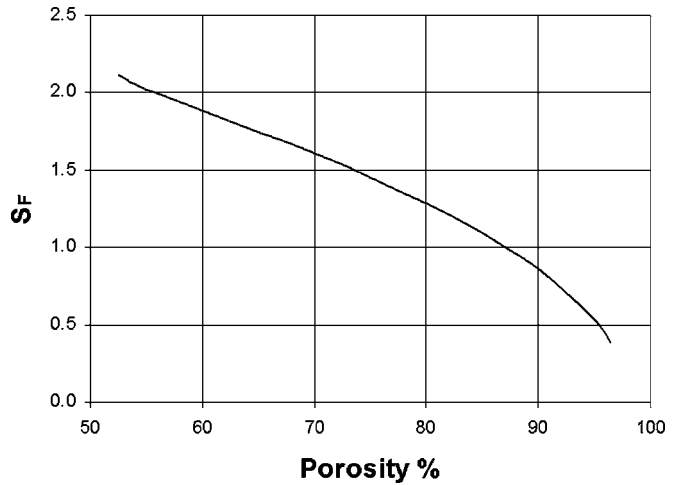
Fig. 8 Plot showing the variation of the surface area factor, S_F, as a function of porosity

$$S_{2y} = H^2 - \left(\pi r^2 - 4\frac{r^2}{2}(\theta - \sin\theta) \right) \qquad (7)$$

where r and H' for S_{2y} are the same as that described above for S_{1y}, and $\theta = 2\cos(H/2r)$. The average flat cross-section surface area from c to $H/2$ is determined to be

$$S_{\text{avg2}} = \frac{1}{\left(\frac{H}{2} - c\right)} \int_c^{H/2} S_{2y} dy \qquad (8)$$

Then the average flat cross-section area from 0 to $H/2$, S_{favg}, is obtained by averaging S_{1y} and S_{2y} over H, and is expressed by

$$S_{\text{favg}} = \frac{2\left(S_{\text{avg1}} c + S_{\text{avg2}}\left(\frac{H}{2} - c \right) \right)}{H} \qquad (9)$$

The opened spherical wall surface area, S_s, is given by (assuming the pore is cut at the pore center plane)

$$S_s = \frac{S_{\text{int-wall}}}{2} \qquad (10)$$

Finally, the total average opened surface area at the exposed layer, S_{exp}, is the sum of S_{favg} and S_s, and is given by

$$S_{\text{exp}} = S_{\text{favg}} + S_s \qquad (11)$$

which is inserted into Eq. (4). Figure 8 shows the relationship between the surface area factor S_F and the porosity for a fixed pore diameter. It is found that the exposed surface area factor S_F decreases as the porosity increases and it reaches a maximum value of 2.15 at a porosity of 0.5236, and a value of 1 at porosity of 0.8722. This means that if a fluid flowing across the foam does not penetrate the foam surface, the available area for heat transfer is the same as that of a smooth plate (of the same plan dimensions) when $\varepsilon = 0.8722$. For the more commonly observed case where the fluid penetrates the foam, large increases in surface area are made available, resulting in increased heat transfer.

2.3 Absolute Surface Roughness of the Exposed Pore Surface R_A. The absolute surface roughness of the exposed pore surface is required to determine the resistance due to the open surface for applications where the flow is not forced directly into the foam. R_A is defined as the radius of the inter-connected pore diameter (radius of the pore window) and is determined by
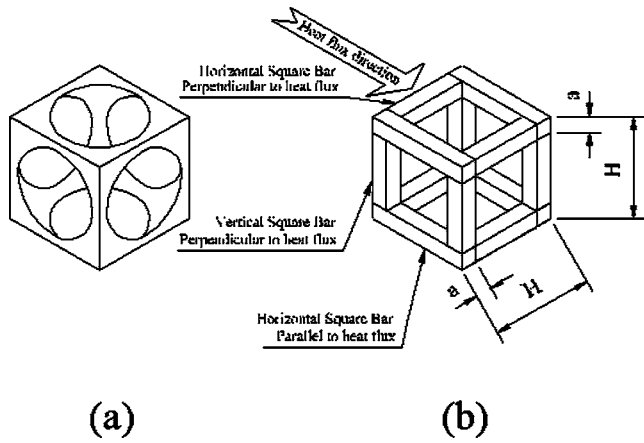
Fig. 9 (*a*) Carbon foam-spherical void phase pore structure; (*b*) equivalent solid square bar structure with the same porosity

$$R_A = \frac{d}{2} = \frac{1}{2}\sqrt{D^2 - H^2} \tag{12}$$

Parameters of the geometric model are now used to develop an analytical model for the effective thermal conductivity of the unit-cube structure and for the hydrodynamic loss associated with flow through the porous material.

3 Thermal Model

The thermal model consists of two parts and is required for the application of the unit-cube model in engineering calculations. The effective thermal conductivity is required to quantify the rate at which energy is entrained into the foam structure and the convective model to quantify the rate at which energy can be removed by the infiltrated fluid.

3.1 Effective Thermal Conductivity. The effective or stagnant thermal conductivity of a porous material is a function of the thermal conductivities of the solid and the fluid, the porosity and the structure of the foam, and is another important parameter characterizing the porous material. The equivalency technique is applied to the solid phase volume since the solid phase is the controlling factor for the effective thermal conductivity of the porous carbon foam material. The effective thermal conductivity is based on the following assumptions:

1. No air flow exists in the inter-connected pore channel. Therefore, no convection between the air and the solid takes place in the pore channel.
2. There is no net radiation heat transfer in the inter-connected pore channel.
3. A local thermal equilibrium exists between the solid and fluid phases at the pore level, which means that the temperature difference between the solid and void phases is negligible.

Figure 9 shows the volume equivalency process for simplifying the pore-level geometry while preserving the volume ratio of solid/fluid (porosity). The square bar size a is determined by solving the following cubic equation obtained from the volume equivalency

$$a^3 - \frac{3}{4}a^2 - \frac{1-\varepsilon}{16}H^3 = 0 \tag{13}$$

Figure 10 shows the details of the equivalency and electrical analogy processes used to obtain the effective thermal conductivity of the carbon foam. The equivalent square bar structure is first divided into parallel and series parts as shown in Fig. 10(*b*). The
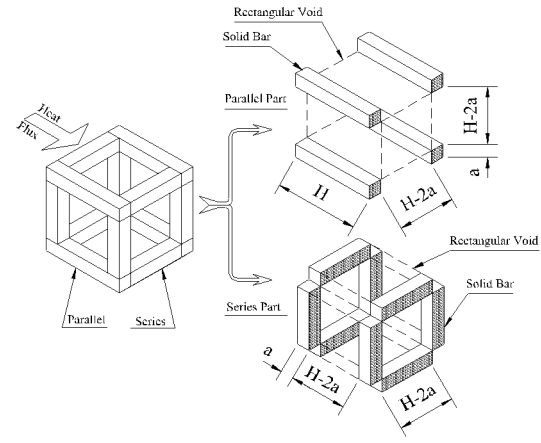
Fig. 10 (*a*) Square bar equivalent for thermal-electric analogy; (*b*) equivalent parallel and series parts; (*c*) simplified parallel and series parts; (*d*) equivalent heat transfer circuits

parallel and series parts are then converted into the simple forms shown in Fig. 10(*c*) by applying the equivalency method to the volume. The top view of Fig. 10(*d*) shows the equivalent heat transfer circuit that represents the parallel part, and the bottom view shows the equivalent heat transfer circuit that represents the series part. The simplified parallel part is presented as a pure parallel circuit consisting of the solid and void parts as shown in the top view of Fig. 10(*d*), and its effective thermal conductivity k_{ep} is calculated by [9]

$$k_{ep} = \frac{\left(\dfrac{1}{t} - 1\right)^2 + \sigma}{\left(\dfrac{1}{t} - 1\right)^2 + 1} k_f \tag{14}$$

where k_f is the thermal conductivity of the fluid and k_s for the solid, $t = 2a/H$ is the normalized thickness of the square bar, and σ is the ratio of the thermal conductivity of the solid phase to the fluid phase: $\sigma = k_s/k_f$. The simplified series part is represented as a pure series circuit consisting of the solid and void parts as shown in the bottom view of Fig. 10(*d*), and its effective thermal conductivity k_{es} is calculated as [9]

Fig. 11 Plot showing the effective thermal conductivity of porous carbon foam as a function of porosity for k_s =1300 W/m K
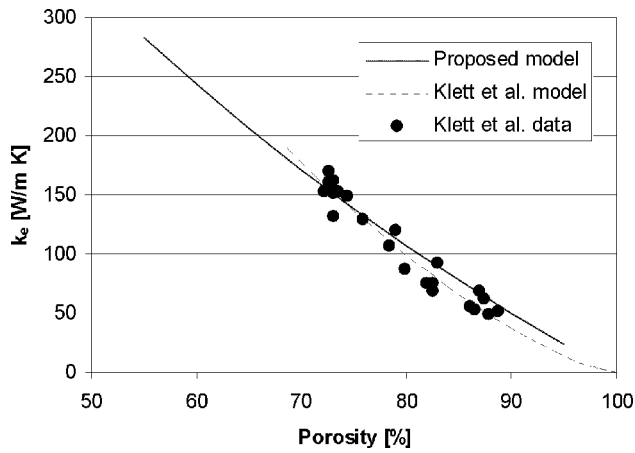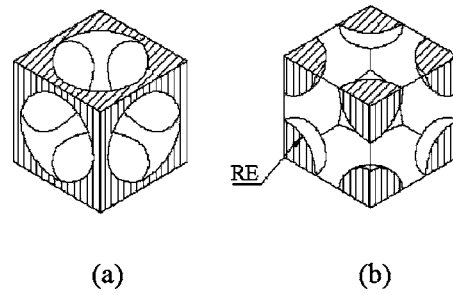

Fig. 12 Graphical representation of the equivalent sphere particle diameter: (a) the actual spherical void phase and (b) the equivalent solid particle obtained from Eq. (21)

$$k_{es} = \frac{k_s}{(1-t)\sigma + t} \quad (15)$$

The effective thermal conductivity of a porous material is given by

$$k_e = \varepsilon_e k_{ep} + (1 - \varepsilon_e)k_{es} \quad (16)$$

where ε_e is the volume ratio of the parallel part to the sum of the series part and the parallel part, and is determined by

$$\varepsilon_e = 1 - 2t + 2t^2 \quad (17)$$

When Eqs. (14), (15), and (17) are substituted into Eq. (16), the final expression for the effective thermal conductivity of the spherical void porous material is obtained

$$k_e = (1 - 2t - 2t^2)\left(\frac{\left(\frac{1}{t} - 1\right)^2 + \sigma}{\left(\frac{1}{t} - 1\right)^2 + 1} \right)k_f + \frac{2t(1-t)}{(1-t)\sigma + t}k_s \quad (18)$$

Figure 11 shows the variation of k_e with ε as predicted by Eq. (18) (solid line). The effective conductivity is seen to decrease with increasing porosity due to the reduction of solid phase material with increasing ε. Included in Fig. 11 is measured data reported by Klett et al. [12]; the data were converted from density to porosity form assuming a ligament density of 2.23 g/cm³ [12]. Figure 11 also compares predictions of the model relation developed by Klett et al. [12]. It is clear from the figure that both models are in good agreement with the measured data. The virtue of the present model is that there are no parameters to adjust; the predicted result is obtained using the geometry of the foam and the solid and fluid phase thermal conductivities only. As such, the proposed model can be applied in engineering heat transfer models and in computational fluid dynamics codes without special tuning.

It is important to note that the heat transfer is not dictated by the effective conductivity alone. That is, for low porosity, the effective conductivity is high, which means that heat is readily transferred into the porous material, but it is difficult for fluid to penetrate the foam resulting in lower convection and an imbalance in the conductive-convective resistances. For high porosity, the effective conductivity is low meaning that conduction into the foam is low, but it is easy for fluid to penetrate the foam so the convective resistance is lower. As such, the optimal porosity must be obtained by considering the rate at which heat is transferred into the foam and the rate at which heat can be removed by internal convection.

3.2 Convective Heat Transfer. The convective heat transfer can be estimated using the internal area factor β combined with an appropriate relation for the internal, pore-level Nusselt number. Though no known relation exists specifically for a spherical void phase porous material, reasonable estimates of heat transfer can be obtained from relations for porous materials with an interconnected internal structure. To this end, studies have been conducted to quantify the internal convective heat transfer and pressure drop across porous media with an interconnected void structure (Refs. [4,16]). Additional reviews have been compiled by Bear and Corapcioglu [17–19] and Kakac et al. [20]. Recent studies on the fundamentals and applications of the flow and heat transfer in porous media have also been edited in detail by Vafai et al. [21]. Gamson et al. [22] proposed

$$\text{Nu}_{sf} = 1.064 \, \text{Re}_d^{0.59} \text{Pr}^{1/3} \quad (19)$$

for turbulent particle Reynolds numbers greater than 750, where $\text{Re}_d = uD_P/\nu$, and D_P is the mean particle diameter. Kar and Dybbs [23] proposed

$$\text{Nu}_{sf} = 0.004 \, \text{Re}_d^{1.35} \text{Pr}^{1/3} \quad (20)$$

for Re_d smaller than 75. To fill in the range of Re_d, Hwang et al. [5] proposed the use of linear interpolation between Eqs. (19) and (20) to obtain values between $75 < \text{Re}_d < 750$. To use these relations with the proposed model, an equivalent solid sphere particle diameter D_E is introduced, where D_E is the particle diameter that preserves the internal area of the unit cell specified by Eq. (1) for a given porosity and pore diameter. D_E is obtained using the expression for the area to volume ratio for a packed spherical bed [4]

$$D_E = \frac{6(1 - \varepsilon)}{\beta} \quad (21)$$

but β is obtained from the unit-cube model (Eq. (3)) for a given porosity and pore diameter. Since the porosity and area-to-volume ratio used in Eq. (21) are for the spherical void geometry, the resulting diameter will not generally correspond to the packed-bed diameter. In fact for a spherical void phase material, the porosities are generally much higher than for packed beds. Figure 12 illustrates the equivalency of the two cases; part (a) shows the spherical void geometry and part (b) shows the same unit cell with the equivalent solid spherical particle distributed at the eight corners of the cube (this could also be illustrated as a sphere floating in the center of the unit cube). The equivalent particle diameter is used in the Reynolds numbers to obtain estimates of the internal convective heat transfer using the method described above.

Figure 13 shows predictions of the internal convective heat transfer obtained using the above relations combined with the internal area ratio β for the case of water forced through a block of porous foam block heated from one side. The predictions are compared to experimental data reported by Straatman et al. [24] for three foams that are summarized in Table 1. Because the blocks are heated from only one side, the present results are obtained by
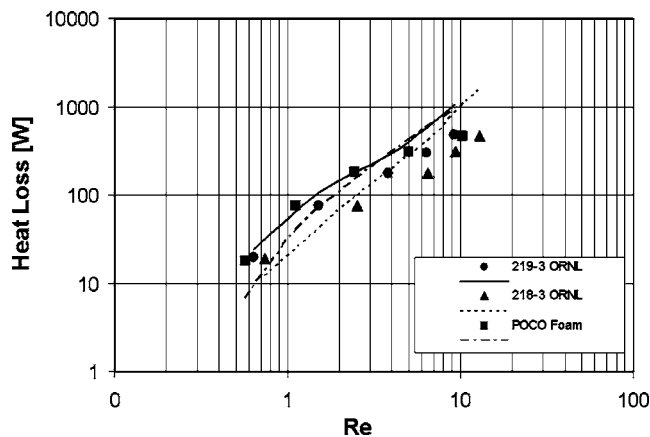
Fig. 13 Plot showing the heat transfer as a function of Re for three porous carbon foam specimens reported by Straatman et al. [24]. The heat transfer is computed using the area-to-volume ratio β combined with the correlations described in Sec. 3.2.

considering the foam block to be an extended surface. In this manner, the area used in the calculation of q is the effective surface area: $A_{\mathrm{eff}} = \eta A_f + A_b$, where η is the equivalent micro-fin efficiency of the foam obtained using the Taylor model [25]; A_f is the interior wall surface area of the foam specimen obtained from $A_f = \beta V$, where V is the volume of the specimen; and A_b is the bare surface area of the heater that is not covered by the porous foam. Figure 13 indicates that the general trends are predicted reasonably well, but that there is some discrepancy, particularly for Re above 5. It is felt that these discrepancies are due mainly to differences in the flow between the spherical void phase foam and the packed spherical bed for which Eq. (20) was devised. Though calibration of the coefficients would lead to better agreement, it is clear that there is a need for research directed at establishing pore-level Nusselt number expressions for spherical void materials that take into account the porosity, pore diameter, and flow characteristics.

4 Hydrodynamic Model

A hydrodynamic model is required to estimate the fluid pressure drop through the inter-connected void structure and thus to estimate the energy necessary to force fluid through the foam. The fluid pressure drop for a porous material is quantified by the Darcy-Forchheimer extended equation [26]

$$\frac{\Delta P}{dx} = \frac{\mu}{K}\nu + \frac{c_f}{\sqrt{K}}\rho\nu^2 \qquad (22)$$

where ν is the filter velocity (based on the open channel flow) at the film temperature, μ is the fluid viscosity, K is the permeability, and c_f is the Forchheimer coefficient (or Ergun's coefficient) determined using the Forchheimer model. Equation (22) is suitable to characterize the pressure drop across a spherical void phase structure provided appropriate values for the permeability and Forchhiemer coefficients are established.

Table 1 Summary of properties for the carbon foam specimens tested by Straatman et al. [24]

Specimen	Porosity (%)	Average Void Dia. (μm)	β[a] (m^2/m^3)	k_{eff} (W/m K)
219-3	86	350	6850	72
218-3	88	400	5640	61
POCO™	82	500	5240	120

[a]As obtained from Eq. (3).

Table 2 Summary of the equivalent particle diameter and A and B coefficients (see Eqs. (23) and (24)) for the carbon foam specimens tested by Straatman et al. [24]

Specimen	D_E (μm)	A	B
219-3	123	2056	31.8
218-3	128	1841	17.8
POCO™	206	1161	14.9

4.1 Permeability K. The most suitable generic expression for the permeability of a packed bed of spheres is given as [14]

$$K = \frac{\varepsilon^3 D_P^2}{A(1-\varepsilon)^2} \qquad (23)$$

where D_P is the spherical particle diameter and A is a constant that characterizes the *ease* at which fluid can pass through the porous structure. For a packed bed of spheres, $A = 147$ [14]. For a spherical void phase material such as porous carbon foam, the value of A is considerably higher owing to the hydrodynamic pressure loss associated with flow passage through the cell windows connecting the voids. As is evident from Fig. 1, the cell windows can be a wide range of sizes and shapes and differ significantly from the smooth and uniform openings of the unit-cube geometry model. Thus, the unit-cube model represents an ideal structure in terms of the distribution of cell window openings. On the basis of the difference between the predicted and observed cell window openings, it is possible that the unit-cube model slightly underpredicts the internal surface area, however, it is felt the presence of variance and isolated pores more than offsets these differences.

4.2 Forchheimer Coefficient. The Forchhiemer coefficient can be expressed as

$$c_f = \frac{B}{\sqrt{A}\varepsilon^{3/2}} \qquad (24)$$

where B is a constant that takes the value 0.65 for a packed bed of spheres. For fibrous materials, B was found to vary between 0.65 and 2.6 [27].

In essence A and B need to be calibrated to give the correct physical balance between the viscous Darcy term and the Forchhiemer form drag term. To use Eq. (22) to predict the pressure drop associated with flow through porous carbon foam, the equivalent particle diameter D_E, obtained using Eq. (21), is used in Eq. (23) and suitable values for A and B are obtained by calibration with the experimental data reported in [24]. As such, the geometry of the foam is characterized in D_E and the fluid resistance is captured by A and B, all of which have been calculated and summarized in Table 2 for the foams described in Ref. [24]. Figure 14 shows the pressure drop as a function of Reynolds number Re for the foams summarized in Tables 1 and 2. The figure clearly shows that the pressure drop for porous carbon foam is well characterized using Eq. (22). For the coefficients used, the trend with Re is reproduced with very high accuracy. The POCO™ foam described in Ref. [24] has a more open internal structure and thus, a much higher permeability and lower pressure drop. In contrast, the 219-3 foam was described as having much poorer interconnectivity between the cells and, thus, a lower permeability and higher pressure drop. This is reflected in the A and B coefficients in Table 2, where both the viscous and form drag terms are noted to be highest for the 219-3 foam.

The unit-cube geometry and the thermal and hydrodynamic models were also used as the basis for a complete thermal engineering model of a water-to-air heat exchanger [28]. The engineering model predicted performance ratings to within 11.5% of
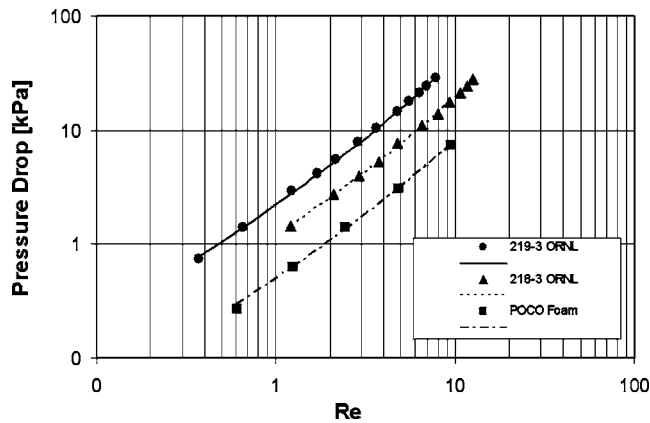
Fig. 14 Plot showing the pressure drop as a function of Re for three porous carbon foam specimens reported by Straatman et al. [24].

those obtained in laboratory experiments, thus further validating the utility of the proposed approach for characterizing porous carbon foam.

5 Summary

An engineering model has been developed for porous carbon foam based on a unit-cube geometry model. The geometry model is based on sphere-centered, interconnected unit cubes, where the spheres represent the fluid or void phase of the porous media. The geometry model was used to derive all of the geometric parameters required to calculate the internal convective heat transfer and pressure drop through the porous material. The model was also used to develop an analytical expression for the effective (stagnant) conductivity of porous carbon foam. The effective conductivity model was developed using a volume equivalency (i.e., by preserving the porosity) and was shown to accurately predict the thermal conductivity as a function of porosity without the need for calibration. Thus, the model has the potential for wide applicability in engineering and CFD models. The internal area ratio β obtained from the unit-cube model was then used in combination with existing expressions for the pore-level Nusselt number to obtain estimates of the heat transfer obtained by passing water through porous carbon foam blocks. Comparisons with experiments showed that while the trends were reasonable, significant discrepancies between the predicted and measured heat transfer were evident at moderate Re, suggesting the need for a Nusselt number expression that is specific to the spherical void phase geometry. In terms of hydrodynamics, comparisons with experimental data showed that the Darcy-Forchhiemer law accurately characterized the pressure drop as a function of Re once the model parameters were properly calibrated. In this regard, further work is also required to express the permeability and Forchhiemer coefficient over a range of porosities and pore diameters.

Acknowledgment

Nomenclature

A = constant
a = square bar of the equivalent square bar structure
B = constant
c_f = Forcheimer coefficient
D = pore (void phase) diameter of the foam
D_E = diameter of the equivalent spherical particle

d_v = equivalent diameter of void phase
h = height of the cube
K = permeability of the foam
k_e = effective thermal conductivity of the foam
k_f = thermal conductivity of the fluid
k_s = thermal conductivity of the solid
Nu = Nusselt number
P = pressure
Pr = Prandtl number
R = radius of the pore, thermal resistance
R_A = absolute surface roughness of the exposed pore surface
R_E = radius of the equivalent spherical particle
Re_d = particle Reynolds number
S = surface area
S_F = surface area factor at the exposed pore surface
ν = filter velocity (based on open channel flow)
V = volume

Greek Symbols

β = interior wall surface area to volume ratio
ε = porosity
ε_e = volume ratio of the parallel part to the sum of the series part and the parallel part
ρ = density
μ = viscosity

Subscripts

f = fluid
pb = pore block
s = solid
t = total
ν = void

References

[1] Klett, W. J., 2000, "Process for Making Carbon Foam," United State Patent No. 6,033,506.
[2] Klett, W. J., Hardy, R., Romine, E., Walls, C., and Burchell, T., 2000, "High-Thermal Conductivity, Mesophase-Pitch-Derived Carbon Foam: Effect of Precursor on Structure and Properties," Carbon, **38**, pp. 953–973.
[3] Gallego, C. N., and Klett, W. J., 2003, "Carbon Foams for Thermal Management," Carbon, **41**, pp. 1461–1466.
[4] Dullien, F. A. L., 1979, *Porous Media Fluid Transfer and Pore Structure*, Academic, New York.
[5] Hwang, G. J., Wu, C. C., and Chao, C. H., 1995, "Investigation of Non-Darcy Forced Convection in an Asymmetrically Heated Sintered Porous Channel," ASME J. Heat Transfer, **117**, pp. 725–731.
[6] Paek, W. J., Kang, H. B., Kim, Y. S., and Hyum, M. J., 2000, "Effective Thermal Conductivity and Permeability of Aluminum Foam Materials," Int. J. Thermophys., **21**(2), 453–464.
[7] Deissler, R. G., and Boegli, J. S., 1958, "An Investigation on Effective Thermal Conductivity of Powders in Various Gases," Trans. ASME, October, pp. 1417–1425.
[8] Batchelor, G. K., and O'Brien, R. W., 1977, "Thermal or Electrical Conduction Through a Granular Material," Proc. R. Soc. London, Ser. A, **355**, pp. 313–333.
[9] Luikov, A. V., Shashkov, A. G., Vasiliev, L. L., and Fraiman, Y. E., 1968, "Thermal Conductivity of Porous System," Int. J. Heat Mass Transfer, **11**, pp. 117–140.
[10] Bhattacharya, A., Calmidi, V. V., and Mahajan, R. L., 2002, "Thermophysical Properties of High Porosity Metal Foams," Int. J. Heat Mass Transfer, **45**, pp. 1017–1031.
[11] Tee, C. C., Klett, J. W., Stinton, D. P., and Yu, N., 1999, "Thermal Conductivity of Porous Carbon fFam," *Proceedings of the 24th Biennial Conference on Carbon*, Charleston, SC.
[12] Klett, J. W., McMillan, A. D., Gallego, N. C., and Walls, C., 2004, "The Role of Structure on the Thermal Properties of Graphitic Foams," J. Mater. Sci., **39**, 3659–3676.
[13] Ergun, S., 1952, "Fluid Flow Through Packed Columns," Chem. Eng. Prog., **48**, pp. 89–94.
[14] Nakayama, A., and Kuwahara, F., 2000, "Numerical Modeling of Convective Heat Transfer in Porous Media Using Microscopic Structures," in *Handbook of Porous Media*, K. Vafai and H. A. Hadim, eds., Marcel Dekker, New York, 449 pp.
[15] Ward, C. J., 1964, "Turbulent Flow in Porous Media," J. Hydraulics Division, Proceeding of the American Society of the Civil Engineers, HY5, pp. 1–11.

[16] Kaviany, M., 1995, *Principles of Heat Transfer in Porous Media*, 2nd ed., Springer, New York.

[17] Bear, J., and Corapcioglu, M. Y., 1984, *Fundamentals of Transport Phenomena in Porous Media*, J. Bear and M. Y. Corapcioglu, eds., Martinus Nijhoff, Dordrecht.

[18] Bear, J., and Corapcioglu, M. Y., 1987, *Advances in Transport Phenomena in Porous Media*, J. Bear and M. Y. Corapcioglu, eds., Martinus Nijhoff, Dordrecht.

[19] Bear, J., and Corapcioglu, M. Y., 1991, *Transport Processes in Porous Media*, J. Bear and M. Y. Corapcioglu, eds., Kluwer Academic, Dordrecht.

[20] Kakac, S., Killis, B., Kulacki, A. F., and Arinc, F., 1991, *Convetinve Heat and Mass Transfer in Porous Media*, S. Kakac, B. Killis, F. A. Kulacki, and F. Arinc, eds., Kluwer Academic, Dordrecht.

[21] Vafai, K., and Hadim, A. H., 2000, *Handbook of Porous Media*, K. Vafai and H. A. Hadim, eds., Marcel Dekker, New York.

[22] Gamson, B. W., Thodos, G., and Hougen, O. A., 1943, "Heat, Mass and Momentum Transfer in the Flow Gases Through Granular Solid," Trans. Am. Inst. Chem. Eng., **39**, pp. 1–35.

[23] Kar, K. K., and Dybbs, A., 1982, "Internal Heat Transfer Coefficients of Porous Metals," in *Heat Transfer in Porous Media*, J. V. Beck and L. S. Yao, eds., HTD-22, ASME.

[24] Straatman, A. G., Gallego, N. C., Yu, Q., and Thompson, B. E., 2005, "Characterization of Porous Carbon Foam as a Material for Compact Recuperators," *Proceedings of ASME Turbo Expo 2006*, Paper No. GT2006–50958, Barcelona, Spain, May 2006.

[25] Taylor, G. I., 1971, "A Model for the Boundary Condition of a Porous Material. Part 1," J. Fluid Mech., **49**, pp. 319–326.

[26] Dybbs, A., and Edwards, R. V., 1984, "A New Look at Porous Media Fluid Mechanics-Darcy to Turbulent," in *Fundamentals of Transport Phenomena in Porous Media*, J. Bear and M. Y. Corapcioglu, eds., Martinus Nijhoff, Dordrecht, pp. 199–254.

[27] Tadrist, L., Miscevic, M., Rahli, O., and Topin, F., 2004, "About the Use of Fibrous Materials in Compact Heat Exchangers," Exp. Therm. Fluid Sci., **28**, pp. 193–199.

[28] Yu, Q., Straatman, A. G., and Thompson, B. E., 2006, "Carbon Foam Finned-Tubes in Air-Water Heat Exchangers," Appl. Therm. Eng., **26**, pp. 131–143.

Flame Radiation and Soot Emission From Partially Premixed Methane Counterflow Flames

Hemant P. Mungekar[1]
e-mail: Hemant_Mungekar@amat.com

Arvind Atreya
e-mail: aatreya@umich.edu

Department of Mechanical Engineering,
University of Michigan,
Ann Arbor, MI 48109

Motivated by heat transfer and environmental concerns, a study of flame radiation and soot particulate emission is reported for partial premixing in low strain-rate (<20 s^{-1}) methane counterflow flames. Temperature, OH concentration, and soot volume fraction distributions were measured along the stagnation streamline for progressive addition of oxygen to methane. These measurements along with an optically thin model for soot and gas radiation were used to study the effect of partial premixing on flame radiation and soot emission. It was found that with progressive partial premixing, the peak soot loading and the thickness of the soot zone first decreased and then increased, and while the gas radiation was enhanced, the gas radiative fraction (gas radiation per unit chemical energy release) showed a systematic decrease. The net radiative fraction (soot+gas), however, first decreased and then increased. A configuration with the soot zone spatially entrapped between the premixed and non-premixed reaction zones was experimentally found. This flame configuration has the potential to enhance radiative heat transfer while simultaneously reducing soot and NO$_x$ emissions. [DOI: 10.1115/1.2165204]

Keywords: flame radiation, soot, partial premixing

1 Introduction

Soot formation in flames is of concern because radiation is an important mode of heat transfer in industrial furnaces, and soot emission from combustion equipment poses health and environmental hazard. Hence, it is important to identify flame configurations where soot radiation can be enhanced and soot pollution can be minimized. In this work, by investigating flames in the counterflow geometry, it is shown that such flame configurations exist for partially premixed flames (PF).

The term "partial premixing" commonly refers to the technique of adding oxygen (in quantities less than required for rich flammability limit) to the fuel. In industrial burners, intentional partial premixing is practiced for flame stabilization and pollutant emission control. Unintentional partial premixing occurs as a result of incomplete mixing due to geometric limitations for turbulent premixed combustion and to flame extinction reignition mechanisms in non-premixed combustion devices. In this study, to systematically investigate the effect of partial premixing on flame radiation and sooting tendency a well-defined flame configuration, namely, the counterflow flame, is utilized. The counterflow flame is stabilized between opposing flows of fuel and oxidizer and is pertinent to turbulent combustion via the flamelet modeling approach [1,2].

Yamaoka and Tsuji [3,4] observed that with partial premixing the counterflow methane-air "flame" was actually a "double flame" with a premixed reaction zone and a non-premixed reaction zone. In their study, for small amounts of oxygen added to the fuel the premixed reaction zone was indistinguishable from the non-premixed reaction zone and the temperature and species profiles measured in the flames were similar to those in a non-premixed diffusion flame. Such partially premixed flames were termed "merged flames." For progressively higher levels of partial premixing, the premixed flame became stronger with clear spatial separation between the two reaction zones. The premixed reaction zone was dependent on the non-premixed reaction zone for supply of heat while it supplied CO and H$_2$ "fuel" to the non-premixed reaction zone. Such flames were identified as flames in the "interdependent flame" regime.

In our previous work [5], we discussed the structure of sooty counterflow diffusion flames (CFDFs) in the two scenarios schematically shown in Figs. 1(*a*) and 1(*b*), where the non-premixed flames (NF) were located on the oxidizer and fuel side of the stagnation plane (SP), respectively. In the first case, soot formation begins on the fuel-rich side of the NF and soot grows as it is driven toward the particle stagnation plane by the flow field. In this case, as soot volume fraction increases from soot growth, the temperature at corresponding spatial location decreases as soot moves further away from the NF. This is not favorable for radiation heat transfer by soot. Furthermore, in this case soot leaves the flame at the stagnation plane. In contrast to first configuration, the "soot formation oxidation configuration," shown in Fig. 1(*b*), soot is oxidized in the flame as it is driven by the flow field into the OH-rich zone of the flame. Although the soot luminosity is high, as the soot region overlaps with the high-temperature region of the flame, the downside of this configuration is that it is difficult to control the width of the soot zone. The soot region in this configuration is thin, typically $\leqslant 2$ mm wide, even for low strain rate flames studied in our laboratory. Control of the soot region width with simultaneous ability to oxidize the soot within the flame can be achieved in the flame configuration proposed in Fig. 1(*c*). The flame configuration in Fig. 1(*c*) corresponds to a partially premixed flame in the "interdependent flame" regime, obtained by adding oxygen to the fuel side of the flame configuration shown in Fig. 1(*a*). In this case, the soot growth takes place in the high-temperature region between the premixed and non-premixed flames. Soot is driven by the flow field into the OH-rich region of the NF before it reaches the particle stagnation plane. This configuration is suitable for enhanced flame radiation with simulta-
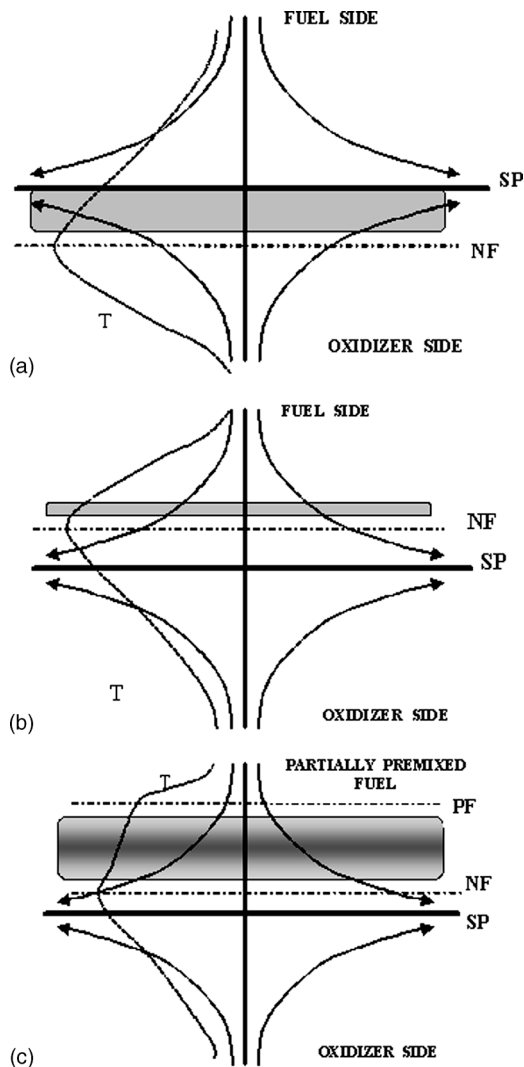
Fig. 1 Location of soot region in CFDF residing on (a) oxidizer side of SP, (b) fuel side of SP, and (c) interdependent regime partially premixed flame

figuration shown in Fig. 1(a) to that in Fig. 1(c). This is done to systematically investigate the effect of partial premixing on flame radiation enhancement by soot entrapment between the PF and the NF.

In this study, experiments were conducted in a unique low-strain-rate counterflow burner where oxygen was incrementally added to the fuel side of a diluted originally non-premixed sooty methane-oxygen flame. The experimental measurements included axial distributions of temperature using coated thermocouples, [OH] using saturated laser induced fluorescence and soot volume fraction f_v using laser light scattering and extinction. Computations with full chemistry and transport using the OPPDIFF code were made to *post process* the measured distributions of f_v and radiation corrected flame temperature, as well as to compute soot radiation and evaluate changes in the distribution of energy release and gas radiation with progressive partial premixing.

2 Experimental

Experiments were conducted in a unique low strain rate $(10–20 \text{ s}^{-1})$ counterflow flame burner, where laminar, steady, axi-symmetric flames were aerodynamically stabilized between opposing flows of fuel and oxidizer issuing from inlet ports separated by a burner gap of 2.9 cm. Careful design of burner and experiments insured buoyant stabilization of low-strain-rate flames. Some special precautions included:

a. Light (heavy) diluent gas was added to the top (bottom) inlets for buoyant stabilization.
b. Burner flanges were designed to avoid flow separation at nozzle exits and prevent outside air entrainment.
c. A fine screen surrounded the burner to isolate the convection cells in the room air.

Measurements were carried along the axis of symmetry. One dimensionality of scalar variables was confirmed by measured radial distribution of temperature and axial component of velocity using flow-visualization experiments [21]. All gases used were of chemical purity grade $(>99.9\%)$. The inlet flow rates of gases were monitored using calibrated sonic orifice meters (measurement error $\pm 1\%$) and rotameters (measurement error $\pm 2\%$).

Soot volume fraction distribution was determined by laser light extinction and scattering measurements using 514.5 nm Ar$^+$ ion laser [22]. In a typical flame, the laser extinction path was $\sim 3–5$ cm in the central region of the flame along a diameter. The laser light was carried in glass tubes outside these regions in the flame. The path length was thus measured as the distance between the glass tubes. The incident laser beam was mechanically interrupted by a chopper at a frequency of 1000 Hz. The signals for intensity before and after attenuation through the sooty zone were recorded using a lock-in amplifier. Representative error in measurement of f_v, which is of order 1×10^{-7}, is estimated to be $\pm 2\%$ by considering uncertainty in the measurement of path length and laser signal intensity. Mie scattering theory for spherical particles, a lognormal size distribution, and soot complex refractive index[2] of 1.57–0.56i were assumed to infer volume fraction from the measured extinction coefficient. Based on the recent work of Zhu et al. [23], this value of the soot refractive index may not be correct. However, we will use this value of the soot refractive index primarily to be consistent with our previous work and that of other researchers for the sake of comparison. Smyth and Shaddix [24] have discussed the validity of this value for the soot complex refractive index. Use of a tomographic inversion (such as the Abel inversion) was not needed as the extinction path length of the laser light was limited to the "core" of the flame, using quartz tubes to protect the laser light in the "outer" regions of the

neous oxidation of soot particles. The enhanced heat loss from the reaction zone by flame radiation also helps to reduce the flame temperature and NO$_x$ production rate. A study of this flame configuration is reported here, and its radiation characteristics are compared to the base non-premixed flame configuration.

Several studies [6–20] have considered soot formation in partially premixed flames. Although methane is a major component of natural gas, a fuel of commercial importance, and partial premixing accounts for a significant portion of natural gas consumption, limited literature [8,13,17] is available on this subject. Although it has been reported that the chemical effect of oxygen added to methane [13] and propane [10] is to inhibit soot inception, no studies of soot growth, except for our recent work [19,20], have been reported for methane partial premixing. Our previous work emphasized that although dilution and chemical effects of oxygen addition were important for the soot inception studies reported in literature, the location of the flame front relative to the stagnation plane and the resulting temperature time histories of soot aggregates can result in either enhancement or reduction of peak soot loading in the flame. The resulting trends of flame radiation for the flame configuration (Fig. 1(c)) are complex because of the nontrivial dependence of peak soot loading with progressive partial premixing. Therefore, a few intermediate levels of partial premixing are considered in going from the con-

---

[2]Although hotly debated, this is the commonly used value of the soot refractive index. However, the extinction data presented here can be easily scaled if a more reliable value of the soot refractive index is proposed in the future.

Table 1 Flame Specifications

Flame	Fuel Side Conditions
A*	$T_{ad}=2928$ K $\varepsilon=11.38$ 1/s 50.7% CH_4 + 49.3% N_2 $V=10.68$ cm/s, $T=531$ K
A	$T_{ad}=2933$ K $\varepsilon=12.12$ 1/s 46.1% CH_4 + 44.9% N_2 + 9.0% O_2 $V=12.09$ cm/s, $T=547$ K
B	$T_{ad}=2939$ $\varepsilon=12.78$ 1/s 43.3% CH_4 + 42.2% N_2 + 14.5% O_2 $V=13.10$ cm/s, $T=557$ K
C	$T_{ad}=2942$ K $\varepsilon=13.63$ 1/s 41.4% CH_4 + 40.4% N_2 + 18.2% O_2 $V=14.22$ cm/s, $T=578$ K
D	$T_{ad}=2956$ K $\varepsilon=15.65$ 1/s 39.1% CH_4 + 38.1% N_2 + 22.8% O_2 $V=15.98$ cm/s, $T=614$ K

Oxidizer Side composition: 76.1% O_2 + 23.9% He

flame. Flame temperature was measured using a Pt/Pt-10% Rh (S-type) thermocouple of wire diameter 0.20 mm. The thermocouple bead was coated with a SiO_2 film to prevent catalytic reactions on the surface and the measured temperature was corrected for radiation loss. The typical difference between the peak-measured and the peak-radiation corrected temperature was about 200 K for the flames studied. These temperature measurements were estimated to be accurate within ±30 K after radiation correction. However, the repeatability was within ±10 K. This includes uncertainty in Nusselt number (due to departure from ideal spherical geometry for the thermocouple bead), estimation of average thermocouple diameter based on pictures taken with a camera-equipped optical microscope and emissivity of the silica-coated platinum thermocouple bead. The emissivity for high temperatures (1800–2000 K) was obtained by using different size beads and calibration by using computed flame temperature in a diluted H_2-O_2 flame. The value of thermal conductivity for Nusselt number evaluation was based on computed species distribution using the CHEMKIN database with the OPPDIF code. The OH radical concentration was measured by using saturated laser-induced fluorescence (LIF) technique. A dye laser was tuned such that its frequency-doubled output excites the $Q_1(3)$ line of the $A^2\Sigma(v'=0) \leftarrow X^2\Pi(v''=0)$ system of OH. The fluorescence signal collected by the collection optics was spectrally resolved using a spectrograph with a 2400 line/mm grating and detected using a cooled intensified CCD camera. The fluorescence spectrum was averaged over 200 laser excitations, each of pulse duration of ~10 ns. The spectrum of the fluorescence signal in the wavelength range of 298–333 nm was collected, and the peak background corrected the signal count, which occurred around 310 nm, was recorded. The OH LIF signal was calibrated using the peak signal from a reference H_2 counterflow diffusion flame.

Previous work [5] has confirmed excellent comparison (±2%) between OPPDIFF computations and gas chromatographic measurements for major species (CH_4, CO, H_2O, and CO_2) in several counterflow flames. Spatial distribution of these species is required to calculate gas radiation from the flame. Thus, computed distribution of major stable species were used for the evaluation of gas radiation in these flames.

The specifications of the non-premixed methane flame, flame A*, used in this study are given in Table 1. The four partially premixed variants A, B, C, and D had 9%, 14.5%, 18.2%, and 22.8% oxygen by volume in the inlet fuel stream. Further addition of oxygen entailed the risk of flashback. Oxidizer-side composition for all the flames was O_2 76.1% and He 23.9% on molar basis. Representative global strain rates in these flames were about 11–16 s^{-1}. The global strain rate ε is defined as the difference of
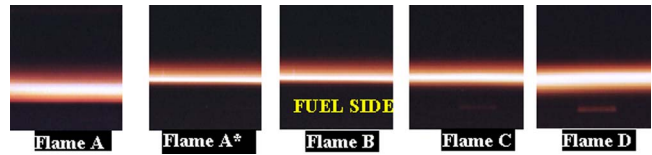

Fig. 2 Soot luminosity photographs

centerline axial velocities at the two burner inlet ports divided by the burner gap. The precise value of the strain rate may be obtained from the computed flow field; the global strain rate defined here is relevant to identifying the boundary conditions. Visual observation of soot luminosity in these flames is shown in Fig. 2.

3 Computational

Computations with the OPPDIFF [25] code were used to postprocess the measured distribution of f_v and radiation-corrected temperature to compute soot radiation as well as evaluate changes in the distribution of energy release and gas radiation with progressive partial premixing. The GRIMech 3.00 mechanism [26] and the recommended multicomponent transport and thermochemical database were used. The boundary conditions included measured inlet temperature, velocity, and the species flux at each of the two inlets, 2.9 cm apart.

The energy equation in the original OPPIDIF code was modified to include soot and gas radiation, as follows:

$$\frac{d}{dz}\left(\lambda\frac{dT}{dz}\right) - \rho C_p v \frac{dT}{dz} - \sum_{k=1}^{K} \rho Y_k V_k C_{pk} \frac{dT}{dz} - \sum w_k W_k h_k + \nabla \vec{q}_{gas} + \nabla \vec{q}_{soot} = 0 \tag{1}$$

In Eq. (1), z is the distance measured from the fuel side inlet. Y_k, C_{pk}, h_k, w_k, W_k, and V_k are the mass fraction, heat capacity at constant pressure, enthalpy, volumetric molar reaction rate, molar mass, and diffusion velocity of the kth species. λ, ρ, C_p, and v are the thermal conductivity, density, heat capacity at constant pressure, and convective velocity of the mixture, respectively. The last two terms in the energy equation correspond to the volumetric gas and soot radiation, respectively. The energy equation was decoupled from species and momentum equation during the solution with OPPDIFF since radiation-corrected temperature distribution was provided as an input to the code.

3.1 Gas Radiation. An optically thin gas-radiation model [27], including contribution from CO, CO_2, and H_2O was used, and the predictions from the model agreed well with RADCAL [30]. The Planck mean absorption coefficients for gases were obtained from Abu-Romia and Tien [28]. Computed distributions of CO, CO_2, and H_2O were used.

3.2 Soot Radiation. Since there are concerns about models for soot formation and oxidation in flames, *measured* soot volume fraction distribution was specified as *input* to the modified OPPDIF code for the purpose of calculating soot radiation. This obviates the need for a soot model to calculate soot radiation. Thus, the volumetric soot radiation term was computed by the expression

$$\nabla \vec{q}_{soot} = 4\pi a_{ps}\sigma(T^4 - T_{mid}^4) \tag{2}$$

where the value of the Planck mean absorption coefficient for soot a_{ps}, suggested by Atreya and Agrawal [29] as $a_{ps}=11.86f_v\,T$ cm^{-1} was used. Here, f_v and σ are the soot volume fraction and the Stefan-Boltzmann constant. Soot was assumed to be at the gas temperature. The surrounding mean temperature T_{mid} was approximated as the average of the two inlet port temperatures. This optically thin treatment of gas and soot radiation was adequate for understanding the effect of partial premixing on enhancement of soot and gas radiation in counterflow flames because the flame radiation thickness was about 10 mm and the solid angle along the
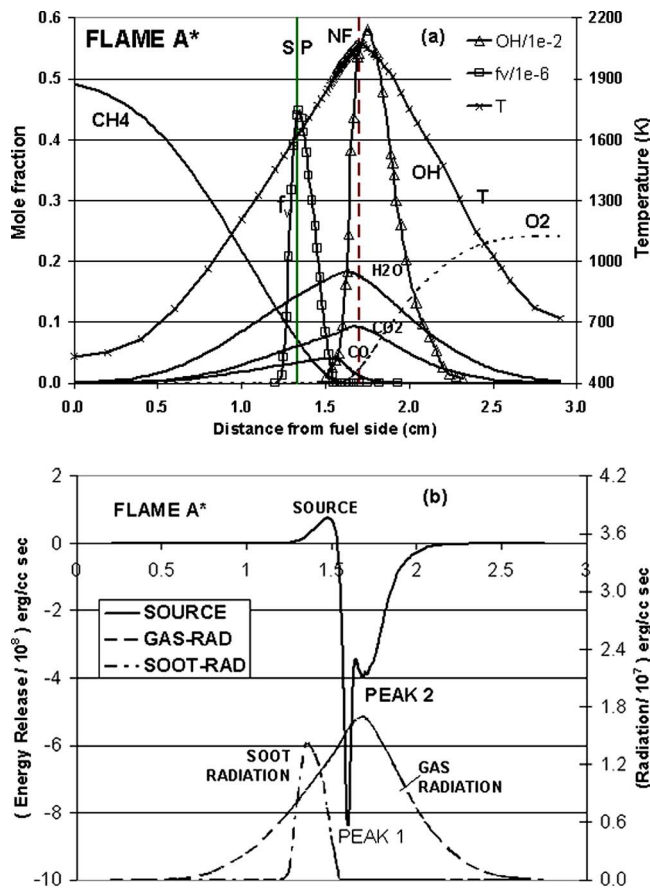
Fig. 3 (*a*) Measured temperature, OH and f_v with computed locations of SP and major stable species, (*b*) flame radiation and energy release in non-premixed flame, Flame A*

Fig. 4 (*a*) Measured temperature, OH and f_v with computed locations of SP and major stable species, (*b*) flame radiation and energy release in PP flame, Flame B

flame was small. The adequacy of the optically thin treatment was confirmed with RADCAL calculations.

To compare radiation from different flames, we first define radiative fraction, χ, for gas radiation, soot radiation, and total radiation as

$$\chi_{gas} = \frac{\int_0^l \nabla \vec{q}_{gas} dz}{\int_0^l \sum_k^K w_k W_k h_k dz} \qquad (3)$$

$$\chi_{soot} = \frac{\int_0^l \nabla \vec{q}_{soot} dz}{\int_0^l \sum_k^K w_k W_k h_k dz} \qquad (4)$$

$$\chi = \chi_{gas} + \chi_{soot} \qquad (5)$$

In these definitions, the denominator is the chemical energy release rate and the integration limits are from the fuel-side inlet to the oxidizer-side inlet.

4 Results

4.1 Flame Structure. Computed distribution of CH_4, O_2, and major stable product species are shown in Figs. 3(*a*)–6(*a*). Measured distribution of radiation-corrected temperature, OH, and soot volume fraction are shown by symbols in these figures. The
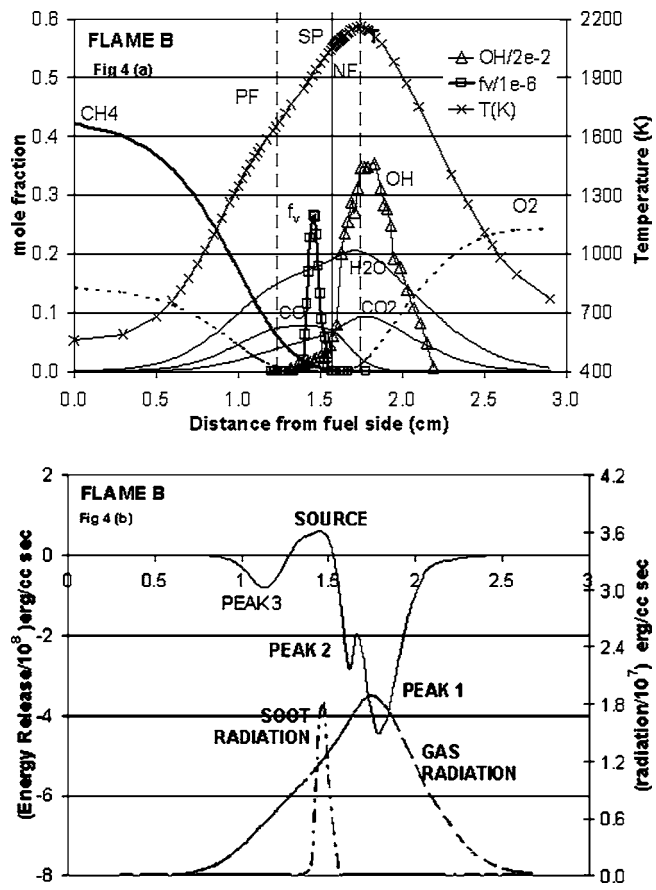
computed locations of gas stagnation flame, non-premixed flame, and premixed flame are indicated by vertical lines marked as SP, NF, and PF, respectively. With progressive partial premixing, the non-premixed reaction zone comes closer to the fuel side (also the stagnation plane) due to the combined effect of dilution of the fuel side by the added oxygen as well as the consumption of a fraction of the fuel in the PF. In flame D (Fig. 6(*a*)), the premixed flame is on fuel side of the stagnation plane while the non-premixed flame coincides with the gas stagnation plane. The temperature and species distribution in this flame are typical of interdependent flame regime.

4.1.1 Soot Formation. Figure 3(*a*) shows soot volume fraction distribution in the non-premixed flame, flame A*. With the non-premixed "flame" (reaction zone) on the oxidizer side of the stagnation plane, soot formation begins on the fuel side of the OH zone and soot grows as soot particles are driven by the flow-field toward the particle stagnation plane [21]. The thickness of the soot zone is limited to the distance between the flame and the (particle) stagnation plane. In this flame, the soot volume fraction has a sharp falloff on the fuel side of the soot distribution (Fig. 3(*a*)), as soot leaves the flame at the particle stagnation plane.

4.1.2 Effects of Partial Premixing

4.1.2.1 Width of the soot zone. As shown in the soot luminosity photographs (Fig. 2), the soot zone thickness first decreased and then increased with progressive partial premixing. The initial decrease in soot zone thickness is attributed to movement of the non-premixed flame toward the stagnation plane due to dilution of the fuel and consumption of a fraction of the fuel by oxygen. This also limits the soot formation region to between NF and PF, or SP.
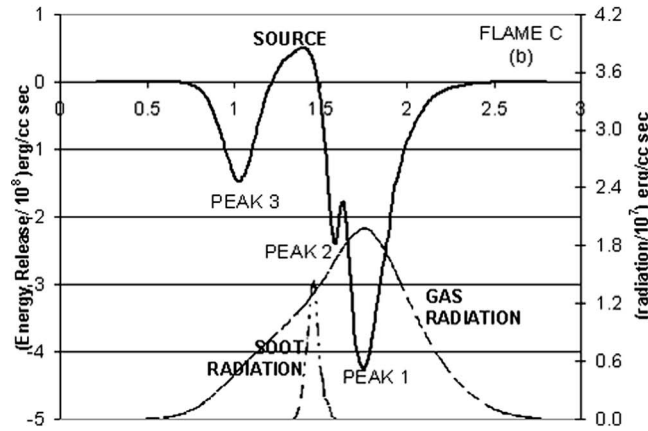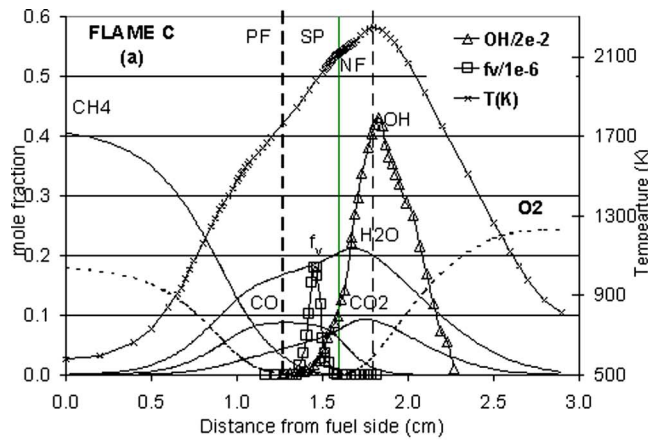
Fig. 5 (*a*) Measured temperature, OH and f_v with computed locations of SP and major stable species, (*b*) flame radiation and energy release in PP flame, Flame C

Fig. 6 (*a*) Measured temperature, OH and f_v with computed locations of SP and major stable species, (*b*) flame radiation and energy release in PP flame, Flame D

However, with progressive addition of O_2 to the fuel side, an increase in the thickness of the soot zone occurs. This is attributed to transition from the merged flame regime to the interdependent flame regime with soot formation taking place between spatially separated NF and PF regions, as seen in Fig. 6(*a*).

4.1.2.2 Peak soot loading. The initial decrease in the peak soot loading (Fig. 3(*a*)) is attributed to dilution and suppressive chemical effects of oxygen [18]. The subsequent increase is attributed to favorable temperature time histories [22]. It is interesting to note that although flames D and A* have similar peak soot loading; they have significantly different soot emission characteristics. In flame A*, soot leaves the flame at the particle stagnation plane where the soot volume fraction has reached its maximum, whereas in flame D all the soot produced along the stagnation streamline is consumed within the OH zone as soot is driven toward the stagnation plane by the flow field. There is significant overlap of OH and soot volume fraction distribution (Fig. 6(*a*)). To our knowledge, this is the first reported measurement of OH and soot in flames in the interdependent flame regime.

4.2 Energy Release and Flame Radiation

4.2.1 Energy Release. Computed distribution of energy release, gas radiation, and soot radiation is shown in Figs. 3(*b*)–6(*b*). In the non-premixed hydrocarbon flame, conversion of hydrocarbon fuel to CO_2 and H_2O takes place in two steps, in the first step, the hydrocarbon fuel is oxidized to CO and H_2, which is, in turn, oxidized to CO_2 and H_2O in the second step. These two energy-release processes represent the two peaks in the chemical energy-release distribution shown as peak 1 and peak 2 in Fig. 3(*b*). For
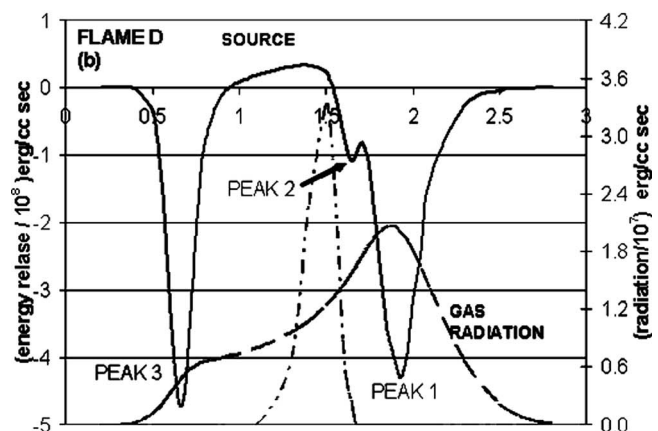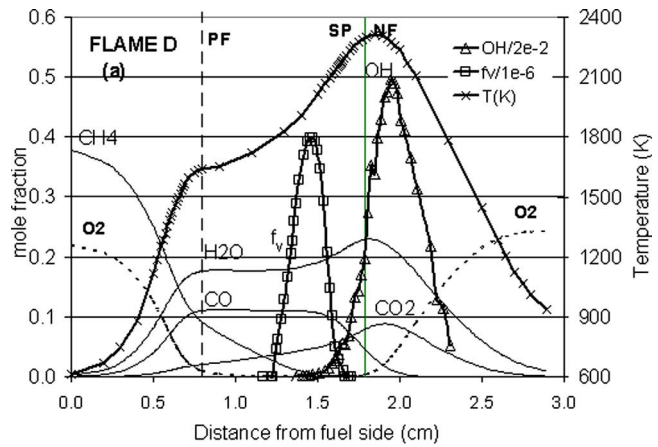
the partially premixed flames, in addition to the two non-premixed energy-release peaks, a third energy-release peak (shown as peak 3 in Figs. 4, 5, and 6(*b*)) is observed that corresponds to consumption of oxygen added to the fuel. For small levels of partial premixing, the area under the premixed energy-release peak is small compared to the non-premixed energy-release peaks, as shown in Fig. 4(*b*). Corresponding temperature profile for the flame B is indicative of the "merged-flame" regime. With further partial premixing, the energy-release contribution of the premixed reaction zone becomes comparable to that of the non-premixed flame (see Fig. 6(*b*)). Corresponding temperature distribution for flame D is representative of the "interdependent-flames" regime, where the premixed reaction zone has become strong and shows clear spatial separation from the non-premixed reaction zone.

With progressive partial premixing, the peak flame temperature increased (Figs. 3–5 and 6(*a*)). This is, in part, due to addition of pure O_2 to the fuel side, while the oxidizer for the non-premixed flame was O_2 with He as a diluent. Furthermore, the O_2 added to the fuel side consumes CH_4 on the fuel side of the SP; fuel that would have otherwise escaped unburned from the fuel side of the stagnation plane. This results in an increase in energy release with progressive partial premixing. Consequently, energy comparisons are made by introducing fractions defined in Eqs. (3)–(5).

4.2.2 Soot Radiation. The increase in soot luminosity (Fig. 2) is qualitatively in agreement with a trend for peak soot radiation in the flames (Figs. 3(*b*), 4(*b*), 5(*b*), and 6(*b*)). Soot radiative fraction and soot radiation from the flame, defined as $\int_0^l \nabla \vec{q}_{soot} dz$, first decreased and then increased for progressive levels of partial premixing, as shown in Fig. 7. This trend follows the measured
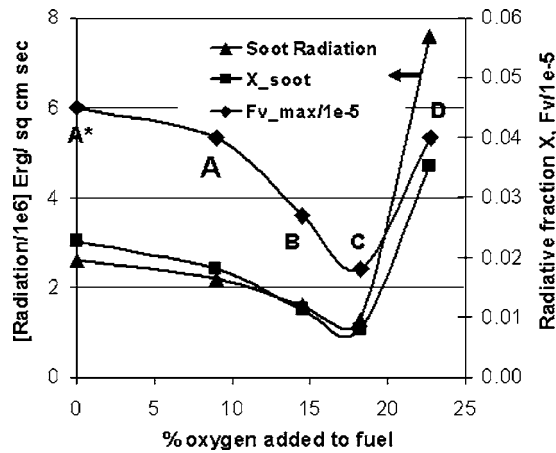
Fig. 7 Soot loading trends

Fig. 8 Computed trends for soot radiation, energy release, and radiation fraction

trend for peak soot volume fraction in these flames. Although flame A* and flame D have similar peak soot loading, soot radiative fraction is significantly enhanced because the thick soot zone coincides with the wide temperature profile between the premixed and the non-premixed reaction zones and an overall increase in the flame temperature. The "interdependent regime" flame configuration is therefore advantageous for enhancing soot radiation while minimizing soot particulate emission.

4.2.3 Gas Radiation. Gas radiation, defined as $\int_0^l \nabla \vec{q}_{gas} dz$, systematically increased for progressive levels of partial premixing as shown in Figs. 8. This increase is attributed to (i) an increase in the measured peak flame temperature and (ii) the profiles of CO, CO_2, and H_2O get broader, especially in the interdependent flame regime. The broad profiles of the radiating species also coincide with broad temperature distribution as shown in Fig. 6(*a*). However, despite an increase in the gas radiation from the flame, the gas radiative fraction decreased. As is evident in Figs. 3(*b*), 4(*b*), 5(*b*), and 6(*b*), with progressive partial premixing, the energy release in the flame increases, primarily as more and more fuel is consumed in the premixed reaction zone. The incremental increase in the net energy release was bigger than the incremental increase in gas radiation from the flame as oxygen was progressively added into the fuel stream.

Combining both soot and gas radiation contributions, it was found that the net radiative fraction first decreased and then increased as oxygen was progressively added to the fuel side.

5 Conclusions

Effects of fuel-side partial premixing on sooting tendency was studied for progressive addition of oxygen to the fuel side of methane counterflow flames. A novel flame configuration is reported (flame D in this study), where soot is formed and oxidized between the premixed and the non-premixed reaction zones on the fuel side of the stagnation plane. This flame configuration has the potential for lower soot particulate and NO_x emissions with simultaneous enhancement of radiation heat transfer from flamelets.

The following observations can be made from these experiments:

1. The peak soot volume fraction, as well as the soot zone thickness first decreased and then increased with progressive partial premixing.
2. Computed volumetric energy release increased with progressive partial premixing along with the relative importance of energy release in the premixed reaction zone.
3. Soot radiation from the flame as well as radiative fraction for soot radiation first decreased and then increased in the interdependent-flame regime.
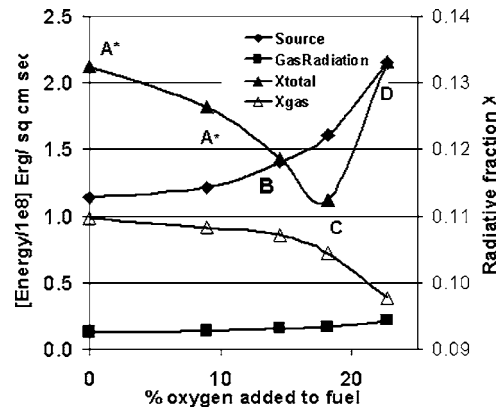
4. Computed gas radiation increased with partial premixing. The radiative fraction for the gas radiation, however, decreased due to a bigger increase in the net chemical energy release in the partially premixed flames.

These results are applicable to turbulent partially premixed flames through the laminar flamelet theory. These results indicate that if highly radiative turbulent flames are desired to increase heat transfer and reduce NO_x formation, then the correct amount of partial premixing must be achieved to obtain the interdependent-flame regime and the strain rate must be adjusted to give sufficient residence time for soot formation. Previous observations show that the flame length of a turbulent coflow flame decreases with progressive partial premixing for a variety of fuels, indicating an increase in the volumetric energy release, which agrees with the increase in the volumetric energy release at the flamelet level. These studies also report an increase in the peak flame temperature due to decrease in radiation as a fraction of chemical energy release. The flamelet results presented in this paper explain this observation via an observed decrease in the gas radiation fraction. However, this can be compensated by making conditions appropriate for soot formation and oxidation and increasing the soot radiation fraction.

References

[1] Carrier, G. F., Fendell, F. E., and Marble, F. E., 1974, SIAM J. Appl. Math., **28**(2), pp. 463–500.
[2] Peters, N., 1986, "Laminar Flamelet Concepts in Turbulent Combustion," *Proc. Combust. Inst.*, Combustion Institute, Philadephia, Vol. 21, pp. 1231–1250.
[3] Yamaoka, I., and Tsuji, H., 1974, "Flame Structure of Rich Methane Air Counter Flow Flame," *Proc. Combustion Inst.*, Combustion Institute, Philadelphia, Vol. 15, pp. 637–644.
[4] Yamaoka, I., and Tsuji, H., 1977, "Flame Structure of Rich Methane Air Counter Flow Flame," *Proc. Combustion Inst.*, Combustion Institute, Philadelphia, Vol. 16, pp. 1145–1154.
[5] Atreya, A., Zhang, C., Kim, H. K., Shamim, T., and Suh, J., 1996, "The Effect of Changes in the Flame Structure on Formation and Destruction of Soot and NO_x in Radiating Diffusion Flames," *Proc. Combustion Inst.*, Combustion Institute, Philadelphia, Vol. 26, pp. 2181–2189.
[6] Chakraborty, B. B., and Long, R., 1968, "The Formation of Soot in Diffusion Flames: III," Combust. Flame, **12**, pp. 469–476.
[7] Wey, C., Powell, E. I., and Jagoda, J. I., 1985, "The Effect on Soot Formation of Oxygen in the Fuel of a Diffusion Flame," *Proc. Combustion Institute*, Combustion Institute, Philadelphia, Vol. 20, pp. 1017–1024.
[8] Saito, K., Williams, F. A., and Gordon, A. S., 1986, "Effects of Oxygen on Soot Formation in Methane Diffusion Flames," Combust. Sci. Technol., **47**, pp. 117–138.
[9] Hura, H. S., and Glassman, I., 1987, "Fuel Oxygen Effects on Soot Formation in Counterflow Diffusion Flames," Combust. Sci. Technol., **53**, pp. 1–21.
[10] Hura, H. S., and Glassman, I., 1988, "Soot Formation in Diffusion Flames of Fuel/Oxygen Mixtures," *Proc. Combustion Institute*, Combustion Institute, Philadelphia, Vol. 22, pp. 371–378.
[11] Du, D. X., Axelbaum, R. L., and Law, C. K., 1989, "Experiments on the Sooting Limits of Aerodynamically-Strained Diffusion Flames," *Proc. Com-*

bustion Institute, Combustion Institute, Philadelphia, Vol. 22, p. 1501.

[12] Peters, N., 1994, *Soot Formation in Combustion*, Chemical Physics 59, H. Bockhorn, ed., Springer-Verlag, Berlin, pp. 325–349.

[13] Guilder, O. L., 1995, "Effects of Oxygen on Soot Formation in Methane, Propane, and n-Butane Diffusion Flames," Combust. Flame, **101**(4), pp. 302–310.

[14] Hwang, J. Y., Chung, S. H., and Lee, W., 1998, "Effects of Oxygen Addition on Soot Formation in Counter-Flow Ethylene Flames and the Role of C3 Chemistry," *Proc. Combustion Institute*, Combustion Institute, Philadelphia, Vol. 27, pp. 1531–1538.

[15] Mitrovich, A., and Lee, T. W., 1998, "Soot Formation Characteristics of Laminar Partially Premixed Flames," Combust. Flame, **115**(4), pp. 437–442.

[16] McEnally, C. S., and Pfeffrele, L. D., 2000, "Experimental Study of Non-Fuel Hydrocarbons and Soot in Coflowing Partially Premixed Ethylene/Air Flames," Combust. Flame, **121**(3), pp. 575–593.

[17] McEnally, C. S., and Pfeffrele, L. D., 1999, "Experimental Study of Non-Fuel Hydrocarbon Concentrations in Coflowing Partially Premixed Methane/Air Flames," Combust. Flame, **118**(4), pp. 619–632.

[18] Peters, N., and Pels Leudsen, C., 2000, "Experimental and Numerical Analysis of the Influence of Oxygen on Soot Formation in Laminar Counterflow Flames of Acetylene," *Proc. Combustion Inst.*, Combustion Institute, Philadelphia, Vol. 28, 2619–2625.

[19] Mungekar, H. P., and Atreya, A., 2000, "Flame Structure of Partially Premixed Flames," 34th NHTC, Pittsburgh, ASME Paper No. 2000-12316.

[20] Mungekar, H. P., and Atreya, A., 2001, "Soot Radiation and Soot Emission Control in Partially Premixed Flames," 35th NHTC, Anaheim, ASME, Paper No. 2001-14316.

[21] Mungekar, H. P., Atreya, A., and Everest, D., 2003, "Flow Visualization Using Particle Track Imaging in Sooty Laminar Flames," J. Flow Visualization Image Process., **10**, pp. 1–15.

[22] Mungekar, H. P., and Atreya, A., 2006, "Effect of Partial Premixing on Sooting Structure of Methane Flames," Combust. Flame, **144**, pp. 336–348.

[23] Zhu, J., Irerra, A., Choi, M. Y., Mullohard, G. W., Gritzo, L., and Suo-Antilla, J., 2004, "Measurement of Light Extinction Coefficient of JP-8 Soot in Visible and Near IR Spectrum," Int. J. Heat Mass Transfer, **47**, pp. 3643–3648.

[24] Smyth, K. C., and Shaddix, C. R., 1996, "The Elusive History of $m=1.57 -0.56i$ for RI of Soot," Combust. Flame, **107**, pp. 314–320.

[25] Lutz, A. E., Kee, R. J., Grcar, J. F., and Rupley, F. M., 1996, Report No. SAND96-8243, Sandia National Laboratories.

[26] http://www.me.berkeley.edu/gri mech/

[27] Kim, H. K., 1998, Ph.D. thesis, University of Michigan, Ann Arbor.

[28] Abu-Romia, M. M., and Tien, C. L., 1967, "Appropriate Mean Absorption Coefficient for Infrared Radiation of Gases," ASME J. Heat Transfer, **89**, pp. 321–327.

[29] Atreya, A., and Agrawal, S., 1998, "Effect of Radiative Heat Loss on Diffusion Flames in Quiescent Microgravity Atmosphere," Combust. Flame, **115**(3), pp. 372–382.

[30] Grosshandler, W. L., 1993, "RADCAL: A Narrow-Band Model for Radiation Calculations in a Combustion Environment," NIST Technical Note 1402.

Unsteady Mixed Convection From a Moving Vertical Slender Cylinder

S. Roy
e-mail: sjroy@iitm.ac.in

D. Anilkumar
e-mail: anil@iitm.ac.in

Department of Mathematics,
Indian Institute of Technology Madras,
Chennai, 600036 India

A general analysis has been developed to study flow and heat transfer characteristics of an unsteady laminar mixed convection on a continuously moving vertical slender cylinder with surface mass transfer, where the slender cylinder is inline with the flow. The unsteadiness is introduced by the time-dependent velocity of the slender cylinder as well as that of the free stream. The calculations of momentum and heat transfer on slender cylinders considered the transverse curvature effect, especially in applications such as wire and fiber drawing, where accurate predictions are required. The governing boundary layer equations along with the boundary conditions are first cast into a dimensionless form by a nonsimilar transformation, and the resulting system of nonlinear coupled partial differential equations is then solved by an implicit finite difference scheme in combination with the quasi-linearization technique. Numerical results are presented for the skin friction coefficient and Nusselt number. The effects of various parameters on the velocity and temperature profiles are also reported here. [DOI: 10.1115/1.2165206]

Keywords: mixed convection, slender cylinder, quasi-linearization, nonsimilar solution

1 Introduction

Unsteady mixed convection flows do not necessarily admit similarity solutions in many practical situations. The unsteadiness and nonsimilarity in such flows may be due to the freestream velocity or due to the curvature of the body or due to the surface mass transfer or even possibly due to all these effects. Because of the mathematical difficulties involved in obtaining nonsimilar solutions for such problems, most investigators have confined their studies either to steady nonsimilar flows or to unsteady semi-similar or self-similar flows [1–3].

Flows over cylinder are usually considered to be two-dimensional as long as the body radius is large compared to the boundary layer thickness. On the other hand, for a slender cylinder, the radius of the cylinder may be of the same order as that of the boundary layer thickness. Therefore, the flow may be considered as axisymmetric instead of two-dimensional. The flow nature on a slender body is much characterized by its two surface curvatures, viz., the longitudinal one in the meridian plane and the transverse one in a plane normal to the axis of symmetry. The former is a quantity that is associated with any curved surface that causes centrifugal force in the flow. In the usual treatment of boundary layer analysis, longitudinal curvature is assumed to be very small compared to unity. Therefore, the effect of the longitudinal curvature in the boundary layer is negligible.

The governing equations contain the transverse curvature term, which strongly influences the velocity and temperature fields and, correspondingly, the skin friction and heat transfer rate at the wall. Among the earlier studies, the magnitude of the transverse curvature effect has been investigated for isothermal laminar flows by Stewartson [4] and Cebeci [5] and the results show that the local skin friction can be altered by an order of magnitude due to an appropriate change in the ratio of boundary layer thickness to cylinder radius. It is therefore evident that the calculations of momentum and heat transfer on slender cylinders should consider the transverse curvature effect, especially in applications such as wire

and fiber drawing, where accurate predictions are required and thick boundary layers can exist on slender or near-slender bodies.

Mixed convection flow over a slender vertical cylinder due to the thermal diffusion has been considered by Chen and Mucoglu [6] and Mucoglu and Chen [7] for the constant wall temperature and constant heat flux conditions, respectively. They solved the partial differential equations, approximately, using the local non-similarity method. Subsequently, Bui and Cebeci [8], Lee et al. [9], Wang and Kleinstruver [10], and, most recently, Takhar et al. [11] have solved this problem using an implicit finite difference scheme. All of the above studies pertain to steady flows. In many practical problems, the flow could be unsteady due to the velocity of the moving slender cylinder, which varies with time, or due to the impulsive changes in the cylinder velocity or due to the freestream velocity, which varies with time. There are several transport processes with surface mass transfer, i.e., injection (or suction) in industry where the buoyancy force arises from thermal diffusion caused by the temperature gradient, such as a polymer fiber coating or the coating of wires, etc. In these applications, the careful control of the yarn-quenching temperature or the heating and cooling temperature has a strong bearing on the final product quality [12]. When the ratio of the boundary layer thickness to the radius of the cylinder becomes larger than 1, the curvature effect leads to an increase of the heat transfer coefficient compared to that characterizing the flat-plate situation [13]. Therefore, as a step toward the eventual development on unsteady mixed convection flows, it is interesting as well as useful to investigate the combined effects of transverse curvature, viscous dissipation, and thermal diffusion on a continuously moving vertical slender cylinder, where the cylinder velocity and freestream velocity vary arbitrarily with time.

The objective of the present investigation is to obtain a non-similar solution for the unsteady mixed convection flow along a slender vertical heated cylinder that is moving in the same direction as that of freestream velocity. The nonsimilar solution of the coupled nonlinear partial differential equations governing the mixed convection flow has been obtained numerically using the method of quasi-linearization with the combination of an implicit finite difference scheme [14]. Particular cases of the present results have been compared to those of Chen and Mucoglu [6] and Takhar et al. [11].
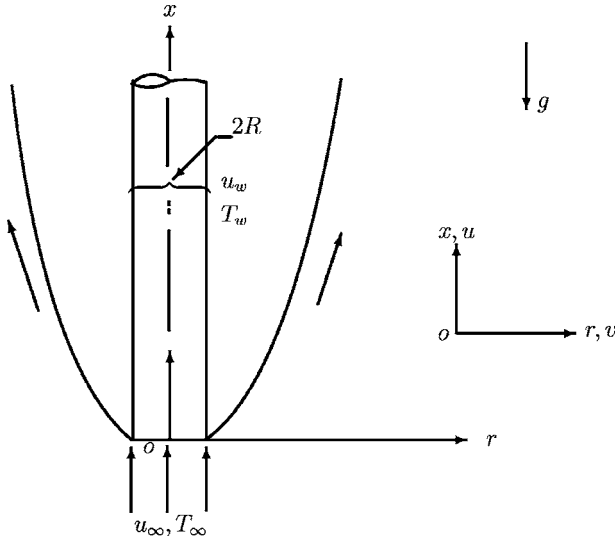

Copyright © 2006 by ASME

Fig. 1 Physical model and coordinate system

2 Analysis

We consider the unsteady laminar mixed convection flow along a heated vertical slender cylinder with injection and suction. The blowing rate is assumed to be small and does not affect the inviscid flow at the edge of the boundary layer. It is assumed that the injected fluid processes the same physical properties as the boundary layer fluid and has a static temperature equal to the wall temperature. The unsteadiness in the flow field is introduced by the cylinder velocity and freestream velocity, which vary with time. The flow is taken to be axisymmetric, and Fig. 1 shows the coordinate system and the physical model. Thermophysical properties of the fluid in the flow model assumed to be constant except the density variations causing a body force term in the momentum equation. The Boussinesq approximation is invoked for the fluid properties to relate density changes to temperature changes, and to couple in this way the temperature field to the flow field [15]. Under the above assumptions, the governing boundary layer equations can be expressed as [11,16,17]

$$\frac{\partial(ru)}{\partial x} + \frac{\partial(rv)}{\partial r} = 0 \tag{1}$$

$$\frac{\partial u}{\partial t} + u\frac{\partial u}{\partial x} + v\frac{\partial u}{\partial r} = \frac{\partial u_e}{\partial t} + (\nu/r)\frac{\partial}{\partial r}\left(r\frac{\partial u}{\partial r}\right) + g\beta(T - T_\infty) \tag{2}$$

$$\frac{\partial T}{\partial t} + u\frac{\partial T}{\partial x} + v\frac{\partial T}{\partial r} = \frac{\nu}{\Pr}\frac{1}{r}\frac{\partial}{\partial r}\left(r\frac{\partial T}{\partial r}\right) + \frac{\mu}{\rho c_p}\left(\frac{\partial u}{\partial r}\right)^2 \tag{3}$$

The initial conditions are

$$u(0,x,r) = u_i(x,r), \quad v(0,x,r) = v_i(x,r), \quad T(0,x,r) = T_i(x,r) \tag{4}$$

and the boundary conditions are given by

$$u(t,x,R) = u_w(t) = u_{w,0}\phi(t^*), \quad v(t,x,R) = v_w, \quad T(t,x,R) = T_w$$

$$u(t,x,\infty) = u_e(t) = u_\infty\phi(t^*), \quad T(t,x,\infty) = T_\infty \tag{5}$$

Applying the following transformations:

$$\xi = \left(\frac{4}{R}\right)\left(\frac{\nu x}{u_\infty}\right)^{1/2}, \quad \eta = \left(\frac{\nu x}{u_\infty}\right)^{-(1/2)}\left[\frac{r^2 - R^2}{4R}\right], \quad t^* = \frac{\nu}{R^2}t$$

$$\frac{r^2}{R^2} = [1 + \xi\eta], \quad \psi(x,r,t) = R(\nu u_\infty x)^{1/2}\phi(t^*)f(\xi,\eta,t^*)$$

$$u = \frac{1}{r}\frac{\partial\psi}{\partial r}, \quad v = -\frac{1}{r}\frac{\partial\psi}{\partial x}, \quad f_\eta(\xi,\eta,t^*) = F(\xi,\eta,t^*)$$

$$u = \frac{1}{2}u_\infty\phi f_\eta = \frac{1}{2}u_\infty\phi F(\xi,\eta,t^*),$$

$$v = \frac{1}{2r}R\phi\left(\frac{\nu u_\infty}{x}\right)^{1/2}\left(\eta f_\eta - f - \xi\frac{\partial f}{\partial \xi}\right)$$

$$G(\xi,\eta,t^*) = \frac{T - T_\infty}{T_w - T_\infty}, \quad \mathrm{Ec} = \frac{u_\infty^2}{4c_p(T_w - T_\infty)}, \quad \lambda = \frac{Gr_x}{\mathrm{Re}_x^2}$$

$$\Pr = \frac{\nu}{\alpha}, \quad Gr_x = g\beta x^3(T_w - T_\infty)/\nu^2, \quad \mathrm{Re}_x = \frac{u_\infty x}{\nu} \tag{6}$$

to Eqs. (1)–(3), we find that Eq. (1) is identically satisfied, and Eqs. (2) and (3) reduce to

$$[(1 + \xi\eta)F_\eta]_\eta + \phi f F_\eta + 8\lambda\phi^{-1}G + \left(\frac{\xi^2}{4}\right)[\phi^{-1}\phi_{t^*}(2 - F) - F_{t^*}]$$
$$= \phi\xi[FF_\xi - F_\eta f_\xi] \tag{7}$$

$$\Pr^{-1}[(1 + \xi\eta)G_\eta]_\eta + \phi f G_\eta + \mathrm{Ec}(1 + \xi\eta)\phi^2 F_\eta^2 - \frac{\xi^2}{4}G_{t^*}$$
$$= \phi\xi[FG_\xi - G_\eta f_\xi] \tag{8}$$

The boundary conditions for these equations are expressed by

$$F(\xi,0,t^*) = \alpha_2, \quad G(\xi,0,t^*) = 1 \quad \text{for} \quad 0 \le t^*, \quad \xi \le 1$$

$$F(\xi,\infty,t^*) = 2, \quad G(\xi,\infty,t^*) = 0 \quad \text{for} \quad 0 \le t^*, \quad \xi \le 1 \tag{9}$$

$$\text{where} \quad \alpha_2 = 2\left(\frac{u_w}{u_e}\right) \quad \text{and} \quad f(\xi,\eta,t^*) = \int_0^\eta F dx + f_w$$

$$f_w = \left(\frac{-Rv_w\xi}{4\nu\phi}\right) = \left(\frac{A\xi}{\phi}\right), \quad A = \left(\frac{-Rv_w}{4\nu}\right) = \text{const}$$

The surface mass transfer parameter $A > 0$ or $A < 0$ according to whether there is a suction or injection. We have assumed that the flow is steady at time $t^* = 0$ and becomes unsteady for $t^* > 0$ due to the time-dependent freestream velocity $[u_e(t) = u_\infty\phi(t^*)]$ and the cylinder velocity $[u_w(t) = u_{w,0}\phi(t^*)]$, where $\phi(t^*) = 1 + \varepsilon t^{*2}; \varepsilon \lessgtr 0$. Hence, the initial conditions (i.e., conditions at $t^* = 0$) are given by the steady-state equations obtained from Eqs. (7) and (8) by substituting $\phi(t^*) = 1$, $d\phi/dt^* = F_{t^*} = G_{t^*} = 0$ when $t^* = 0$. The corresponding boundary conditions are obtained from (9) when $t^* = 0$. It may be noted that the steady-state equations in the absence of viscous dissipation for $\alpha = 1$ are the same as those of Chen and Mucoglu [6] and Takhar et al. [11] with $N = 0$.

The quantities of physical interest are as follows [16,17]:

The local surface skin friction coefficient given by

$$C_f = \frac{2\tau_w}{\rho u_\infty^2} = \frac{2\left[\mu\frac{\partial u}{\partial r}\right]_w}{\rho u_\infty^2} = 2^{-1}\mathrm{Re}_x^{-(1/2)}\phi(t^*)(F_\eta)_w$$

Thus,

$$\mathrm{Re}_x^{1/2}C_f = 2^{-1}\phi(t^*)(F_\eta)_w$$

The local Nusselt number can be expressed as

$$\mathrm{Re}_x^{-(1/2)}Nu = -2^{-1}(G_\eta)_w \tag{10}$$

where

$$Nu = -\frac{\left[x\left(\frac{\partial T}{\partial r}\right)\right]_w}{T_w - T_\infty}$$

Table 1 Comparison of the steady-state results $(f_{\eta\eta}(\xi,0), -G_\eta(\xi,0))$ with those of Chen and Mucoglu [6] and Takhar et al. [11]

ξ	λ	Present results		Chen and Mucoglu [6]		Takhar et al. [11]	
		$f_{\eta\eta}(\xi,0)$	$-G_\eta(\xi,0)$	$f_{\eta\eta}(\xi,0)$	$-G_\eta(\xi,0)$	$f_{\eta\eta}(\xi,0)$	$-G_\eta(\xi,0)$
0	0	1.3282	0.5854	1.3282	0.5854	1.3281	0.5854
0	1	4.9664	0.8220	4.9666	0.8221	4.9663	0.8219
0	2	7.7122	0.9304	7.7126	0.9305	7.7119	0.9302
1	0	1.9169	0.8666	1.9172	0.8669	1.9167	0.8666
1	1	5.2580	1.0621	5.2584	1.0621	5.2578	1.0617
1	2	7.8871	1.1688	7.8871	1.1690	7.8863	1.1685

3 Method of Solution

The set of dimensionless equations (7) and (8) under the boundary conditions (9) with the initial conditions obtained from the corresponding steady-state equations has been solved numerically using an implicit finite difference scheme in combination with the quasi-linearization technique. Since the method is described by Inouye and Tate [14] and also explained in a recent paper by Roy and Saikrishnan [18], its detailed description is not presented here for the sake of brevity. In brief, the nonlinear coupled partial differential equations were replaced by an iterative sequence of linear equations following quasi-linearization technique. The resulting sequence of linear partial differential equations were expressed in difference form using central difference scheme in η direction and backward difference scheme in ξ and t^* directions. In each iteration step, the equations were then reduced to a system of linear algebraic equations with a block tridiagonal structure, which is solved by using the Varga algorithm [19].

To ensure the convergence of the numerical solution to the exact solution, the step sizes $\Delta\eta$, $\Delta\xi$, and Δt^* have been optimized and the results presented here are independent of the step sizes, at least up to the fourth decimal place. The step sizes $\Delta\eta$, $\Delta\xi$, and Δt^* have been taken as $0.01, 0.02$, and 0.01, respectively. A convergence criteria based on the relative difference between the current and previous iteration values are employed. When the difference reaches $<10^{-4}$, the solution is assumed to have converged and the iterative process is terminated.

4 Results and Discussion

The computations have been carried out for various values of $\Pr(0.7 \leq \Pr \leq 7.0)$, $\lambda(0 \leq \lambda \leq 3)$, $\alpha_2(0 \leq \alpha_2 \leq 2)$, $Ec(0 \leq Ec \leq 0.3)$, and $A(-0.5 \leq A \leq 0.5)$. The edge of the boundary layer η_∞ is taken

between 3 and 5, depending on the values of parameters. The results have been obtained for both accelerating $[\phi(t^*)=1+\epsilon t^{*2}, \epsilon>0, 0 \leq t^* \leq 1]$ and decelerating $[\phi(t^*)=1+\epsilon t^{*2}, \epsilon<0, 0 \leq t^* \leq 1]$ freestream velocities of the fluid. In order to validate our method, we have compared steady-state results of skin-friction and heat transfer coefficients $[F_\eta(0,0), G_\eta(0,0)]$ with those of Chen and Mucoglu [6] and Takhar et al. [11]. The results are found in excellent agreement, and comparisons are shown in Table 1.

The effects of surface curvature parameter ξ (or the axial distance) and buoyancy parameter λ on velocity and temperature profiles (F, G) for accelerating flow $\phi(t^*)=1+\epsilon t^{*2}, \epsilon=0.5$, when $\alpha_2=1$, $Ec=0.1$, $A=0$, $\Pr=0.7$ and 7.0, are displayed in Figs. 2 and 3. Also, the effects of ξ and λ on the skin friction and heat transfer coefficients $(Re_x^{1/2}C_f, Re_x^{-1/2}Nu)$ are presented in Fig. 4. The action of the buoyancy force shows the overshoot in the velocity profiles (F) near the wall for lower Prandtl number $(\Pr=0.7)$, but for higher Prandtl number $(\Pr=7.0)$, the velocity overshoot in F is not observed as shown in Fig. 2. The magnitude of the overshoot increases with the buoyancy parameter λ. The reason is that the buoyancy force (λ) effect is larger in a low Prandtl number fluid $(\Pr=0.7,$ air$)$ due to the lower viscosity of the fluid, which enhances the velocity as the assisting buoyancy force acts like a favorable pressure gradient and the velocity overshoot occurs. For higher Prandtl number fluid $(\Pr=7.0,$ water$)$, the velocity overshoot is not present because higher Prandtl number fluid implies more viscous fluid, which makes it less sensitive to the buoyancy parameter λ. The effect of λ is comparatively less on the temperature (G) as shown in Fig. 2. Because of the increase in surface curvature parameter ξ, the steepness in velocity and temperature profiles (F, G) near the wall increases, but the magnitude of the
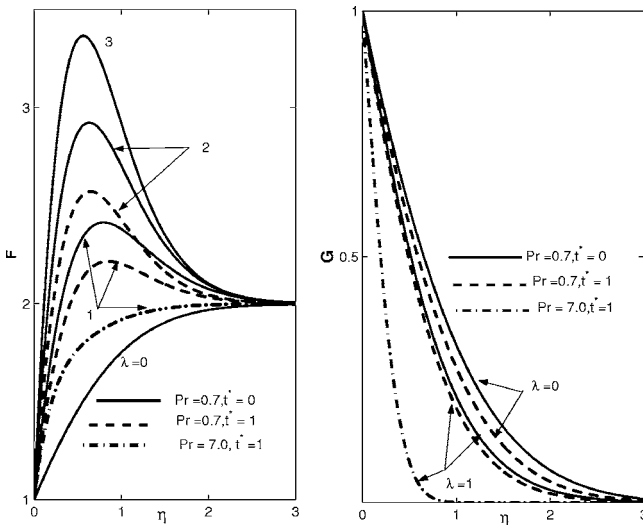

Fig. 2 Effects of λ and Pr on F and G for $\phi(t^*)=1+\epsilon t^2$, $\epsilon=0.5$ when Ec=0.1, $\alpha_2=1$, $\xi=0.5$, and $A=0$
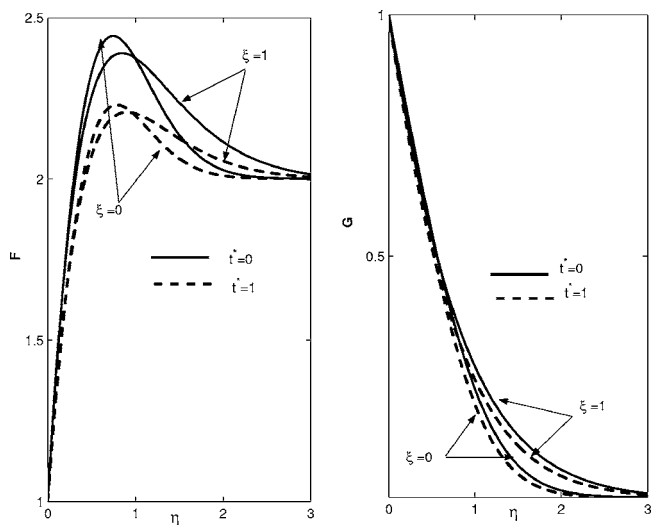
Fig. 3 Effect of ξ on F and G for $\phi(t^*)=1+\epsilon t^2$, $\epsilon=0.5$ when $\lambda=1$, Pr=0.7, Ec=0.1, $\alpha_2=1$, and $A=0$
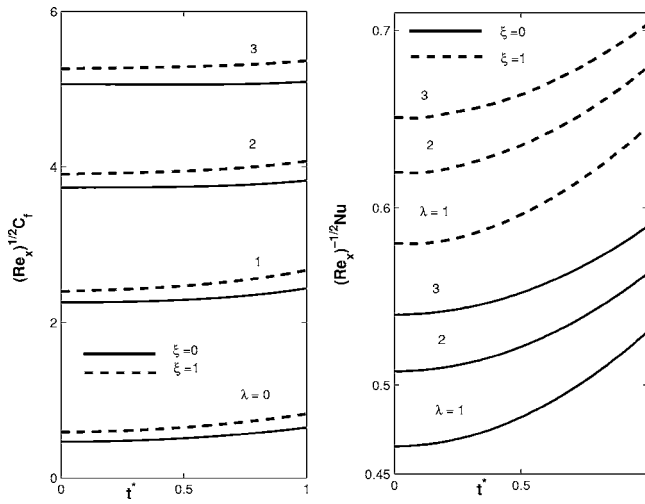
Fig. 4 Effects of λ and ξ on $\mathrm{Re}_x^{1/2}C_f$ and $\mathrm{Re}_x^{-1/2}\mathrm{Nu}$ for $\phi(t^*)=1+\epsilon t^{*2}$, $\epsilon=0.5$ when Pr=0.7, Ec=0.1, $\alpha_2=1$, and $A=0$

Fig. 6 Effects of A and α_2 on F for $\phi(t^*)=1+\epsilon t^{*2}$, $\epsilon=0.5$ when $\lambda=1$, Pr=0.7, $\xi=0.5$, and Ec=0.1

velocity overshoot slightly decreases, as can be seen in Fig. 3. The increase in ξ acts as a favorable pressure gradient, and the effect of ξ is small so that it does not cause the velocity profiles to increase the magnitude of the overshoots further, as in buoyancy-aided flow. Similar trends have been observed by Chen and Mucoglu [6] and Takhar et al. [11] for the steady-state case. Furthermore, from Fig. 4, it is observed that the skin friction and heat transfer coefficients ($\mathrm{Re}_x^{1/2}C_f$, $\mathrm{Re}_x^{-1/2}\mathrm{Nu}$) increase with the increase of buoyancy parameter (λ). The physical reason is that the positive buoyancy force ($\lambda>0$) implies favorable pressure gradient, and the fluid gets accelerated, which results in thinner momentum and thermal boundary layers. Consequently, the local skin friction ($\mathrm{Re}_x^{1/2}C_f$) and the local Nusselt number ($\mathrm{Re}_x^{-1/2}\mathrm{Nu}$) are also increased at any time (t^*), as shown in Fig. 4. For example, for $\alpha_2=1.0$, Pr=0.7, Ec=0.1, and $A=0.0$ at time $t^*=0.5$, Fig. 4 shows that the percentage increases, in $\mathrm{Re}_x^{1/2}C_f$ and $\mathrm{Re}_x^{-1/2}\mathrm{Nu}$ for the increase of λ from 1 to 3 are approximately 121% and 14%, respectively.

The effects of wall velocity α_2 and mass transfer parameter A on skin friction and heat transfer coefficients for $\phi(t^*)=1+\epsilon t^{*2}$, $\epsilon=0.5$, $\alpha_2=1$, Pr=0.7, and Ec=0.1 are presented in Fig. 5. In
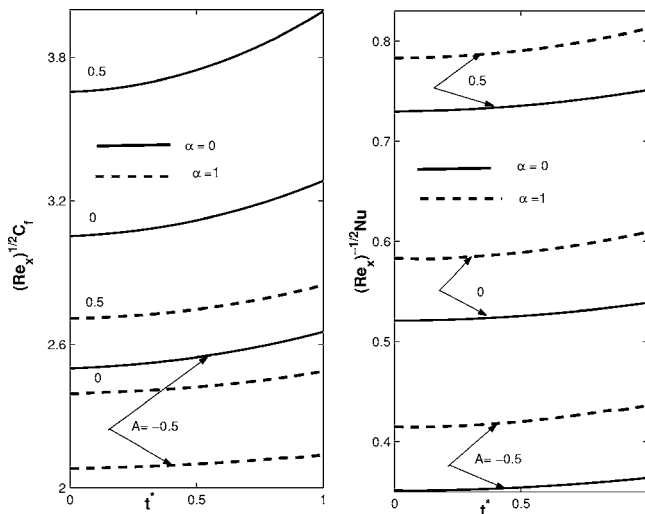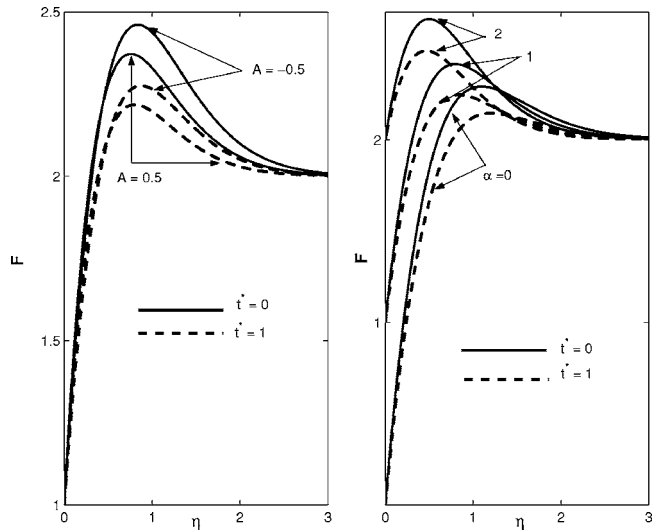
addition, Fig. 6 displays the effect of α_2 and A on velocity profiles (F) for time $t^*=0$ and $t^*=1$. Results indicate that the skin friction coefficient ($\mathrm{Re}_x^{1/2}C_f$) decreases, but the heat transfer rate at the wall increases for all values of A and time t^* due to the increase of the wall velocity α_2. Actually, the increase of the wall velocity (α_2) gives a slip over the surface as a result of which skin friction coefficient decreases. For the sake of clarity, we also present some of the results quantitatively. For example, for $t^*=1.0$ and $A=-0.5$, the skin friction coefficient ($\mathrm{Re}_x^{1/2}C_f$) reduces approximately by 19% and the heat transfer coefficient ($\mathrm{Re}_x^{-1/2}\mathrm{Nu}$) increases approximately by 25% as the wall velocity α_2 increases from 0 to 1. Figure 5 also shows that for all time t^*, both $\mathrm{Re}_x^{1/2}C_f$ and $\mathrm{Re}_x^{-1/2}\mathrm{Nu}$ increase with suction($A>0$) but decrease with the increase of injection ($A<0$). In case of injection, the fluid is carried away from the surface, causing reduction in velocity gradient as it tries to maintain the same velocity over a very small region near the surface, and this effect is reversed in the case of suction. The graphs of the velocity profiles (F) versus η in Fig. 6 show that the injection ($A<0$) as well as the wall velocity (α_2) cause a decrease in the steepness of the profiles (F) near the wall, but the steepness of the profiles (F) increases with suction. For all the cases, the profiles (F) at a later time $t^*=1.0$ are comparatively less steeper near the wall than those at the initial time $t^*=0.0$.

Figures 7 and 8 display the effects of Prandtl number and Eckert number for accelerating and decelerating freestream flows [$\phi(t^*)=1+\epsilon t^{*2}$, $\epsilon=0.5$, and $\epsilon=-0.5$] on the local skin friction and heat transfer coefficients ($\mathrm{Re}_x^{1/2}C_f$, $\mathrm{Re}_x^{-1/2}\mathrm{Nu}$), where $\alpha_2=1.0$, $\lambda=1.0$, and $A=0.0$. Also, the effects of Pr and Ec on temperature profiles (G) for accelerating freestream flows [$\phi(t^*)=1+\epsilon t^{*2}$, $\epsilon=0.5$] with the same data are shown in Fig. 9. It is found from Fig. 7 that the skin friction coefficient decreases with the increase of the Prandtl number. Because the higher Prandtl number fluid means more viscous fluid, which increases the boundary layer thickness and, consequently, reduces the shear stress. On the other hand, Figs. 8 and 9 reveal that the surface heat transfer rate increases significantly with Pr (see Fig. 8) as the higher Pr number fluid has a lower thermal conductivity, which results in the thinner thermal boundary layer (see Fig. 9) and, hence, a higher heat transfer rate at the wall. To be more specific, for $\lambda=1$, $\alpha_2=1$, $A=0$, Ec=0.1, and $t^*=0.5$ as Pr increases from 0.7 to 7.0, $\mathrm{Re}_x^{1/2}C_f$ decreases by about 36% and $\mathrm{Re}_x^{-1/2}\mathrm{Nu}$ increases by 114%, respectively. Thus, the heat transfer rate at the wall can be reduced by using a low Prandtl number fluid, such as air (Pr=0.7). It is ob-

Fig. 5 Effects of A and α_2 on $\mathrm{Re}_x^{1/2}C_f$ and $\mathrm{Re}_x^{-1/2}\mathrm{Nu}$ for $\phi(t^*)=1+\epsilon t^{*2}$, $\epsilon=0.5$ when $\lambda=1$, Pr=0.7, and Ec=0.1
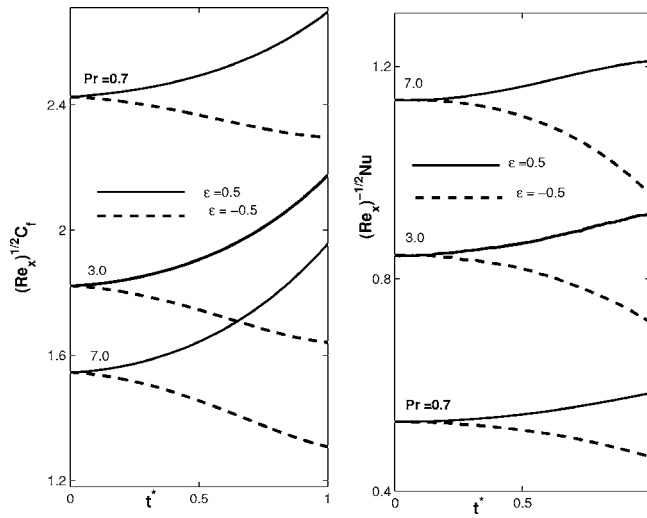
Fig. 7 Effect of Pr on $Re_x^{1/2}C_f$ and $Re_x^{-1/2}Nu$ for $\phi(t^*)=1+\epsilon t^2$, $\epsilon=0.5$ and $\epsilon=-0.5$ when $\lambda=1$, Ec=0.1, $\alpha_2=1$, $A=0$, and $\xi=0.5$

Fig. 9 Effects of Pr and Ec on G for $\phi(t^*)=1+\epsilon t^2$, $\epsilon=0.5$ when $\lambda=1$, $A=0$, $\alpha_2=1$, and $\xi=1.0$

served from Fig. 8 that, due to an increase of the viscous dissipation parameter Ec, $Re_x^{1/2}C_f$ increases, but $Re_x^{-1/2}Nu$ decreases and the effect is more pronounced on the heat transfer coefficient ($Re_x^{-1/2}Nu$). In particular, it is found for accelerating flow ($\epsilon=0.5$) that the percentage decrease of $Re_x^{-1/2}Nu$ for an increase in Ec from 0 to 0.2 at $t^*=1.0$ is 100% as compared to 10% of $Re_x^{1/2}C_f$ for the same data. This behavior is in support of the common fact that the viscous dissipation affects the thermal boundary layer more than the momentum boundary layer. In case of accelerating flow, Fig. 7 shows that both the skin friction coefficient and the heat transfer rate increase with time t^* and the effect of the time variations is found to be more pronounced on the skin friction coefficient than on heat transfer rate, because the change in the freestream velocity with time strongly affect the velocity component. For example, for Pr=7.0 the values of $Re_x^{1/2}C_f$ and $Re_x^{-1/2}Nu$ increase by about 25% and 6%, respectively, when the time t^* increases from 0 to 1.

5   Conclusions

Nonsimilar solution of an unsteady mixed convection flow over a continuously moving slender cylinder has been obtained for both accelerating and decelerating freestream velocities. Results indicate that the skin friction and heat transfer coefficients are significantly affected by the time-dependent freestream velocity distributions. It is found that the buoyancy force (λ) enhances the skin friction coefficient and Nusselt number. In the presence of the buoyancy force ($\lambda>0$), the velocity profile exhibits velocity overshoot for lower Prandtl number and the buoyancy parameter tends to increase its magnitude. For a fixed buoyancy force, the Nusselt number increases with Prandtl number, but the skin friction coefficient decreases. In fact, the increase in Prandtl number causes a significant reduction in the thickness of thermal boundary layer. As expected, both skin friction and heat transfer coefficients increase with suction but decrease with the increase of injection. In contrast, the effect of wall velocity is to decrease the skin friction but to increase the heat transfer rate. Furthermore, it is noted that the curvature parameter steepens both the velocity and temperature profiles, but injection ($A<0$) does the reverse. The heat transfer rate is found to depend strongly on viscous dissipation, but the skin friction is little affected by it.

Nomenclature

A = surface mass transfer parameter
C_f = local skin friction coefficient
c_p = specific heat at constant pressure
Ec = Eckert number
f, f_η = dimensionless stream function, velocity component
g = acceleration due to gravity (ms^{-2})
G = dimensionless temperature
Gr_x = Grashof number.
k = thermal conductivity (W m^{-1}K^{-1})
Nu = local Nusselt number.
Pr = Prandtl number
r = radial coordinate
Re_x = Reynolds number
R = radius of cylinder
t, t^* = dimensional and dimensionless times, respectively
T = temperature (K)
u = axial velocity component (ms^{-1})
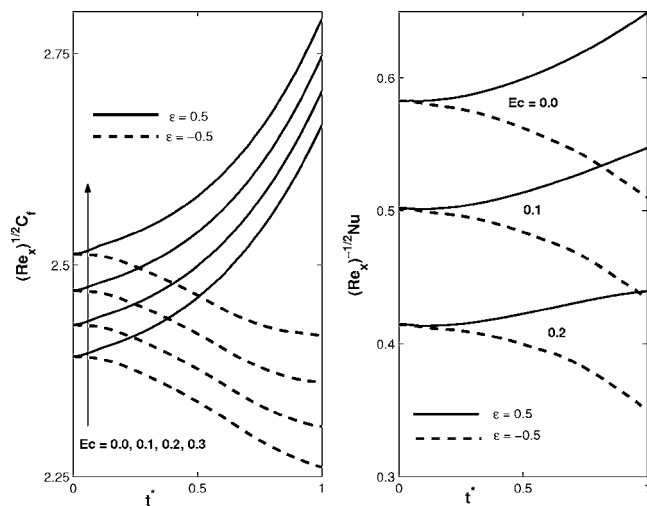v = radial velocity component (ms^{-1})
x = axial coordinate

Fig. 8 Effect of Ec on $Re_x^{1/2}C_f$ and $Re_x^{-1/2}Nu$ for $\phi(t^*)=1+\epsilon t^2$, $\epsilon=0.5$ and $\epsilon=-0.5$ when $\lambda=1$, Pr=0.7, $\alpha_2=1$, $A=0$, and $\xi=0.5$
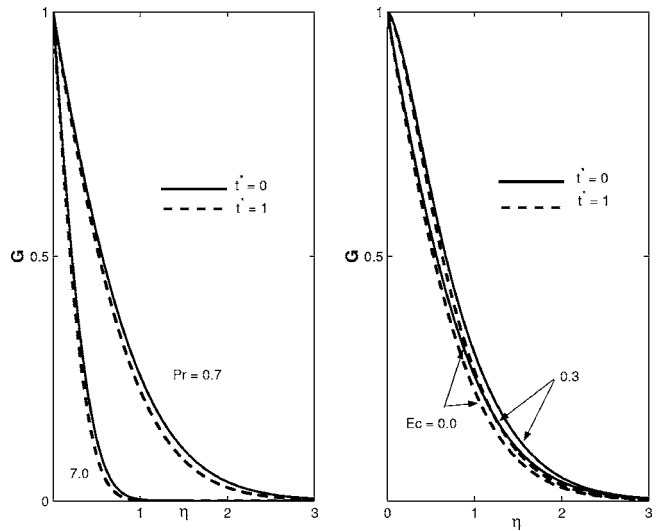
Greek Symbols

α = thermal diffusivity (m^2s^{-1})

α_2 = wall velocity

β = volumetric coefficient of the thermal expansion (K^{-1})

ϵ = constant

η = nondimensional parameter

λ = buoyancy parameter

μ = dynamic viscosity ($kg\ m^{-1}\ s^{-1}$)

ν = kinematic viscosity ($m^2\ s^{-1}$)

ξ = transverse curvature

$\phi(t^*)$ = function of t^* with first order continuous derivative

ρ = density (kg m^{-3})

Subscripts

i = initial condition

o = value at the wall for $t^*=0$

w,∞ = conditions at the wall and infinity, respectively

t,x,r = denote the partial derivatives with respect to these variables, respectively

η,ξ,t^* = denote the partial derivatives with respect to these variables, respectively

References

[1] Anilkumar, D., and Roy, S., 2004, "Self-Similar Solution of the Unsteady Mixed Convection Flow in the Stagnation Point Region of a Rotating Sphere," Heat Mass Transfer, **40**, pp. 487–493.

[2] Roy, S., and Anilkumar, D., 2004, "Unsteady Mixed Convection From a Rotating Cone in a Rotating Fluid Due to the Combined Effects of Thermal and Mass Diffusion," Int. J. Heat Mass Transfer, **47**, pp. 1673–1684.

[3] Vargas, J. V. C., Laursen, T. A., and Bejan, A., 1995, "Non-Similar Soutions for Unsteady Mixed Convection on a Wedge Embedded in a Porous Medium," Int. J. Heat Fluid Flow, **16**, pp. 211–216.

[4] Stewartson, K., 1955, "The Asymptotic Boundary Layer on a Circular Cylinder in Axial Incompressible Flow," Q. Appl. Math., **13**, pp. 113–122.

[5] Cebeci, T., 1974, "Laminar Free-Convective Heat Transfer From the Outer Surface of a Vertical Slender Circular Cylinder," *Proceedings of 5th International Conference, Society of Heat Transfer of Japan*, 3, pp. 15–19.

[6] Chen, T. S., and Mucoglu, A., 1975, "Buoyancy Effects on Forced Convection Along a Vertical Cylinder," ASME J. Heat Transfer, **97**, pp. 198–203.

[7] Mucoglu, A., and Chen, T. S., 1976, "Buoyancy Effects on Forced Convection Along a Vertical Cylinder With Uniform Surface Heat Flux," ASME J. Heat Transfer, **98**, pp. 523–525.

[8] Bui, M. N., and Cebeci, T., 1985, "Combined Free and Forced Convection on Vertical Slender Cylinders," ASME J. Heat Transfer, **107**, pp. 476–478.

[9] Lee, S. L., Chen, T. S., and Armaly, E. F., 1987, "Mixed Convection Along Vertical Cylinders and Needles With Uniform Surface Heat Flux," ASME J. Heat Transfer, **109**, pp. 711–716.

[10] Wang, T. Y., and Kleinstruver, C., 1989, "General Analysis of Steady Mixed Convection Heat Transfer on Vertical Slender Cylinders," ASME J. Heat Transfer, **111**, pp. 393–398.

[11] Takhar, H. S., Chamkha, A. J., and Nath, G., 2000, "Combined Heat and Mass Transfer Along a Vertical Moving Cylinder With a Free Stream," Heat Mass Transfer, **36**, pp. 237–246.

[12] Ziabicki, A., 1976, *Fundamentals of Fibre Formation*, Wiley, New York.

[13] Sparrow, E. M., and Yu, H. S., 1971, "Local Non-Similarity Thermal Boundary Layers," ASME J. Heat Transfer, **93**, pp. 328–334.

[14] Inouye, K., and Tate, A., 1974, "Finite Difference Version Quasilinearization Applied to Boundary Layer Equations," AIAA J., **12**, pp. 558–560.

[15] Schlichting, H., 2000, *Boundary Layer Theory*, Springer, New York.

[16] Pop, I., and Ingham, D. B., 2001, *Convective Heat Transfer: Mathematical and Computational Modelling of Viscous Fluids and Porous Media*, Pergaman, London.

[17] Bejan, A., 1994, *Convective Heat Transfer*, Wiley, New York.

[18] Roy, S., and Saikrishnan, P., 2003, "Non-Uniform Slot Injection (Suction) Into Steady Laminar Water Boundary Layer Flow Over a Rotating Sphere," Int. J. Heat Mass Transfer, **46**, pp. 3389–3396.

[19] Varga, R. S., 2000, *Matrix Iterative Analysis*, Printice-Hall, Englewood Cliffs, NJ.

Medium Resolution Transmission Measurements of Water Vapor at High Temperature

Sudarshan P. Bharadwaj

Michael F. Modest[1]
Fellow ASME
e-mail: mfmodest@psu.edu

Robert J. Riazzi

Department of Mechanical and
Nuclear Engineering,
The Pennsylvania State University,
University Park, PA 16802

Medium-resolution transmissivities of water vapor were measured at temperatures between 600 and 1550 K for all-important vibration-rotation bands as well as part of the purely rotational band. Measurements were made with an improved drop tube design, which ensures a relatively isothermal high-temperature gas column. Data were collected with a Fourier-transform-infrared-spectrometer, allowing for much better spectral resolution than most previous high-temperature measurements. The measured data were compared to the HITEMP database, as well as with the data of Phillips for the 2.7 μm band of H_2O. The data show minor discrepancies with the high-resolution database, particularly at higher temperatures, but, in general, agreement is acceptable.
[DOI: 10.1115/1.2165209]

1 Introduction

Knowledge of radiative properties of combustion gases is required to accurately predict radiative fluxes in a number of physical systems, such as fires and combustion systems. Unfortunately, absorption coefficients of absorbing gases are not known with sufficient accuracy to make reliable heat transfer calculations, especially at high temperatures. Spectra of gases broadened by N_2, air, and other buffer gases have been investigated by a number of researchers. For example, Rinsland et al. [1] describe atmospheric measurements of water-vapor absorption using a telescope and a Fourier-transform-infrared (FTIR) spectrometer. Atmospheric measurements have also been made with FTIR spectrometers for ozone [2,3] and CO [4]. Atmospheric measurements permit long optical paths, at the cost of isothermality and homogeneity of the path. And, of course, it is not possible to make high-temperature atmospheric measurements.

Laboratory measurements are made with window cells (uncooled [5–7] or water-cooled [8–10]), nozzle seal cells [11–14], and free jet devices [15,16]. Hot-window cells consist of a gas column confined within a container by windows at the ends. Although isothermality of the gas is ensured, such measurements are usually limited to temperatures of below 800 K [17]. Cold-window cells use water-cooled windows, thus allowing higher temperatures. However, it is impossible to obtain a truly isothermal gas column with such a device [8]. Nozzle seal cells contain the combustion gases within open flow cells by means of layers of inert gases (N_2 or argon) on either end. Although these cells eliminate some of the problems associated with windows, they may cause density and temperature gradients near the seal, as well as scattering by the turbulent eddies of the mixing flows [18]. Free jet devices use a burner and jet, and may thus be used for extremely high temperatures, at the cost of considerable uncertainty in the gas temperature and density distribution, as well as the path length.

Radiation measurements have been made for various water-vapor bands by other researchers. Esplin et al. [19] have measured line positions and line intensities for lines in the 720–1400 cm^{-1} spectral region of H_2O. Their measurements were made at 20 Torr

and 1000 K, in a heated 1.75 m single-pass absorption cell. Phillips [20] has made moderately high-resolution measurements (0.06 cm^{-1}) for the 2.7 μm band of H_2O at temperatures of up to a 1000 K, which were later degraded to 25 cm^{-1}. These measurements were made with a Nicolet 8000 FTIR spectrometer equipped with a CaF$_2$ beam splitter and a globar source. The data were obtained over a range of optical depths from 0.4 to 20.3 atm cm. Band-model parameters were obtained from the averaged data, assuming a combined Lorentz-Doppler model, and comparisons were made to other band-model data and with line-by-line calculations.

Fleckl et al. [21] have made comparisons of experimental and HITEMP [22] transmissivities for CO, CO_2, and H_2O for temperatures of up to 1100°C. Their measurements were made at a resolution of 0.5 cm^{-1} and required subtraction of the emission signal from the total of emission and reflection. Their results for CO_2 show higher absorption than HITEMP at 1100°C in the wings of the 4.3 μm band, similar to our earlier CO_2 measurements [17,23]. Fleckl's high-temperature data for H_2O show higher absorption than HITEMP for some parts of the 6 μm band, and less absorption than HITEMP for other parts of the same band, similar to the data presented below. In some cases, their measured absorptances are as much as 50% off from HITEMP predictions.

In the present work, medium resolution (4 cm^{-1}) transmission measurements were made for the rotational, 6.3, 2.7, and 1.8 μm bands of H_2O with a drop-tube mechanism and FTIR spectrometer. These measurements were made at a total pressure of 1 atm, for H_2O/N_2 mixtures at temperatures of up to 1550 K. The setup used for our earlier CO_2 measurements [17,23] was modified for these measurements. These modifications consisted of opening up the optical path (using larger mirrors and openings) so as to allow a better signal, as well as switching the locations of the source and the detector [24] to eliminate furnace emission. Remodulated furnace emission was eliminated by taking advantage of the cube-corner optics within the FTIR spectrometer, as described in [24].

These measurements were compared to transmissivities obtained from the HITEMP database [22]. This database lists line locations, strengths, and half-widths for various gases. These line data were used to obtain narrowband transmissivities, using a custom-written code. For further details of the code, as well as of the procedure adopted to obtain transmission data from HITEMP, the reader is referred to [17,23].

Copyright © 2006 by ASME
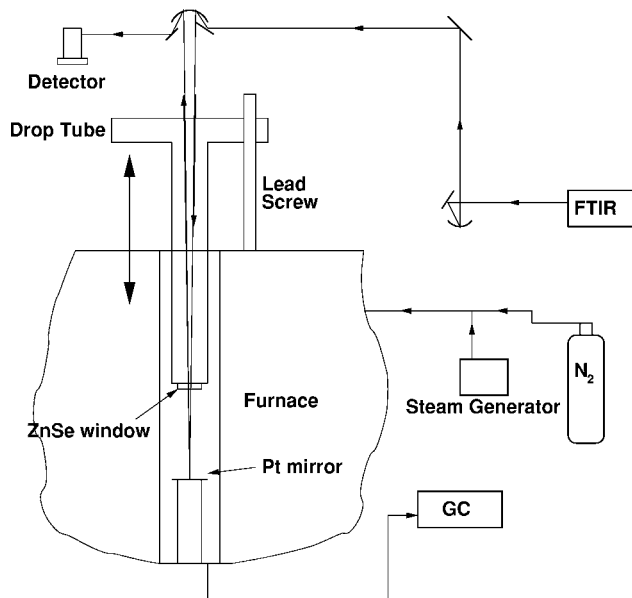
Fig. 1 Experimental setup (not to scale)

Fig. 2 Relative and absolute uncertainties in $\bar{\tau}$

2 Experimental Details

Narrowband H_2O transmission measurements were made at temperatures of up to 1550 K with a resolution of 4 cm^{-1} using a drop-tube mechanism and FTIR spectrometer. A diagram of the setup is shown in Fig. 1.

The setup used for our earlier CO_2 measurements [17,23] was modified so as to (i) allow a larger signal and (ii) eliminate modulated furnace emission. As Fig. 1 shows, steam from a steam generator was mixed with preheated N_2. The mole fraction of H_2O was varied by varying the flow rates of N_2 and steam. An Agilent series Micro Gas Chromatograph was used to measure the mole fraction of H_2O within the furnace. A ZnSe window at the bottom of the drop tube prevented the absorbing mixture from entering the rest of the optical path, which was purged with dry N_2 to eliminate atmospheric CO_2 and H_2O. Further details of the setup may be found in [23,17].

The transmissivity of H_2O at a given temperature and pressure path length was obtained by ratioing the signal obtained with the required concentration of H_2O at that temperature with the signal obtained without H_2O (i.e., with the furnace filled with N_2) at the same temperature. Six spectra were taken with 0% H_2O at each length and temperature, and these were averaged to give the base signal at that length and temperature. Another six spectra were taken at each measurement condition (length, temperature, and H_2O mole fraction), and these spectra were ratioed with the base spectra at that length and temperature to obtain the transmissivity for that measurement condition. The six transmission spectra were then used to calculate an average narrowband transmissivity, as well as a standard deviation as an estimate of the random error of the measurement.

Since the modulated emission from the furnace was eliminated [24], it was no longer necessary to subtract the emission signal from the total of the emission and reflection as described in [17]. Data were collected using a wideband MCT detector with a KBr beamsplitter and an IR source for the rotational, 6.3 and 2.7 μm bands of H_2O, and an InGaAs detector with a Quartz beamsplitter and tungsten-halogen source for the 1.8 μm band.

3 Data Analysis

The measured data at each temperature are compared to results from the HITEMP database. The linelist calculated for a nominal 100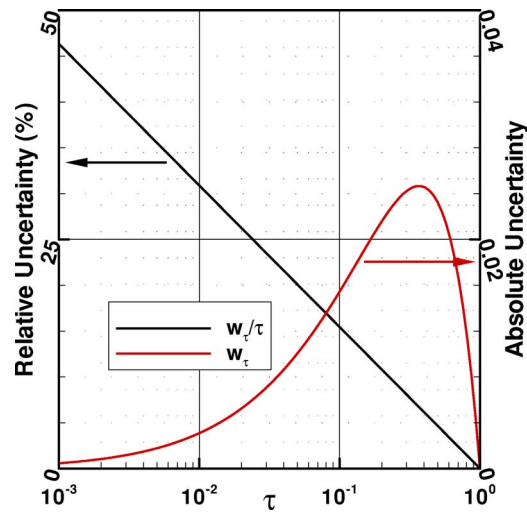0 K for water vapor was used to make the comparisons. Areas of differences and agreement with the database are identified. Line data from the HITEMP database are used to calculate narrowband transmissivities at the measured resolution, taking into account instrument broadening by the FTIR spectrometer. The spectrometer used triangular apodization with a half-width at the base of 4 cm^{-1}, and thus a sinc^2 function was used to model the instrument broadening, as explained in [23]. The measurements were made over a period of 8–12 hr for each temperature, which made it necessary to correct for the drift in the strength of the signal at the detector. This drift could be due to temperature fluctuations of the optical components (mirrors and beamsplitters) or varying detectivity of the cryogenic MCT detector. Since the transmissivity was obtained as the ratio of two signals, the "baseline transmissivity," which is the transmissivity in the regions of the spectrum over which the gas does not absorb radiation, is expected to be 100%. However, since the signal may be varying with time, the baseline transmissivity could be different from 100% in these regions. Thus, an estimate of the factor by which the signal has changed at each spectral location within the bands may be obtained by interpolating the baseline transmissivity in the band regions. The experimental transmissivity in the bands is then divided by the interpolated transmissivity to correct for the drift. The maximum drift was of the order of 10%, i.e., the transmission spectra obtained had a baseline of between 90% and 110% transmission.

In some cases, there were no optically thin regions of the spectrum outside the bands where the transmissivity was close to unity. This was especially the case for the rotational band of H_2O, which extends to zero on the wave-number scale. Since the wideband MCT detector has a useful range of between 600 and 4000 cm^{-1}, the transmissivities predicted by HITEMP at these wave numbers were used to calculate the baseline.

It was also noted that the locations of the peaks in the experimental transmission spectra did not precisely match those predicted by HITEMP, especially at higher wave numbers (by a maximum of $\sim$3.5 cm^{-1}). These differences could be due to incorrect FTIR calibration, instrument line function, or incorrect line center locations in the HITEMP database. These differences could be of the order of 2 cm^{-1} [25], although differences of 3.5 cm^{-1} are somewhat large. Thus, the experimental spectral locations were also modified so as to line up the experimental peaks with those obtained from the HITEMP databank. An analysis of the experimental error was also performed, as outlined below.

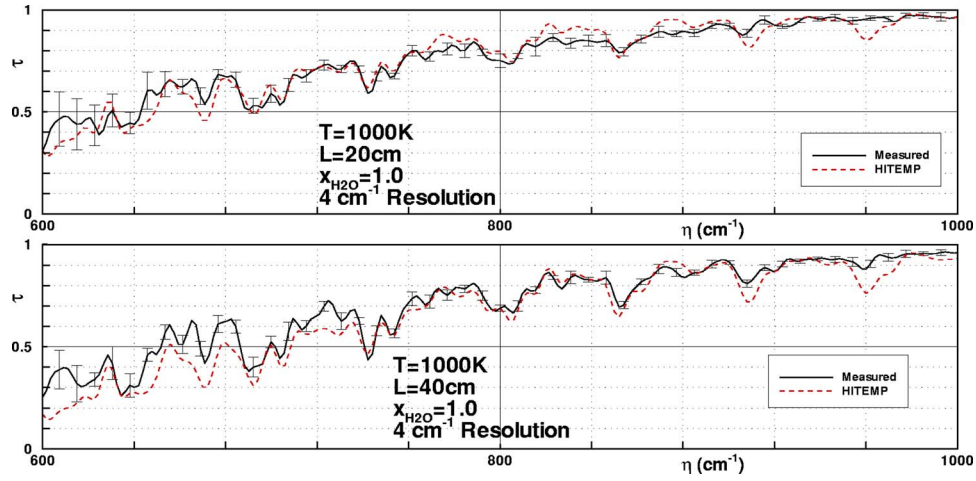The narrowband (mean) absorption coefficient $\bar{\kappa}$ is defined as

Fig. 3   Comparison of experimental data with HITEMP (1000 K, rotational band of H$_2$O)

$$\bar{\tau} = \exp(-\bar{\kappa}xl) \tag{1}$$

where $\bar{\tau}$ is the narrowband transmissivity, x is the mole fraction of water vapor and l is the path length. The uncertainty in the transmissivity results from uncertainties in temperature, mole fraction, and path length. Assuming that the temperature uncertainty affects the narrowband absorption coefficient only through the gas density,

$$\bar{\kappa} \propto \frac{1}{T} \tag{2}$$

and

$$\frac{\partial \bar{\kappa}}{\partial T} = -\frac{\bar{\kappa}}{T} \tag{3}$$

Thus, the root-sum-of-squares (RSS) error (w) in the narrowband transmissivity may be obtained as

$$w_{\bar{\tau}} = \sqrt{\left(\frac{\partial \bar{\tau}}{\partial T}w_T\right)^2 + \left(\frac{\partial \bar{\tau}}{\partial x}w_x\right)^2 + \left(\frac{\partial \bar{\tau}}{\partial l}w_l\right)^2} \tag{4}$$

But

$$\frac{\partial \bar{\tau}}{\partial T} = \frac{\partial \bar{\tau}}{\partial \bar{\kappa}}\frac{\partial \bar{\kappa}}{\partial T} = -\exp(-\bar{\kappa}xl)xl\left(-\frac{\bar{\kappa}}{T}\right) \tag{5}$$

since the temperature does not affect x and l. Thus,

$$w_{\bar{\tau}} = \exp(-\bar{\kappa}xl)(\bar{\kappa}xl)\sqrt{\left(\frac{w_T}{T}\right)^2 + \left(\frac{w_x}{x}\right)^2 + \left(\frac{w_l}{l}\right)^2} \tag{6}$$

i.e.,

$$\frac{w_{\bar{\tau}}}{\bar{\tau}} = \bar{\kappa}xl\sqrt{\left(\frac{w_T}{T}\right)^2 + \left(\frac{w_x}{x}\right)^2 + \left(\frac{w_l}{l}\right)^2} \tag{7}$$

or

$$\frac{w_{\bar{\tau}}}{\bar{\tau}} = (-\log\bar{\tau})\sqrt{\left(\frac{w_T}{T}\right)^2 + \left(\frac{w_x}{x}\right)^2 + \left(\frac{w_l}{l}\right)^2} \tag{8}$$

The uncertainty in temperature was $<2\%$ at all temperatures. The Micro GC used to measure the H$_2$O mole fraction was accurate to 5%, while the error in the distance between the bottom of the drop tube to the platinum mirror was around 1 mm, owing to uncertainty in the exact location of the platinum mirror in the furnace, which results from mirror distortion at high temperatures as well as tilting of the mirror during optical alignment. Thus, at the minimum path length of 10 cm, the uncertainty in the length was $\sim2\%$ (since the path length is twice the minimum 5 cm distance between the bottom of the drop tube and the mirror). Figure 2 shows the resulting uncertainty in the narrowband transmissivity. As the figure shows, the maximum absolute error in the transmissivity caused by T, x, and l is <0.03.
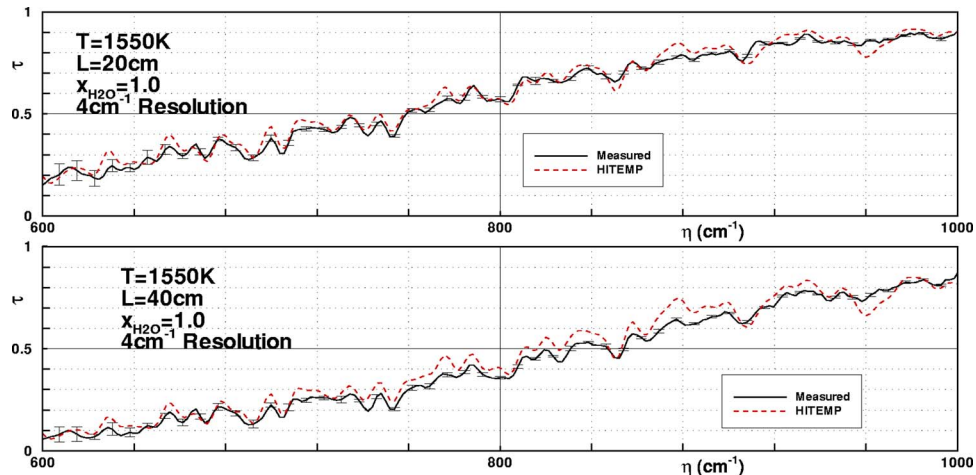

Fig. 4   Comparison of experimental data with HITEMP (1550 K, rotational band of H$_2$O)
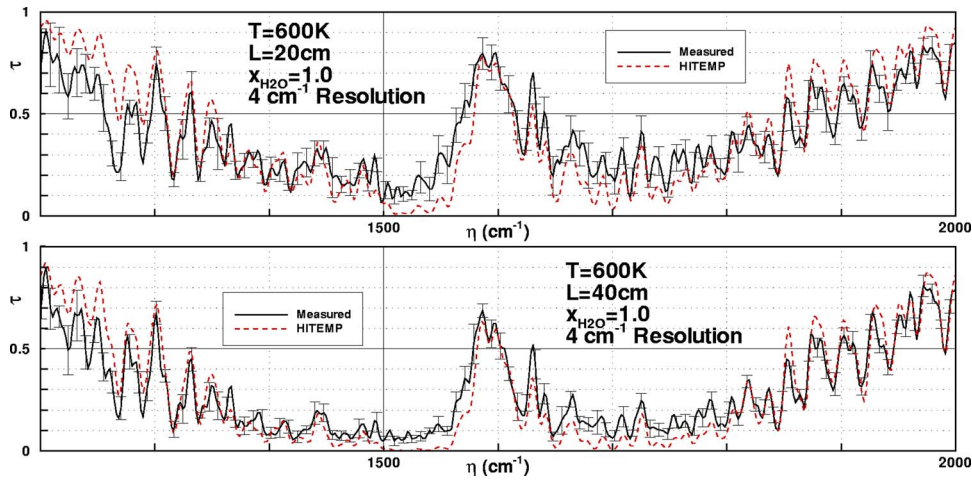
Fig. 5 Comparison of experimental data with HITEMP (600 K, 6.3 μm band of H$_2$O)

4 Results and Discussion

Figure 3 compares the measurements for pure water vapor ($x_{H_2O}=1$) at 1000 K for the rotational band of H$_2$O with the transmissivities predicted by HITEMP. The figure also shows error bars, which come from the experimental standard deviations of the six different sets of transmission spectra, as described earlier. Though the rotational band essentially goes to 0 cm^{-1} (or infinity on wavelength scale), the wideband MCT detector used for these measurements is only accurate above $\sim$600 cm^{-1}, as the larger standard deviations at the low wave-number end indicate. It is seen from the figure that HITEMP is fairly accurate for this band (above 600 cm^{-1}), though there are regions where the database shows somewhat more absorption than measurement, perhaps indicating the presence of incorrectly extrapolated lines. Data for the rotational band at 600 K were deemed unreliable, owing to large inconsistencies between the six transmissivity spectra, which resulted in large error bars and widely varying transmissivities over the band, and thus these data are not presented here.

Figure 4 compares the experimental data for the same band with HITEMP at 1550 K. The database is seen to agree with experiment over most of the band, with minor differences at the high wave-number end. The error bars are seen to be small at this temperature.

Figure 5 compares the experimental data for pure water vapor at 600 K for the 6.3 μm band of H$_2$O with the transmissivities predicted by HITEMP. As the figure shows, HITEMP predicts

somewhat less absorption than experiment below $\sim$1300 cm^{-1} and more absorption than experiment above this wave number. This trend seems to be reversed at 1000 K (Fig. 6), with HITEMP predicting marginally less absorption than experiment beyond $\sim$1500 cm^{-1}. A similar trend is seen at 1550 K, with HITEMP showing more absorption than experiment below $\sim$1300 cm^{-1} and less absorption above this wave number (Fig. 7). The standard deviations of the measurement (error bars) are seen to be reasonably small at 1000 and 1550 K. However, at 600 K, the deviations are much larger, perhaps indicating that these data are less reliable than those at higher temperatures, as the large differences with the HITEMP database in the wings of the 6.3 μm band indicate.

The measured data for the 2.7 μm band of H$_2$O are compared to HITEMP at the same three temperatures in Figs. 8–10. At 600 K, HITEMP is seen to show less absorption than experiment in the band wings (below $\sim$3300 cm^{-1} and above $\sim$4000 cm^{-1}) and more absorption in the center of the band. The opposite seems to be true at 1000 K (Fig. 9), perhaps indicating that the database has incorrectly extrapolated lines or is missing some high-temperature lines. At 1550 K, agreement between measurement and HITEMP is generally good, with HITEMP predicting somewhat less absorption than the experimental data in the center of the band. This might indicate missing lines in the database. Again, the standard deviations are rather large at 600 K, and the experimental data at this temperature may not be as reliable as desired.

Measured data at 600 K for the 1.8 μm band of H$_2$O are com-

Fig. 6 Comparison of experimental data with HITEMP (1000 K, 6.3 μm band of H$_2$O)

Fig. 7 Comparison of experimental data with HITEMP (1550 K, 6.3 μm band of H_2O)

Fig. 8 Comparison of experimental data with HITEMP (600 K, 2.7 μm band of H_2O)

Fig. 9 Comparison of experimental data with HITEMP (1000 K, 2.7 μm band of H_2O)

Fig. 10 Comparison of experimental data with HITEMP (1550 K, 2.7 μm band of H_2O)

Fig. 11 Comparison of experimental data with HITEMP (600 K, 1.8 μm band of H_2O)

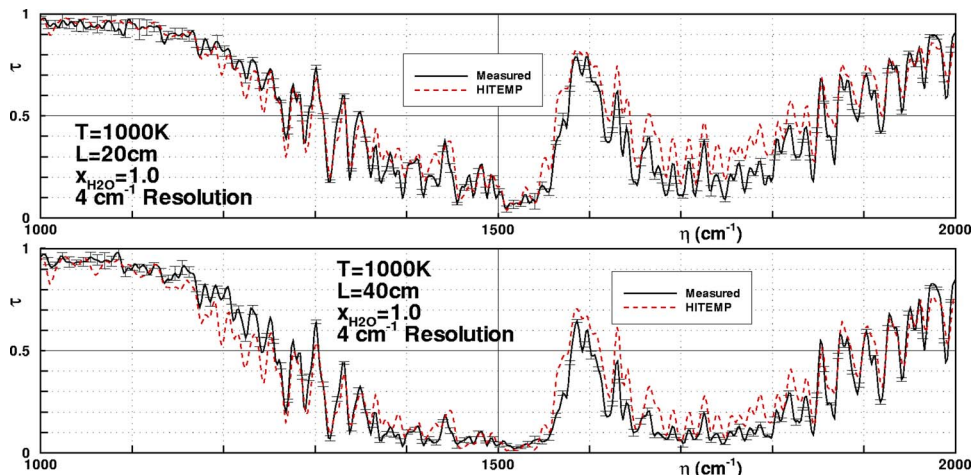Fig. 12 Comparison of experimental data with HITEMP (1000 K, 1.8 μm band of H_2O)

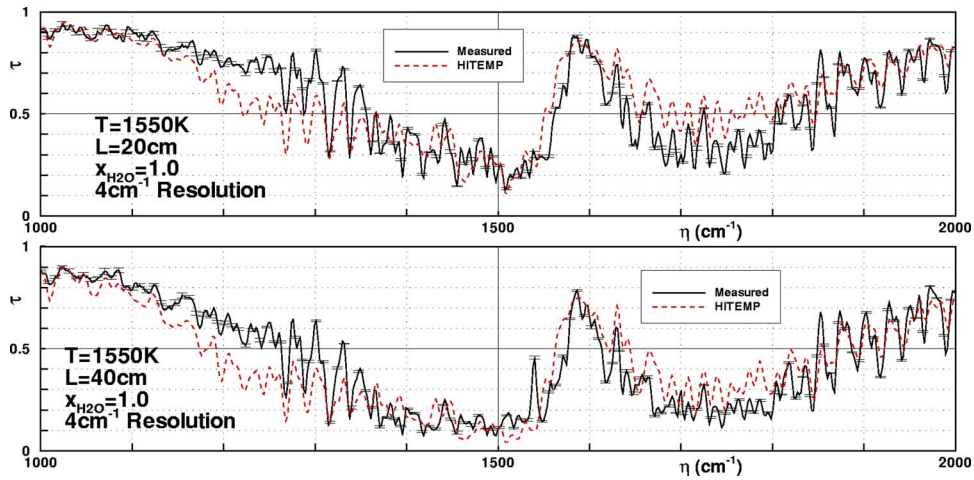**Fig. 13 Comparison of experimental data with HITEMP (1550 K, 1.8 μm band of H_2O)**
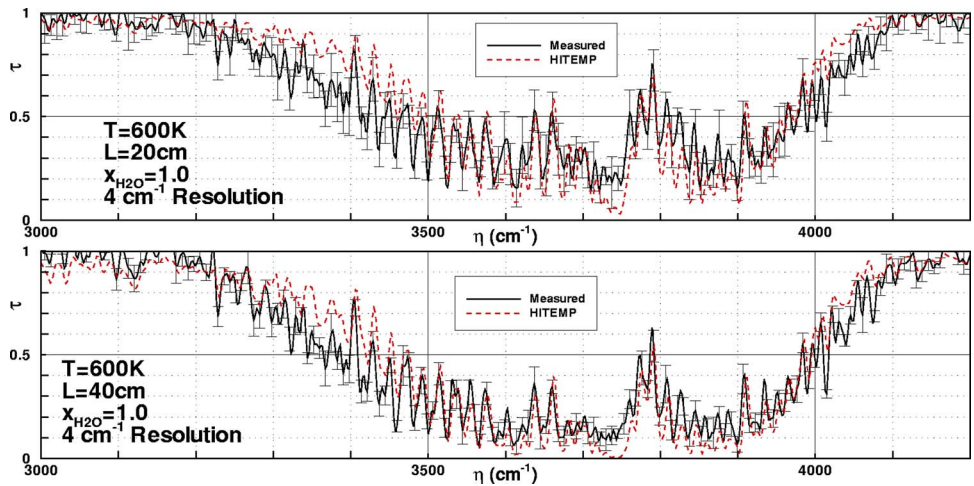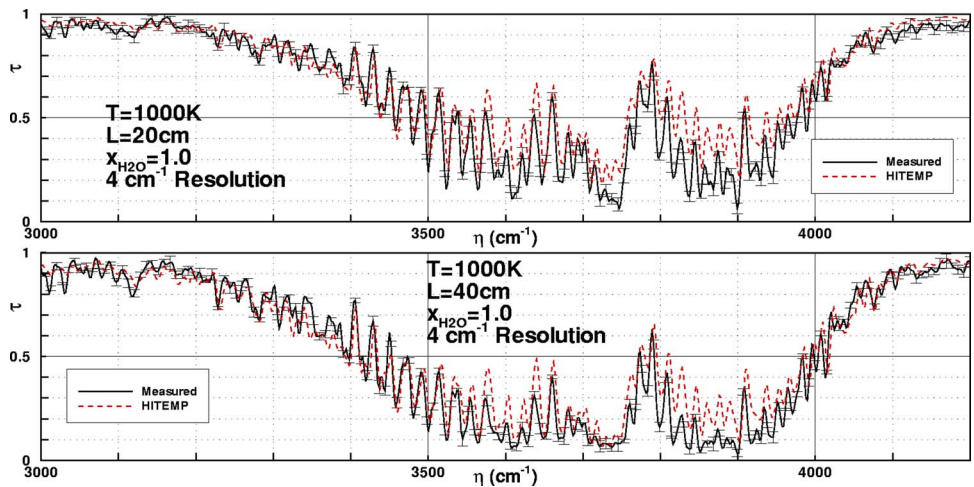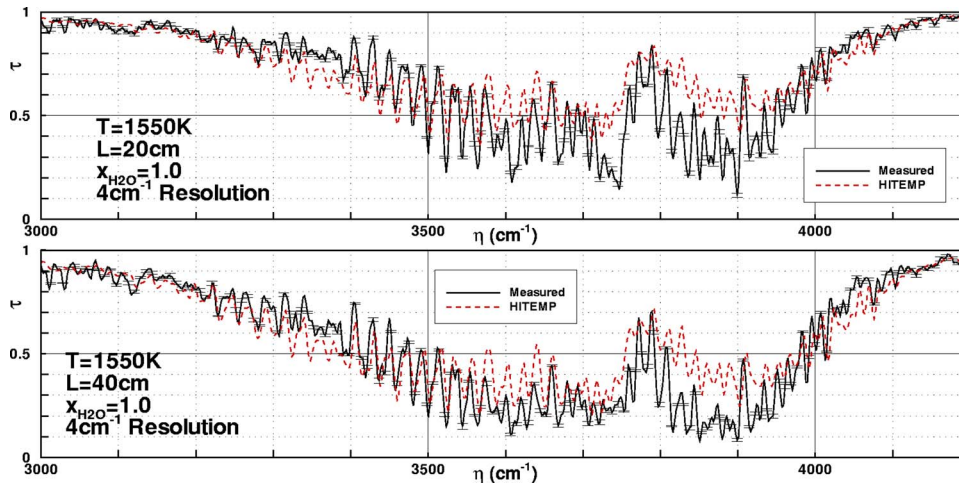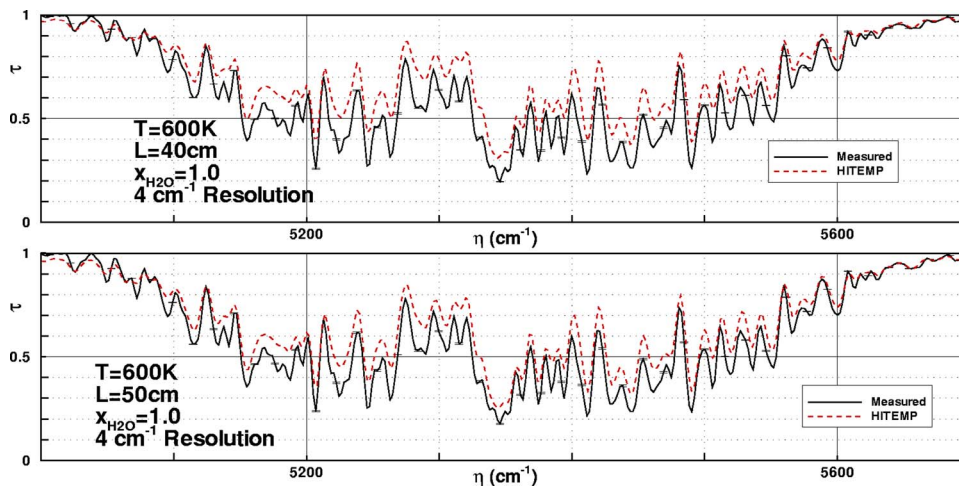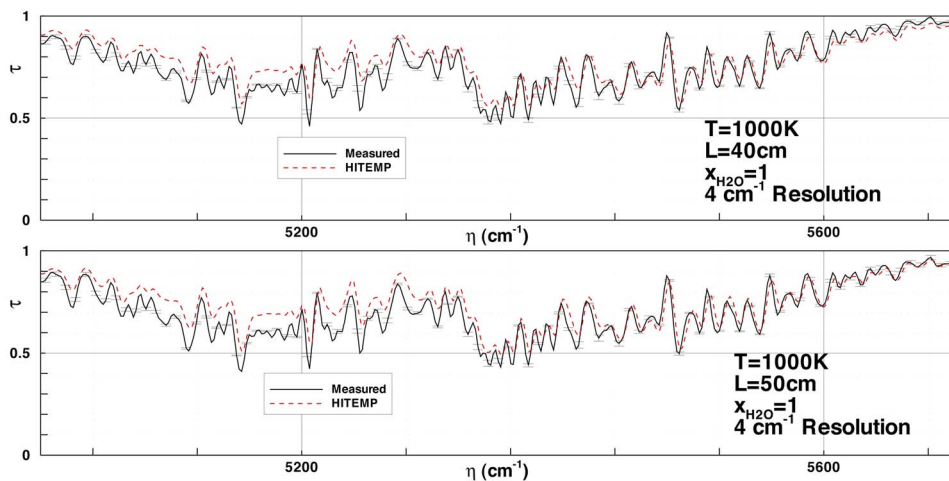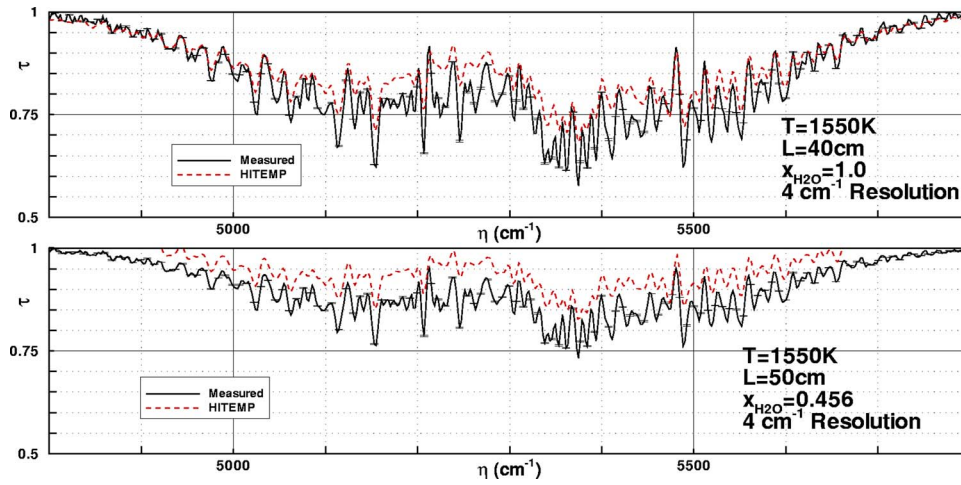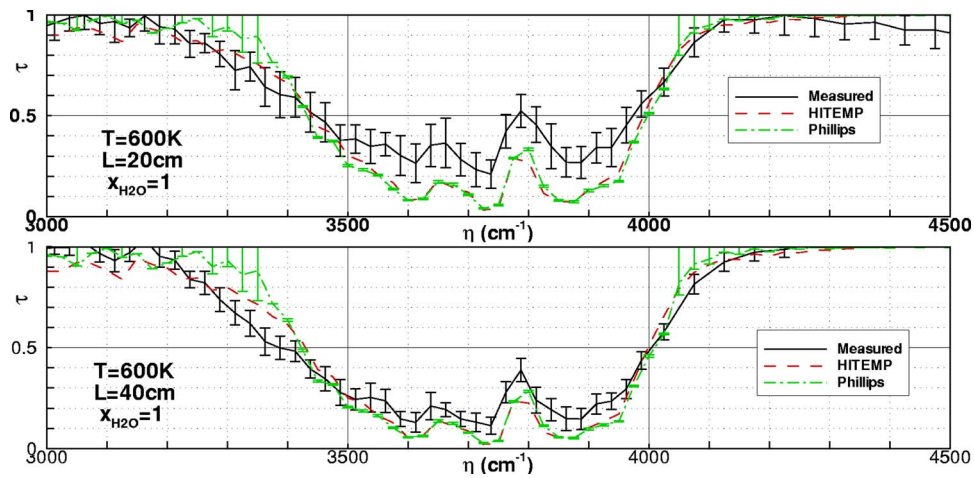

Fig. 14 Comparison of experimental data with HITEMP and Phillips (600 K, 2.7 μm band of H_2O)
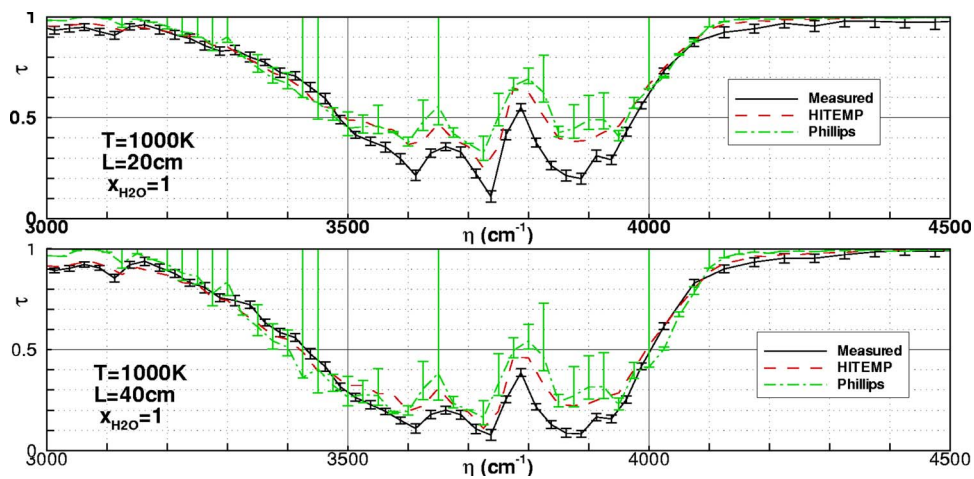

Fig. 15 Comparison of experimental data with HITEMP and Phillips (1000 K, 2.7 μm band of H_2O)

pared to HITEMP in Fig. 11. As the figure shows, HITEMP shows less absorption than measurement over the entire band. The same is true at 1000 K (Fig. 12) and at 1550 K (Fig. 13), which may indicate missing high-temperature lines in the database.

The figures shown in this section are a representative sample showing the accuracy of HITEMP at elevated temperatures. Many more data for myriad conditions may be found in [24].

The measured data for the 2.7 μm band of H_2O were also compared to the data of Phillips [20]. The experimental data at 4 cm^{-1} were degraded to the 25 cm^{-1} resolution of Phillips' data. Figure 14 compares the current measurements to HITEMP and Phillips at 600 K. The error bars of his data were obtained from the standard deviations provided in [20]. The error bar on top was obtained by subtracting one standard deviation from both the k and d' parameters, whereas the lower one was obtained by adding a standard deviation to the band model parameters. As the figure shows, Phillips' data are in closer agreement with HITEMP over most of the band. However, as stated above, the 600 K data from the current measurements may not be reliable.

Figure 15 compares the degraded experimental data at 1000 K to HITEMP and Phillips. Phillips' data show large error bars, but are in closer agreement with HITEMP. The current measurements show small error bars and predict more absorption than HITEMP, which might indicate missing/incorrectly extrapolated lines in the database.

5 Conclusions

Narrowband transmission measurements were made for the rotational, 6.3, 2.7, and 1.8 μm bands of H_2O at temperatures ranging from 600 to 1550 K. These measurements were compared to transmission data obtained from the HITEMP database, as well as with the data of Phillips for the 2.7 μm band of H_2O. Areas of similarity and differences between the experimental and HITEMP data were identified. Phillips' data were seen to be in closer agreement with HITEMP, but showed large error bars at higher temperatures. HITEMP was seen to show slightly less absorption than experiment over most of the bands at all the temperatures considered, indicating that the database may be missing some lines. However, overall data from HITEMP follow experiment rather closely, thus allowing confident use of the database for temperatures up to 1600 K.

References

[1] Rinsland, C. P., Goldman, A., Smith, M. A. H., and Devi, V. M., 1991, "Measurements of Lorentz Air-Broadening Coefficients and Relative Intensities in the H$_2$^{16}O Pure Rotational and ν_2 Bands From Long Horizontal Path Atmospheric Spectra," Appl. Opt., **20**, pp. 1427–1438.
[2] Bouazza, S., Barbe, A., Plateaux, J. J., Flaud, J. -M., and Camy-Peyret, C., 1993, "The $3\nu_1$ and $\nu_1 + 3\nu_3 - \nu_2$ Absorption Bands of $^{16}O_3$," J. Mol. Spectrosc., **160**, pp. 371–377.
[3] Flaud, J. M., Camy-Peyret, C., Perrin, A., Devi, V. M., Barbe, A., Bouazza, S., Plateaux, J. J., Rinsland, C. P., Smith, M. A. H., and Goldman, A., 1993, "Line Parameters for Ozone Hot Bands in the 3.3-μm Spectral Region," J. Mol. Spectrosc., **160**, pp. 378–386.
[4] Farrenq, R., Guelachvili, G., Sauval, A. J., Grevesse, N., and Farmer, C. B., 1991, "Improved Dunham Coefficients for CO From Infrared Solar Lines of High Rotational Excitation," J. Mol. Spectrosc., **149**, pp. 375–390.
[5] Goldstein, R. J., 1964, "Measurements of Infrared Absorption by Water Vapor at Temperatures to 1000 K," J. Quant. Spectrosc. Radiat. Transf., **4**, pp. 343–352.
[6] Oppenheim, U. P., and Goldman, A., 1965, "Spectral Emissivity of Water Vapor at 1200 K," Tenth Symposium (International) on Combustion, Combustion Institute, pp. 185–188.
[7] Tien, C. L., Modest, M. F., and McCreight, C. R., 1972, "Infrared Radiation Properties of Nitrous Oxide," J. Quant. Spectrosc. Radiat. Transf., **12**, pp. 267–277.
[8] Tien, C. L., and Giedt, W. H., 1965, "Experimental Determination of Infrared Absorption of High-Temperature Gases," *Advances in Thermophysical Properties at Extreme Temperatures and Pressures*, ASME, New York, pp. 167–173.
[9] Abu-Romia, M. M., and Tien, C. L., 1966, "Measurements and Correlations of Infrared Radiation of Carbon Monoxide at Elevated Temperatures," J. Quant. Spectrosc. Radiat. Transf., **6**, pp. 143–167.
[10] Chan, S. H., and Tien, C. L., 1971, "Infrared Radiation Properties of Sulfur Dioxide," ASME J. Heat Transfer, **93**, pp. 172–177.
[11] Hottel, H. C., and Mangelsdorf, H. G., 1935, "Heat Transmission by Radiation From Non-Luminous Gases II. Experimental Study of Carbon Dioxide and Water Vapor," AIChE J., **31**, pp. 517–549.
[12] Plass, G. N., 1959, "Spectral Emissivity of Carbon Dioxide From 1800–2500 cm^{-1}," J. Opt. Soc. Am., **49**, pp. 821–828.
[13] Edwards, D. K., 1965, "Absorption of Radiation by Carbon Monoxide Gas According to the Exponential Wide-Band Model," Appl. Opt., **4**(10), pp. 1352–1353.
[14] Weiner, M. M., and Edwards, D. K., 1968, "Non-Isothermal Gas Radiation in Superposed Vibration–Rotation Bands," J. Quant. Spectrosc. Radiat. Transf., **8**, pp. 1171–1183.
[15] Ludwig, C. B., Malkmus, W., Reardon, J. E., and Thomson, J. A. L., 1973, "Handbook of Infrared Radiation From Combustion Gases," Tech. Rep. SP-3080, NASA.
[16] Ferriso, C. C., and Ludwig, C. B., 1964, "Spectral Emissivities and Integrated Intensities of the 2.7 μm H$_2$O band between 530 and 2200 K," J. Quant. Spectrosc. Radiat. Transf., **4**, pp. 215–227.
[17] Modest, M. F., and Bharadwaj, S. P., 2002, "High-Resolution, High-Temperature Transmissivity Measurements and Correlations for Carbon Dioxide-Nitrogen Mixtures," J. Quant. Spectrosc. Radiat. Transf., **73**(2–5), pp. 329–338.
[18] Edwards, D. K., 1976, "Thermal Radiation Measurements," *Measurements in Heat Transfer*, E. R. G. Eckert and R. J. Goldstein, eds., Hemisphere, Washington, DC, Ch. 10.
[19] Esplin, M. P., Wattson, R. B., Hoke, M. L., and Rothman, L. S., 1998, "High-Temperature Spectrum of H$_2$O in the 720 to 1400 cm^{-1} region," J. Quant. Spectrosc. Radiat. Transf., **60**(5), pp. 711–739.
[20] Phillips, W. J., 1990, "Band Model Parameters of the 2.7 μm Band of H$_2$O," J. Quant. Spectrosc. Radiat. Transf., **43**, pp. 13–31.
[21] Fleckl, T., Jäger, H., and Obernberger, I., 2002, "Experimental Verification of Gas Spectra Calculated for High Temperatures Using the HITRAN/HITEMP Database," J. Phys. D, **35**(23), pp. 3138–3144.
[22] Rothman, L. S., Camy-Peyret, C., Flaud, J. -M., Gamache, R. R., Goldman, A., Goorvitch, D., Hawkins, R. L., Schroeder, J., Selby, J., E. A., and Wattson, R. B., 2000, HITEMP, the High-Temperature Molecular Spectroscopic Database, available through http://www.hitran.com
[23] Bharadwaj, S. P., 2000, "Medium Resolution Transmission Measurements of CO$_2$ at High Temperature," Master's thesis, The Pennsylvania State University, Department of Mechanical Engineering, University Park, PA.
[24] Bharadwaj, S. P., 2005, "Medium Resolution Transmission Measurements of CO$_2$ and H$_2$O at High Temperature and a Multiscale Malkmus model for Treatment of Inhomogeneous Gas Paths," PhD thesis, The Pennsylvania State University, Department of Mechanical Engineering, University Park, PA.
[25] Private communication, 2005, Mattson Instruments, now Thermo Nicolet Corporation.

Spectral-Directional Emittance of CuO at High Temperatures

Peter D. Jones[1]
e-mail: pjones@eng.auburn.edu

George Teodorescu

Ruel A. Overfelt

Department of Mechanical Engineering,
Auburn University,
Auburn, Alabama 36849

Spectral-directional emittance measurements for cupric oxide (CuO) are presented. The data cover polar angles of 0–84 deg from the surface normal, wavelengths between 1.5 and 8 μm, and temperatures between 400 and 700°C. The data were generated using a radiometric, direct emission measurement method. The oxide was grown on a very clean, smooth, and mirror-like copper surface, heated in air at 700°C until emission measurements became constant (270 h). X-ray diffraction and EDS analyses were performed to characterize the spatial and molecular composition of the copper oxide layer. It is generally found that CuO emittance decreases with increasing polar angle, increases with increasing wavelength, and increases with increasing temperature. Spectral-directional emittance values calculated from the Fresnel relations show good agreement with the measurements up to polar angles of 72 deg. [DOI: 10.1115/1.2165207]

Introduction

Thermal management of copper components in electrical machinery and integrated circuit systems requires knowledge of the radiative heat transfer properties of copper. More specifically, since copper oxidizes in air at elevated temperatures, long-term thermal management of an electrical or electronic device requires knowledge of the radiative properties of copper oxide. The asymptotic composition of copper oxide, when oxygen-annealed at 1 atm pressure and less than 1100°C, is cupric oxide, CuO. CuO films have utility as high temperature superconductors [1], suggesting another source of interest in the radiative properties of CuO.

The radiative properties of CuO have been addressed in a number of works [2–5]. Features considered in these earlier studies that impact thermal management are: temperature of the oxide, the thickness of the oxide, the CuO concentration in the oxide and the wavelength range over which radiative properties are obtained. Drobny and Pulfrey [2] report on CuO produced by reactive sputtering in an oxygen/argon mixture. The complex index of refraction was calculated from reflectance and transmittance measurements over the mainly visible range of 0.4–0.8 μm for CuO thickness of 225 Å at room temperature. Wieder and Czanderna [3] present similar measurements for a film thickness of 880 Å, grown in air, as do Karlsson et al. [4]. These results are all in qualitative agreement, though there is significant quantitative deviation between them. Jones et al. [5] present the spectral-directional emittance of copper oxide from emission measurements at higher temperatures (399–697°C) and wavelengths (1.5–10 μm) that are of interest in radiative heat transfer studies. The real part of refractive index was reduced. However, x-ray diffraction studies of the samples in Ref. [5] indicated the presence of cupric oxide, CuO and cuprous oxide, Cu$_2$O. Some anomalous data were reported.

The objective of the present work is to refine and expand the CuO radiative properties addressed in Ref. [5]. Greater care is taken in sample preparation and composition assessment, and both the real and imaginary parts of the refractive index are determined from emittance measurements.

Oxidation of Copper

Copper forms only two oxides which are thermodynamically stable, CuO—cupric oxide and Cu$_2$O—cuprous oxide. For oxidation temperatures of about 700°C in an O$_2$ atmosphere of less than 1 atm pressure, those stable phases are indicated by a pressure-temperature diagram, Fig. 1 (from Ref. [6]). Due to higher oxygen partial pressure on the surface, the CuO—cupric oxide phase is expected to be the outer layer and Cu$_2$O—cuprous oxide is expected to be next to the copper substrate.

Oxidation of copper at high temperatures was studied by Paidassi [7], Lahiri, et al. [8], and Yongfu et al. [9], and the presence of the two distinct layers was identified in each of these by x-ray diffraction and/or SEM/EDX.

Experimental Apparatus

CuO was grown on copper plates mounted on a temperature controlled heater block. An apparatus for measurement of radiation intensity was used to determine the spectral-directional emittance of the copper oxide layer. The apparatus is described more fully in Ref. [5]. Radiative flux is measured within a finite solid angle (Fig. 2) of 0.02 sr (maximum polar variation of 9 deg). Radiation leaving the sample (2) is reflected from an off-axis parabolic gold-coated mirror (4) into a collimated beam. The collimated beam is then trimmed by a beam trimming plate (5), which has an aperture of 19 mm diameter. The 19 mm beam is chopped (6) in order to help distinguish the intensity signal from background noise. The modulated beam is passed through a set of optical filters (7) to attenuate over and undertones and is refocused by a second off-axis parabolic mirror (8) into a 1/8 grating monochromator (9) in order to achieve spectral discrimination.

The output of the monochromator, which represents the radiative flux within a certain bandwidth, is focused onto a pyroelectric detector head (10). The signal of the pyroelectric detector is amplified and read by a radiometer. The radiometer reading is calibrated using a blackbody (massive radiating cavity) controlled to the same temperature as the sample. The first mirror used in the optical path can be rotated using a rotation mechanism (11) and the sample and heater block assembly can be set in different positions on its rack (1). This allows the surface of the sample to be viewed from different angles between normal and 84 deg from the normal.

A sample of pure copper plate (99.9%), 75 × 75 × 6 mm thick, polished smooth to a mirror-like surface, was used in the experiment. The plate was held at high temperature for an extended period to oxidize, and then radiative emittance was measured.

Fig. 3   Micrograph of copper oxide removed from copper substrate

After cooling the sample, it was seen that the copper oxide is comprised of two distinct layers. Figure 3 shows the copper oxide micrograph removed from the copper substrate. The presence of the outer CuO layer can be seen on the left side and the Cu_2O on the right side. Also, a porous region is apparent between the copper oxide layers. X-ray diffraction analysis performed on both layers shows that the upper layer is cupric oxide (CuO), for which all the peaks were identified, and the lower layer is cuprous oxide (Cu_2O). Later EDS analyses of these layers indicate that the outer layer has an O/Cu atomic concentration ratio of approximately $r=1$, whereas the ratio of the second layer was $r=1/2$. The CuO grown layer was uncontaminated and optically smooth, with a nominal surface roughness of 0.832 μm.

Comparison of the x-ray diffraction and EDS results suggests that the ratios $r=1$ and $r=1/2$ are associated with CuO and Cu_2O phases. The thicknesses of both oxides were determined from micrograph pictures to be about 106 μm for CuO and 209 μm for Cu_2O.

Fig. 2   Experimental setup

Emittance Measurements

Copper plates were held at 700°C for oxidation. The change in normal emittance was monitored as the oxide grew. Stable normal emittance was achieved after 270 h of continuous heating. Surface temperature was measured using a thermocouple embedded through the heater block and extended into the copper plate to a point just beneath its radiating surface and a heat flux based extrapolation from there to the actual surface is performed. Radiation measurement series were taken at 700°C (maximum operating temperature for copper components) and then decreased in 100°C increments to 400°C (minimum operating temperature for emitted flux measurement using the present apparatus). Measurements of surface emittance were performed at different wavelengths by adjusting the grating angles in the monochromator and the exclusion range of the filters. Measurements at different angles to the surface normal were achieved by adjusting both the parabolic collecting mirror and the sample holder position on the slotted arc rack. A radiating cavity blackbody source, kept at the same temperature as the sample surface temperature, is used for online calibration of the intensity measurement system. The 63.5-mm-diam blackbody cavity is machined into 152-mm-diam copper stock and has a covering aperture plate with a 9.5-mm-diam aperture and a 15 deg emission cone. The blackbody wall temperature is controlled by a PID temperature controller to the same temperature as the oxidizing plate. The blackbody is insulated with 76-mm-thick ceramic wool blanket. Ten complete calibration spectra measurements of intensity performed on the blackbody indicate a standard deviation of less than 1% from the mean for all considered temperatures and wavelengths of interest. Measurements performed on the sample surface were compared with the calibration measurements to determine the sample surface emittance. A calibration factor C for the intensity measurement system is determined according to

$$C(\lambda, T_c) = \frac{1}{R_c(\lambda, T_c)} \left[\int_{\lambda - \delta\lambda/2}^{\lambda + \delta\lambda/2} I_{\lambda b}(T_c) d\lambda \right] \delta\Omega \quad (1)$$

where R_c is the radiometer measurement taken with the blackbody source set at temperature T_c, λ is the wavelength setup, $\delta\lambda$ is the wavelength measurement interval about wavelength λ, $I_{\lambda b}$ is the blackbody intensity, θ is the polar angle relative to the surface normal, and $\delta\Omega$ is the finite measurement solid angle. The spectral-directional emittance ε is determined by

$$\varepsilon_{\lambda,\theta}(T_s) = \frac{R_\varepsilon(\lambda,\theta,T_s) * C(\lambda,T_s)}{\left[\int_{\lambda-\delta\lambda/2}^{\lambda+\delta\lambda/2} I_{\lambda b}(T_s)d\lambda\right]\delta\Omega} \qquad (2)$$

where R_ε is the sample surface radiometer measurement and T_s is the sample surface temperature. The measurement solid angle $\delta\Omega$ about θ and the wavelength band measurement are kept the same between the radiometer measurement using blackbody source R_c and from the sample surface R_ε. Therefore, the data reduction system of the above equations is simplified to the ratio of R_ε to R_c as long as T_s and T_c are equal. The intensity emitted from cupric oxide surface at considered temperatures is assumed to be unpolarized. However the sample was rotated and no bias was found due to orientation.

The uncertainty of the spectral-directional emittance may be derived by combining the above equations as

$$u_\varepsilon^2 = \left(\frac{\delta\varepsilon}{\delta R_\varepsilon} * u_{R_\varepsilon}\right)^2 + \left(\frac{\delta\varepsilon}{\delta R_C} * u_{R_C}\right)^2 + \left(\frac{\delta\varepsilon}{\delta T_C} * u_{T_C}\right)^2 + \left(\frac{\delta\varepsilon}{\delta T_S} * u_{T_S}\right)^2 \qquad (3)$$

where the uncertainties are denoted by u and their subscripts, and $\delta\Omega$ and $\delta\lambda$ are considered to be perfectly repeatable. Further, considering that $T_c \approx T_s$, and $I_{\lambda b}(T_c) \approx I_{\lambda b}(T_s)$, the uncertainty may be reduced to

$$u_\varepsilon^2 = (1 + \varepsilon^2)\left[t_{9,95} * \left(\frac{S_{R_C}}{R_C}\right)\right]^2 + \left(\frac{4\varepsilon}{T_S}\right)^2 * (u_{T_C}^2 + u_{T_S}^2) \qquad (4)$$

for ten complete calibration spectra and a 95% confidence interval, where S is the sample standard deviation and t is a t-test distribution parameter. For the data presented it may be shown that the uncertainty of the emittance is dominated by the uncertainty of the radiometer measurement. Other sources of uncertainty are relatively insignificant. The uncertainty in spectral-directional emittance was found to be approximately 1% of the emittance value. Spectral-directional emittance reduced data for CuO are shown in Table 1 for surface temperatures of 400, 500, 600, and 700°C. Due to low emissive power, for 400°C and the wavelength of 1.5 μm the measurements could not be performed. Since the sample surface temperature cannot be known until the oxide thickness is accurately known, an identical sample was heated in the same conditions and for the same period of time, and upon cooling the oxide thickness was measured. Then the temperature of the sample surface was calculated from

$$\frac{T_{th} - T_s}{(t/k)_{Cu} + (t/k)_{CuO}} = Nu\frac{4k_a}{a}(T_s - T_a) + \varepsilon\sigma_b(T_s^4 - T_\infty^4) \qquad (5)$$

The Nusselt number corresponds to a hot, horizontal square surface facing up [10]

$$Nu = 0.54\left[\frac{ga^3}{1/2(T_s + T_a)\nu_a\alpha_a}(T_s - T_a)\right]^{1/4} \qquad (6)$$

where t, k and their subscripts denote the material thickness (m) and thermal conductivity (W/m K), T_{th} and T_s are the temperature measured by the near-surface thermocouple and sample surface temperature, a is the side dimension of the square sample (m), T_a, T_∞ are the temperature of the air over the sample surface (K) and surroundings visible to sample surface, and ν_a α_a are the kinematic viscosity of air over the sample surface (m²/s) and the thermal diffusivity of air (m²/s). All the thermophysical properties above were taken from data of Refs. [1,10], and a, t_{Cu} were measured. T_a, T_∞ were taken to be equal and T_{th} is recorded from each experiment setup. Upon cooling the sample, the oxide flakes off and t_{CuO} was measured. In practice, T_s was determined to be 1–3°C lower than T_{th}. This analysis allows the corresponding setup temperature T_{th} (the temperature measured by the thermocouple just beneath the copper surface) to be specified in order to

obtain a desired surface temperature. Using the Fresnel relations [11]

$$\varepsilon_{\lambda,\theta} = 1 - \frac{1}{2}\left(\frac{(n_\lambda\beta - \cos\theta)^2 + (n_\lambda^2 + k_\lambda^2)\alpha - n_\lambda^2\beta^2}{(n_\lambda\beta + \cos\theta)^2 + (n_\lambda^2 + k_\lambda^2)\alpha - n_\lambda^2\beta^2}\right.$$
$$\left. + \frac{(n_\lambda\gamma - \alpha/\cos\theta)^2 + (n_\lambda^2 + k_\lambda^2)\alpha - n_\lambda^2\gamma^2}{(n_\lambda\gamma + \alpha/\cos\theta)^2 + (n_\lambda^2 + k_\lambda^2)\alpha - n_\lambda^2\gamma^2}\right) \qquad (7)$$

where, $\quad \alpha^2 = \left(1 + \frac{\sin^2\theta}{n_\lambda^2 + k_\lambda^2}\right)^2 - \frac{4n_\lambda^2}{n_\lambda^2 + k_\lambda^2}\left(\frac{\sin^2\theta}{n_\lambda^2 + k_\lambda^2}\right) \qquad (8)$

$$\beta^2 = \frac{n_\lambda^2 + k_\lambda^2}{2n_\lambda^2}\left(\frac{n_\lambda^2 - k_\lambda^2}{n_\lambda^2 + k_\lambda^2} - \frac{\sin^2\theta}{n_\lambda^2 + k_\lambda^2} + \alpha\right) \qquad (9)$$

$$\gamma = \frac{n_\lambda^2 - k_\lambda^2}{n_\lambda^2 + k_\lambda^2}\beta + \frac{2n_\lambda k_\lambda}{n_\lambda^2 + k_\lambda^2}\left(\frac{n_\lambda^2 + k_\lambda^2}{n_\lambda^2}\alpha - \beta^2\right)^{1/2} \qquad (10)$$

the complex index of refraction was computed using the full data set that includes spectral as well as directional data. A curve fitting algorithm based on the secant iteration method which minimizes the deviation between the Fresnel relations and the present data was used to compute the complex index of refraction according to Ref. [5]. The spectral-hemispherical emittance determined by integrating the data over polar angle according to Ref. [5] and the complex index of refraction are presented in Table 2.

The optical thickness of CuO was approximated for all considered temperatures neglecting the scattering coefficient according to Ref. [11] and it is shown in Fig. 4. The optical thickness was found to decrease with increasing wavelength from 1.5 to 8 μm and a sudden drop was observed in spectral range between 3 and 4.5 μm. The influence of temperature on optical thickness is generally not significant excepting the spectral range from 3 to 5.5 μm where decreases with increasing temperature. The 106 μm CuO layer was found to be optically thick for all considered wavelengths and temperatures.

Figure 5 shows the emittance data of CuO as a function of direction (polar plot) at various wavelengths between 2 and 8 μm and a temperature of 700°C. From the polar plot it may be seen that normal emittance increases with wavelength from 0.697 for $\lambda = 2$ μm to 0.9 for $\lambda = 8$ μm. Also, from the same plot, it can be
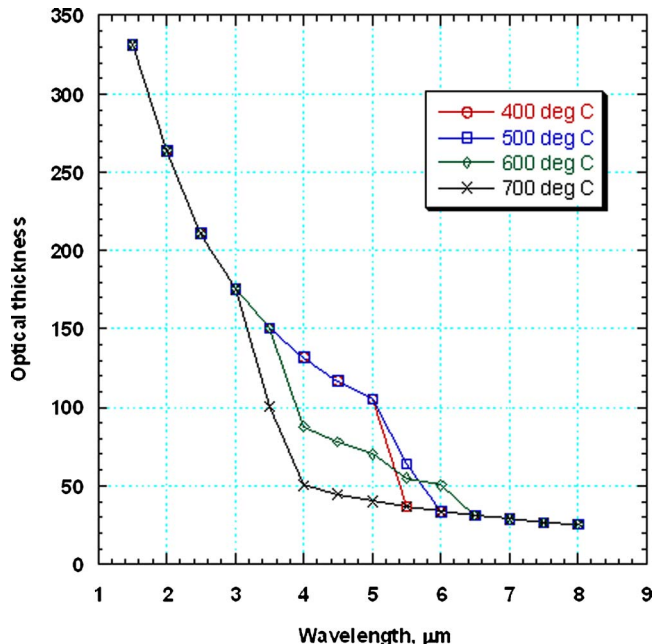

Fig. 4 Optical thickness of CuO versus wavelength

Table 1 Measured spectral-directional emittance of CuO at 400°C (first row), 500°C (second row), 600°C (third row), and 700°C (fourth row)

	Polar angle, deg								
λ, μm	0°	12°	24°	36°	48°	60°	72°	78°	84°
1.5	—	—	—	—	—	—	—	—	—
	0.520	0.515	0.519	0.515	0.506	0.515	0.524	0.381	0.242
	0.654	0.648	0.641	0.620	0.600	0.600	0.587	0.419	0.248
	0.658	0.650	0.642	0.636	0.626	0.601	0.582	0.413	0.267
2.0	0.532	0.525	0.521	0.510	0.515	0.525	0.538	0.413	0.368
	0.591	0.587	0.585	0.584	0.577	0.562	0.556	0.473	0.299
	0.681	0.677	0.667	0.658	0.636	0.628	0.595	0.471	0.280
	0.697	0.694	0.685	0.675	0.656	0.632	0.606	0.467	0.289
2.5	0.580	0.584	0.569	0.565	0.549	0.548	0.550	0.480	0.317
	0.639	0.637	0.633	0.629	0.621	0.609	0.583	0.529	0.342
	0.716	0.707	0.698	0.711	0.688	0.648	0.613	0.543	0.317
	0.738	0.733	0.734	0.727	0.719	0.682	0.628	0.542	0.389
3.0	0.629	0.628	0.621	0.614	0.595	0.590	0.572	0.534	0.354
	0.684	0.680	0.672	0.668	0.664	0.652	0.593	0.575	0.371
	0.749	0.742	0.729	0.745	0.722	0.687	0.632	0.592	0.347
	0.772	0.768	0.768	0.759	0.749	0.719	0.664	0.589	0.412
3.5	0.680	0.679	0.673	0.666	0.649	0.644	0.622	0.581	0.320
	0.720	0.719	0.714	0.708	0.705	0.691	0.631	0.614	0.324
	0.770	0.763	0.753	0.748	0.740	0.725	0.666	0.624	0.280
	0.796	0.790	0.787	0.784	0.771	0.743	0.702	0.617	0.324
4.0	0.714	0.714	0.707	0.698	0.683	0.679	0.635	0.622	0.338
	0.745	0.742	0.738	0.735	0.729	0.715	0.660	0.645	0.335
	0.782	0.773	0.765	0.761	0.760	0.738	0.684	0.642	0.289
	0.798	0.791	0.791	0.789	0.775	0.749	0.716	0.626	0.348
4.5	0.736	0.733	0.728	0.720	0.706	0.701	0.683	0.648	0.344
	0.755	0.753	0.749	0.746	0.741	0.727	0.675	0.663	0.333
	0.787	0.777	0.769	0.773	0.772	0.744	0.690	0.653	0.278
	0.805	0.805	0.797	0.791	0.787	0.755	0.721	0.631	0.347
5.0	0.764	0.759	0.753	0.748	0.733	0.728	0.713	0.682	0.355
	0.775	0.773	0.769	0.765	0.760	0.747	0.701	0.675	0.341
	0.805	0.794	0.786	0.780	0.789	0.765	0.717	0.685	0.276
	0.818	0.813	0.811	0.808	0.797	0.767	0.728	0.668	0.353
5.5	0.777	0.774	0.767	0.764	0.747	0.743	0.726	0.705	0.355
	0.794	0.790	0.787	0.785	0.783	0.768	0.726	0.710	0.345
	0.821	0.811	0.806	0.809	0.808	0.789	0.744	0.716	0.275
	0.838	0.834	0.832	0.828	0.822	0.788	0.753	0.701	0.299
6.0	0.796	0.800	0.797	0.788	0.777	0.770	0.739	0.724	0.519
	0.824	0.821	0.812	0.811	0.808	0.804	0.767	0.765	0.517
	0.847	0.845	0.833	0.838	0.839	0.818	0.768	0.741	0.480
	0.876	0.870	0.873	0.864	0.863	0.835	0.777	0.762	0.479
6.5	0.810	0.806	0.803	0.798	0.787	0.776	0.746	0.738	0.511
	0.836	0.834	0.827	0.824	0.820	0.818	0.770	0.742	0.499
	0.860	0.850	0.844	0.846	0.841	0.821	0.775	0.756	0.491
	0.887	0.884	0.885	0.876	0.875	0.843	0.788	0.780	0.516
7.0	0.814	0.810	0.806	0.806	0.794	0.785	0.752	0.740	0.508
	0.839	0.835	0.827	0.825	0.824	0.819	0.775	0.750	0.510
	0.862	0.850	0.847	0.844	0.846	0.827	0.775	0.772	0.501
	0.889	0.885	0.887	0.881	0.875	0.847	0.792	0.790	0.518
7.5	0.825	0.820	0.815	0.816	0.805	0.796	0.755	0.748	0.516
	0.848	0.845	0.837	0.832	0.829	0.826	0.771	0.755	0.501
	0.870	0.855	0.854	0.852	0.852	0.835	0.780	0.770	0.518
	0.891	0.890	0.891	0.889	0.881	0.853	0.797	0.790	0.516
8.0	0.838	0.832	0.824	0.830	0.819	0.808	0.761	0.760	0.506
	0.858	0.856	0.853	0.846	0.840	0.839	0.775	0.758	0.508
	0.884	0.868	0.867	0.868	0.855	0.843	0.783	0.784	0.516
	0.900	0.898	0.899	0.898	0.892	0.860	0.804	0.795	0.526

seen the emittance increases with wavelength for all directions and there is a significant drop of emittance beyond 72 deg.

The real part of the refractive index of CuO, Fig. 6, is seen to decrease with increasing temperature and wavelength and the imaginary part, Fig. 7, is seen to be very low and constant for short wavelengths ($2 \leq \lambda \leq 4.5 \ \mu$m), decreases steeply for intermediate wavelengths ($4.5 \leq \lambda \leq 6 \ \mu$m), and is constant (0.001) for long wavelengths ($6 \leq \lambda \leq 8 \ \mu$m).

The ratio of hemispherical to normal emissivity was calculated for all considered temperatures and compared with the ratio of hemispherical to normal emissivity given by Jakob. The mean difference found between Jakob reported correction factor and our calculated ratio was 5.0% with a standard deviation of 2.2%.

Discussion

Spectral-normal emittance was computed from the refractive index of CuO reported by Drobny and Pulfrey [2], by Wieder and Czanderna [3], and Karlsson et al. [4]. All of the above, together with the spectral-normal emittance reported by Jones et al. [5] and the present work data, are shown in Fig. 8.

Even though the data from Refs. [2–4] are in the same spectral region (visible) there is not a good agreement among them. Further, the spectral-normal emittance from Ref. [3] is seen to increase between 0.4 and 0.983 over the same spectral region rather than decrease as seen in Refs. [2,4]. The measurements of Refs. [2–4] were performed at room temperature, the oxide thicknesses

Table 2 Spectral-hemispherical emittance and complex refractive index of CuO at considered temperatures

	400°C			500°C			600°C			700°C		
λ, μm	ε_λ	n_λ	k_λ	ε_λ	n_λ	k_λ	ε_λ	n_λ	k_λ	ε_λ	n_λ	k_λ
1.5	—	—	—	0.417	5.625	0.099	0.557	3.988	0.099	0.564	3.977	0.099
2.0	0.494	5.705	0.099	0.535	4.649	0.099	0.588	3.726	0.099	0.600	3.555	0.099
2.5	0.527	4.896	0.099	0.577	4.072	0.099	0.627	3.357	0.099	0.655	3.135	0.099
3.0	0.571	4.203	0.099	0.617	3.677	0.099	0.661	3.061	0.099	0.689	2.854	0.099
3.5	0.613	3.668	0.099	0.647	3.294	0.099	0.674	2.970	0.099	0.702	2.710	0.007
4.0	0.643	3.356	0.099	0.672	3.091	0.099	0.688	2.857	0.040	0.709	2.681	0.007
4.5	0.667	3.175	0.091	0.682	3.002	0.099	0.694	2.789	0.009	0.720	2.636	0.003
5.0	0.693	2.973	0.006	0.701	2.819	0.012	0.711	2.635	0.006	0.729	2.534	0.002
5.5	0.706	2.849	0.006	0.721	2.670	0.007	0.731	2.475	0.001	0.744	2.375	0.001
6.0	0.746	2.636	0.001	0.764	2.466	0.001	0.779	2.285	0.001	0.800	2.087	0.001
6.5	0.753	2.574	0.001	0.773	2.375	0.001	0.787	2.229	0.001	0.815	2.013	0.001
7.0	0.757	2.545	0.001	0.777	2.354	0.001	0.792	2.192	0.001	0.821	1.999	0.001
7.5	0.766	2.474	0.001	0.783	2.290	0.001	0.798	2.149	0.001	0.822	1.971	0.001
8.0	0.775	2.379	0.001	0.793	2.223	0.001	0.808	2.114	0.001	0.830	1.910	0.001
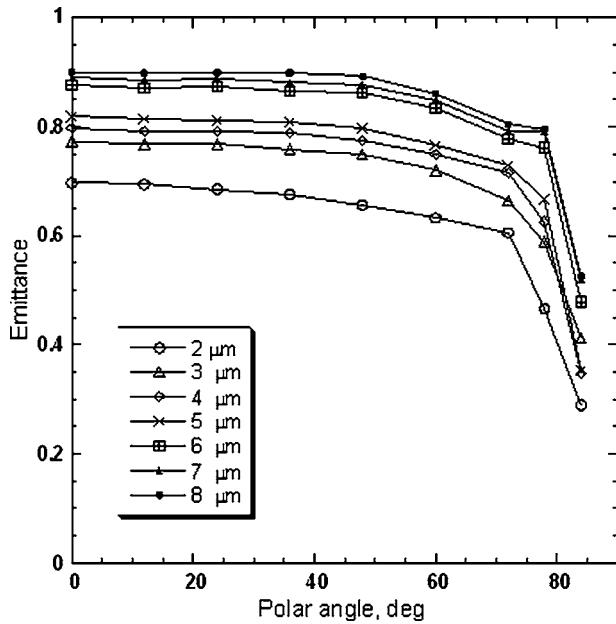
Fig. 5 Spectral-directional emittance of CuO at 700°C
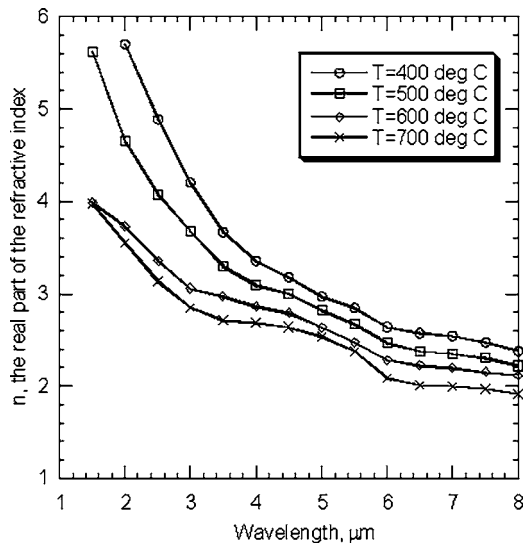
were 2.25 μm [2], 0.088 μm [3], and 0.08 μm [4] respectively, and the spectral range was beneath that of the present data. Jones et al. [5] performed spectral-directional emittance measurements of oxidized copper, but failed to ensure that the top layer of oxidized copper was pure CuO. The temperatures considered differ from the present work just by a few degrees Celsius and the spectral range is even wider than that of the present work. Generally, the spectral-normal emittance is seen to increase with wavelength and temperature for the spectral range considered in Ref. [5] and in present work. The values of spectral-normal emittance from the present work are slightly higher than those of Ref. [5] for short wavelengths ($2 \leq \lambda \leq 6$ μm), and very close at long wavelengths. We believe that the difference comes from the composition of copper oxide which in Ref. [5] showed the presence of Cu_2O. Furthermore, the anomalous points (decrease of normal emittance) between 6 and 7 μm which appear in Ref. [5] were not seen in the present work.

Figure 9 shows a comparison between spectral-directional emittance of CuO from the present work at 700°C and the spectral-directional emittance of oxidized copper comprised mostly of CuO from Ref. [5] at 697°C for wavelengths of 3.5 and 7 μm. From Fig. 9 it may be seen that the spectral-directional emittance of CuO from the present work is less directional than that from

Fig. 6 Spectral real part of the refractive index at considered temperatures
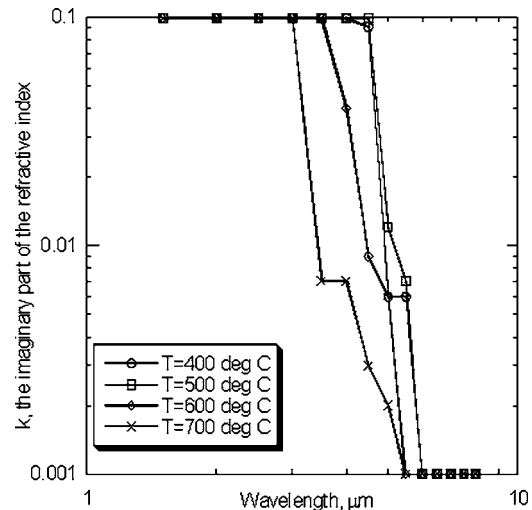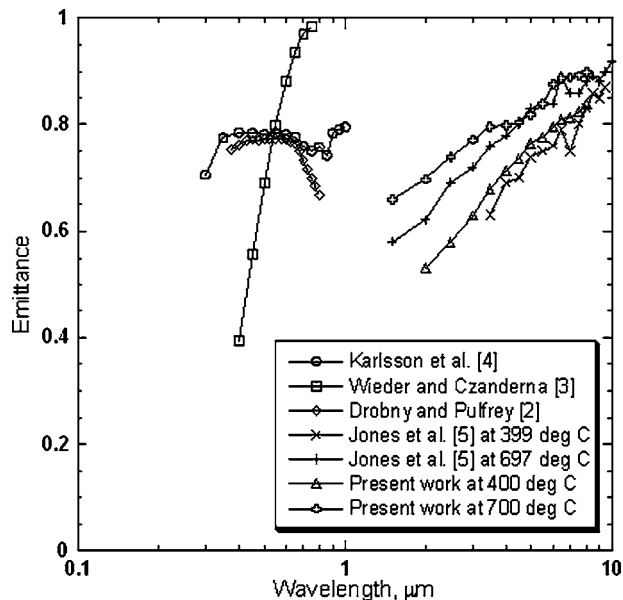

Fig. 7 Spectral imaginary part of the refractive index at considered temperatures

Fig. 8 Spectral normal emittance of CuO as a function of wavelength

Fig. 9 Spectral-directional emittance of CuO at 700°C from present work and oxidized copper at 697°C from Ref. [5]
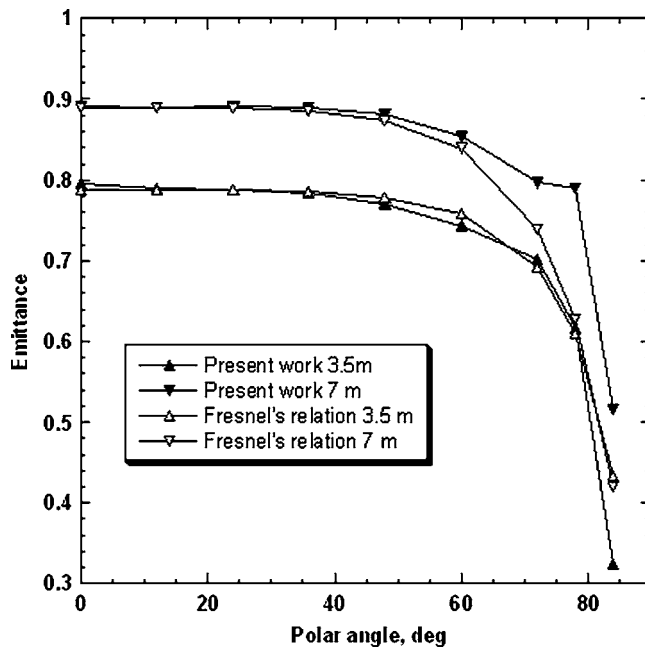
Fig. 10 Spectral-directional emittance of CuO from present work and from electromagnetic theory for 3.5 and 7.5 μm

Ref. [5], which suggests that CuO behaves as a dielectric material. In both the present work and in Ref. [5], emittance is shown to slowly decrease as the polar angle goes from the surface normal to 65 deg, and to decrease rapidly from 65 deg to grazing.

Figure 10 represents spectral-directional emittance of CuO both as measured in the present work and as derived from the general Fresnel relations using the experimentally derived, best-fit complex index of refraction.

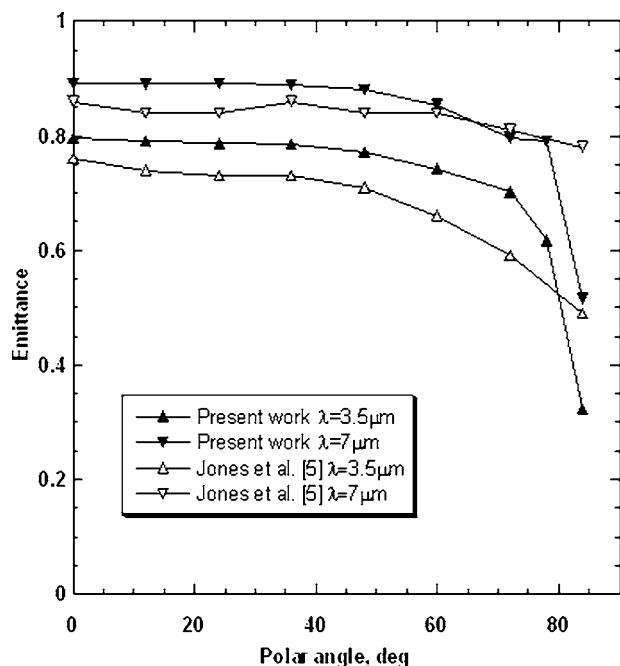The error between the Fresnel relations and the experimental data is no greater than 8% for all angles from normal to 72 deg, and has a variance of 2.5%. Greater errors are obtained for longer wavelengths and angles near grazing, indicating a possible effect of surface roughness.

Conclusions

The spectral-directional emittance of cupric oxide (CuO) with a thickness of 106 μm, grown by oxidizing pure copper plate at elevated temperatures, is determined from measurements of radiative intensity leaving the surface. The layer of copper oxide is grown by heating the pure sample of copper at high temperature until the emissive power detected reaches an asymptotic level. The micrograph picture of the copper oxide shows two distinct layers separated by pores. X-ray diffraction and EDS analyses performed on the outer oxide layer proved the presence of cupric oxide (CuO) as expected, and the presence of cuprous oxide (Cu_2O) on the interior layer. The spectral-normal emittance of CuO is seen to increase with both temperature (400–700°C) and wavelength ($1.5 \leq \lambda \leq 8$ μm). The cupric oxide (CuO) is seen to exhibit a directional variation of emittance for the range of wavelengths considered here which is in good agreement with theoretical predictions for dielectrics. The complex index of refraction is reduced from spectral-directional emittance data. A good agreement is found between the Fresnel relations and the complex index of refraction reduced from spectral-directional emittance measurements.

Acknowledgment

Nomenclature

a = square sample side dimension, m
C = radiometer calibration factor
g = acceleration of gravity
$I_{\lambda b}$ = spectral blackbody intensity, W/(m^2 μm sr)
k = thermal conductivity, W/m K

k_λ = spectral imaginary part of the refractive index
Nu = Nusselt number
n_λ = spectral real part of the refractive index
R = radiometer reading
S = standard deviation of sample
t = sample thickness, m
$t_{9,95}$ = t-test distribution parameter with 9 degrees of freedom and 95% confidence interval = 1.834
T = temperature, K
u = uncertainty
α = thermal diffusivity, m^2/s
$\delta\Omega$ = optical solid angle, sr
$\delta\lambda$ = monochromat or wavelength interval, μm
ε = emittance
n = kinematic viscosity, m^2/s
σ_b = Stefan Boltzmann constant

Subscripts

a = air over the article surface
Cu = copper
CuO = copper oxide
s = sample surface
th = sample subsurface
∞ = surroundings visible to sample surface

References

[1] Touloukian, Y. S., and DeWitt, D. P., 1972, *Thermophysical Properties of Matter*, IFI/Plenum, New York.

[2] Drobny, V. F., and Pulfrey, D. L., 1979, "Properties of Reactively-Sputtered Copper Oxide Thin Films," Thin Solid Films, **61**, pp. 89–98.

[3] Wieder, H., and Czanderna, A. W., 1966, "Optical Properties of Copper Oxide Films," J. Appl. Phys., **37**(1), pp. 184–187.

[4] Karlsson, B., Ribbing, C. G., Roos, A., Valkonen, E., and Karlsson, T., 1982, "Optical Properties of Some Metal Oxides in Solar Absorbers," Phys. Scr., **25**(6), pp. 111–119.

[5] Jones, P. D., Dorai-Raj, D. E., and McLeod, D. G., 1996, "Spectral-Directional Emittance of Oxidized Copper," J. Thermophys. Heat Transfer, **10**(2), pp. 343–349.

[6] Jian, L., Vizkelethy, G., Revesz, P., and Mayer, J. W., 1991, "Oxidation and Reduction of Copper Oxide Thin Films," J. Appl. Phys., **69**(2), pp. 1020–1029.

[7] Paidassi, J., 1958, "Oxidation of Copper at 600–1000°C," Acta Metall., **6**, pp. 216–219.

[8] Lahiri, S. K., Waalib Singh, N K. Heng, K. W., Ang, L., and Goh, L. C., 1998, "Kinetics of Oxidation of Copper Alloy Leadframes," Microelectron. J., **29**, pp. 335–341.

[9] Yongfu, Z., Mimura, K., Ishikawa, Y., and Isshiki, M., 2001, "High Temperature Oxidation of High Purity Copper," J. Jpn. Copper Brass Res. Assoc., **40**, pp. 96–100.

[10] Incropera, F. P., and DeWitt, D. P., 2002, *Fundamentals of Heat and Mass Transfer*, 5th ed., Wiley, New York.

[11] Siegel, R., and Howell, J., 2002, *Thermal Radiation Heat Transfer*, 4th ed., Taylor&Francis, New York.

Stabilization of Flow Boiling in Microchannels Using Pressure Drop Elements and Fabricated Nucleation Sites

Satish G. Kandlikar[1]
Fellow ASME
e-mail: sgkeme@rit.edu

Wai Keat Kuan
e-mail: wxk0320@rit.edu

Daniel A. Willistein
e-mail: daw7820@rit.edu

John Borrelli
e-mail: jxb9224@rit.edu

Thermal Analysis and Microfluidics Laboratory,
Mechanical Engineering Department,
Rochester Institute of Technology,
Rochester, New York, 14623

The flow boiling process suffers from severe instabilities induced due to nucleation of vapor bubbles in a superheated liquid environment in a minichannel or a microchannel. In an effort to improve the flow boiling stability, several modifications are introduced and experiments are performed on $1054 \times 197~\mu m$ parallel rectangular microchannels (hydraulic diameter of 332 μm) with water as the working fluid. The cavity sizes and local liquid and wall conditions required at the onset of nucleation are analyzed. The effects of an inlet pressure restrictor and fabricated nucleation sites are evaluated as a means of stabilizing the flow boiling process and avoiding the backflow phenomenon. The results are compared with the unrestricted flow configurations in smooth channels.
[DOI: 10.1115/1.2165208]

Introduction

Presently, many advanced technologies, such as high speed processor chips and electronics components in high power lasers, have the requirement to dissipate increasingly high heat fluxes while maintaining specified surface temperatures. For heat fluxes above 1 MW/m^2 (100 W/cm^2), alternatives to the air cooling option are needed. Single-phase liquid cooling and flow boiling options are being considered in these high heat flux ranges. The flow boiling option has the advantage of a lower mass flow rate due to utilization of latent heat of vaporization. It can also be directly coupled with a refrigeration system to provide a lower coolant temperature.

There are, however, complexities associated with vaporization in multiple narrow channel arrays that are not completely understood. The phenomenon characterized by vapor expansion in both the upstream and downstream directions causing flow reversal was observed by Kandlikar et al. [1] and also by Kandlikar and Balasubramanian [2]. Both employed a high-speed digital video camera to observe this behavior in minichannels and microchannels. Similar instabilities were observed by Hetsroni et al. [3] and Peles [4], among other investigators.

This paper addresses two methods to suppress the instabilities during flow boiling in a set of six $1054 \times 197~\mu m$ parallel channels. Inlet area restriction and artificial nucleation sites are studied alone and in conjunction with each other. Flow instabilities are characterized by visual observations and the pressure fluctuations measured between the inlet and outlet manifolds.

For the present study, channel size is classified by the smallest channel dimension D according to the following modified list, originally proposed by Kandlikar and Grande [5]:

Conventional channels: $D > 3$ mm
Minichannels: $3~\text{mm} \geq D > 200~\mu m$

Microchannels: $200~\mu m \geq D > 10~\mu m$
Transitional channels: $10~\mu m \geq D > 0.1~\mu m$

    Transitional microchannels: $10~\mu m \geq D > 1~\mu m$
    Transitional nanochannels: $1~\mu m \geq D > 0.1~\mu m$

Molecular channels: $0.1~\mu m \geq D$

where D is the minimum channel dimension.

According to this convention, the channels used in this study with a gap size of 197 μm can be considered as microchannels, although they could be referred to as minichannels because of the closeness to the boundary of 200 μm.

Because of the rapid bubble growth accompanied by the fluctuations in pressure drop, two phase flow boiling in minichannels and microchannels introduces instabilities. This condition has adverse effects on the heat transfer performance. Presently, the local reversed flow phenomenon is not well understood and not well studied, and few attempts have been reported to control it. The onset of boiling and the subsequent two-phase flow interactions are greatly dependent on the channel surface temperature, local liquid temperature, local heat transfer coefficient prior to nucleation, and availability of nucleation cavities. Uneven flow and pressure fluctuations lead to flow reversal, which may introduce vapor back into the inlet manifold and exacerbate the instability generated in the channels. When a large vapor bubble passes through a channel, the transient heat conduction and interface evaporation enhance heat transfer in the channel and reduce the local channel surface temperatures. Cho et al. [6] reported that modifying the channels with a cross-linked pattern improves the flow distribution and reduces the range of temperatures seen in microchannels with uneven heating. Very few researchers have tried to prevent the flow reversal phenomenon in microchannels.

The basic issues related to the instabilities associated with flow boiling in microchannels were presented by Kandlikar [7]. One of the major results of the instabilities is the severe reduction in the critical heat flux. A detailed survey of this effect was presented by Bergles and Kandlikar [8]. The available experimental data on the CHF by Jiang et al. [9], Bowers and Mudawar [10], Qu and Mudawar [11] indicate the severe reduction in CHF due to the associated instabilities. It may be noted that the CHF values re-
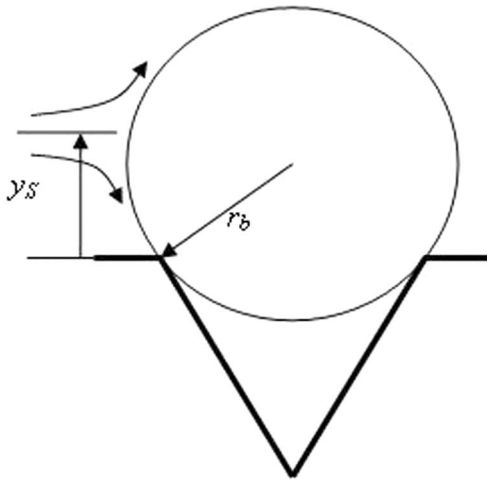
Fig. 1 Location of the stagnation point over a nucleating bubble, Kandlikar et al. [18]

Fig. 2 Comparison of experimental data with different nucleation criteria (representing the lowest wall superheat at which a cavity will nucleate), Kandlikar et al. [18]

ported in the microchannel geometries are in some cases lower than even the pool boiling CHF values for water at the same pressure. Addressing flow reversal is expected to improve the heat transfer performance. Further research into the understanding and modeling of this behavior is needed. The objective of the present work is to address the basic causes of instabilities and to study the effects of pressure drop elements and fabricated nucleation sites on the flow reversal phenomenon and the corresponding heat transfer performance of the microchannels.

Nucleation in Microchannel and Minichannel Geometries

The heat transfer mechanisms during flow boiling in microchannels and minichannels were analyzed by Kandlikar [12]. The instability resulting from the rapid expansion of a nucleating bubble was seen as one of the main reasons for instability. Under unstable conditions, bubbles nucleate in the flow and cause severe flow fluctuations as they grow rapidly in both forward and backward directions to the main flow direction. On the other hand, under stable boiling conditions, inception of the first nucleating bubble on the wall followed by its steady growth in the flow direction is desired. Under such stable operation, the conditions at the onset of nucleation and bubble growth in the flow direction become relevant.

A number of researchers proposed the nucleation criteria for the onset of nucleation during flow boiling. Hsu and Graham [13], Hsu [14], Bergles and Rohsenow [15], Sato and Matsumura [16], and Davis and Anderson [17] provided the underlying theory relating the temperature distribution in the liquid prior to nucleation to the local nucleation condition. Comparing the liquid temperature on the vapor bubble interface at the farthest location from the wall with the saturation temperature inside the bubble of a certain critical size resulted in their nucleation criteria. At the inception of nucleation, Hsu and Graham [13] assumed a contact angle of 53.1 deg, Bergles and Rohsenow [15], and Sato and Matsumura [16] used a hemispherical bubble shape (90 deg contact angle), while Davis and Anderson [17] left the contact angle as a variable.

Kandlikar et al. [18] numerically modeled the flow over a bubble attached to a channel wall at a given contact angle and noted that a streamline corresponding to a stagnation point on the upstream interface of the bubble swept over the top of the bubble as shown in Fig. 1. The location of this stagnation point was found to be given by the following equation for a wide range of contact angles and flow Reynolds numbers

$$y_S = 1.10 r_b \qquad (1)$$

where y_S is the distance of the stagnation location from the heated wall, and r_b is the radius of the bubble at nucleation.

Using the liquid temperature at this location in deriving the nucleation criterion, they obtained the following equation for the range of active nucleation cavities

$$\{r_{c,\min}, r_{c,\max}\} = \frac{\delta_t \sin \theta_r}{2.2} \left(\frac{\Delta T_{Sat}}{\Delta T_{Sat} + \Delta T_{Sub}} \right)$$
$$\times \left[1 \mp \sqrt{1 - \frac{8.8 \sigma T_{Sat}(\Delta T_{Sat} + \Delta T_{Sub})}{\rho_V h_{LV} \delta_t \Delta T_{Sat}^2}} \right] \qquad (2)$$

where $r_{c,\min}$ and $r_{c,\max}$ are the minimum and maximum radii of the nucleating cavities, ΔT_{Sat} and ΔT_{Sub} are the wall superheat and liquid subcooling, θ_r is the receding contact angle, σ is the surface tension, h_{LV} is the latent heat of vaporization, ρ_V is the vapor density, and δ_t the thickness of the thermal boundary layer, $=k_L/h$, with k_L the liquid thermal conductivity and h the heat transfer coefficient in the liquid prior to nucleation. Note that there is a typographical error in the original publication by Kandlikar et al. [18], the correct constant is 8.8, as given in Eq. (2), whereas the constant was incorrectly typed as 9.2 in the original publication (although their results were plotted using the correct value).

Figure 2 compares different nucleation criteria with the experimental results obtained for subcooled water at atmospheric pressure and 80°C by Kandlikar et al. [18] in a 3 mm × 40 mm rectangular channel. Note that the nucleation criteria represent the lowest temperature at which a cavity of a given size will nucleate. These cavities will continue to nucleate at higher superheats as seen in Fig. 2. It should be noted that if the cavities of this radius are not available, the onset of nucleation will be delayed into the downstream part of the channel until the wall superheat condition at nucleation corresponding to the available cavity sizes is met. The results from Hsu [14] and Kandlikar et al. [18] models yield very similar results for this case, while Davis and Anderson's [17] criterion predicts somewhat higher wall superheat and Bergles and Rohsenow's [15] model predicts somewhat lower wall superheat as seen from Fig. 2.

Instabilities Due To Nucleation and Rapid Bubble Growth. The local liquid conditions play an important role in the stability of the flow boiling phenomenon at the onset of nucleation. Assuming nucleation cavities of appropriate sizes are available, the local wall superheat at the inception location is obtained by setting the term under the radical sign in Eq. (2) to zero
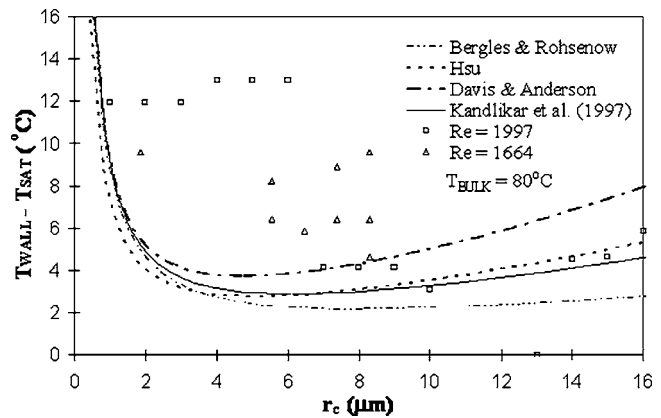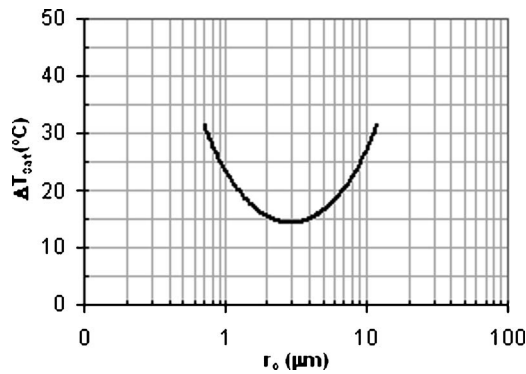
Fig. 3 Range of active cavities given by Eq. (2) for a given wall superheat, saturated water in 1054×197 μm channel, G =120 kg/m² s; q''=300 kW/m²

Fig. 5 Local wall and liquid temperatures corresponding to onset of nucleation over a given cavity radius, replotted data from Fig. 4, water in 1054×197 μm channel, G=120 kg/m² s; q''=300 kW/m²

$$\Delta T_{\mathrm{Sat,ONB}} = \sqrt{8.8\sigma T_{\mathrm{Sat}}q''/(\rho_V h_{\mathrm{LV}}k_L)} \qquad (3)$$

and the local liquid subcooling is obtained by using the single-phase heat transfer equation prior to nucleation

$$\Delta T_{\mathrm{Sub,ONB}} = \frac{q''}{h} - \Delta T_{\mathrm{Sat,ONB}} \qquad (4)$$

Figure 3 shows the range of active cavity radii that will nucleate, if present, for a given wall superheat as calculated from Eq. (2). The onset of nucleation occurs over cavities of radius 3 μm, and the minimum wall superheat required to initiate nucleation in the channel under the given conditions is 15°C. If cavities of 3 μm radius are not available, the wall superheat will be higher as given by the plot.

Considering subcooled liquid inlet into a 1054×197 μm channel, Fig. 4 is plotted to show the local wall and bulk liquid temperatures at the nucleation condition. Figure 5 shows the actual wall and liquid temperatures as a function of the nucleation cavity radius.

The effect of reducing the channel size is seen in Fig. 6, which shows a plot of local wall and bulk liquid temperatures similar to Fig. 5 at the nucleation location. For this case, since the heat transfer coefficient is very high, the bulk liquid is superheated over the entire nucleation cavity size range. As a bubble nucleates in the superheated liquid environment, the evaporation rate is very high due to release of the liquid superheat at the bubble interface. The bubble continues to grow and encounters other heated walls as it fills the channel. The availability of heat from (a) the superheated liquid layer near the other walls and (b) the superheated liquid across the liquid vapor interfaces on the upstream as well as the downstream sides of the expanding bubble leads to a very

rapid expansion of the bubble. The bubble expansion in the reverse direction to the overall flow direction, and introduction of vapor into the inlet manifold have been identified as the main sources of instability during flow boiling.

Methods to Reduce Instabilities. In order to suppress or completely eliminate the instabilities, it is desirable to have the wall superheat at the nucleation location as low as possible. This can be achieved by introducing nucleation cavities of desirable radii as shown in Fig. 3. It is also observed that the wall superheats at the onset of nucleate boiling (ONB) condition are in general quite high in microchannels, even in the presence of the right sized cavities. Introduction of artificial nucleation cavities alone therefore may not be enough to suppress the instabilities arising due to rapid bubble expansion. In such cases, introduction of pressure drop elements at the entrance to each channel is expected to reduce the reverse flow condition. The PDEs introduce a significant increase in the flow resistance in the reversed flow direction. The effect of area reduction at the entrance was studied through a numerical simulation of an expanding bubble by Mukherjee and Kandlikar [19]. Their results clearly demonstrated the efficacy of the PDEs in reducing the reversed flow. In the present paper, the effects of artificial nucleation cavities and the pressure drop elements of different area reduction ratios on flow boiling stability are studied experimentally. For the conditions of the experiments that will be studied, the desired cavity radius for a minimum wall superheat condition is around 5 μm. To ascertain a wider range of operation, cavities of diameters 5–30 μm are drilled using a laser beam.

The pressure drop effects will be studied by introducing area

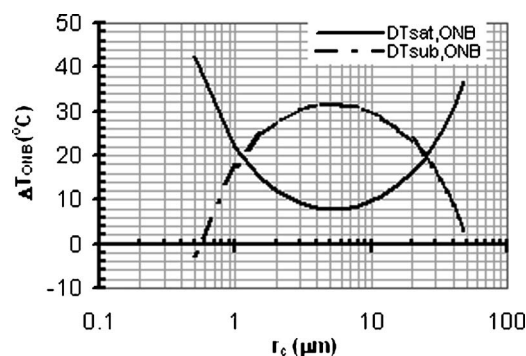**Fig. 4 Local wall superheat and liquid subcooling corresponding to onset of nucleation over a given cavity radius, Eqs. (3) and (4), water in 1054×197 μm channel, G=120 kg/m² s; q'' =300 kW/m²**

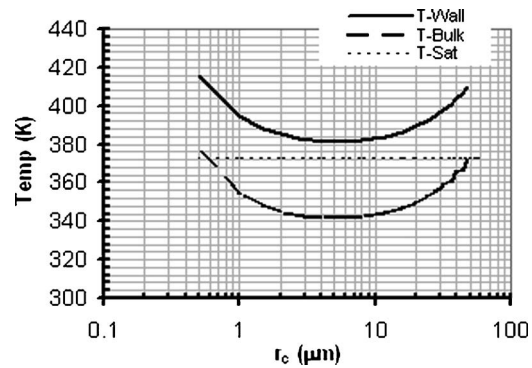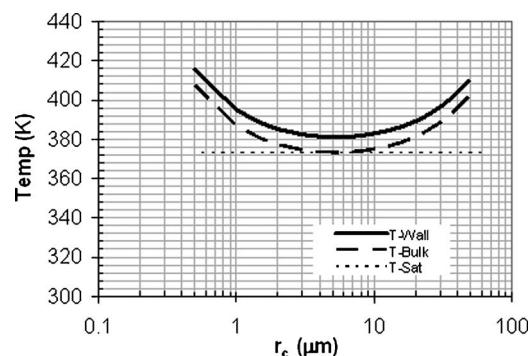**Fig. 6 Local wall and liquid temperatures corresponding to onset of nucleation over a given cavity radius, water in 1054 ×50 μm channel, G=120 kg/m² s; q''=300 kW/m²**

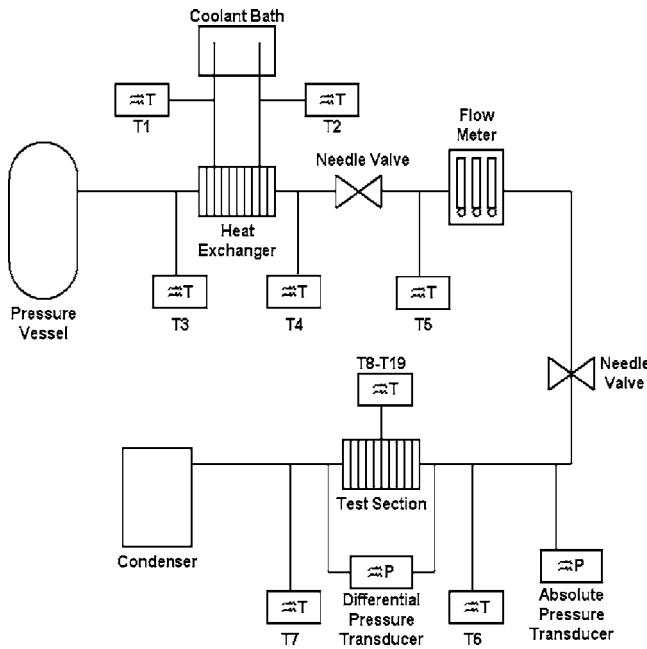**Fig. 7 Water supply loop and test section**

Fig. 9 Cross section views of inlet restriction details

reductions of 51% and 4% at the inlet of each channel. The details of the experimental setup and the results are presented in the next sections.

Experimental Setup

The experimental setup is shown in Fig. 7 and consists of a water supply loop, the test section, data acquisition system, and the high-speed digital video system. The experimental setup is designed to provide degassed water at a constant flow rate and temperature to the test section. For simplicity, Fig. 7 shows only the water supply loop and the test section.

The details of the test section are shown in Fig. 8. It is very similar to the test section used by Kandlikar and Balasubramanian [2]. It is comprised of three different layers. The top layer (a) is made of an optically clear polycarbonate known as Lexan, which has a thermal conductivity of 0.19 W/m K. This layer provides a direct view of vapor activity in the microchannels below it. It however limits the operating temperature to about 115°C, which is the temperature at which the polycarbonate will begin softening. The second layer (b) is the copper microchannel block. The copper is an Electrolytic Tough Pitch alloy number C11000 which is 99.9% copper and 0.04% oxygen (by weight). It has a thermal conductivity of 388 W/m K at 20°C. The third layer (c) is a phenolic plate which acts as an insulating layer on the bottom surface of the copper block as well as a means of securing the test

Fig. 8 Test section details

section together with 10 mounting screws. The top surface of the copper block was lap-finished to provide a leakproof assembly with the Lexan top cover. The phenolic is a laminate of paper and epoxy and has a thermal conductivity of 0.2 W/m K. Also shown is the resistive cartridge heater that supplies heat to the test section when a dc voltage is applied.

Six parallel microchannels 63.5 mm long are machined into the copper block as shown in Fig. 8. The channel depth, D, and width, W, are measured at six locations along the channel length using a microscopic measuring system. The average channel dimensions are 1054 μm wide by 197 μm deep with a hydraulic diameter of 332 μm. The width and the height of the channels were measured at several locations and were noted to fall within ± 10 μm and ± 3 μm of the average values, respectively. This represents an uncertainty of $\pm 1\%$ in the width measurement and $\pm 1.5\%$ in the height measurement. The resulting uncertainty in the hydraulic diameter is estimated to be $\pm 1.4\%$.

The test section is held together with ten mounting screws that provide the force necessary to seal the copper block to the Lexan without using a gasket. At the pressures experienced within the microchannels this contact force is enough to prevent water from escaping the test section.

To reduce heat transfer in the manifold, the inlet manifold is machined into the Lexan and the water is delivered at the very beginning of the microchannels. Each microchannel has a dedicated inlet machined into the Lexan consisting of a 0.368-mm-diam hole.

The diagram in Fig. 9 shows how each inlet connects to the inlet manifold on the Lexan cover. Water enters through the inlet manifold and is diverted through each restriction hole and into the corresponding microchannel. This small diameter hole has 51% of the cross-sectional area of a single microchannel and is 1.6 mm long. It acts as the physical pressure drop element (PDE) that is being studied. A more restrictive inlet header is also machined

with 102-μm-diam holes, giving a flow area of 4% of the channel cross-sectional area. The pressure drop is measured across the inlet and outlet manifolds. Temperatures are measured at six locations along the length.

Experimental Procedure

The experimental procedure for obtaining degassed water is the same degassing procedure as described by Kandlikar et al. [1], and Steinke and Kandlikar [20]. A heat exchanger in conjunction with a coolant bath (see Fig. 7) maintains the temperature of the degassed water delivered to the test section at a set value. The water then passes through a flow meter before entering the test section via the inlet manifold.

Once the test loop is built and well insulated, heat loss experiments are performed at steady state. The cartridge heater provides a constant heat input to the test section. A heat loss calibration chart is constructed by plotting the temperature difference between the microchannel surface and the ambient air ($T_s - T_{Amb}$) versus the corresponding steady state electrical power input, q_{in}. Heat losses, q_{loss}, were found to be a linear function of the temperature difference between the microchannel surface and the ambient air and generally ranged between 3 and 4 W for ($T_s - T_{Amb}$) of 40–50 °C, respectively. During the actual experiments, this chart is used to calculate the actual heat carried away by the microchannel array.

Water flow rate and inlet temperature are set and the electrical power is applied to the microchannels. Steady state is achieved when the surface temperature of the microchannels remains constant over a 15 min time interval. The flow meter is calibrated and is used to set the flow for the test section. LabView software is used as the data acquisition system and is used to monitor temperatures of all of the thermocouples and pressure transducers.

All of the image sequences are recorded with a high-speed digital camera system once the test section has reached steady state. The camera frame rate is set to 6000 frames/s to capture the details of the rapid two-phase flow interactions and events occurring within each microchannel. Sequences of individual frames are selected to illustrate the boiling characteristics and behavior at the set flow rate and heat flux conditions.

Uncertainty

The uncertainty of the experimental data is calculated. The uncertainty in the hydraulic diameter is estimated to be ±1.4%. The accuracies of the digital signals are reported as: Voltage = ±0.05 V, I = ±0.005 A, T = ±0.1 °C, ΔP = ±0.1 kPa. The flow meter has a volumetric flow accuracy of ±0.0588 cc/min. Heat loss measurements were conducted and a plot of heat loss versus copper block temperature was plotted. The actual heat supplied to the fluid was then calculated by subtracting the heat loss obtained from the plot from the electric power supplied to the cartridge heater. The uncertainty in the heat supplied is estimated to be less than 1%. The thermal uniformity of the test section temperature distribution was verified using temperature measurements and numerical simulation as described in detail in a previous publication by Steinke and Kandlikar [21]. The pressure drop was measured with a pressure transducer with a 1 kHz frequency. Further details on the pressure fluctuations and pressure measurements were given in an earlier publication by Balasubramanian and Kandlikar [22].

Results

The evaluation of pressure drop elements (PDE) and manufactured nucleation sites for stabilizing the flow boiling process is presented in this section. Flow stability is determined through high-speed visual observations and measurement of pressure drop fluctuations across the channels. All tests are conducted with microchannels in the horizontal orientation.

In the video images shown in the paper, the large nucleation cavities seen in the center of the channel are 100-μm-diam punch marks. These "cavities" were too large for nucleation and did not initiate nucleation. This is in accordance with the active cavity size plot shown in Fig. 3. Also, the largest natural cavity sizes observed on the machined channel surfaces were noted to be relatively few and were 1 to 2 μm in diameter. The observed wall superheat was between 12 and 14 °C, as confirmed by the earlier experiments conducted by Balasubramanian and Kandlikar [22].

The results are reported for the following five cases:

Case (a) Base case, no PDE (pressure drop element), no ANS (artificial nucleation sites)

Case (b) 51% PDE only

Case (c) ANS only

Case (d) 51% PDE with ANS

Case (e) 4% PDE with ANS

The test section with the fabricated nucleation sites was tested with three different headers. The first header with no pressure drop elements was employed in cases (a) and (c). The second header with 51% area PDEs at the inlet of each flow channel was used in cases (b) and (d). Finally, the third header with 4% area PDEs at the entrance to each flow channel was used in case (e). For cases (c), (d), and (e), the manufactured artificial nucleation sites were incorporated. The results show the visual observations of these two headers in combination with the artificial nucleation sites.

Case (a) Base Case. The results for the base case were presented in earlier publications [21,22]. Severe pressure drop fluctuations and flow reversal were observed indicating unstable operation.

Case (b) Effect of Pressure Drop Elements Only. Pressure drop elements offering 51% area were added in the passage leading from the inlet manifold to the individual microchannels. The manifold incorporates inlet openings of 368 μm diameter at the inlet to each channel, giving an open area that is 51% of the area of a 1054 × 197 μm microchannel. These pressure restrictors are expected to prevent the backflow by forcing an expanding vapor bubble in the downstream direction and not allowing the liquid-vapor mixture to enter the inlet manifold. Flow reversal was still present and is depicted in Fig. 10.

The sequence of frames in Fig. 10 shows an expanding vapor bubble nucleating and moving backward as well and eventually reaching the inlet manifold. Frame (*a*) shows a vapor bubble nucleating from a nucleation site near the corner of the channel. Frame (*c*) shows the bubble developing into a plug as it begins to push water upstream and downstream. The smaller bubbles seen in the flow upstream also move in the reverse direction rather than slipping around the vapor slug. Finally, Frame (*f*) shows the vapor reaching the inlet manifold and the channel drying out.

As seen from the above discussion, the 51% area pressure drop elements do not eliminate the reverse flow. Comparing these results with those presented by Kandlikar and Balasubramanian [2], the 51% area pressure drop elements in the inlet manifold seem to reduce the severity of backflow but they do not completely eliminate it. Apparently, the area reduction is not sufficient to prevent the reverse flow in the channels. Another indicator of stability is the magnitude of pressure fluctuations across the microchannels. A pressure drop fluctuation comparison is presented in a later section.

Case (c) Effect of Nucleation Sites Only. Nucleation sites were created at regular intervals on the bottom surface of the microchannels. The sites consisted of cavities created by a laser engraving process to achieve their very small sizes. According to the nucleation theory presented earlier, there is a range of nucleation site sizes that are active for a given set of operating conditions. For this reason, a range of 5- to 30-μm-diam cavities was created. The cavities were spaced at a regular interval of 762 μm
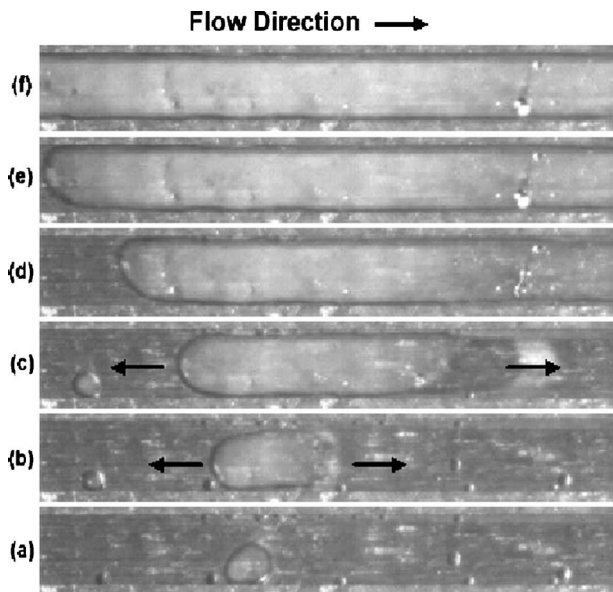
Fig. 10 Flow reversal in 51% area pressure drop manifold with no artificial nucleation sites. Successive frames from (*a*) to (*f*) taken at 1.67 ms time interval illustrating partially stabilized flow in a single channel from a set of six parallel horizontal microchannels. G=120 kg/m^2 s, q''=308 kW/m^2, T_s=113°C.

slightly offset from the center of each of the six microchannels for their entire length. Figure 11 shows images of two typical laser drilled holes created. The cavities were slightly deeper than their width at the mouth. Imaging software was used to capture images of the holes and to measure the sizes of their features.

In a few events, nucleation was observed at naturally occurring, 1- to 2-μm-diam nucleation cavities close to the walls of the microchannel. These sites were generated as a result of the machining process and were limited to diameters smaller than 1 to 2 μm as noted above.

The addition of only nucleation sites however caused a significant increase in the flow instability. The backflow was seen to be more pronounced. The pressure drop fluctuations were also higher. The availability of nucleation sites closer to the inlet manifold facilitated their backflow into the manifold.

Case (d) Effect of Combined 51% PDE and ANS. The visual images for this case are shown in Fig. 12. A bubble is seen to nucleate near the corner of the microchannel and grow in both the upstream and downstream directions until the channel is eventually dried out. The flow is observed to be unstable, but the severity of the flow reversal is seen to be somewhat reduced as compared to the base case (a).

With partial stabilization seen by the 51% area pressure drop
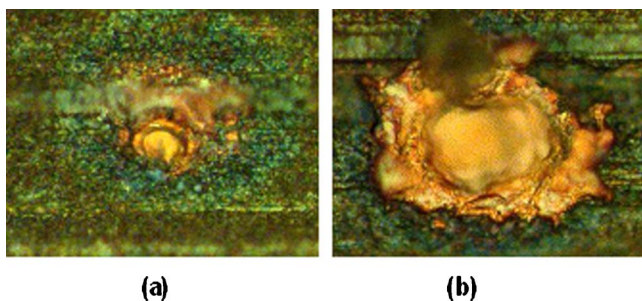
Fig. 11 Laser drilled holes on microchannel surface. Cavity in image (*a*) has an average diameter of 8 μm and cavity in image (*b*) has an average diameter of 22 μm.
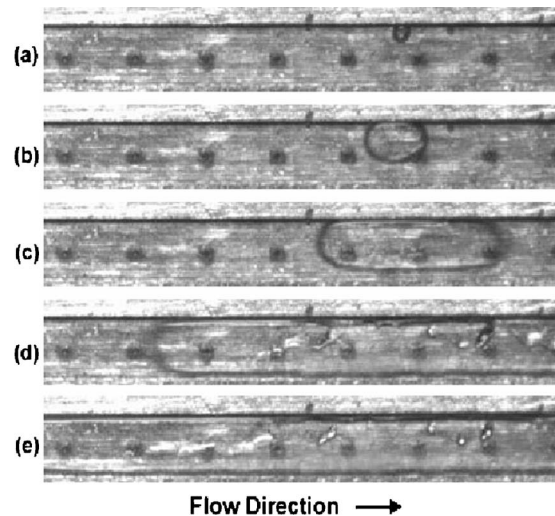
Fig. 12 Unstable flow with 51% area pressure drop elements and fabricated nucleation sites. Successive frames from (*a*) to (*e*) taken at 1.17 ms time interval illustrating normal flow reversal in a single channel from a set of six parallel horizontal microchannels. G=120 kg/m^2 s, q''=298 kW/m^2, T_s=112.4°C.

elements and fabricated nucleation sites, and occasional stable boiling patterns seen with natural and fabricated nucleation sites alone, a manifold with an even greater area reduction was tested next.

Case (e) Effect of Combined 4% PDE and ANS. The third manifold incorporates inlet openings of 102 μm diameter at the inlet to each channel, giving an open area that is 4% of the area of a 1054×197 μm microchannel. All of the conditions were held constant as the effect of the 4% area pressure drop element manifolds in conjunction with the fabricated nucleation sites was tested. The sequence of frames in Fig. 13 shows extremely stable flow boiling in the channels. Unlike previous cases, flow reversal was not seen at any time and a pattern recognized as truly stabi-
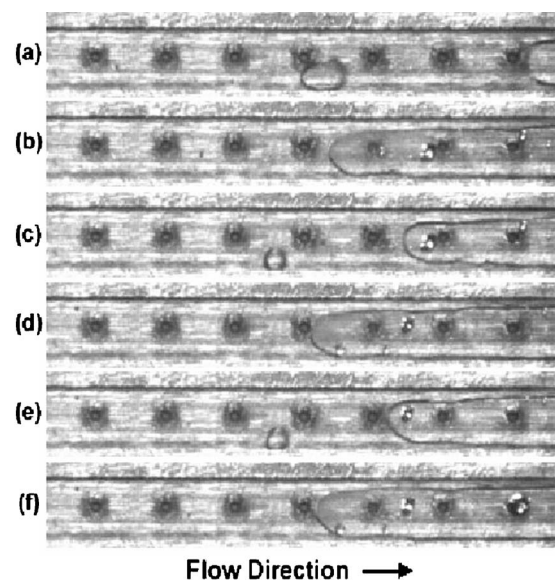
Fig. 13 Stable flow with 4% area pressure drop elements and fabricated nucleation sites. Successive frames from (*a*) to (*f*) taken at 11.7 ms time intervals illustrating extremely stabilized flow in a single channel from a set of six parallel horizontal microchannels. G=120 kg/m^2 s, q''=298 kW/m^2, T_s=111.5°C.
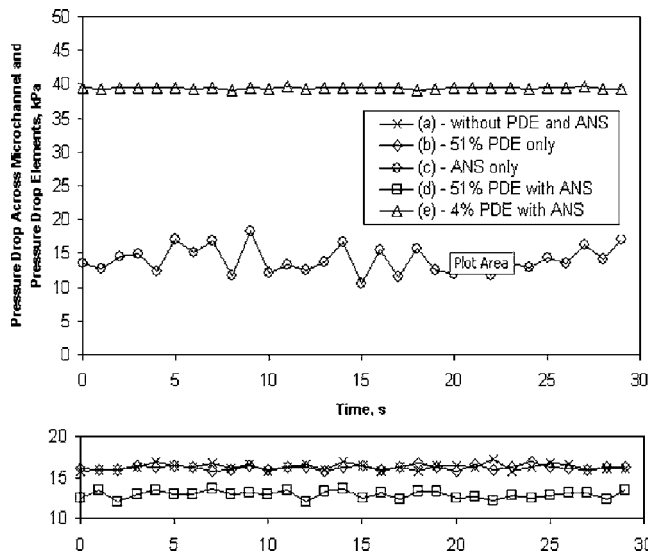
Fig. 14 Comparison of transient pressure drop data across microchannels and pressure drop elements

lized was seen. Figure 13 shows longer durations between the frames (11.7 ms) to illustrate that the pattern was stable over long period of operation. This was the case in all six channels. Bubbles often formed at the fabricated nucleation sites as well in the corners of the microchannels and expanded in the downstream direction.

Comparison of Pressure Drop, Pressure Fluctuations, and Heat Transfer. Figure 14 shows a comparison of the transient pressure drop behavior for the five cases studied. The base case, case (a), shows significant pressure fluctuations indicating instability. Case (b) with 51% PDEs shows partially stable flow with lower pressure drop fluctuations.

The presence of 51% PDEs in case (b) helped in improving the stability, but did not completely stop the reversed flow. Interestingly, the total pressure drop remained almost identical with case (a). Case (c) with the nucleation sites alone actually increased the pressure fluctuations and reduced the total pressure drop. The early nucleation in the channel closer to the inlet manifold provided a lower resistance in the backflow direction leading to unstable operation.

Case (d) with 51% PDEs and ANS reduced the instability, and made the flow boiling partially stable. It also resulted in a reduction in the pressure drop as well compared to cases (a)–(c). Finally, case (e) with 4% PDEs and ANS provided a stable flow, but a very high pressure drop value.

Table 1 summarizes the pressure drop, pressure fluctuations,

Table 1   Summary of test results

Case	Average surface temp (°C)	Pressure drop kPa	Pressure fluctuation (±kPa)	Stability
(a) base case—without PDE or ANS	114.5	16.3	1.4	unstable
(b) with 51% PDE only	115.0	16.2	0.8	partially stable
(c) with ANS only	112.4	14.0	3.8	unstable
(d) with 51% PDE and ANS	113.0	12.9	0.9	partially stable
(e) with 4% PDE and ANS	111.5	39.4	0.3	completely stable

and heat transfer results for the five cases studied. The results for case (c) show an increased pressure fluctuation with the presence of ANS as compared to the base case (a). The presence of nucleation sites alone increased the instabilities. Case (d) provides partially stabilized flow with a decrease in the pressure drop. The improvement in flow stability contributes to a lower pressure drop as well. Case (e) provides the most stable flow, but the pressure drop is significantly higher due to the inlet restrictors. In this study, the actual channel pressure drop could not be measured and only the pressure drops between the two headers are reported.

The heat transfer performance is presented in Table 1 through the wall temperatures for the five cases. The presence of ANS clearly shows an improvement in the heat transfer performance as seen in cases (c), (d), and (e). Introducing only ANS in case (c) increased the instability, but lowered the wall temperatures. Case (e) offers the best heat transfer performance, although the pressure drop is very high. Case (d) offers an intermediate result, indicating a need for further experimental study to cover a wider range of PDEs.

Conclusions

1. The present study focused on evaluating the effect of pressure drop elements and artificial nucleation sites on the instability observed during flow boiling in microchannels. Their individual as well as combined effects were studied experimentally using high speed video imaging and pressure drop measurements. The artificial nucleation sites of diameters $5-30$ μm, derived from the nucleation criterion, and inlet area restrictors providing 51% and 4% open channel area were studied. All cases were studied under the same mass flow and heat flux conditions.
2. Introduction of pressure drop elements alone partially reduced the instabilities. Introduction of nucleation sites alone increased the instabilities.
3. Introduction of nucleation sites in conjunction with the 51% area pressure drop elements was seen to partially reduce the reverse flow phenomenon. Partially stabilized flow was observed for the first time. The reverse flow did not extend into the inlet manifold and the pressure drop fluctuations were reduced considerably.
4. Fabricated nucleation sites in conjunction with the 4% area pressure drop elements completely eliminated the instabilities associated with the reverse flow. Early indications of increased thermal performance were also seen. Use of pressure drop elements in conjunction with fabricated nucleation sites is recommended based on this study.
5. Stable flow provided an improvement in heat transfer as seen by a reduction in the channel wall temperatures.
6. Further research is warranted to study the effect of different pressure drop elements, and different size and distribution of the nucleating cavities on stability of the flow boiling phenomena.

Acknowledgment

Nomenclature

A_{HT} = heat transfer area, m^2
CHF = critical heat flux, W/m^2
D = minimum dimension of rectangular channel, μm
G = mass flux, kg/m^2 s
h = heat transfer coefficient, W/m^2 K
h_{LV} = latent heat of vaporization, J/kg
I = electrical current, A

k_L = thermal conductivity of liquid, W/m K
ONB = onset of nucleate boiling
ΔP = Pressure drop, Pa
PDE = pressure drop element
q_{in} = power input to the test section, W
q_{loss} = heat loss from the test section, W
q'' = heat flux, W/m^2
r_b = radius of the bubble at nucleation, m
$r_{c,max}$ = maximum radius of nucleating cavity, m
$r_{c,min}$ = minimum radius of nucleating cavity, m
T_s = surface temperature, °C
T_{Amb} = ambient air temperature, °C
T_{Bulk} = bulk temperature, °C
T_{Sat} = saturation temperature, °C
ΔT_{Sat} = wall superheat, $=T_{Wall}-T_{Sat}$, °C
ΔT_{Sub} = liquid subcooling, $=T_{Sat}-T_{Bulk}$, °C
T_{Wall} = wall temperature, °C
W = width of microchannel, m
y_S = stagnation location from wall, m

Greek Letters

δ_t = thermal boundary layer thickness, $=k_L/h$, m
θ_r = Receding contact angle, deg
ρ_V = vapor density, kg/m^3
σ = Surface tension, N/m

Subscripts

ONB = onset of nucleate boiling
Sat = saturation
Sub = subcooling

References

[1] Kandlikar, S. G., Steinke, M. E., Tian, S., and Campbell, L. A., 2001, "High Speed Photographic Observation of Flow Boiling of Water in Parallel Minichannels," paper presented at the ASME National Heat Transfer Conference, Los Angeles, CA, June 10–12.

[2] Kandlikar, S. G., and Balasubramanian, P., 2005, "An Experimental Study on the Effect of Gravitational Orientation on Flow Boiling of Water in 1054 ×197 µm Parallel Minichannels," ASME J. Heat Transfer, **127**, pp. 820–829.

[3] Hetsroni, G., Klein, D., Mosyak, A., Segal, Z., and Pogrebnyak, E., 2003, "Convective Boiling in Parallel Microchannels," First International Conference on Microchannels and Minichannels, ASME, Rochester, NY, April 24–25, pp. 59–67.

[4] Peles, Y., 2003, "Two-Phase Flow in Microchannels–Instabilities Issues and Flow Regime Mapping," First International Conference on Microchannels and Minichannels, ASME, Rochester, NY, April 24–25, pp. 559–566.

[5] Kandlikar, S. G., and Grande, W. J., 2003, "Evolution of Microchannel Flow Passages--Thermohydraulic Performance and Fabrication Technology," Heat Transfer Eng., **24**(1), pp. 3–17.

[6] Cho, E. S., Koo, J., Jiang, L., Prasher, R. S., Kim, M. S., Santiago, J. G., Kenny, T. W., and Goodson, K. E., 2003, "Experimental Study on Two-Phase Heat Transfer in Microchannel Heat Sinks With Hotspots," paper presented at the 19th IEEE SEMI-THERM Symposium.

[7] Kandlikar, S. G., 2002, "Fundamental Issues Related to Flow Boiling in Minichannels and Microchannels," Exp. Therm. Fluid Sci., **26**(2–4), pp. 389–407.

[8] Bergles, A. E., and Kandlikar, S. G., 2005, "On the Nature of Critical Heat Flux in Microchannels," J. Heat Transfer, **127**(1), pp. 101–107.

[9] Jiang, L., Wong, M., and Zohar, Y., 1999, "Phase Change in MicroChannel Heat Sinks With Integrated Temperature Sensors," J. Microelectromech. Syst., **8**, pp. 358–365.

[10] Bowers, M. B., and Mudawar, I., 1994, "High Flux Boiling in Low Flow Rate, Low Pressure Drop Mini-Channel and Micro-Channel Heat Sinks," Int. J. Heat Mass Transfer, **37**, pp. 321–332.

[11] Qu, W., and Mudawar, I., 2004, "Measurement and Correlation of Critical Heat Flux in Two-Phase Micro-Channel Heat Sinks," Int. J. Heat Mass Transfer, **47**, pp. 2045–2059.

[12] Kandlikar, S. G., 2004, "Heat Transfer Mechanisms During Flow Boiling in Microchannels," J. Heat Transfer, **126**, pp. 8–16.

[13] Hsu, Y. Y., and Graham, R. W., 1961, "An Analytical and Experimental Study of the Thermal Boundary Layer and Ebullition Cycle in Nucleate Boiling," NASA TN-D-594.

[14] Hsu, Y. Y., 1962, "On the Size Range of Active Nucleation Cavities on a Heating Surface," J. Heat Transfer, **84**, pp. 207–216.

[15] Bergles, A. E., and Rohsenow, W. M., 1964, "The Determination of Forced-Convection Surface Boiling Heat Transfer," J. Heat Transfer, **86**, pp. 365–372.

[16] Sato, T., and Matsumura, H., 1964, "On the Conditions of Incipient Subcooled Boiling With Forced Convection," Bull. JSME, **7**(26), pp. 392–398.

[17] Davis, E. J., and Anderson, G. H., 1966, "The Incipience of Nucleate Boiling in Forced Convection Flow," AIChE J., **12**(4), pp. 774–780.

[18] Kandlikar, S. G., Mizo, V. R., Cartwright, M. D., and Ikenze, E., 1997, "Bubble Nucleation and Growth Characteristics in Subcooled Flow Boiling of Water," HTD-Vol. 342, *ASME Proceedings of the 32nd National Heat Transfer Conference*, Vol. 4, pp. 11–18.

[19] Mukherjee, A., and Kandlikar, S. G., 2004, "Numerical Study of an Evaporating Meniscus on a Moving Heated Surface," ASME Heat Transfer/Fluids Engineering Summer Conference, Charlotte, NC, July 11–15.

[20] Steinke, M. S., and Kandlikar, S. G., 2004, "Control and Effect of Dissolved Air in Water During Flow Boiling in Microchannels," Int. J. Heat Mass Transfer, **47**(8–9), pp. 1925–1935.

[21] Steinke, M. E., and Kandlikar, S. G., 2004, "An Experimental Investigation of Flow Boiling Characteristics of Water in Parallel Microchannels," J. Heat Transfer, **126**(4), pp. 518–526.

[22] Balasubramanian, P., and Kandlikar, S. G., 2005, "An Experimental Study of Flow Patterns, Pressure Drop and Flow Instabilities in Parallel Rectangular Minichannels," Heat Transfer Eng., **26**(3), pp. 20–27.

An Exact Solution to Steady Heat Conduction in a Two-Dimensional Annulus on a One-Dimensional Fin: Application to Frosted Heat Exchangers With Round Tubes

A. D. Sommers
Graduate Research Assistant
e-mail: asommers@uiuc.edu

A. M. Jacobi
Professor of Mechanical Engineering
e-mail: a-jacobi@uiuc.edu

Department of Mechanical
and Industrial Engineering,
University of Illinois,
1206 West Green Street,
Urbana, IL 61801

The fin efficiency of a high-thermal-conductivity substrate coated with a low-thermal-conductivity layer is considered, and an analytical solution is presented and compared to alternative approaches for calculating fin efficiency. This model is appropriate for frost formation on a round-tube-and-fin metallic heat exchanger, and the problem can be cast as conduction in a composite two-dimensional circular cylinder on a one-dimensional radial fin. The analytical solution gives rise to an eigenvalue problem with an unusual orthogonality condition. A one-term approximation to this new analytical solution provides fin efficiency calculations of engineering accuracy for a range of conditions, including most frosted-coated metal fins. The series solution and the one-term approximation are of sufficient generality to be useful for other cases of a low-thermal-conductivity coating on a high-thermal-conductivity substrate. [DOI: 10.1115/1.2165210]

Keywords: frost, fin efficiency, conduction, sector method, heat transfer

Introduction

Xia and Jacobi [1] presented the solution to heat conduction in a two-dimensional slab on a one-dimensional straight fin, and using a numerical solution to the fully two-dimensional problem they identified the parameter space for which that simplified model is appropriate. Moreover, they applied this heat transfer model to frost growth on a straight metallic fin, typical to a flat-tube heat exchanger operating under frosting conditions. However, most heat exchangers operating under frosted-surface conditions are constructed with plain fins and round tubes. The analytical solution presented for the straight fin is not valid for the round-tube geometry.

For round-tube heat exchangers, the so-called sector method is often used. In this method, the fin surface is divided into hexagonal or rectangular regions around each tube, and circular sectors are fit to the geometric profile of the selected region. Typically, these regions are subdivided into eight zones and then further divided into sectors as shown in Fig. 1. The radius of each edge of the sector is approximated according to the hexagonal pattern and then used to calculate the radius ratio and surface area of each sector, RR_n and S_n, respectively. The overall fin efficiency is found by summing the product of the individual efficiencies and surface areas for each sector and dividing by the total surface area of the eight zones. This method is based on the assumptions of radial conduction in each sector and an adiabatic tip for each sector. Thus, the widely used sector method—a method used for complicated fin-and-tube heat exchangers—has the efficiency of a circular fin as its basis. The well-known expression for circular fin efficiency involves Bessel functions, and in 1949 Schmidt [2] provided an approximation to this expression in terms of the hyperbolic tangent function. This solution is still used by some engineers today when calculating fin efficiency by the sector method. The application of the sector method to various round-tube-and-fin geometries is detailed in the Appendix.

Under condensing or frosting conditions the fin efficiency calculation must account for sensible and latent heat effects. A common practice is to include an additional source term in the fin heat diffusion equation for the latent heat due to mass transfer along the surface. In this approach, the final form of the governing differential equation is the same as for dry-surface conditions, but it includes two dependent variables: θ, the nondimensional temperature difference, and W_s, the humidity ratio at the surface of the fin. For condensing conditions, McQuiston [3] assumed $(W_a\text{-}W_s)$ to be linearly related to $(T_a\text{-}T_s)$ and in this way eliminated one of the dependent variables. However, this ad hoc approximation requires a priori knowledge of the temperature range, in order to evaluate the constant of proportionality between humidity ratio and temperature. Wu and Bong [4] improved upon this idea by using a psychrometric relationship between the humidity ratio of saturated air at the surface, W_s, and T_s. When the difference between the fin base temperature and the fin tip temperature is small, this assumption is excellent, and the relationship is linear and thermodynamically known. However, Wu and Bong developed their approach for wet fins and not frosted fins, and therefore their method does not account for the effect that a frost conduction resistance has on the fin efficiency. In a similar study of fin efficiency under condensing conditions, Hong and Webb [5] suggested a modification to the Schmidt solution that more accurately approximates the Bessel function solution; they then followed the approach of McQuiston [3] in deriving a wet fin efficiency solution and pointed out that for high-humidity conditions the difference between the dry-surface fin efficiency and the wet-surface fin efficiency can be as high as 35%.

In a paper on frosted coil performance, Mago and Sherif [6] computed the fin efficiency of a frosted rectangular fin using an equivalent circular area. In order to account for frost, they included the mass transfer effects in defining the air-side convective
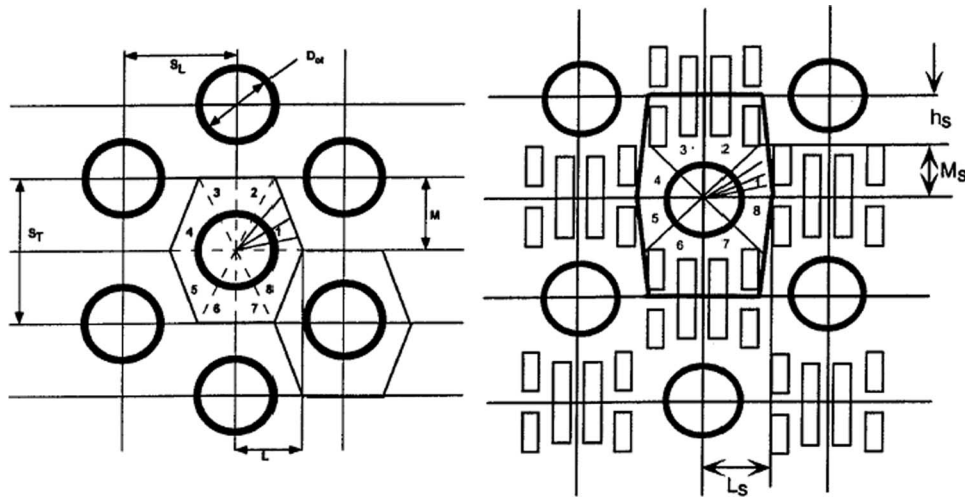
Fig. 1 Two different examples of the hexagonal pattern that emerges when using the sector method [9]

coefficient and defined the fin efficiency in terms of enthalpies rather than temperatures. Their method, however, neglects conduction in the frost layer and requires knowledge about the slope of the saturated enthalpy-temperature curve evaluated at the frost surface temperature. In a paper on pin-fin heat exchangers, Kondepudi and O'Neal [7] calculated fin efficiency using a modified fin parameter, m, to account for the frost conduction resistance. They found that the presence of a 1-mm-thick frost layer on the fin can reduce the fin efficiency by as much as 10% in comparison to the dry, unfrosted fin. Their analysis, however, assumes one-dimensional conduction in the frost layer and uses the hyperbolic tangent function as a simplification to the modified-Bessel solution.

There have been a number of related papers on heat conduction in composite slabs, as reviewed by Xia and Jacobi [1]. The current study extends that earlier research and is motivated by a desire for a convenient expression for fin efficiency that accounts for the frost conduction resistance and latent heat effects and is appropriate for operating conditions typical to refrigeration and heat pumping systems. In this paper, we consider an annular conduction domain and develop expressions for the fin efficiency of circular fins; the results of which can be used directly or in conjunction with the sector method.

Problem Formulation

The physical situation of interest, frost on a metallic fin, is shown in Fig. 2 for a round-tube heat exchanger with constant-thickness fins. Assuming a uniform convection coefficient, conduction in the ϕ-direction is neglected due to symmetry, and a two-dimensional analysis will be performed. As shown by Xia and Jacobi [1], for cases where $Bi > 0.05$ and $\psi < 0.1$, this assumption is valid, and the fin can be approximated as one-dimensional with a two-dimensional coating. This situation represents the parametric range of most importance for frost on a metallic fin. The following assumptions will also be invoked: steady-state, no internal generation, and constant thermophysical properties. The frost layer is assumed to be of uniform thickness, and zero contact resistance is assumed between the fin and the frost. The convection coefficient, free-stream temperature, and base temperature considered in this analysis are fixed and assumed to be known. With these assumptions, the fin temperature is a function of r only (i.e., $T_1(r)$), and the temperature within the frost layer is a function of r and z (i.e., $T_2(r,z)$).

The governing equation for the temperature distribution along the fin, material 1, is

$$\frac{k_1 t}{r}\frac{d}{dr}\left(r\frac{dT_1}{dr}\right) + k_2 \left.\frac{\partial T_2}{\partial z}\right|_{z=0} = 0 \quad \text{in } R_1 < r < R_2 \qquad (1)$$

The heat diffusion equation in the frost layer, material 2, is

$$\frac{1}{r}\frac{\partial}{\partial r}\left(r\frac{\partial T_2}{\partial r}\right) + \frac{\partial^2 T_2}{\partial z^2} = 0 \quad \text{in } R_1 < r < R_2, \ 0 < z < \delta \qquad (2)$$

Equations (1) and (2) are subject to the boundary conditions

$$\left.\frac{dT_1}{dr}\right|_{r=R_2} = 0, \qquad \left.\frac{\partial T_2}{\partial r}\right|_{r=R_2} = 0 \qquad (3a)$$

$$T_1(R_1) = T_b \quad T_2(R_1,z) = T_b \qquad (3b)$$

$$T_1(r) = T_2(r,0) \qquad (3c)$$

$$\left.\frac{\partial T_2}{\partial z}\right|_{z=\delta} = \frac{h}{k_2}(T_\infty - T_2(r,\delta)) \qquad (3d)$$
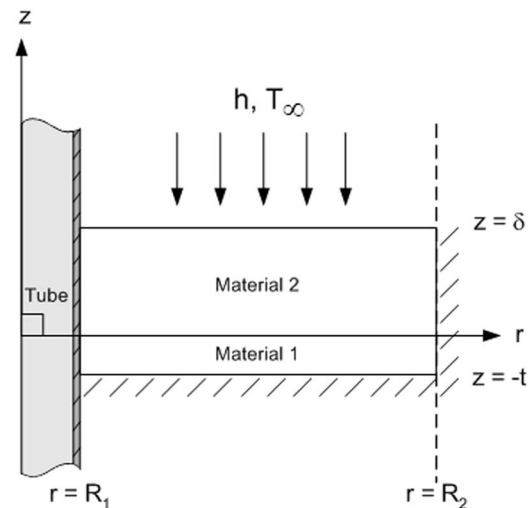

Fig. 2 Schematic of the composite slab, with the one-dimensional fin (material 1) and the two-dimensional frost layer (material 2)

Substituting Eq. (3c) into Eq. (1), we arrive at the following four boundary conditions for $T_2(r,z)$

$$\left.\frac{\partial T_2}{\partial r}\right|_{r=R_2} = 0 \tag{4a}$$

$$T_2(R_1,z) = T_b \tag{4b}$$

$$\frac{k_1 t}{r}\frac{d}{dr}\left(r\frac{dT_2}{dr}\right)\Bigg|_{z=0} + k_2 \left.\frac{\partial T_2}{\partial z}\right|_{z=0} = 0 \tag{4c}$$

$$\left.\frac{\partial T_2}{\partial z}\right|_{z=\delta} = \frac{h}{k_2}(T_\infty - T_2(r,\delta)) \tag{4d}$$

Now, we define the following nondimensional variables

$$\theta = \frac{T_2 - T_\infty}{T_b - T_\infty} \quad r^* = \frac{r}{R_2} \quad z^* = \frac{z}{\delta} \tag{5}$$

Substituting, the boundary value problem for $T_2(r,z)$ becomes

$$\frac{1}{r^*}\frac{\partial}{\partial r^*}\left(r^*\frac{\partial \theta}{\partial r^*}\right) + \left(\frac{R_2}{\delta}\right)^2 \frac{\partial^2 \theta}{\partial z^{*2}} = 0 \tag{6}$$

with

$$\frac{\partial \theta}{\partial r^*} = 0 \quad \text{at } r^* = 1 \tag{7a}$$

$$\theta = 1 \quad \text{at } r^* = \frac{R_1}{R_2} \tag{7b}$$

$$\frac{k_1 t}{r^* R_2^2}\frac{d}{dr^*}\left(r^*\frac{d\theta}{dr}\right) + \frac{k_2}{\delta}\frac{\partial \theta}{\partial z^*} = 0 \quad \text{at } z^* = 0 \tag{7c}$$

$$\frac{\partial \theta}{\partial z^*} + \frac{h\delta}{k_2}\theta = 0 \quad \text{at } z^* = 1 \tag{7d}$$

Please note that from this point forward, the asterisk superscript will be dropped from the spatial coordinates for convenience, with the r and z variables taken as dimensionless unless otherwise stated. It should also be noted that the boundary condition (7b) conflicts with (7d) at location $(r,z)=(0,1)$. To resolve this conflict, the singularity was removed by replacing boundary condition (7b) with the following at $r=0$

$$\theta = f(z) = \begin{cases} 1 & 0 \le z < (1-\varepsilon) \\ 1 - \dfrac{[z-(1-\varepsilon)]^2}{[(2\varepsilon k_2/h\delta)+\varepsilon^2]} & (1-\varepsilon) \le z \le 1 \end{cases} \tag{7e}$$

where $0 < \varepsilon \ll 1$. We now have

$$\left.\frac{\partial \theta}{\partial z}\right|_{(0,1)} + \left.\frac{h\delta}{k_2}\theta\right|_{(0,1)} = 0 \tag{8}$$

and it can be seen that Eq. (7e) → Eq. (7b) as $\varepsilon \to 0$. Perhaps more important, $f(z)$ is twice-differentiable on $0 \le z \le 1$, and only one non-homogeneous boundary condition remains.

Therefore, separation of variables is pursued. We assume $\theta(r,z)=R(r)Z(z)$ which yields

$$\frac{1}{RM^2}\left[\frac{1}{r}\frac{dR}{dr} + \frac{d^2R}{dr^2}\right] = \frac{1}{Z}\left[-\frac{d^2Z}{dz^2}\right] = \beta_m^2 \tag{9}$$

where $M^2 = (R_2/\delta)^2$. Accordingly, $R(r)$ should satisfy

$$\frac{d^2R_0}{dr^2} + \frac{1}{r}\frac{dR_0}{dr} - \beta_m^2 M^2 R_0 = 0 \quad \text{in } 1 < r < (R_1/R_2) \tag{10}$$

$$\text{with} \quad R_0' = 0 \quad \text{at } r = 1 \tag{11}$$

where the subscript zero denotes no ϕ-dependence. Similarly, $Z(z)$ must satisfy

$$\frac{d^2Z}{dz^2} + \beta_m^2 Z = 0 \quad \text{in } 0 < z < 1 \tag{12}$$

with

$$Z' + \frac{h\delta}{k_2}Z = 0 \quad \text{at } z = 1 \tag{13}$$

$$\frac{k_1 t}{R_2^2}\left[R_0''Z + \frac{R_0'}{r}Z\right] + \frac{k_2}{\delta}RZ' = 0 \quad \text{at } z = 0 \tag{14}$$

Substituting Eq. (10) into Eq. (14), the last boundary condition can be rewritten as

$$Z' + N\beta_m^2 Z = 0 \quad \text{at } z = 0 \tag{15a}$$

where

$$N = \frac{k_1 t}{\delta k_2} \tag{15b}$$

The second-order differential equations for $R(r)$ and $Z(z)$ are solved, and three of the four constants are determined using boundary condition equations (11) and (13), and (15). The eigenfunctions are

$$R_0 = C_1 \gamma_m [K_0(\gamma_m r)I_1(\gamma_m) - K_1(\gamma_m)I_0(\gamma_m r)] \tag{16}$$

$$Z = C_2 \left[\frac{k_2}{h\delta}\beta_m \cos\beta_m(1-z) + \sin\beta_m(1-z)\right] \tag{17}$$

noting that $\gamma_m^2 = \beta_m^2 M^2$. The solution is thus

$$\theta(r,z) = \sum_{m=1}^{\infty} C_m \gamma_m \left[\frac{k_2}{h\delta}\beta_m \cos\beta_m(1-z) + \sin\beta_m(1-z)\right]$$
$$\cdot [K_0(\gamma_m r)I_1(\gamma_m) + K_1(\gamma_m)I_0(\gamma_m r)] \tag{18}$$

where the eigenvalues β_m satisfy the following eigencondition

$$\tan(\beta_m) = \frac{\left[1 - \left(\dfrac{k_1 t}{h}\right)\left(\dfrac{\beta_m}{\delta}\right)^2\right]}{\left[\dfrac{k_2}{h\delta}\beta_m + \dfrac{k_1 t}{\delta k_2}\beta_m\right]} \quad n = 1,2,3,\dots \tag{19}$$

The last boundary condition (7b) yields

$$f(z) = \sum_{m=1}^{\infty} C_m \gamma_m \left[\frac{k_2}{h\delta}\beta_m \cos\beta_m(1-z) + \sin\beta_m(1-z)\right]$$
$$\cdot \left[K_0\left(\gamma_m \frac{R_1}{R_2}\right)I_1(\gamma_m) + K_1(\gamma_m)I_0\left(\gamma_m \frac{R_1}{R_2}\right)\right] \tag{20}$$

Now from Eq. (12), it can be shown that

$$\int_0^1 Z_n Z_m dz = \frac{1}{\beta_m^2 - \beta_n^2} \int_0^1 (Z_n'' Z_m - Z_m'' Z_n) dz \qquad (21)$$

Integrating by parts and applying boundary conditions, Eqs. (13) and (15a), it follows

$$\int_0^1 Z_n Z_m dz = \frac{1}{\beta_m^2 - \beta_n^2} [Z_n' Z_m - Z_m' Z_n]_0^1 = -N(Z_n Z_m)_{z=0} \qquad (22)$$

Thus,

$$\int_0^1 Z_n Z_m dz + N(Z_n Z_m)_{z=0} = 0 \text{ for } n \neq m \qquad (23)$$

Equation (23) is needed to determine C_m; first Eq. (20) must be multiplied on both sides by Z_n and integrated from zero to one. The term $N(Z_n Z_m)_{z=0}$ is then added and subtracted from each integral, and using Eq. (23) and the fact that $f(0) = \Sigma\ C_m\ \gamma_m Z_m(0)R_0$, an expression for C_m is obtained. (A general derivation of Eq. (24) was provided by Xia and Jacobi [1].)

$$C_m = \frac{\displaystyle\int_0^1 f(z')Z(\beta_m;z')dz' + Nf(0)Z(\beta_m;0)}{\gamma_m R_0\left(\gamma_m; r = \dfrac{R_1}{R_2}\right)\left\{\displaystyle\int_0^1 [Z(\beta_m;z')]^2 dz' + N[Z(\beta_m;0)]^2\right\}} \qquad (24)$$

where as $\varepsilon \to 0$

$$C_m = \frac{\displaystyle\int_0^1 Z(\beta_m;z')dz' + NZ(\beta_m;0)}{\gamma_m R_0\left(\gamma_m; r = \dfrac{R_1}{R_2}\right)\left\{\displaystyle\int_0^1 [Z(\beta_m;z')]^2 dz' + N[Z(\beta_m;0)]^2\right\}} \qquad (25)$$

Thus finally,

$$C_m = \frac{\dfrac{1}{\beta_m} + \left(\dfrac{\beta_m k_1 t}{\delta^2 h} - \dfrac{1}{\beta_m}\right)\cos(\beta_m) + \dfrac{(k_2^2 + h k_1 t)}{\delta h k_2}\sin(\beta_m)}{\gamma_m R_0\left\{\displaystyle\int_0^1 [Z(\beta_m;z')]^2 dz' + N[Z(\beta_m;0)]^2\right\}} \qquad (26a)$$

where

$$R_0 = \left[K_0\left(\gamma_m \frac{R_1}{R_2}\right)I_1(\gamma_m) + K_1(\gamma_m)I_0\left(\gamma_m \frac{R_1}{R_2}\right)\right] \qquad (26b)$$

$$\int_0^1 [Z(\beta_m;z')]^2 dz' = \frac{1}{2} + \frac{k_2}{h\delta}\sin^2(\beta_m) - \frac{1}{4\beta_m}\sin(2\beta_m)$$
$$+ \frac{\beta_m k_2^2}{4h^2\delta^2}(2\beta_m + \sin(2\beta_m)) \qquad (26c)$$

$$N[Z(\beta_m;0)]^2 = \frac{k_1 t}{h^2\delta^3 k_2}[k_2\beta_m \cos(\beta_m) + h\delta \sin(\beta_m)]^2 \qquad (26d)$$

Finally, the temperature distribution inside the two-dimensional

frost layer using dimensional variables is

$$\frac{T_2(r,z) - T_\infty}{T_b - T_\infty}$$
$$= \sum_{m=1}^\infty C_m \beta_m M\left[\beta_m\left(\frac{k_2}{h\delta}\right)\cos\beta_m\left(1 - \frac{z}{\delta}\right) + \sin\beta_m\left(1 - \frac{z}{\delta}\right)\right]$$
$$\cdot \left[K_0\left(\beta_m\frac{r}{\delta}\right)I_1(M\beta_m) + K_1(M\beta_m)I_0\left(\beta_m\frac{r}{\delta}\right)\right] \qquad (27)$$

where β_m and C_m are given by Eqs. (19) and (26a)–(26d), respectively. The expression for the temperature along the one-dimensional fin is obtained by evaluating Eq. (27) at $z=0$ which yields

$$\frac{T_1(r) - T_\infty}{T_b - T_\infty} = \sum_{m=1}^\infty C_m \beta_m M\left[\beta_m\left(\frac{k_2}{h\delta}\right)\cos\beta_m\right.$$
$$\left. + \sin\beta_m\right] \cdot \left[K_0\left(\beta_m\frac{r}{\delta}\right)I_1(M\beta_m)\right.$$
$$\left. + K_1(M\beta_m)I_0\left(\beta_m\frac{r}{\delta}\right)\right] \qquad (28)$$

The conduction heat transfer through the fin is found by differentiating Eq. (28) and using Fourier's law at $r=R_1$. Similarly, the heat flowing through the frost layer is found by differentiating Eq. (27), applying Fourier's law at $r=R_1$, and then integrating from $z=0$ to $z=\delta$. Finally, the fin efficiency is calculated by dividing the fin heat transfer rate by the maximum heat transfer rate which would exist were the entire frost surface at the base temperature, T_b. This calculation yields

$$\eta_f = \frac{2R_1}{(R_2^2 - R_1^2)h}\sum_{m=1}^\infty C_m\left(\frac{\beta_m}{\delta}\right)^2 R_2\left[I_1\left(\beta_m\frac{R_2}{\delta}\right)K_1\left(\beta_m\frac{R_1}{\delta}\right)\right.$$
$$\left. - I_1\left(\beta_m\frac{R_1}{\delta}\right)K_1\left(\beta_m\frac{R_2}{\delta}\right)\right] \cdot \left\{k_1 t\beta_m\left(\frac{k_2}{h\delta}\right)\cos\beta_m + k_1 t \sin\beta_m\right.$$
$$\left. + \frac{k_2\delta^2}{\beta_m} + \frac{k_2^2\delta}{h}\sin\beta_m - \frac{k_2\delta^2}{\beta_m}\cos\beta_m\right\} \qquad (29)$$

The series solution to the fin efficiency using four terms (i.e., $m = 4$) is shown in Fig. 3 for two different values of the convection coefficient, $h=20$ W m^{-2} K^{-1} and $h=40$ W m^{-2} K^{-1}, for a range of frost thicknesses. These results were obtained using Eqs. (19), (26), and (29) as well as the geometric parameters detailed in Table 1. The sector method was chosen to approximate the heat flow in a rectangular-plate fin of repeating hexagonal regions. Each of the eight zones was subdivided into fourteen sectors to ensure a high degree of numerical accuracy. It should be noted that while the fin efficiency depends on t, δ, R_1, R_2, h, k_1, and k_2, it does not depend on the temperatures T_∞ and T_b The fin efficiency does not go to unity for a frost layer of zero thickness because the metallic substrate used in the example is not a perfect conductor of heat. Furthermore, as the frost thickness approaches zero thickness, the analytical solution yields the fin efficiency as predicted by Schmidt's [2] sector method solution for dry fins to within 1%. It should also be noted that the error that would have occurred had conduction through the frost layer been neglected could be as high as 18% for the conditions used in this example, and this error would be more pronounced for thicker frost layers. This finding emphasizes the need for including these effects and suggests that an expression which properly accounts for conduction through both the frost layer and the fin is preferred.
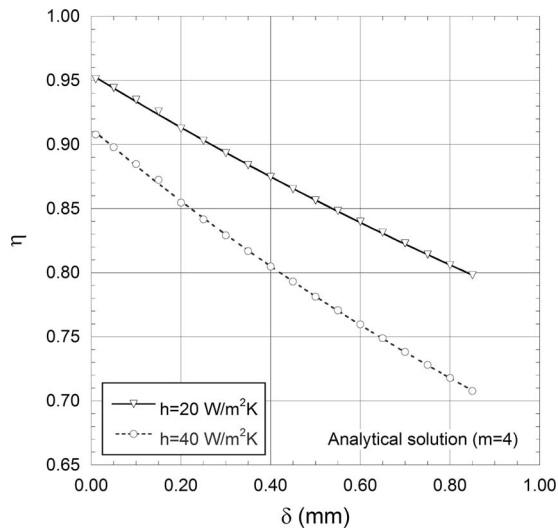
Fig. 3 Using the conditions of Table 1, example fin efficiencies are shown for two values of the convective heat transfer coefficient over a range of frost thicknesses. The effect of neglecting conduction through the frost layer is clearly seen.
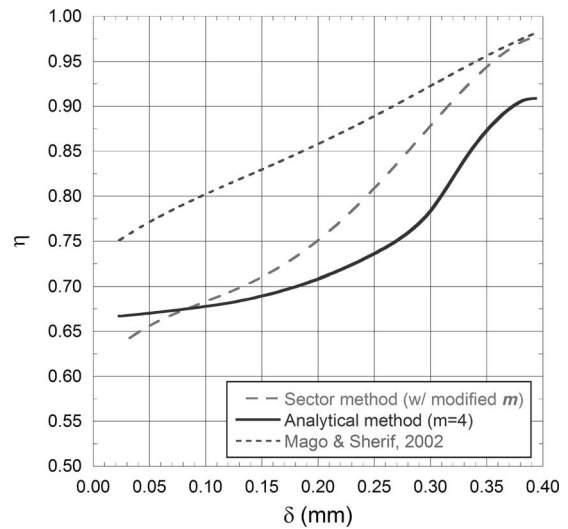

Fig. 4 Using the data from Table 2, the fin efficiency is calculated and shown for different methods and compared to the analytical solution. Note that the convective heat transfer coefficient is not constant; it decreases with frost thickness.

In Fig. 4, the fin efficiency calculated using data from Table 2 and Eq. (29) is compared to two alternate approaches: that of Wu and Bong [4], where the m term is modified to account for latent effects, and that of Mago and Sherif [6], which uses a graphical approach. It should be noted that while both of these approaches seek to account for the transfer of heat by latent effects, neither includes the effect of conduction through the frost layer. Therefore, the observed difference between these two methods is due predominantly to their method of handling the latent effects. The analytical solution yields fin efficiencies several percent lower than the other two methods and deviates the most for large frost thicknesses. It should be noted that the approach by Mago and Sherif [6] does not use the sector method but instead uses equivalent circular areas and requires interpolation from a graph which does not lend itself easily to numerical programming. Unlike Fig. 3, this plot of fin efficiency is derived from actual measured data.

Therefore, the convective heat transfer coefficient is not constant but decreases with the thickness of the frost layer, because the air flow rate through the heat exchanger decreases as frost accumulates on the air-side surface.

One-Term Approximation

Because the complete series solution is cumbersome, it is desirable to identify cases for which a one-term approximation to the series solution is sufficient. In order to make such an assessment, consider the eigencondition

$$\tan^{-1}(\beta_m) = \frac{k_1 k_2 t}{\delta(k_2^2 + hk_1 t)}\left[\left(\frac{h\delta^2}{k_1 t}\right)\frac{1}{\beta_m} - \beta_m\right] \quad (30)$$

From Xia and Jacobi [1], the following is known about the first eigenvalue

$$0 < \beta_1 < \sqrt{\frac{h\delta^2}{k_1 t}} \quad (31)$$

Therefore, when

$$\sqrt{\frac{h\delta^2}{k_1 t}} \ll 1 \quad (32)$$

we have $\tan(\beta_m) \approx \beta_m$, and the first root of Eq. (19) can be approximated as

Table 1 Parameters for an example with fixed *h*

δ	0 to 1.0 mm
h	20, 40 W m^{-2} K^{-1}
k_1	237 W m^{-1} K^{-1}
k_2	0.175 W m^{-1} K^{-1}
t	0.0635 mm
R$_1$	3.868 mm

(Radius Ratios and Surface Area for Sectors in Zones 1, 4, 5, and 8)		(Radius Ratios and Surface Area for Sectors in Zones 2, 3, 6, and 7)	
RR$_1$=1.235	S_1=0.3650 mm^2	RR$_1$=3.105	S_1=3.472 mm^2
RR$_2$=1.246	S_2=0.3770 mm^2	RR$_2$=3.109	S_2=3.463 mm^2
RR$_3$=1.267	S_3=0.3999 mm^2	RR$_3$=3.119	S_3=3.447 mm^2
RR$_4$=1.299	S_4=0.4316 mm^2	RR$_4$=3.133	S_4=3.422 mm^2
RR$_5$=1.340	S_5=0.4693 mm^2	RR$_5$=3.152	S_5=3.391 mm^2
RR$_6$=1.389	S_6=0.5105 mm^2	RR$_6$=3.175	S_6=3.353 mm^2
RR$_7$=1.446	S_7=0.5531 mm^2	RR$_7$=3.202	S_7=3.310 mm^2
RR$_8$=1.509	S_8=0.5950 mm^2	RR$_8$=3.234	S_8=3.262 mm^2
RR$_9$=1.579	S_9=0.6352 mm^2	RR$_9$=3.269	S_9=3.211 mm^2
RR$_{10}$=1.654	S_{10}=0.6729 mm^2	RR$_{10}$=3.307	S_{10}=3.158 mm^2
RR$_{11}$=1.733	S_{11}=0.7076 mm^2	RR$_{11}$=3.349	S_{11}=3.102 mm^2
RR$_{12}$=1.817	S_{12}=0.7393 mm^2	RR$_{12}$=3.394	S_{12}=3.046 mm^2
RR$_{13}$=1.903	S_{13}=0.7679 mm^2	RR$_{13}$=3.442	S_{13}=2.989 mm^2
RR$_{14}$=1.993	S_{14}=0.7937 mm^2	RR$_{14}$=3.493	S_{14}=2.932 mm^2

Table 2 Parameters for an example with varying *h*

δ (mm)	h_{sens} (W m^{-2} K^{-1})	h_{eff} (W m^{-2} K^{-1})	k_1 (W m^{-1} K^{-1})	k_2 (W m^{-1} K^{-1})
0.02	180	218	237	0.40
0.06	156	197	237	0.32
0.14	124	150	237	0.23
0.23	75.9	97.2	237	0.19
0.30	41.4	61.0	237	0.18
0.34	17.6	27.8	237	0.18
0.37	9.5	16.7	237	0.19
0.38	7.3	13.0	237	0.19
0.39	6.5	12.3	237	0.20

$$\beta_1 \approx \delta \sqrt{\frac{h}{k_1 t + \delta\left(\frac{k_1 h t}{k_2} + k_2\right)}} \qquad (33)$$

Furthermore, it can be shown from Eq. (30) that when

$$\frac{k_1 k_2 t}{\delta(k_2^2 + h k_1 t)} \gg 1 \qquad (34)$$

we can approximate $\sin(\beta_m) \rightarrow \beta_m$ and $\cos(\beta_m) \rightarrow 1$. Therefore, Eqs. (26a)–(26d) reduce to

$$C_1 \approx \frac{\left(\dfrac{\delta}{R_2}\right) \cdot \left(\dfrac{k_1 t}{\delta^2 h} + \dfrac{k_2}{h\delta} + \dfrac{k_1 t}{k_2 \delta}\right)}{\left[K_0\left(\gamma_1 \dfrac{R_1}{R_2}\right)I_1(\gamma_1) + K_1(\gamma_1)I_0\left(\gamma_1 \dfrac{R_1}{R_2}\right)\right] \cdot \left[\dfrac{\beta_1^2 k_2}{h\delta} + \left(\dfrac{\beta_1 k_2}{h\delta}\right)^2 + \dfrac{k_1 t}{h^2 \delta^3 k_2}(k_2 \beta_1 + h\delta\beta_1)^2\right]} \qquad (35)$$

The one-term approximation to the series solution in the frost layer is then

$$\frac{T_2(r,z) - T_\infty}{T_b - T_\infty} \approx \frac{\beta_1 \cdot \left(\dfrac{k_1 t}{\delta^2 h} + \dfrac{k_2}{h\delta} + \dfrac{k_1 t}{k_2 \delta}\right)}{\left[\dfrac{\beta_1^2 k_2}{h\delta} + \left(\dfrac{\beta_1 k_2}{h\delta}\right)^2 + \dfrac{k_1 t}{h^2 \delta^3 k_2}(k_2 \beta_1 + h\delta\beta_1)^2\right]} \cdot \left[\beta_1\left(\dfrac{k_2}{h\delta}\right)\cos \beta_1\left(1 - \dfrac{z}{\delta}\right) + \sin \beta_1\left(1 - \dfrac{z}{\delta}\right)\right]$$
$$\cdot \frac{\left[K_0\left(\beta_1 \dfrac{r}{\delta}\right)I_1\left(\beta_1 \dfrac{R_2}{\delta}\right) + K_1\left(\beta_1 \dfrac{R_2}{\delta}\right)I_0\left(\beta_1 \dfrac{r}{\delta}\right)\right]}{\left[K_0\left(\beta_1 \dfrac{R_1}{\delta}\right)I_1\left(\beta_1 \dfrac{R_2}{\delta}\right) + K_1\left(\beta_1 \dfrac{R_2}{\delta}\right)I_0\left(\beta_1 \dfrac{R_1}{\delta}\right)\right]} \qquad (36)$$

and in material 1,

$$\frac{T_1(r) - T_\infty}{T_b - T_\infty} \approx \frac{\beta_1 \cdot \left(\dfrac{k_1 t}{\delta^2 h} + \dfrac{k_2}{h\delta} + \dfrac{k_1 t}{k_2 \delta}\right)}{\left[\dfrac{\beta_1^2 k_2}{h\delta} + \left(\dfrac{\beta_1 k_2}{h\delta}\right)^2 + \dfrac{k_1 t}{h^2 \delta^3 k_2}(k_2 \beta_1 + h\delta\beta_1)^2\right]} \cdot \left[\beta_1\left(\dfrac{k_2}{h\delta}\right)\cos \beta_1 + \sin \beta_1\right]$$
$$\cdot \frac{\left[K_0\left(\beta_1 \dfrac{r}{\delta}\right)I_1\left(\beta_1 \dfrac{R_2}{\delta}\right) + K_1\left(\beta_1 \dfrac{R_2}{\delta}\right)I_0\left(\beta_1 \dfrac{r}{\delta}\right)\right]}{\left[K_0\left(\beta_1 \dfrac{R_1}{\delta}\right)I_1\left(\beta_1 \dfrac{R_2}{\delta}\right) + K_1\left(\beta_1 \dfrac{R_2}{\delta}\right)I_0\left(\beta_1 \dfrac{R_1}{\delta}\right)\right]} \qquad (37)$$

where β_1 is given by Eq. (33). Under the one-term approximation, the fin efficiency is

$$\eta' = \frac{2R_1}{(R_2^2 - R_1^2)h} \cdot \left(\frac{\beta_1^2}{\delta}\right) \cdot \frac{\dfrac{k_1 t}{\delta^2 h} + \dfrac{k_2}{h\delta} + \dfrac{k_1 t}{k_2 \delta}}{\left[\dfrac{\beta_1^2 k_2}{h\delta} + \left(\dfrac{\beta_1 k_2}{h\delta}\right)^2 + \dfrac{k_1 t}{h^2 \delta^3 k_2}(k_2 \beta_1 + h\delta\beta_1)^2\right]} \cdot \frac{\left[K_1\left(\beta_1 \dfrac{R_1}{\delta}\right)I_1\left(\beta_1 \dfrac{R_2}{\delta}\right) - K_1\left(\beta_1 \dfrac{R_2}{\delta}\right)I_1\left(\beta_1 \dfrac{R_1}{\delta}\right)\right]}{\left[K_0\left(\beta_1 \dfrac{R_1}{\delta}\right)I_1\left(\beta_1 \dfrac{R_2}{\delta}\right) + K_1\left(\beta_1 \dfrac{R_2}{\delta}\right)I_0\left(\beta_1 \dfrac{R_1}{\delta}\right)\right]}$$
$$\cdot \left\{k_1 t \beta_1\left(\frac{k_2}{h\delta}\right)\cos \beta_1 + k_1 t \sin \beta_1 + \frac{k_2 \delta^2}{\beta_1} + \frac{k_2^2 \delta}{h}\sin \beta_1 - \frac{k_2 \delta^2}{\beta_1}\cos \beta_1\right\} \qquad (38)$$

It should be noted that while the series solution is completely intractable apart from the use of a computer, the one-term approximation is solvable on almost any hand-held calculator. In Fig. 5, the difference between η and η' is shown as a function of the frost thickness for the conditions given in Table 1. The one-term approximation over-estimates the fin efficiency by up to a few percent at the lowest fin efficiency. For fin efficiencies greater than 75%, the incurred penalty of using the one-term approximation over the series solution ($m=4$), Eqs. (38) and (29), respectively, is less than 2.3%.

Modifying the Heat Transfer Coefficient

Because the heat transfer in this problem is occurring by both sensible and latent modes of transport, the sensible convective coefficient, h, should be modified to include the latent transfer of heat. In this way, the mass transfer effects are accounted for in a modified air-side convective heat transfer coefficient, for the purpose of calculating fin efficiency. The effective heat transfer coefficient in this case is defined as
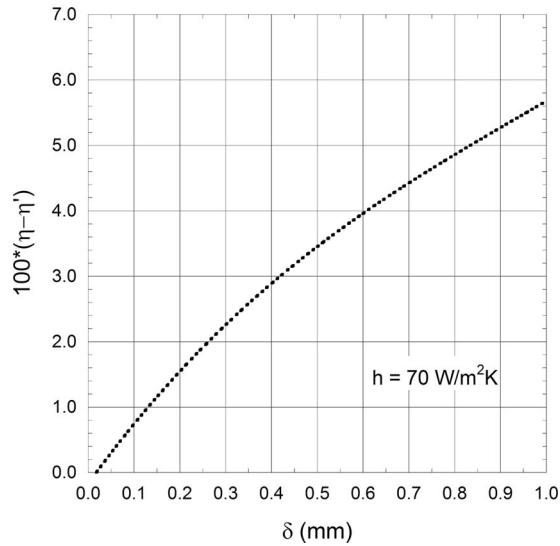
Fig. 5 The difference between the series solution and the one-term approximation is shown using the conditions of Table 1

$$h_{\text{eff}} = \left(h + \frac{Q_{\text{latent}}}{Q_{\text{sensible}}} h \right) = h + \frac{\dot{m}_f i_f}{A_{\text{tot}} \Delta T_{\text{lm},s}} \qquad (39)$$

where $\dot{m}_f$ represents the mass deposition rate of the frost, i_f is the ablimation energy, and A_{tot} is the heat exchanger total surface area. In this definition, $\Delta T_{\text{lm},s}$ represents the log-mean temperature difference between the air-stream temperature and the frost surface temperature and is defined as

$$\Delta T_{\text{lm},s} = \frac{(T_{a,\text{up}} - T_f) - (T_{a,\text{down}} - T_f)}{\ln[(T_{a,\text{up}} - T_f)/(T_{a,\text{down}} - T_f)]} \qquad (40)$$

This effective heat transfer coefficient should be used in place of h in the above equations. The effect of using this modified heat transfer coefficient is small, but it can lower the fin efficiency by 2.3%–5.3% as shown in Fig. 6, which was based on the data of Table 2. It should be pointed out that the idea of using a modified heat transfer coefficient has already been suggested in the litera-
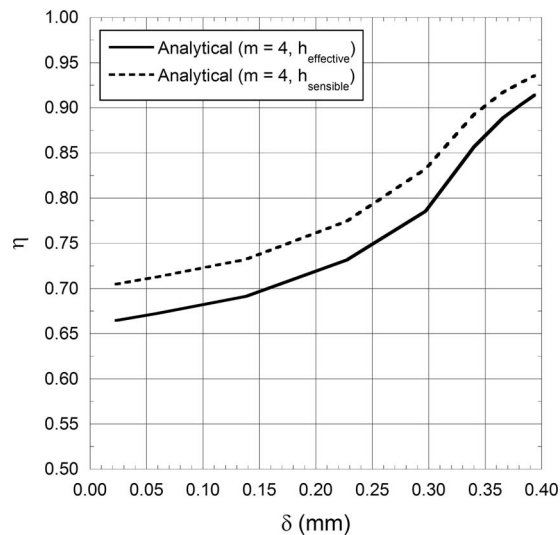

Fig. 6 The difference between using the sensible heat transfer coefficient and the modified convective coefficient in the calculations is shown using the data from Table 2. Note that the convective heat transfer coefficient is not constant; it decreases with frost thickness.

ture. For example, Lin et al. [8] purport this idea in their work on the effect of inlet relative humidity on wet fin efficiency but define their modified convective coefficient using a linear temperature difference. All the results presented earlier were based on the effective heat transfer coefficient described above.

Conclusions

The fin efficiency for a two-dimensional frost layer on a one-dimensional fin has been presented. An exact solution was obtained by separation of variables exploiting an unusual orthogonality condition. Unlike previous solutions for frosted-fin efficiency, this new solution accounts for two-dimensional conduction in the frost layer and necessitates fewer simplifying assumptions. It was demonstrated that even when mass transfer effects are lumped into the air-side convective coefficient, neglecting the frost conduction resistance may result in an overestimate of the fin efficiency by several percent. Conditions are also developed under which a one-term approximation to the solution is sufficient. The analytical solution presented in this paper, and the one-term approximation, have broad applicability in addition to their use for calculating fin efficiency of frost-coated fins.

Acknowledgment

Appendix

Sector Method for Plain-Fin Geometries. The radius ratio, RR_n, and the surface area of each sector, S_n, are calculated as follows:

Sectors with constant M edge (in Fig. 1, zones 2, 3, 6, and 7)

$$\text{RR}_n = \frac{M}{r_{if}} \sqrt{\left(\frac{2n-1}{2N} \right)^2 + \left(\frac{L}{M} \right)^2}$$

$$S_n = \frac{r_{if}^2}{2}(\text{RR}_n^2 - 1)\left[\tan^{-1}\left(\frac{nM}{NL} \right) - \tan^{-1}\left(\frac{(n-1)M}{NL} \right) \right]$$

where $r_{if} = (D_{ot} + 2t)/2$ is the inner radius corrected for fins with collars touching the adjacent fin and $n = 1, 2, 3, \ldots. N$ is the number of sectors in each zone.

Sectors with constant L edge (in Fig. 1, zones 1, 4, 5, and 8)

$$\text{RR}_n = \frac{M}{r_{if}} \sqrt{\left(\frac{2n-1}{2N} \right)^2 \left(\frac{L}{M} \right)^2 + 1}$$

$$S_n = \frac{r_{if}^2}{2}(\text{RR}_n^2 - 1)\left[\tan^{-1}\left(\frac{nL}{NM} \right) - \tan^{-1}\left(\frac{(n-1)L}{NM} \right) \right]$$

where $M = S_T/2$ and $L = S_L/2$.

The total efficiency is then the sum of the multiplication of the appropriate fin efficiency and S_n for each sector in each zone divided by the sum of the surface area for all sectors in each zone

$$\eta_f = \frac{\sum_{n=1}^{N} S_n \eta_n}{\sum_{n=1}^{N} S_n}$$

again where $n = 1, 2, 3, \ldots. N$ is the number of sectors in a zone.

Sector Method for Slit-Fin Geometries. For heat exchangers with slit fins, the radius ratio RR_n has been modified to better estimate the fin efficiency. For these surfaces, the constant M edge is replaced by a constant M_s edge, and the L edge is replaced by a constant L_s edge. Since the accurate calculation of the inner radius is particularly complicated for these geometries, the height of the slits is simply added to the sectors of constant M_s edge, and dividing sectors are assumed as before. (Note: The surface area and radius ratio for the sectors of constant L_s edge are calculated in the same manner as the plain fin heat exchanger.) *Sectors with*

constant M_s edge (in Fig. 1, zones 2, 3, 6, and 7)

$$RR_n = \frac{\left(M_s \sqrt{\left(\frac{2n-1}{2N}\right)^2 + \left(\frac{L}{M}\right)^2} \right) + h_s}{r_{if}}$$

where $n=1,2,3,\ldots N$ is the number of sectors in each zone and h_s is the height of the slits as measured directly from the fin surface.

Nomenclature

A = heat exchanger surface area (m^2)
Bi = Biot number, $h\delta/k_2 \, (1+\psi)$
h = convective heat transfer coefficient ($\text{W m}^{-2}\,\text{K}$)
i = enthalpy of ablimation (J kg^{-1})
k = thermal conductivity ($\text{W m}^{-1}\,\text{K}$)
$\dot{m}$ = mass deposition rate (kg s^{-1})
M = dimensionless group, R_2/δ
N = dimensionless group defined in Eq. (15b)
R_1 = tube radius, see Fig. 2 (m)
R_2 = fin radius; half the distance between tubes, see Fig. 2 (m)
t = half fin thickness, see Fig. 2 (m)
T = temperature (K)

Greek Symbols

β = eigenvalue satisfying Eq. (19)
δ = frost thickness (m)
ϵ = a small parameter, see Eq. (7e)
γ = modified eigenvalue, $M\beta$
η = fin efficiency, see Eq. (29)
η' = fin efficiency approximation, from a one-term approximation, see Eq. (38)

ψ = ratio of transverse thermal conduction resistances, $tk_2/\delta k_1$

Subscripts and Superscripts

1 = in the material of the fin
2 = in the material of the frost
a = of the air stream
b = at the fin base
eff = effective
f = frost
lm = log-mean difference
s = at the frost surface
tot = total
∞ = in the environment

References

[1] Xia, Y., and Jacobi, A. M., 2004, "An Exact Solution to Steady Heat Conduction in a Two-Dimensional Slab on a One-Dimensional Fin: Application to Frosted Heat Exchangers," Int. J. Heat Mass Transfer, **47**, pp. 3317–3326.
[2] Schmidt, T. E., 1949, "Heat Transfer Calculations for Extended Surfaces," Refrig. Eng., **57**, pp. 351–357.
[3] McQuiston, F. C., 1975, "Fin Efficiency With Combined Heat and Mass Transfer," ASHRAE Trans., **81**, pp. 350–355.
[4] Wu, G., and Bong, T. Y., 1994, "Overall Efficiency of a Straight Fin With Combined Heat and Mass Transfer," ASHRAE Trans., **100**(1), pp. 367–374.
[5] Hong, K. T., and Webb, R. L., 1996, "Calculation of Fin Efficiency for Wet and Dry Fins," HVAC&R Res., **2**(1), pp. 27–41.
[6] Mago, P. J., and Sherif, S. A., 2002, "Modeling the Cooling Process Path of a Dehumidifying Coil Under Frosting Conditions," J. Heat Transfer, **124**(6), pp. 1182–1191.
[7] Kondepudi, S. N., and O'Neal, D. L., 1993, "A Simplified Model of Pin Fin Heat Exchangers Under Frosting Conditions," ASHRAE Trans., **99**(1), pp. 754–761.
[8] Lin, Y.-T., Hsu, K.-C., Chang, Y.-J., and Wang, C.-C., 2001, "Performance of Rectangular Fin in Wet Conditions: Visualization and Wet Fin Efficiency," J. Heat Transfer, **123**(5), pp. 827–836.
[9] Kim, G. J., and Jacobi, A. M., 1999, "Condensate Accumulation Effects on the Air-Side Thermal Performance of Slit-Fin Surfaces," M.S. thesis, University of Illinois at Urbana-Champaign, IL.

Fully Developed Laminar Free Convection With Variable Thermophysical Properties Between Two Open-Ended Vertical Parallel Plates Heated Asymmetrically With Large Temperature Differences

Asterios Pantokratoras

School of Engineering,
Democritus University of Thrace,
67100 Xanthi, Greece
e-mail: apantokr@civil.duth.gr

The steady laminar fully developed flow between two isothermal parallel plates is studied in this paper. The investigation concerns air, engine oil, and water taking into account the variation of all physical properties (μ, k, and ρ) with temperature. The results are obtained with the direct numerical solution of the governing equations and cover large temperature differences not treated until now. The largest differences of volume flow rate and vertical heat flux from the corresponding constant properties values reach 1568% and 2120% in air, 139% and 247% in oil, and 62% and 55% in water. [DOI: 10.1115/1.2175154]

1 Introduction

The study of fully developed free convection between parallel plates at constant temperature has been initiated by Ostrach [1]. Sinha [2] studied this problem using as a working fluid water at low temperatures where the relation between density and temperature is nonlinear. However the other water properties (viscosity and thermal conductivity) have been considered constants. The first exact solutions for free convection in a vertical parallel plate channel with asymmetric heating for a fluid with constant properties (c.p.) was presented by Aung [3]. Vajravelu and Sastri [4] reconsidered the problem treated by Sinha using a more accurate relation between water density and temperature, ignoring again the variation of other water properties with temperature. Vajravelu [5], in a subsequent paper, treated the same problem using water

and air as working fluids and considering all fluid thermophysical properties (ρ, μ, k, c_p) as linear functions of temperature. However, the results are valid for room temperatures between 10 and 25 °C. Chenoweth and Paolucci [6] presented exact solutions for a perfect gas using the Sutherland law for viscosity and thermal conductivity and considering the ambient fluid temperature equal to the reference temperature (mean temperature of the two plates). Chenoweth and Paolucci [7] extended the previous work to cases where the ambient fluid temperature is different from the reference temperature. The presented results in both works are valid for the temperature range between 120 K and 480 K.

The objective of the present paper is to present results for free convection between vertical parallel plates with large temperature differences for three fluids taking into account the variation of all thermophysical properties (ρ, μ, k) with temperature. The fluids are air, engine oil, and water and the temperature ranges are 150–3000 K, 273–430 K, and 0–40 °C, respectively.

2 The Mathematical Model

Consider laminar flow between two vertical plates with u and v denoting, respectively, the velocity components in the x and y direction, where x is vertically upwards and y is the coordinate perpendicular to x. For steady, two-dimensional flow the equations appropriate to the variable property situation are

$$\text{continuity equation:} \quad \frac{\partial(\rho u)}{\partial x} + \frac{\partial(\rho v)}{\partial y} = 0 \qquad (1)$$

momentum equation:

$$\rho\left(u\frac{\partial u}{\partial x} + v\frac{\partial u}{\partial y}\right) = -\frac{\partial p}{\partial x} + \frac{\partial}{\partial y}\left(\mu\frac{\partial u}{\partial y}\right) + (\rho_a - \rho)g \qquad (2)$$

$$\text{energy equation:} \quad \rho c_p\left(u\frac{\partial T}{\partial x} + v\frac{\partial T}{\partial y}\right) = \frac{\partial}{\partial y}\left(k\frac{\partial T}{\partial y}\right) \qquad (3)$$

where ρ is the fluid density, ρ_a is the ambient fluid density, μ is the dynamic viscosity, p is the dynamic pressure (pressure due to the motion of the fluid), T is the fluid temperature, k is the fluid thermal conductivity, and c_p is the fluid specific heat. When the channel height is much larger than the channel spacing, the flow in the channel may reach a state in which steamlines are parallel to one another. In this case the quantities v, $\partial T/\partial x$, $\partial u/\partial x$ are zero in the entire cross section and the flow is called fully developed. Except that in fully developed flow of free convection in a vertical channel with both ends open to the ambient fluid, with constant plate temperature, the dynamic pressure gradient is also zero ([2,3,5] and Aung and Worku [8]). Thus, for fully developed flow the above equations reduce to

$$\text{momentum equation:} \quad \frac{\partial}{\partial y}\left(\mu\frac{\partial u}{\partial y}\right) + (\rho_a - \rho)g = 0 \qquad (4)$$

$$\text{energy equation:} \quad \frac{\partial}{\partial y}\left(k\frac{\partial T}{\partial y}\right) = 0 \qquad (5)$$

Table 1 Flow rate (M) and vertical heat flux (Q) for air in upward flow

T_1 K	T_2 K	T_a K	M	M c.p.	Difference $(M-M_{cp})/M$ %	Q	Q c.p.	Difference $(Q-Q_{cp})/Q$ %
150	3000	150	0.0793	0.0417	47	0.0551	0.0222	60
150	2000	150	0.0838	0.0417	50	0.0512	0.0222	57
150	1000	150	0.0763	0.0417	45	0.0445	0.0222	50
150	500	150	0.0659	0.0417	37	0.0382	0.0222	42
150	200	150	0.0486	0.0417	14	0.0270	0.0222	18
150	151	150	0.0417	0.0417	0	0.0222	0.0222	0
200	3000	150	0.0792	0.0424	46	0.0552	0.0229	59
1000	3000	150	0.0782	0.0541	31	0.0596	0.0358	40
2000	3000	150	0.0807	0.0687	15	0.0699	0.0568	19
2500	3000	150	0.0823	0.0760	8	0.0762	0.0694	9
3000	3000	150	0.0833	0.0833	0	0.0833	0.0833	0

The following boundary conditions were applied at the two plates:

$$x > 0 \quad y = 0 \quad u = 0, \ T = T_1 \tag{6}$$

$$x > 0 \quad y = b \quad u = 0, \ T = T_2 \tag{7}$$

where T_1 is the first plate temperature and T_2 is the temperature of the second plate which lies at a distance b from the first plate.

Normal air is a transparent, nonparticipating fluid and the boundary conditions in the present problem are prescribed temperature at the plates. This means that the standard equations of motion and energy are valid (Ozisik [9]) and for that reason radiation has not been included in our analysis.

In some special cases Eqs. (4) and (5) may accept analytical solutions. In the present work we solved these equations directly, without any transformation, using the finite difference method of Patankar [10]. The forward step size Δx was 0.01 mm and the lateral grid cell is 500. For a fixed value of lateral grid points the results are independent of Δx. The only thing that changes is the distance from the channel entrance until the results take their final value. However the results are dependent on the number of lateral grid points. We tried different numbers of lateral grid points and we found that usually 100 lateral grid points are sufficient. The $\Delta x = 0.01$ mm and 500 lateral grid points are very efficient and the results of the present work are grid independent.

3 Results and Discussion

Two important quantities for this problem is the nondimensional volume flow rate between the plates and the nondimensional vertical heat flux defined by the following equations ([3])

$$M = \int_0^1 U dY \tag{8}$$

Table 2 Flow rate (M) and vertical heat flux (Q) for air in downward flow

T_1 K	T_2 K	T_a K	M	M c.p.	Difference $(M-M_{cp})/M$ %	Q	Q c.p.	Difference $(Q-Q_{cp})/Q$ %
3000	150	3000	0.0025	0.0417	1568	0.0010	0.0222	2120
3000	500	3000	0.0077	0.0417	442	0.0030	0.0222	640
3000	1000	3000	0.0138	0.0417	202	0.0055	0.0222	304
3000	2000	3000	0.0251	0.0417	66	0.0108	0.0222	106
3000	2500	3000	0.0324	0.0417	29	0.0151	0.0222	47
3000	2999	3000	0.0417	0.0417	0	0.0222	0.0222	0
2500	150	3000	0.0050	0.0490	880	0.0026	0.0297	1042
2000	150	3000	0.0079	0.0563	613	0.0050	0.0386	672
1000	150	3000	0.0191	0.0709	271	0.0160	0.0605	278
500	150	3000	0.0356	0.0782	120	0.0332	0.0734	121
150	150	3000	0.0833	0.0833	0	0.0833	0.0833	0

Table 3 Flow rate (M) and vertical heat flux (Q) for oil in upward flow

T_1 K	T_2 K	T_a K	M	M c.p.	Difference $(M-M_{cp})/M$ %	Q	Q c.p.	Difference $(Q-Q_{cp})/Q$ %
273	430	273	0.0540	0.0417	23	0.0398	0.0222	44
273	380	273	0.0323	0.0417	29	0.0238	0.0222	7
273	350	273	0.0361	0.0417	16	0.0247	0.0222	10
273	300	273	0.0455	0.0417	8	0.0271	0.0222	18
273	280	273	0.0429	0.0417	3	0.0235	0.0222	6
273	274	273	0.0420	0.0417	<1	0.0224	0.0222	<1
280	430	273	0.0532	0.0435	18	0.0394	0.0240	39
300	430	273	0.0509	0.0488	4	0.0379	0.0296	22
350	430	273	0.0645	0.0621	4	0.0510	0.0466	9
380	430	273	0.0702	0.0701	<1	0.0599	0.0590	2
430	430	273	0.0833	0.0833	0	0.0833	0.0833	0

Table 4 Flow rate (M) and vertical heat flux (Q) for oil in downward flow

T_1 K	T_2 K	T_a K	M	M c.p.	Difference $(M-M_{cp})/M$ %	Q	Q c.p.	Difference $(Q-Q_{cp})/Q$ %
430	273	430	0.0205	0.0417	103	0.0064	0.0222	247
430	280	430	0.0210	0.0417	99	0.0068	0.0222	226
430	300	430	0.0224	0.0417	86	0.0081	0.0222	174
430	350	430	0.0345	0.0417	21	0.0157	0.0222	41
430	380	430	0.0383	0.0417	9	0.0191	0.0222	16
430	429	430	0.0417	0.0417	0	0.0222	0.0222	0
400	273	430	0.0305	0.0496	63	0.0133	0.0305	129
380	273	430	0.0230	0.0549	139	0.0121	0.0369	205
350	273	430	0.0371	0.0629	70	0.0254	0.0478	88
300	273	430	0.0724	0.0762	5	0.0654	0.0697	7
280	273	430	0.0812	0.0815	<1	0.0793	0.0797	<1
273	273	430	0.0833	0.0833	0	0.0833	0.0833	0

$$Q = \int_0^1 U\vartheta \, dY \tag{9}$$

The dimensionless vertical velocity U, the dimensionless temperature θ, and the dimensionless distance Y are given by the following equations

$$U = \frac{ub}{\nu_r \, \mathrm{Gr}} \tag{10}$$

$$\vartheta = \frac{T - T_a}{T_2 - T_a} \tag{11}$$

$$Y = \frac{y}{b} \tag{12}$$

where ν_r is the fluid kinematic viscosity calculated at reference temperature $(T_1 + T_2)/2$, Gr is the Grashof number, and T_a is the ambient fluid temperature. The Grashof number is defined as

$$\mathrm{Gr} = \frac{gb^3}{\nu_r^2} \frac{\rho_a - \rho_2}{\rho_r} \tag{13}$$

where ρ_2 is the fluid density at the second plate and ρ_r is the fluid density at reference temperature. In the present work the Rayleigh number is lower than 10^8 (Kakac and Yener [11]) and the flow is laminar.

3.1 Results for Air. The density, dynamic viscosity, and thermal conductivity of air in the temperature range $150 \text{ K} \leqslant T \leqslant 3000 \text{ K}$ are given by Zografos et al. [12]. The volume flow rate and the vertical heat flux calculated by the present method are shown in Table 1 for upward flow. In the same table the quantities calculated by the analytical solutions given by [3] have been also included for comparison (c.p. mean constant properties). In Table 2 the volume flow rate and the vertical heat flux are given for downward flow.

3.2 Results for Engine Oil. The density, dynamic viscosity, and thermal conductivity of oil in the temperature range 273 K

Table 5 Flow rate (M) and vertical heat flux (Q) for water in upward flow

T_1 °C	T_2 °C	T_a °C	M	M c.p.	Difference $(M-M_{cp})/M$ %	Q	Q c.p.	Difference $(Q-Q_{cp})/Q$ %
4	40	4	0.0308	0.0417	35	0.0182	0.0222	22
4	30	4	0.0286	0.0417	46	0.0166	0.0222	34
4	20	4	0.0275	0.0417	52	0.0157	0.0222	41
4	10	4	0.0262	0.0417	59	0.0147	0.0222	51
4	5	4	0.0258	0.0417	62	0.0143	0.0222	55
5	40	4	0.0317	0.0428	35	0.0190	0.0233	23
10	40	4	0.0371	0.0486	31	0.0238	0.0293	23
20	40	4	0.0501	0.0602	20	0.0374	0.0439	17
30	40	4	0.0654	0.0718	10	0.0567	0.0619	9
40	40	4	0.0833	0.0833	0	0.0833	0.0833	0

Table 6 Flow rate (M) and vertical heat flux (Q) for water in downward flow

T_1 °C	T_2 °C	T_a °C	M	M c.p.	Difference $(M-M_{cp})/M$ %	Q	Q c.p.	Difference $(Q-Q_{cp})/Q$ %
40	0	40	0.0559	0.0417	25	0.0269	0.0222	17
40	4	40	0.0526	0.0417	21	0.0256	0.0222	13
40	10	40	0.0494	0.0417	16	0.0245	0.0222	9
40	20	40	0.0460	0.0417	9	0.0234	0.0222	5
40	30	40	0.0432	0.0417	3	0.0225	0.0222	1
40	39	40	0.0417	0.0417	0	0.0222	0.0222	0
30	0	40	0.0684	0.0521	24	0.0416	0.0333	20
20	0	40	0.0783	0.0625	20	0.0580	0.0472	19
10	0	40	0.0838	0.0729	13	0.0731	0.0639	13
0	0	40	0.0833	0.0833	0	0.0833	0.0833	0

$\leqslant T \leqslant 430$ K are given by [12]. The volume flow rate and the vertical heat flux are shown in Tables 3 and 4 for upward and downward flow, respectively.

3.3 Results for Water. The density of water is a function of temperature, salinity, and pressure. In this paper the International Equation of State for Seawater (Fofonoff [13]) is used for the calculation of density. For the calculation of dynamic viscosity and thermal conductivity the formulas given by Kukulka et al. [14] were used. The volume flow rate and the vertical heat flux are shown in Tables 5 and 6 for upward and downward flow, respectively.

From the above tables we see that the variation of physical properties with temperature play an important role in the results. The largest differences of volume flow rate and vertical heat flux from the corresponding constant properties values appear in downward air flow and reach 1568% and 2120%, respectively. For oil the differences reach 139% and 247% in downward flow and for water 62% and 55% near the density extremum $(4°C)$.

References

[1] Ostrach, S., 1952, "Laminar Natural Convection Flow and Heat Transfer of Fluids With and Without Heat Sources in Channels With Constant Wall Temperature," Report No. NACA TN 2863.

[2] Sinha, P. C., 1969, "Fully Developed Laminar Free Convection Flow Between Vertical Parallel Plates," Chem. Eng. Sci., **24**, pp. 33–38.

[3] Aung, W., 1972, "Fully Developed Laminar Free Convection Between Vertical Plates Heated Asymmetrically," Int. J. Heat Mass Transfer, **15**, pp. 1577–1580.

[4] Vajravelu, K., and Sastri, K., 1977, "Fully Developed Laminar Free Convection Flow Between Two Parallel Vertical Walls," Int. J. Heat Mass Transfer, **20**, pp. 655–660.

[5] Vajravelu, K., 1979, "The Effect of Variable Fluid Properties on the Free Convective Flow of Air/Water Confined Between Two Parallel Vertical Walls," Acta Mech., **31**, pp. 199–211.

[6] Chenoweth, D. R., and Paolucci, S., 1985, "Gas Flow in Vertical Slots With Large Horizontal Temperature Differences," Phys. Fluids, **28**, pp. 2365–2374.

[7] Chenoweth, D. R., and Paolucci, S., 1986, "Gas Flow in Open Vertical Slots With Large Horizontal Temperature Differences and Arbitrary External Temperature," Phys. Fluids, **29**, pp. 3187–3198.

[8] Aung, W., and Worku, G., 1986, "Theory of Fully Developed, Combined Convection Including Flow Reversal," ASME J. Heat Transfer, **108**, pp. 485–488.

[9] Ozisik, M. N., 1987, "Interaction of Radiation With Convection," in *Handbook of Single-Phase Convective Heat Transfer*, Wiley, New York.

[10] Patankar, S. V., 1980, *Numerical Heat Transfer and Fluid Flow*, McGraw-Hill, New York.

[11] Kakac, S., and Yener, Y., 1995, *Convective Heat Transfer*, CRC Press, Boca Raton.

[12] Zografos, A. I., Martin, W. A., and Sunderland, J. E., 1987, "Equations of Properties as a Function of Temperature for Seven Fluids," Comput. Methods Appl. Mech. Eng., **61**, pp. 177–187.

[13] Fofonoff, N. P., 1985, "Physical Properties of Seawater: A New Salinity Scale and Equation of State for Seawater," J. Geophys. Res., **90**(C2), pp. 3332–3342.

[14] Kukulka, D. J., Gebhart, B., and Mollendorf, J. C., 1987, "Thermodynamic and Transport Properties of Pure and Saline Water," Adv. Heat Transfer, **18**, pp. 325–363.

Weighting Factors for Single-Step Trapezoidal Method

Fuzhang Zhao

Department of Mechanical Engineering and Mechanics,
Drexel University,
3141 Chestnut Street,
Philadelphia, PA 19104
e-mail: Fuzhang.Zhao@drexel.edu

The uses of a weighting factor along with a time step in a single-step trapezoidal method to solve a first-order parabolic system have been systematically studied. The weighting factors are used in two main types: constants and variables. The most commonly used constant weighting factors can be defined by the ratio of the Fibonacci sequence. Among them, the optimal weighting factor is 0.618, resulting in a balance between the overall accuracy and efficiency. With the finite element formulation, the space and time dimensions can be discretized separately. For the time discretization only, there exists a zero-error dimensionless time step if a weighting factor is within the range of 0.5–1.0. By taking advantage of the zero-error condition, the weighting factor can be correlated with a time step. The influence of spatial dimensions is lumped into a nonzero eigenvalue of the system. Through validity tests of two benchmark linear problems, the variable weighting factor for a single-step trapezoidal method is shown to be accurate, efficient, and stable. The relevant features have been captured. [DOI: 10.1115/1.2175155]

Keywords: weighting factor, time step, single-step trapezoidal method, parabolic system, eigenvalue, finite element method

Introduction

A first-order parabolic system describes many engineering problems. In solving such a system, there are two families of algorithms: trapezoidal and exponential. The most commonly used single-step trapezoidal methods include the Euler forward and backward methods [1], the Crank-Nicolson method [2], the Liniger method [3], and the Galerkin method [4]. The generalized trapezoidal family of algorithms along with the two-step methods and three-step methods has been summarized by Tamma, Zhou, and Kanapady [5]. The practical time-stepping schemes have been reviewed in detail by Wood [6]. For the exponential family of algorithms, an exponential scheme was developed by Patankar and Baliga [7], extended by Chen and Li [8], and generalized by Mercer [9]. As the problems become more and more time consuming, it becomes clear that the efficiency of a solution is just as important as its accuracy. In order to use a relatively large time step without losing solution accuracy, an optimal single-step exponential scheme was developed by Li [10]. The single-step exponential methods are mainly used in the finite difference method.

In numerical simulations of transient heat conduction problems using finite element methods, the single-step trapezoidal families of algorithms are usually adopted due to their simplicities in formulation. The generalized trapezoidal method and its stability have been summarized by Belytschko and Hughes [11], and Hughes [12]. In single-step trapezoidal methods, the use of different combinations of a weighting factor and a time step will significantly influence the numerical results. In order to reduce the overall error from an arbitrary time step, an optimal weighting factor for the single-step trapezoidal method was developed by Zhao [13]. Based on the zero-error between the analytical solution and the numerical solution in time discretization, a weighting factor can be correlated with a time step. The spatial effect can be included for solving general first-order parabolic partial differential equations.

Formulation

In the finite element formulation, discretization of space and time can be conducted separately. A general finite element equation for transient heat conduction problems after discretization on space documented by Zienkiewicz and Taylor [14] reads

$$[C]\{\dot{T}\} + [K]\{T\} = \{Q\} \tag{1}$$

With time discretization using the single-step trapezoidal method, Eq. (1) takes the following form

$$\left(\frac{[C]}{\Delta t} + \theta[K]\right)\{T_{t+\Delta t}\} = \left(\frac{[C]}{\Delta t} - (1-\theta)[K]\right)\{T_t\} + \theta\{Q_{t+\Delta t}\}$$
$$+ (1-\theta)\{Q_t\} \tag{2}$$

A weighting factor θ is bounded within the interval [0, 1]. In these traditional single-step trapezoidal methods, weighting factors are usually the same for all time steps.

In order to study the error purely from a time discretization, the influence of spatial dimensions is temporarily ignored. Solving the one-deg Eq. (1) with $\lambda = K/C$, a constant Q within a time step and a constant initial condition of T_0 yields

$$T = \frac{Q}{K}[1 - \exp(-\lambda t)] + T_0 \exp(-\lambda t) \tag{3}$$

Correspondingly, the recurrence relationship for the numerical solution can be readily obtained from Eq. (2) as

$$T_{t+\Delta t} = \frac{1 - (1-\theta)(\lambda \Delta t)}{1 + \theta(\lambda \Delta t)} T_t + \frac{Q\Delta t/C}{1 + \theta(\lambda \Delta t)} \tag{4}$$

The dimensionless absolute error (DAE) $\bar{\varepsilon}$ as a function of the weighting factor and dimensionless time step (DTS) $\Delta\bar{t} = \lambda\Delta t$ is defined as

$$\bar{\varepsilon} = \frac{\varepsilon}{T_0 - Q/K} = \frac{1 - (1-\theta)\Delta\bar{t}}{1 + \theta\Delta\bar{t}} - \exp(-\Delta\bar{t}) \tag{5}$$

The variation trend of asymptotic dimensionless absolute error with weighting factors as the dimensionless time step approaches infinity can be obtained by

$$E = \lim_{\Delta\bar{t}\to\infty} \bar{\varepsilon} = \lim_{\Delta\bar{t}\to\infty}\left[\frac{1 - (1-\theta)\Delta\bar{t}}{1 + \theta\Delta\bar{t}} - \exp(-\Delta\bar{t})\right] = \frac{\theta-1}{\theta} \tag{6}$$

In order to evaluate $\bar{\varepsilon}$ as a function of $\Delta\bar{t}$ with different θ, weighting factors are chosen to be the ratio of the Fibonacci sequence (0, 1, 1, 2, 3, 5, 8, 13, 21, 34, 55, 89, 144, …) although other values can also be used. They are $0/1$, $1/1$, $1/2$, $2/3$, $3/5$, and 0.618, which correspond to F_0/F_1 (the Euler forward method), F_1/F_2 (the Euler backward method), F_2/F_3 (the Crank-Nicolson method), F_3/F_4 (the Galerkin method), F_4/F_5, and F_{n-1}/F_n as n approaches infinity (the optimal weighting factor [13]), respectively. The calculated results of dimensionless absolute error as a function of the dimensionless time step with different weights are shown in Fig. 1.

It is worthwhile to notice that there exists a zero DAE at a certain DTS corresponding to a weighting factor in the range of $0.5 \leq \theta \leq 1$. Based on this, the weighting factor can be correlated with the time step by letting $\bar{\varepsilon} = 0$ and solving for θ from Eq. (5) as

$$\theta = \frac{1}{1 - \exp(-\lambda\Delta t)} - \frac{1}{\lambda\Delta t} \quad (\lambda > 0) \tag{7}$$
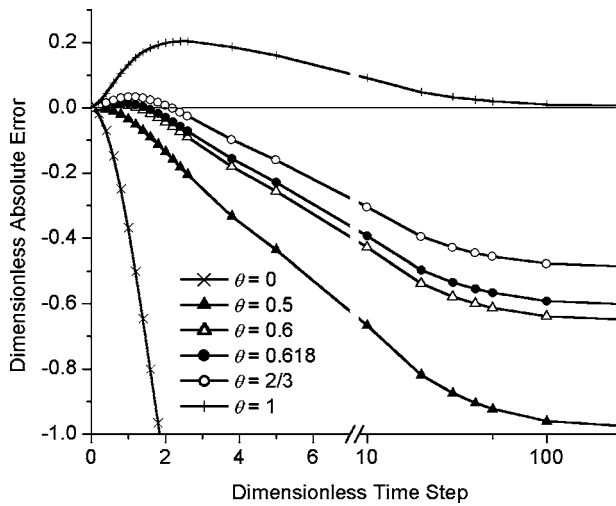
Fig. 1 DAE as a function of DTS with different θ

Fig. 2 Temperature comparison for example 1

For the exponential form of a solution, the effect of space dimensions can be lumped as an eigenvalue problem

$$([K] - \lambda_l[C])\{\psi_l\} = \{0\} \quad l \in \{1, 2, \ldots, m\} \quad (8)$$

For a single-mode problem, the dominant eigenvalue λ can be obtained from an initial condition. For a general multimode problem, the smallest nonzero eigenvalue λ_i will be used in Eq. (7). The smallest eigenvalue was used in the optimal exponential difference scheme [10]. The smallest nonzero eigenvalue could be a dominant one but the dominant eigenvalue is not necessarily the smallest nonzero one.

The single-step trapezoidal method is conditionally stable, the zero-error dimensionless time step does not exist and the asymptotic error is not bounded when the weighting factor is within the range of $0 \leq \theta < 0.5$. It is unconditionally stable, since a zero-error dimensionless time step exists and the asymptotic error is bounded, when the weighting factor is taken from $0.5 \leq \theta \leq 1.0$. If a solution is accurate its stability is certain. An unconditional stability, however, does not guarantee the accuracy of a solution. Since the zero-error dimensionless time step varies from zero to infinity as the weighting factor changes from 0.5 to 1.0, a large time step can be used for a single-step trapezoidal method.

Procedures for Finite Element Scheme

The procedure to systematically determine the matched pair of time step and weighting factor using the finite element scheme is as follows:

(i) Apply boundary conditions and modify the $[K]$ matrix;
(ii) Input the dominant eigenvalue if it is known from initial conditions and go to step (iv);
(iii) Numerically determine the smallest nonzero eigenvalue λ_i from Eq. (8);
(iv) Select a time step Δt based on the need;
(v) Calculate the weighting factor θ based on Eq. (7), using the time step Δt selected by a user and the eigenvalue λ obtained from step (ii) or step (iii);
(vi) Substitute the matched Δt and θ into Eq. (2) to conduct the recurrent calculations.

The approximate total time to reach a steady state, t_s, can be estimated by making, for example, $\exp(-\lambda_i t_s) = 0.001$. The time step can then be selected by $\Delta t = 7/(\lambda N)$.
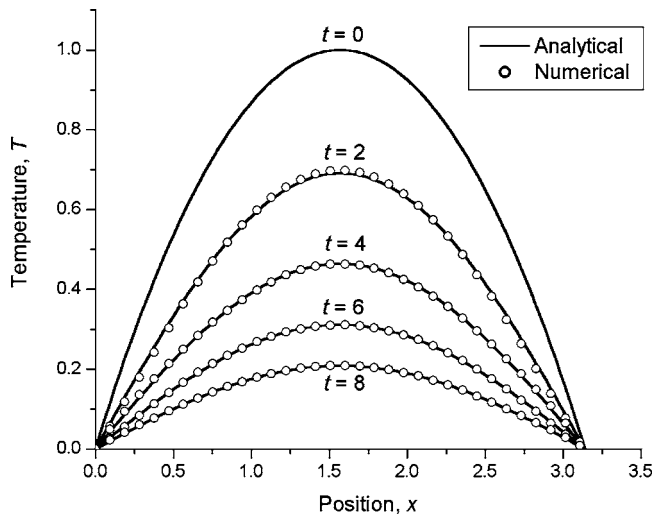
Evaluation of Accuracy

The first example considered involves a one-dimensional bar with nonuniform initial temperatures. The partial differential equation, boundary conditions, and initial condition can be expressed in Eqs. (9)–(11), respectively,

$$\rho c \frac{\partial T}{\partial t} = \frac{\partial}{\partial x}\left(k \frac{\partial T}{\partial x}\right) \quad 0 \leq x \leq L \quad (9)$$

$$T(0, t) = T(L, t) = 0 \quad t > 0 \quad (10)$$

$$T(x, 0) = 4T_0 \left(\frac{x}{L}\right)\left(1 - \frac{x}{L}\right) \quad (11)$$

The first example has the following solution

$$T(x, t) = \frac{16T_0}{\pi^3} \sum_{n=1}^{\infty} \frac{[1 - (-1)^n]}{n^3} \sin\left(\frac{n\pi x}{L}\right) \exp\left[-\frac{k}{\rho c}\left(\frac{n\pi}{L}\right)^2 t\right]$$

$$(12)$$

Constants for the first example are assumed to be $T_0 = 1$, $k = 2$, $\rho c = 10$, and $L = \pi$. In calculations of temperature at different times, 100 two-node elements were used. The numerical result of the smallest eigenvalue is $\lambda_1 = 0.2000164499$. With the value of $\Delta t = 2$, the corresponding weighting factor θ has been calculated as 0.5332475016. The first 1000 nonzero terms were used in the calculation of the analytical solution. The temperature comparisons between the analytical and the numerical results at different times are depicted in Fig. 2. The results of some locations at time $t = 2$ are listed in Table 1.

The T_{ana} and T_{num} are the temperatures calculated based on the analytical solution and numerical solution, respectively.

The second example considered involves a two-dimensional rectangular domain with nonuniform initial temperatures. The partial differential equation, boundary conditions, and initial condition are defined in Eqs. (13)–(15), respectively,

$$\rho c \frac{\partial T}{\partial t} = \frac{\partial}{\partial x}\left(k \frac{\partial T}{\partial x}\right) + \frac{\partial}{\partial y}\left(k \frac{\partial T}{\partial y}\right) \quad 0 \leq x \leq L \text{ and } 0 \leq y \leq W$$

$$(13)$$

$$T(0, y, t) = T(L, y, t) = T(x, 0, t) = T(x, W, t) = 0 \quad t > 0 \quad (14)$$

$$T(x, y, 0) = T_0 \sin\left(\frac{\pi x}{L}\right) \sin\left(\frac{\pi y}{W}\right) \quad (15)$$

Table 1 Temperature comparison at $t=2$ for example 1

x	T_{ana}	T_{num}	$\varepsilon = T_{num} - T_{ana}$
0.0π	0.00000000	0.00000000	0.0000
0.1π	0.21462428	0.20049996	−0.0141
0.2π	0.40762502	0.40023794	−0.0074
0.3π	0.56000292	0.56060599	0.0006
0.4π	0.65733005	0.66254016	0.0052
0.5π	0.69075915	0.69735035	0.0066
0.6π	0.65733005	0.66254016	0.0052
0.7π	0.56000292	0.56060599	0.0006
0.8π	0.40762502	0.40023794	−0.0074
0.9π	0.21462428	0.20049996	−0.0141
1.0π	0.00000000	0.00000000	0.0000

Table 2 Temperature comparisons with different methods

$t=\Delta t$	T_{ana}	Variable θ	T_{num}	Constant θ	T_{num} $(\theta=0.5)$
1	0.77880	0.5208116642	0.77875	0.5	0.77772
2	0.60653	0.5414940825	0.60644	0.5	0.59991
3	0.47237	0.5619218011	0.47226	0.5	0.45443
4	0.36788	0.5819767069	0.36777	0.5	0.33321
5	0.28650	0.6015511185	0.28639	0.5	0.23064
6	0.22313	0.6205502501	0.22302	0.5	0.14272
7	0.17377	0.6388939451	0.17366	0.5	0.06653
8	0.13534	0.6565176427	0.13523	0.5	−0.00014
9	0.10540	0.6733726059	0.10530	0.5	−0.05896
10	0.08208	0.6894254698	0.08199	0.5	−0.11125

The analytical solution can be found as

$$T(x,y,t) = T_0 \sin\left(\frac{\pi x}{L}\right)\sin\left(\frac{\pi y}{W}\right)\exp\left[-\frac{k}{\rho c}\pi^2\left(\frac{1}{L^2}+\frac{1}{W^2}\right)t\right]$$

(16)

In the finite element calculations, five thousand (100×50) four-node square elements with bilinear shape functions were used. The dominant eigenvalue of 0.25 can be determined from the initial condition. Constants for the second example are assumed to be $T_0=1$, $k=2$, $\rho c=10$, $L=2\pi$, and $W=\pi$. The largest error occurs at the center of the rectangular domain. The error as a function of position is depicted in Fig. 3. At the center, the numerically calculated temperature is 0.22302, the analytically calculated temperature is 0.22313 and the absolute error is -1.1×10^{-4}. The results of the temperature at the center location at different time steps solved by the current method and the Crank-Nicolson method ($\theta=0.5$) are compared and listed in Table 2.

The current approach is very accurate through all of the time steps studied from 1 up to 10 shown in Fig. 4 and therefore also very efficient. On the other hand, using the Crank-Nicolson method, the error increases with the time step. In order to keep certain accuracy, small time steps have to be used for the Crank-Nicolson method. Even using a time step as small as 1, the error of −0.00108 from the Crank-Nicolson method is much larger than that of −0.00005 from the current approach.
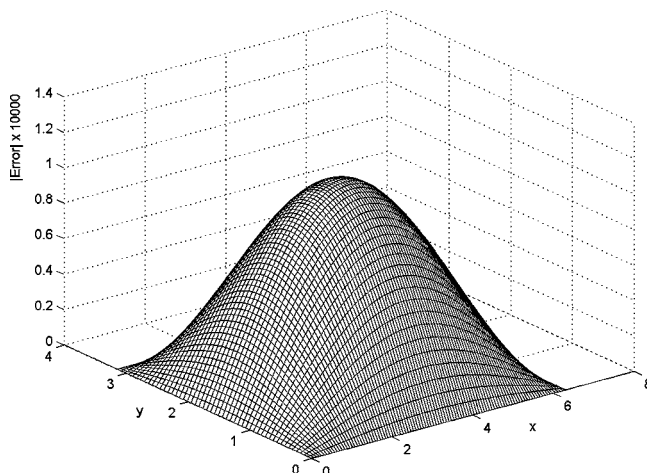
Conclusions

A systematic study of the relationship between errors and parameters including the weighting factor θ and time step Δt for the single-step trapezoidal method has been conducted. There exists a zero-error dimensionless time step for a given weighting factor within the range of 0.5–1.0. By taking advantage of the zero-error condition, the weighting factor can be correlated with a time step. With the correlated weighting factor and time step, the error due to time discretization can be reduced or even eliminated. For single-mode problems, "exact" solutions can be obtained numerically. For multimode problems, not "exact" but still very accurate solutions can be captured using the smallest nonzero eigenvalue of the system.

The numerical results for the two benchmarks agree very well with their corresponding analytical solutions. Therefore, the single-step trapezoidal method with a correlated weighting factor, which is better than the existing constant weighting factor methods, is accurate, efficient, and stable.

The current approach has only been tested for linear problems. In the future, the single-step trapezoidal method with an optimal weighting factor and a correlated weighting factor should be included and modified to solve nonlinear transient heat conduction problems.

Nomenclature

C = capacity for matrix
c = specific heat
E = asymptotic error
F_n = Fibonacci sequence
K = conductivity for matrix

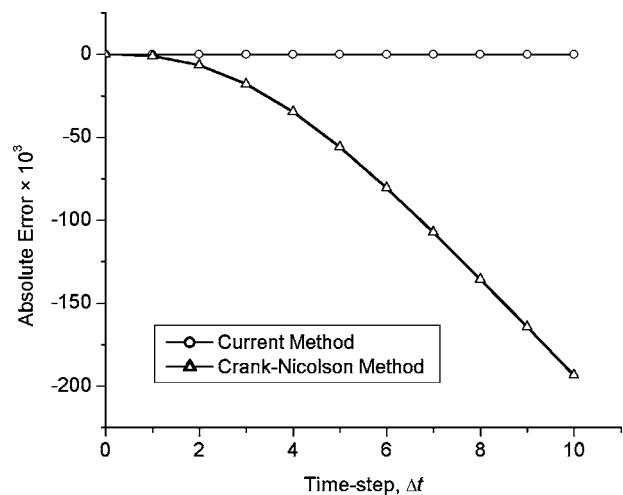**Fig. 3 Error as a function of position for example 2**

Fig. 4 Error comparison as a function of time step and methods

k = thermal conductivity
L = length
l = index for mode number
m = total number of nodes
N = total number of time intervals
n = index for the Fibonacci sequence
Q = thermal load
$\dot{T}$ = derivative of temperature to time
T_0 = constant initial temperature
T = temperature
t = time
W = width
x = horizontal coordinate
y = vertical coordinate

Greek Symbols

$\Delta\bar{t}$ = dimensionless time step
Δt = time step
$\bar{\varepsilon}$ = dimensionless absolute error
ε = absolute error
θ = weighting factor
λ = dominant eigenvalue of system
ρ = density
ψ = eigenvector

References

[1] Euler, L., 1913, "De Integratione Aequationum Differentialium per Approxi-mationem," Opera Omnia, Series Prima, Opera Mathematica, **11**, pp. 424–434.
[2] Crank, J., and Nicolson, P., 1947, "A Practical Method for the Numerical Evaluation of Solutions of Partial Differential Equations of the Heat Conduction Type," Proc. Cambridge Philos. Soc., **43**, pp. 50–67.
[3] Liniger, W., 1968, "Optimization of a Numerical Integration Method for Stiff System of Ordinary Differential Equations," IBM Research Report No. RC2198.
[4] Zlamal, M., 1977, *Finite Element Methods in Heat Conduction Problems*, Academic, New York.
[5] Tamma, K. K., Zhou, X., and Kanapady, R., 2002, "The Time Dimension and A Unified Mathematical Framework for First-Order Parabolic Systems," Numer. Heat Transfer, Part B, **41**, pp. 239–262.
[6] Wood, W. L., 1990, *Practical Time-Stepping Schemes*, Oxford University Press, New York.
[7] Patankar, S. V., and Baliga, B. R., 1978, "A New Finite-Difference Scheme for Parabolic Differential Equations," Numer. Heat Transfer, **1**, pp. 27–37.
[8] Chen, C. J., and Li, P., 1979, "Finite Differential Method in Heat Conduction—Application of Analytical Solution Technique," ASME Winter Annual Meeting, December 2–7, New York, ASME Paper No. 79-WA/T-50.
[9] Mercer, A. M., 1982, "Some New Finite-Difference Scheme for Parabolic Differential Equations," Numer. Heat Transfer, **5**, pp. 199–210.
[10] Li, S., 1988, "Optimal Exponential Difference Scheme for Solving Parabolic Partial Differential Equations," Numer. Heat Transfer, **14**, pp. 357–371.
[11] Belytschko, T., and Hughes, T. J. R., 1983, *Computational Methods for Transient Analysis*, Elsevier Science, North Holland, Amsterdam.
[12] Hughes, T. J. R., 1987, *The Finite Element Method*, Prentice-Hall, Englewood Cliffs, N.J.
[13] Zhao, F., 2003, "Optimal Weighting Factor for Single-Step Trapezoidal Method," 2003 ASME International Mechanical Engineering Congress and Exposition, November 15–21, Washington, D.C., Paper No. IMECE-41109.
[14] Zienkiewicz, O. C., and Taylor, R. L., 2000, *The Finite Element Method*, Butterworth-Heinemann, Boston, Vol. 2.

Highly Accurate Solutions of a Laminar Square Duct Flow in a Transverse Magnetic Field With Heat Transfer Using Spectral Method

Mohammed J. Al-Khawaja
e-mail: khawaja@qu.edu.qa

Mohammed Selmi

Department of Mechanical Engineering,
University of Qatar,
P. O. Box 2713,
Doha, State of Qatar

A liquid metal forced-convection fully developed laminar flow inside a square duct, whose surfaces are electrically insulated and subjected to a constant temperature in a transverse magnetic field, is solved numerically using the spectral method. The axial momentum, induction, and nonlinear energy equations are solved by expanding the axial velocity, magnetic field, and temperature in double Chebyshev series and are collocated at Gauss points. The resulting system of equations is solved numerically by Gauss elimination for the expansion coefficients. The velocity and the magnetic field coefficients are directly solved for, while the temperature coefficients are solved for iteratively. Results show that the velocity profile is flattened in the direction of the magnetic field, but it is more round in the direction normal to it, in a similar fashion to the case of circular tube studied previously. The powerful spectral method resolves the sharp velocity gradient near the duct walls very well leading to accurate calculation of friction factor and Nusselt number. These parameters increase with the strength of the magnetic field due to the increasing flatness of the velocity profile. Comparison with the results for the circular tube shows that the effect of magnetic field on square duct flow is slightly lower from that one for circular pipe flow.
[DOI: 10.1115/1.2177289]

Keywords: square duct flow, MHD flow, MFM flow, heated liquid metal flow, electrically conducted fluid flow, spectral method

1 Importance of the Topic

The flow of liquid metal inside a duct in a magnetic field, which is sometimes called magneto fluid mechanics (MFM) or magneto hydrodynamics (MHD), has been the primary interest of many researchers since the beginning of the last century. The topic has significant applications which have been reported such as the MHD generator, MHD flow meter, MHD pump, and the MHD engine, etc. Some other quite promising applications are in the field of metallurgy such as MHD stirring of molten metal and magnetic-levitation casting. A very useful proposed application which involves MHD is the lithium cooling blanket in a nuclear fusion reactor [1]. Because of the importance of this topic, it is essential to study this type of flow for different geometries (for example, square duct) and obtain some useful results using one of the innovative computational techniques.

Basic Conservation Equations

For incompressible Newtonian liquid metal fluid and steady-state conditions, the modified Navier-Stokes equations under the effect of magnetic field body force including induction and energy equations in vector forms are [2,3], respectively,

$$\rho(\mathbf{V} \cdot \nabla)\mathbf{V} + \nabla\left(p + \mu\frac{|\mathbf{H}|^2}{2}\right) = \mu_f\nabla^2\mathbf{V} + \mu(\mathbf{H} \cdot \nabla)\mathbf{H} \qquad (1)$$

$$\nabla^2\mathbf{H} + \mu\sigma[(\mathbf{H} \cdot \nabla)\mathbf{V} - (\mathbf{V} \cdot \nabla)\mathbf{H}] = 0 \qquad (2)$$

and

$$\rho c(\mathbf{V} \cdot \nabla)T = k\nabla^2 T + \mu_f\mathbf{\Phi} + \frac{|\mathbf{J}|^2}{\sigma} \qquad (3)$$

in addition to the solenoidal conditions on the two vectors

$$\nabla \cdot \mathbf{V} = 0 \text{ and } \nabla \cdot \mathbf{H} = 0 \qquad (4)$$

The induction equation, Eq. (2), can be derived from Maxwell's equations and Ohm's law along with the two solenoidal conditions, Eqs. (4). The last two terms in the right hand of the energy equation, Eq. (3), represent the viscous and Joulean dissipations, respectively. Those terms can be neglected compared to the other ones in the equation.

After simplifications by assuming fully developed flow, i.e., 2-D problem (see Fig. 1), and since the flow is laminar due to damping of the fluctuations of turbulence in the presence of magnetic field, the dimensionless governing equations for this flow become

$$\nabla^2 w^* - M\frac{\partial H^*}{\partial x^*} = 1 \qquad (5)$$

$$\nabla^2 H^* - M\frac{\partial w^*}{\partial x^*} = 0 \qquad (6)$$

and

$$\nabla^2\theta + 4 \text{ Nu } w\theta = 0 \qquad (7)$$

The negative dimensionless pressure gradient γ is related to w^* by

$$\gamma = \frac{1}{\displaystyle\int_0^1\int_0^1 w^* dx^* dy^*} \qquad (8)$$

Equation (7) was derived from the fact that the temperature is uniform at the duct surface and the axial conduction is negligible. From the force and energy balances one can show, respectively, that $f\text{Re} = -2\gamma$ and $\text{Nu} = -1/\theta_m$. The mean dimensionless temperature is given by

$$\theta_m = \frac{\displaystyle\int_0^1\int_0^1 \theta w dx^* dy^*}{\displaystyle\int_0^1\int_0^1 w dx^* dy^*} \qquad (9)$$

The boundary conditions are $w^* = 0$ (no-slip condition), $H^* = 0$ (electrically insulated surface), and $\theta = 0$ (for isothermal surface).

Numerical Method

We approximate the field variables by the following Chebyshev expansions [4–6]

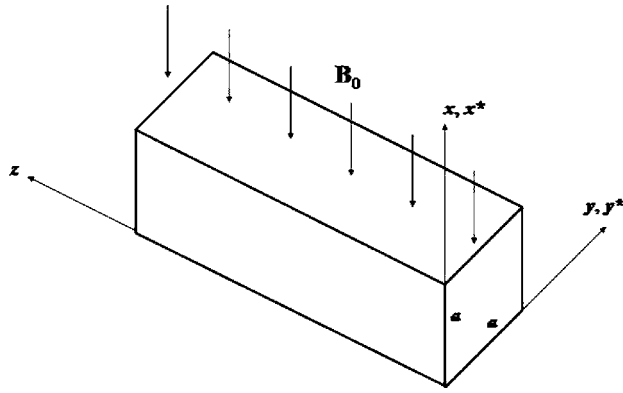$$w^* = \sum_{m=0}^{N_x-1}\sum_{n=0}^{N_y-1} C_{mn}^w X_m^w(\tilde{x})Y_n^w(\tilde{y}) \qquad (10)$$

Fig. 1 Problem geometry which shows the transverse magnetic field along a square duct flow

M	N_x	N_y	fRe	Nu
0	2	2	56.962025	3.142484
	4	4	56.908269	2.977548
	6	6	56.908305	2.977523
	8	8	56.908307	2.977523
	10	10	56.908307	2.977523
100	4	4	207.199209	4.085334
	8	8	466.415669	4.294817
	10	10	464.829611	4.293934
	14	14	464.453886	4.293740
	16	16	464.452197	4.293739
	18	18	464.452118	4.293739
	20	20	464.452115	4.293739
	22	22	464.452115	4.293739
1000	14	14	2692.677298	4.673257
	22	22	4175.508747	4.739214
	30	30	4172.604309	4.739107
	34	34	4168.101350	4.738950
	38	38	4166.978748	4.738912
	42	42	4166.764910	4.738904
	44	44	4166.740179	4.738903
	46	46	4166.730656	4.738903
	48	48	4166.727077	4.738903

$$H^* = \sum_{m=0}^{N_x-1} \sum_{n=0}^{N_y-1} C_{mn}^H X_m^H(\tilde{x}) Y_n^H(\tilde{y}) \tag{11}$$

$$\theta = \sum_{m=0}^{N_x-1} \sum_{n=0}^{N_y-1} C_{mn}^\theta X_m^\theta(\tilde{x}) Y_n^\theta(\tilde{y}) \tag{12}$$

where

$$\tilde{x} = 2x^*; \quad \tilde{y} = 2y^*$$

are algebraic mappings that transform the cross-section of the duct into the domain of Chebyshev polynomials, $[-1,1]$; X_m^w, X_m^H, X_m^θ, Y_n^w, Y_n^H, and Y_n^θ are linear combinations of Chebyshev polynomials, chosen to satisfy the boundary conditions implicitly

$$X_m^w(\tilde{x}) = X_n^H(\tilde{x}) = X_n^\theta(\tilde{x}) = = T_{2n+2}(\tilde{x}) - T_{2n}(\tilde{x}) \tag{13}$$

$$Y_m^w(\tilde{y}) = Y_m^\theta(\tilde{y}) = T_{2m+2}(\tilde{y}) - T_{2m}(\tilde{y}) \tag{14}$$

$$Y_m^H(\tilde{y}) = T_{2m+3}(\tilde{y}) - T_{2m+1}(\tilde{y}) \tag{15}$$

To exploit symmetry, even Chebyshev polynomials are selected for w^* and θ in both directions. Even polynomials are selected for H^* in the y direction and odd ones are chosen in the x direction. This reduces computational time and produces more accurate solutions.

The spectral solution presented here is divided into two parts. First, Eqs. (5) and (6) are solved simultaneously using the first two expansions, Eqs. (10) and (11), and then the energy equation, Eq. (7), is solved second using the third expansion, Eq. (12).
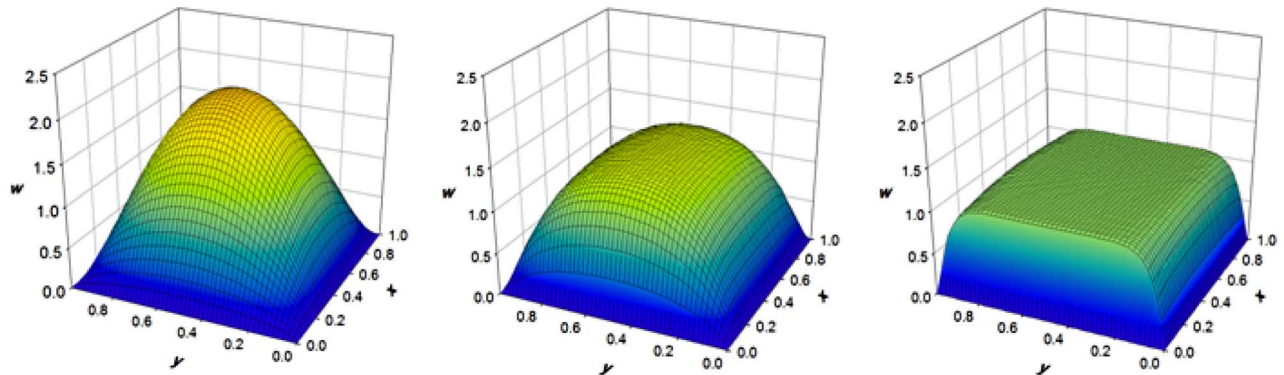
Equations (10) and (11) are substituted into Eqs. (5) and (6), respectively, and the resulting equations are satisfied at the Gauss points

$$(\tilde{x}_i, \tilde{y}_j) = \left(\cos \frac{(2i+1)\pi}{2N_x}, \quad \cos \frac{(2j+1)\pi}{2N_y} \right) \tag{16}$$

where $i = 0,1,2,\ldots,N_x-1$ and $j = 0,1,2,\ldots,N_y-1$. The resulting system of algebraic equations is written symbolically as

$$\mathbf{f}(\mathbf{C};M) = 0 \tag{17}$$

where $\mathbf{C}$ is a vector of size $N = 2N_xN_y$ containing the expansion coefficients C_{mn}^w and C_{mn}^H and $\mathbf{f}$ is a vector-valued function also of size N that contains the discrete form of Eqs. (5) and (6). Equation (17) represents a linear system of algebraic equations and is solved by Gauss elimination to yield the coefficients C_{mn}^w and C_{mn}^H from which the velocity w^* and normalized magnetic field H^* are computed through Eqs. (10) and (11).

Second, Eq. (7) is solved iteratively. Once w^* is known, γ can be computed from Eq. (8); however θ_m, and consequently Nu, cannot be computed from Eq. (9). As a result, a guessed value for Nu is first adopted and then Eq. (7) is solved by substituting Eq. (12) into Eq. (7) and the resulting equation is satisfied at the collocation points, Eq. (16). This yields a system of $N/2$ algebraic equations that is solved for the approximate coefficients of θ, i.e.,
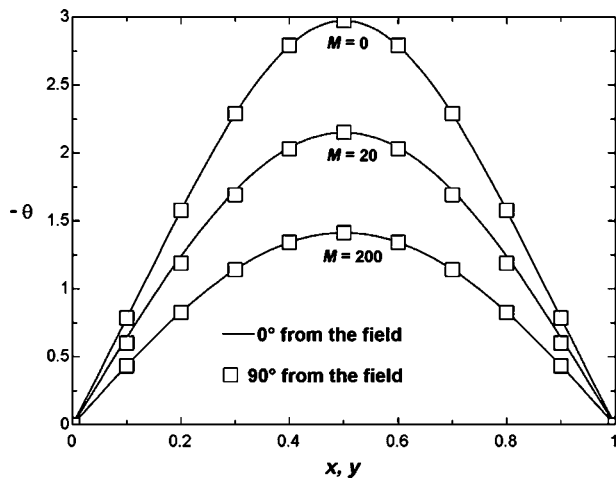

Fig. 2 3-D mesh of the dimensionless axial velocity profiles for (a) M=0, (b) M=20, and (c) M=200

Fig. 3 Negative dimensionless temperature profiles for $M=0$, $M=20$, and $M=200$ in the direction $(0°)$ and normal $(90°)$ to magnetic field
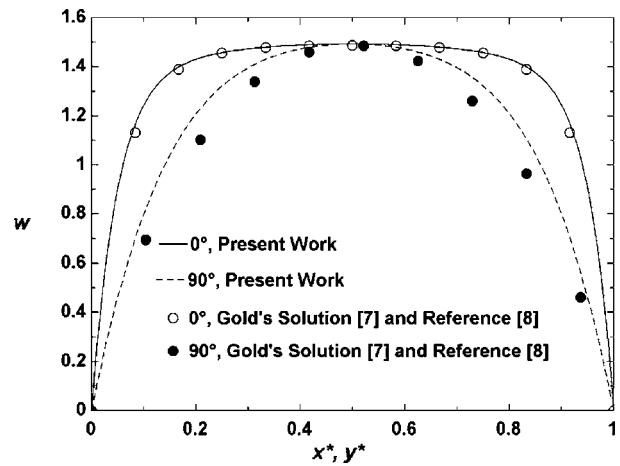

Fig. 4 Comparison between the present work and previous work for dimensionless axial velocity profiles for $M=20$ in the direction $(0°)$ and normal $(90°)$ to magnetic field

C_{mn}^{θ}. Once an approximation to θ is obtained, a more accurate value of Nu can be found from Eq. (9) and another approximation to θ is sought again by solving Eq. (7) using the new value of Nu. This process is repeated until successive approximations become within a small relative error from each other.

Results

The spectral method used gives a very highly accurate solution. Results show that the errors decrease to small values that approach zero as the number of expansion functions is increased. Table 1 shows the computed Nusselt number Nu, and the friction factor times the Reynolds number fRe as functions of the number of expansion functions in the x direction N_x and the number of expansion functions in the y direction N_y for $M=0$, 100, and 1000. As can be seen from the table, for $M \leqslant 100$, Nu and fRe can be computed with a precision of six decimal digits with as little as 6×6 to 8×8 expansion functions for $M=0$ and 16×16 to 20×20 expansion functions for $M=100$. The number of expansion functions yielding a solution with similar precision increases as the value of M increases. For example, for $M=1000$, as many as 44×44 expansion functions are needed to compute Nu with six

decimal digits of precision. This increase in the number of expansion functions yields a denser grid that is required to resolve the flow and temperature in the very thin boundary layers along the walls of the duct. In all cases the computed solutions converge, i.e., Nu=2.977523 for $M=0$, Nu=4.293739 for $M=100$, and Nu =4.738903 for $M=1000$.

Some useful results were obtained and presented in graphical forms. Figures 2(a)–2(c) describe the axial velocity in 3-D for $M=0$, 20, and 200. As M increases, the velocity profile flattens due to the effect of ponder-motive force induced by the magnetic field. For high Hartmann number, $M=200$, the velocity profile would be very steep at the wall and the axial velocity becomes almost uniform across the duct in the direction of the field. The profile is more round for direction normal to the magnetic field; this is because the ponder-motive force there is less effective. However, the directional effect of the magnetic field on temperature is less important. The negative dimensionless temperature profiles, shown in Fig. 3, are almost identical in the direction of the magnetic field and normal to it. Also, we notice from the figure that the temperature over the cross section becomes more homogenous as the Hartmann number increases.
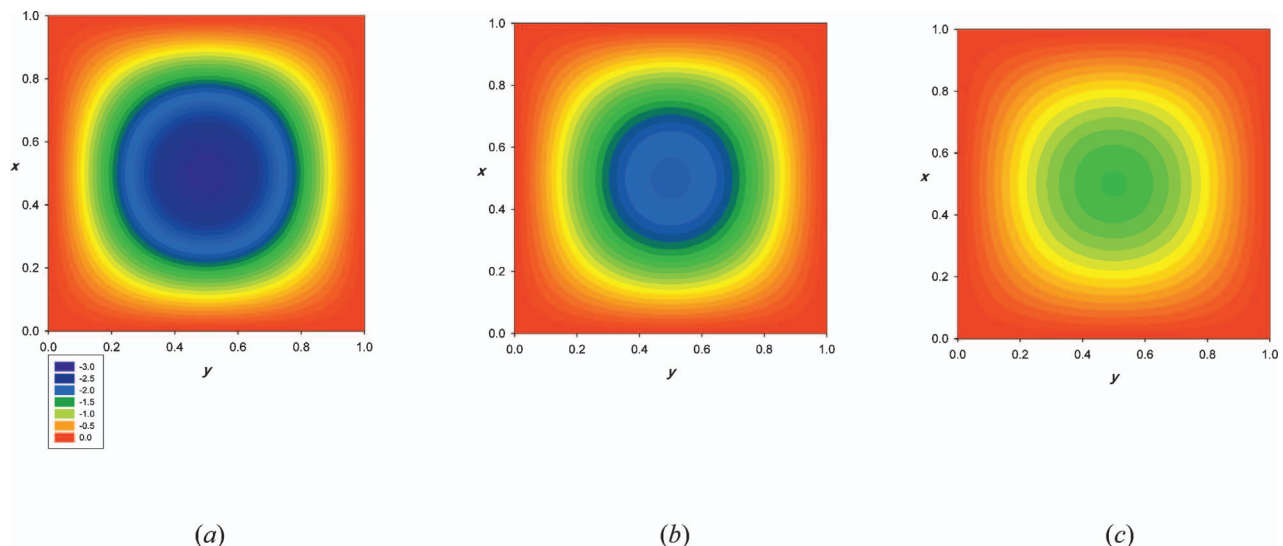

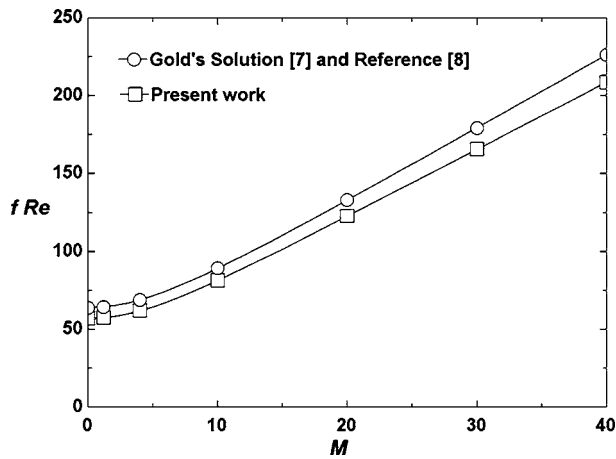**Fig. 5** Temperature contours shown in color bands for (a) $M=0$, (b) $M=20$, and (c) $M=200$

Fig. 6   Friction factor as a function of low and moderate *M* (i.e., *M*<40) for the present work (square duct) and previous work (circular tube)

Fig. 8   Nusselt number as a function of *M* for the present work (isothermal surface square duct) and previous work (uniform surface-heat-flux circular tube)

For the purpose of comparison, the dimensionless axial velocity for $M=20$ for both square duct (present work) and circular tube [7,8] is presented. Figure 4 shows that, in the presence of the magnetic field, the axial velocity in the direction of the field is almost identical for both geometries. However, the situation is different for the normal direction.

The temperature distributions for different Hartmann numbers are presented in Figs. 5(*a*)–5(*c*) as color contour plots. It is obvious that for any of the Hartmann numbers, the temperature is distributed symmetrically over the duct cross section. However the distribution will be more uniform over the cross section as M becomes larger and this is consistent with Fig. 3.

For further comparisons with the circular tube case, Figs. 6–8 show a friction factor for low to moderate M (i.e., $M<40$), a friction factor for higher range of M (i.e., $0<M<200$), and a Nusselt number, respectively, as a function of M for the present work (isothermal surface square-cross section) and previous work (uniform surface-heat-flux circular-cross section), [7–9]. It is evident that as the Hartmann number increases, the friction factor increases and becomes linear for higher Hartmann numbers with the slope for the square duct being slightly smaller than that for the circular tube, see Fig. 7. Similarly, the effect of the magnetic field on the Nusselt number, as seen in Fig. 8, is slightly stronger for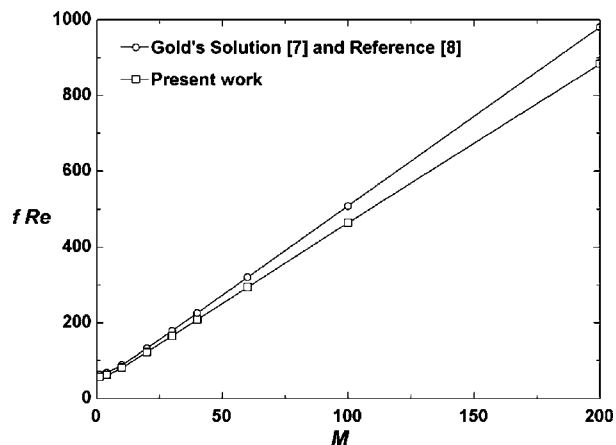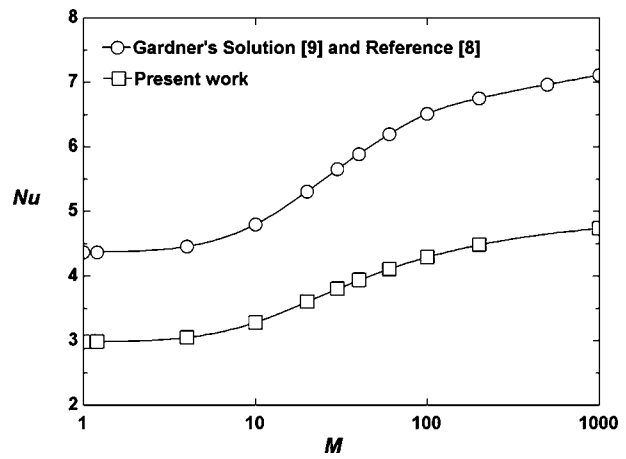 the round tube geometry. We know that for conventional laminar internal flow (i.e., no magnetic field body force) with heat transfer in a circular tube, Nu=3.66 for constant temperature and Nu=4.36 for constant heat flux. For a square duct, Nu=2.98 for constant temperature and Nu=3.61 for constant heat flux. It is clear from this that the heat transfer rate is higher in the case of circular tube and uniform surface heat flux. In the presence of magnetic, Nu (thus heat transfer) increases for both cases. However, Nu for circular tube with uniform heat flux increases more than that for square duct with uniform temperature as the magnetic field becomes stronger. This is shown clearly in Fig. 8. Thus, one can say the effect of the magnetic field on heat transfer is stronger in the case of circular tube with uniform heat flux.

Conclusion

In conclusion, some useful results were obtained for MFM square duct flow with heat transfer. It is found that the effect of the magnetic field on the flow and heat transfer is slightly lower than that for flow in a circular tube with a constant heat flux boundary condition. This effect is an increase in pressure drop and heat transfer due to the uniformity of the axial velocity particularly in the direction of the magnetic field. For very high Hartmann numbers, the Nusselt number in both flows will approach the case where the velocity is uniform along the cross section in any direction.

Nomenclature

B_0 = uniform magnetic induction (T)
c = specific heat (J/kg °C)
D_h = hydraulic diameter (m)
f = friction factor
$\mathbf{H}$ = magnetic field vector (A/m)
H = dimensionless axial magnetic field, $H_z/(V_m(\sigma\mu_f)^{1/2})$
H_z = axial magnetic field (A/m)
H^* = normalized axial magnetic field, H/γ
h_c = heat-transfer coefficient (w/m^2 °C)
$\mathbf{J}$ = electric current density vector (A/m^2)
k = thermal conductivity of fluid (w/m °C)
M = Hartmann number, $B_0D_h(\sigma/\mu_f)^{1/2}$
Nu = Nusselt number, h_cD_h/k
p = fluid pressure (N/m^2)
q = surface heat flux [W/m^2]
Re = Reynolds number, V_mD_h/ν
T = temperature (°C)

Fig. 7   Friction factor as a function of high range of *M* (i.e., 0 <*M*<200) for the present work (square duct) and previous work (circular tube)

T_s = surface temperature (°C)

$\mathbf{V}$ = velocity vector (m/s)

V_m = mean axial velocity (m/s)

V_z = axial fluid velocity (m/s)

w = dimensionless axial velocity, V_z/V_m

w^* = negative normalized axial velocity, w/γ

x^* = dimensionless x-coordinate, x/a

y^* = dimensionless y-coordinate, y/a

Greek Letters

γ = nondimensional pressure gradient, $((\partial p/\partial z)(D_h^2))/V_m\mu_f$

θ = dimensionless temperature, $(T-T_s)/(D_h q/k)$

μ = magnetic permeability of fluid (H/m)

μ_f = dynamic viscosity of fluid (N s/m^2)

ν = kinematic viscosity of fluid, m^2/s

ρ = density of fluid (kg/m^3)

σ = electrical conductivity of fluid (A/V m)

References

[1] Branover, H., 1978, *Magnetohydrodynamic Flow in Ducts*, Keter Publishing House Jerusalem Ltd., Jerusalem.

[2] Al-Khawaja, M. J., Agarwal, R. K., and Gardner, R. A., 1999, "Numerical Study of Magneto-Fluid-Mechanic Combined Free-and-Forced Convection Heat Transfer," Int. J. Heat Mass Transfer, **42**, pp. 467–475.

[3] Al-Khawaja, M. J., 1992, "Combined Free-and-Forced Convection in a Transverse Magnetic Field," DSc. dissertation, Washington University, St. Louis, MO.

[4] Selmi, M., Nandakumar, K., and Finlay, W., 1994, "A Bifurcation Study of the Flow Through a Rotating Curved Duct," J. Fluid Mech., **262** (4), pp. 353–375.

[5] Selmi, M., and Nandakumar, K., 1999, "Bifurcation Study of Flow Through Rotating Curved Ducts," Phys. Fluids, **11**, pp. 2030–2043.

[6] Selmi, M., and Nandakumar, K., 2002, "Highly Accurate Solutions of the Bifurcation Structure of Mixed Convection Heat Transfer Using Spectral Method," Int. J. Numer. Methods Fluids, **40**, pp. 6190–638.

[7] Gold, R., 1962, "Magnetohydrodynamic Pipe Flow Part 1," J. Fluid Mech., **13**, pp. 505–512.

[8] Al-Khawaja, M. J., Gardner, R. A., and Agarwal, R., 1994, "Numerical Study of Magneto-Fluid-Mechanics Forced Convection Pipe Flow," Eng. J. Qatar Univ., **7**, pp. 115–134.

[9] Gardner, R. A., 1968, "Laminar Pipe Flow in a Transverse Magnetic Field with Heat Transfer," Int. J. Heat Mass Transfer, **11**, pp. 1076–1081.